Summer 8-29-2013

Galactic Dark Matter

Benjamin Paul Burch
Washington University in St. Louis

WASHINGTON UNIVERSITY IN ST. LOUIS

Department of Physics

Dissertation Examination Committee:
Ramanath Cowsik, Chair
James Buckley
Martin H. Israel
Michael Ogilvie
Lee Sobotka
Slava Solomatov

Galactic Dark Matter

by

Benjamin P. Burch

A dissertation presented to the
Graduate School of Arts and Sciences
of Washington University in St. Louis in
partial fulfillment of the
requirements for the degree
of Doctor of Philosophy

August 2013

Saint Louis, Missouri

Contents

List of Figures

List of Tables

Acknowledgements

My mother often told me as I was growing up that I had to be a doctor, but it did not matter what kind. Of course, being a stubborn child, I chose the most difficult and therefore interesting subject I could find. Thank you Mom and Dad for enrolling me in science summer camps and for encouraging my interests when I was little. You have been a constant source of support and encouragement during every step of my education. I would not have made it this far without your shoulders to stand on.

I owe an immense debt of gratitude to my advisor Ramanath Cowsik for his generous support and invaluable guidance. Thank you for pushing me down many different roads and for being supportive when I needed advice on how to find my way.

The fellow members of my research group were always there for me when I needed anything, big or small. Thank you Trecia Stumbaugh, Tsitsi Madziwa-Nussinov, Kasey Wagoner, Chris Markle, Adam Archibald, and Mike Abercrombie.

I would like to thank Pijush Bhattacharjee for his hospitality at the Saha Institute of Nuclear Physics in Kolkata, India where I spent two months learning much about the detection of dark matter.

I have many friends who, probably unbeknownst to them, were responsible for my sanity during the most difficult parts of graduate school. The hundreds, if not

thousands, of Spades games, the late nights talking about everything and nothing, the hilarity during coffee hour, and an uncountable number of ridiculous moments will be long remembered. In no particular order, I thank John Flavin, Dimitris Manolidis, Mike DeSantis, and Shawn DeCenzo. You know what you did.

I thank my brother John Burch for sharing my sense of humor and interest in most things with wires. You are always around when I need help with something technical or to listen to my ideas, and for that, I am grateful.

Finally, I would like to thank my loving wife Lizz Callahan and my wonderful children Devin and James. Boys, you keep my improvisational story telling skills sharp and give me endless supply of wonderful distractions from work. Turtle power!

Lizz, your love and support has been essential to the completion of this dissertation. Thank you for giving me a reason to hurry up and finish. I love you.

ABSTRACT OF THE DISSERTATION

Galactic Dark Matter

by

Benjamin P. Burch

Doctor of Philosophy in Physics

Washington University in St. Louis, 2013

Professor Ramanath Cowsik, Chair

The precise phase-space distribution and properties of Galactic dark matter necessary for its direct and indirect detection are currently unknown. Since the distributions of normal and dark matter in the Milky Way are coupled to each other as they both move in the same gravitational potential, constraints on the distribution and properties of dark matter can be derived by studying the distribution of visible matter in the Galaxy and making some general assumptions regarding the phase-space distribution of the dark matter. In this study, the visible components of the Galaxy have been comprehensively reviewed to create an axisymmetric model of the Galaxy that is consistent with the available observations, and the dark matter phase-space distribution is assumed to follow a lowered-isothermal form. Poisson's equations are then solved self-consistently to construct models of the spatial and velocity distribution of Galactic dark matter. The total gravitational potential from normal and dark matter are calculated and compared to the current observations of the rotation curve and to the radial velocity distributions of blue horizontal-branch and blue straggler stars. It is found that this analysis allows for a wide range of parameters for the dark matter. The implications for direct and indirect detection of dark matter are discussed in detail.

In the appendices, two additional projects are presented. In Appendix A, the recent observations of the positron fraction and the total electron spectrum in cosmic rays are addressed by considering a nested leaky-box model for the propagation of cosmic rays in the Galaxy. This is found to obviate the need for exotic processes such as the annihilation or decay of dark matter to explain the recent observations. In Appendix B, we discuss a novel dark matter detector involving triggered cavitation

in acoustic fields. The theory behind the detector is presented in detail, and we discuss the work than has been done to create a prototype at Washington University.

Chapter 1

Introduction

Since Isaac Newton, physicists have tried to understand the dynamical laws that describe the motions of astrophysical objects. While observations of celestial objects have led to the discovery of the laws of gravitation and progressively to the current understanding of the universe, called ΛCDM cosmology, such observations have also given rise to questions that have remained unanswered for several decades. The rotation speeds of galaxies and clusters of galaxies as a function of distance from their center of mass have provided evidence for the presence of unseen matter needed to reconcile the observations with the gravitational force provided by luminous matter alone. These observations along with estimates from Big Bang nucleosynthesis calculations and observations of the cosmic microwave background indicate that this unseen matter has about five times the abundance of normal baryonic matter in the universe.

The discovery of the need for a non-baryonic and non-luminous form of matter in the universe to account for myriad observations on galactic and extra-galactic

scales has been the source of intense study for several decades, but surprisingly, the nature of this dark matter remains largely unknown. While gravitational lensing, numerical simulations of structure formation, and measurements of the rotation curves of numerous galaxies have allowed a glimpse into the distribution of dark matter on galactic and extra-galactic scales, its distribution within our own Galaxy is not well-understood. In this thesis, we aim to derive limits on the phase-space distribution of dark matter in the Milky Way and near Earth where detectors placed underground are already ruling out potential candidates for dark matter. Understanding the local phase-space distribution of dark matter is essential for properly interpreting these dark matter experiments. We also discuss the implications the constrained phase-space distribution has on the possible detection of dark matter.

In this chapter, we review the current understanding of dark matter and the attempts to discern its properties. In Section 1.1, we review the standard model of cosmology, which includes both dark matter and dark energy, and in Section 1.2, we discuss the historical evidence for dark matter and its suspected nature. The properties that a dark matter candidate must possess and some possible candidates are discussed in Section 1.3. In Section 1.4, direct and indirect detection experiments are discussed, and in Section 1.5, the motivation and outline for the rest of the thesis is given.

1.1 The Current Perspective on Cosmology

In the currently accepted standard model of cosmology (see [1] for example), the universe began ∼13.8 billion years ago [2] with a rapid expansion from a singular state called the Big Bang, and since then, the universe has continued to expand and cool. During this expansion, events such as the recombination of electrons and protons into hydrogen and the nucleosynthesis of other light elements have influenced the dynamics and normal matter content in the universe. The cosmological model developed to understand these events is called the ΛCDM model where Λ represents dark (vacuum) energy and CDM stands for cold dark matter.

Evidence for the Big Bang can be traced back to the discovery of Hubble's Law, which indicates that our universe is expanding. The rate of expansion is given by the Hubble parameter defined by

$$H(t) = \frac{\dot{a}(t)}{a(t)}, \tag{1.1}$$

where $a(t)$ is the scale factor factor defined such that $a(0) = a_0 = 1$. The present value of the Hubble constant ($H(0) = H_0$) [3] is

$$H_0 = 73 \pm 3 \text{ km s}^{-1} \text{ Mpc}^{-1}. \tag{1.2}$$

The evolution of the Hubble parameter, and therefore the expansion of the universe, is given by the Friedmann equation

$$H(t)^2 + \frac{k}{a(t)^2} = \frac{8\pi G}{3}\rho_{tot}, \tag{1.3}$$

where k can take on the values -1 (open), 0 (flat), or 1 (closed) and describes the curvature of the universe as noted in parentheses. The parameter ρ_{tot} is the total average energy density of the universe, and G is the gravitational constant. In this formulation, the Friedmann equation is the solution to Einstein's equations for an isotropic and homogeneous universe and neglecting vacuum energy. Including the vacuum energy term, Friendmann's equation becomes

$$H(t)^2 + \frac{k}{a(t)^2} = \frac{8\pi G}{3}\rho_{tot} + \frac{\Lambda c^2}{3}, \tag{1.4}$$

where c is the speed of light and Λ is the cosmological constant.

From the condition that the universe is flat ($k = 0$), one can immediately derive a critical density from eq. 1.3

$$\rho_{crit} = \frac{3H(t)^2}{8\pi G}. \tag{1.5}$$

The density of the various components of the universe is typically scaled in terms of ρ_{crit} and written as

$$\Omega_i = \frac{\rho_i}{\rho_{crit}}, \tag{1.6}$$

where i refers to the substance (matter, radiation, etc.).

The different components of the galaxy are defined by different equations of state which relate the energy density of a component to its pressure by

$$p_i = w_i \rho_i, \tag{1.7}$$

where p is the pressure, ρ is the energy density, and

$$\begin{aligned} w_M &= 0, \\ w_R &= \frac{1}{3}, \\ w_\Lambda &= -1, \end{aligned}$$

where M and R refer to non-relativistic matter and relativistic species, including photons and neutrinos, respectively. From the equation of state (eq. 1.7), the time evolution of the density can be derived [4] and has the form

$$\rho_i \propto a(t)^{-3(1+w_i)}. \tag{1.8}$$

From the choices of w_i above, we can see that

$$\begin{aligned} \rho_M &\propto a(t)^{-3}, \\ \rho_R &\propto a(t)^{-4}, \\ \rho_\Lambda &= \text{constant}. \end{aligned}$$

Note that the density of radiation falls as the fourth power, and its contribution to the total energy density today is negligible ($\Omega_R \sim 5 \times 10^{-5}$ [5]). The total energy density of the universe is the sum of contributions from each component, which can

be seen by rewriting the Friedmann equation as

$$\left(\frac{H(t)}{H_0}\right)^2 = \Omega_\Lambda + \Omega_k\left(\frac{a}{a_0}\right)^2 + \Omega_M\left(\frac{a}{a_0}\right)^3 + \Omega_R\left(\frac{a}{a_0}\right)^4. \tag{1.9}$$

The density Ω_M includes the contributions from both baryonic matter (Ω_B) and cold dark matter (Ω_{CMD}).

Current estimates of the energy density of the various components of the universe come from observations of the cosmic microwave background, the relic from the Big Bang of 2.7 K radiation that permeates the universe, measured by the WMAP experiment [2] and find

$$\Omega_\Lambda = 0.725 \pm 0.016 \tag{1.10}$$

$$\Omega_{CDM} = 0.229 \pm 0.015 \tag{1.11}$$

$$\Omega_B = 0.0458 \pm 0.0016. \tag{1.12}$$

These densities sum to $\Omega_{total} \approx 1$, implying that $\Omega_k \approx 0$, and that the universe is very close to flat. These results also imply that $\sim$95% of the energy density of the universe is comprised of dark energy and dark matter. The nature of neither component is currently well understood.

1.2 Early Evidence for Dark Matter

The historical effort to understand dark matter in the universe can be divided into two categories. The first concerns the dynamical studies of galaxies and clusters, in which

effort is made to infer the dark matter distribution in various systems from observations of the spatial and velocity distributions of stars and galaxies. These studies began with Zwicky's 1933 observations [6] of the velocities of a subset of galaxies in the Coma cluster, which showed that the galaxies were moving too quickly to be bound by the visible matter in the cluster alone. The second category concerns determining the properties of dark matter itself, including what particles constitute dark matter, by what means these particles interact with ordinary matter and themselves, their cosmological origins, and how to test, directly via laboratory experiments or indirectly via astronomical observations, whatever predictions that can be made. Efforts in this second category began in 1972-73 with Cowsik and McClelland's [7, 8] suggestions that weakly-interacting relic particles, such as neutrinos, would dominate the gravitational dynamics of the universe and generically lead to invisible clouds of dark matter, in which galactic structures are imbedded. This could explain the virial discrepancy and other dynamical effects of dark matter. We briefly review the early developments in both categories separately.

1.2.1 Dynamical Studies

The story of the effects of dark matter on galactic dynamics is usually told beginning with Fritz Zwicky's 1933 observations of the Coma cluster [6]. Using the virial theorem, Zwicky found that the dynamics of galaxies in the cluster implied the cluster's mass was 200 times that determined from the luminosity of its constituent galaxies. Zwicky referred to the unseen mass as "dark matter". Around the same time, Oort [9] studied the vertical force on stars located perpendicular to the plane of the

Milky Way and found a need for an unidentified mass concentrated in the plane of the Galaxy. However, it was not until the early 1970s that the presence of invisible gravitating mass on both galactic and extragalactic scales became widely observed and recognized as a serious problem for both galactic dynamics and studies of the large-scale structure of the universe. Observations of the Coma cluster by Rood et al. [10]; Abell [11]; Omer, Page, and Wilson [12]; and others agreed with Zwicky's basic conclusion that the mass-to-light ratio of the cluster is far greater than that seen in individual galaxies. The most straightforward explanation of the excessively high mass-to-light ratio in the Coma cluster is that there is missing mass with a high concentration in the center of the system. Observations of other clusters of galaxies such as M81 [13, 14] and the Seyfert Sextet [15] show similarly high mass-to-light ratios, necessitating an explanation as to how these systems could be bound by the amount of visible mass in the clusters.

Early explanations as to the source of this invisible mass are summarized in Peebles' *Physical Cosmology* [16]. Luminosities may have been underestimated due to unseen dwarf galaxies and intergalactic stars in the clusters. Unseen mass may exist in the form of dust between the galaxies, but there are strong upper limits on the amount of atomic hydrogen in the cluster from observations of 21 cm emission. A "condensed hydrogen snow" may exist between galaxies in clusters, but this population of finely distributed small clusters of hydrogen is limited by the amount of light it would scatter, and the mass of the hydrogen snow ball is limited by its scattering cross section. A dense population of large hydrogen snowballs would quickly vaporize due to collisions. Small black holes distributed throughout the cluster were considered as

possible sources of the extra gravitational mass, but their mass is constrained by gravitational lensing observations and such light black holes may evaporate too quickly to explain dark matter. The observations of missing mass also inspired thoughts of new physics such as the spontaneous creation of galaxies. The missing mass problem was also addressed in Ginzburg's *Key Problems in Physics and Astrophysics* [17] where explanations also included interstellar gas and low-luminosity stars as well as the capture of neutrinos by clusters and galaxies to stabilize halos. While violations of general relativity and exotic processes such as the creation of mass at the centers of galaxies were considered, there were many physicists at the time who believed that a combination of conventional physics and improved observations would solve the excess mass problem.

Measurements of the rotational speeds as a function of galactocentric distance for dozens of galaxies by Rubin, Rood, and others [18, 19, 20, 21] implied that the rotation curve did not exhibit a Keplerian falloff as is expected for galaxies where most of the mass is concentrated in a central bulge. From Newtonian dynamics, the rotation speed v_c at a distance R from the center of mass of the galaxy is given by

$$v_c(r) = \sqrt{\frac{GM(R)}{R}}. \tag{1.13}$$

Instead of falling off as $1/\sqrt{R}$ at large distances from the galactic center, the observed rotation curves remained flat or even slightly increased with galactocentric distance until the very edge of the galaxy. This indicated that the mass of these galaxies is increasing at least linearly with distance. Again, the mass implied by the dynamics

of each galaxy was much larger than that implied from its luminosity. To explain these observations, Cowsik and Ghosh [22] hypothesized that these galaxies reside in a large halo of invisible matter.

Several studies of our own Galaxy have attempted to determine the distribution of Galactic dark matter. Bahcall [23, 24, 25] and Kuijken and Gilmore [26, 27, 28] improved upon Oort's analysis [9] of the dynamics of stars perpendicular to the Galactic plane in order to determine the local visible and dark matter mass density. These studies have been continued by Flynn and Fuchs [29], Holmberg and Flynn [30, 31], and others with the usual conclusion that very little dark matter (less than 10% of the mass density) is found the Galactic disk. Cowsik et al. [32, 33] have self-consistently derived the spatial distribution of dark matter particles and have shown that a wide range of dark matter models will fit the Galactic rotation curve. Sofue, Honma, and Omodaka [34] and others have also used the Galactic rotation curve to constrain the dark matter density distribution in the Galaxy. These studies have shown that there is still much work to be done in understanding the nature of Galactic dark matter as even the basic parameters of dark matter models, such as the local dark matter density and the velocity dispersion, are not well known.

1.2.2 The Nature of Dark Matter

By the 1970s, it was known that massive neutrinos would affect the dynamics and structure of the universe as it expands. In 1973, Cowsik and McClelland [8] proposed weakly-interacting massive particles (specifically, massive neutrinos) as a candidate for the missing mass seen on extragalactic scales. Neutrinos with a rest mass greater

than a few eV/c^2–Cowsik and McClelland had recently shown that the neutrino mass had an upper limit of 8 eV/c^2 from measurements of the expansion of the universe [7]–would dominate the gravitational dynamics of the universe and may have triggered the initial condensation leading to galaxy cluster formation. Then, one would expect to find a large amount of neutrinos in galaxy clusters. Cowsik and McClelland proposed a simple model showing how massive neutrinos could gravitationally bind the Coma cluster [8]. In a key paper, which was a harbinger of cold dark matter, Lee and Weinberg [35] proposed a lower bound on heavy neutrinos of 2 GeV. Neutrinos between 40 eV and 2 GeV are excluded by observations of the photon density in the cosmic microwave background (see Gershtein and Zel'dovich [36]). Szalay and Marx [37] found that neutrinos with a rest mass greater than 15 eV violates observations of the Hubble constant, the deceleration parameter, and the age of the universe. Tremaine and Gunn [38] determined that neutral stable leptons with a mass $\leq$ 1 MeV are unable to support the massive galactic halos seen from dynamical observations though they did not rule out the heavy neutrinos of Lee and Weinberg [35]. While current observations of the neutrino rest mass seem to exclude them as the dominant component of dark matter, other weakly-interacting massive particles were proposed as dark matter candidates.

In the late 1980s, Shandarin and Zeldovich [47] reviewed the need for dark matter from the point of view of the large-scale structure of the universe. If the mass of the universe was dominated by baryons, it would be difficult to explain structure formation and the observations of the cosmic microwave background (CMB). Weakly-interacting massive particles were considered to be the most probable solution with

photinos, neutrinos, and axions among the leading candidates. It was already known, however, that there are not enough neutrinos to drive large-scale structure formation. In 1982, Peebles [48] suggested that a form of weakly-interacting cold dark matter was needed to explain observations of the power spectrum of the CMB. The late 1980's saw the development of experiments to directly detect dark matter via small deposits of energy into cryogenic materials [49, 50], and those efforts are still ongoing in the CDMS, PICASSO, XENON, and LUX experiments [51, 52, 53, 54], among many others. The most favored candidates for dark matter are the suspersymmetric neutralino and the axion due to their possibility of being either discovered or ruled out within the next decade. The axion [39, 40, 41, 42], was originally proposed to solve the strong CP problem [43, 44, 45], and the neautralino arises from supersymmetric extensions of the standard model of particle physics [46]. The axion and neutralino are well-studied, and efforts are underway to detect them in the laboratory. Comprehensive reviews of the history and current state of dark matter research can be found in the literature [46, 55, 56, 57, 58, 59, 60].

1.3 Dark Matter Properties and Candidates

Though the evidence for cold dark matter is strong, its specific properties are still widely unknown. There are, however, observational constraints that can be put on the characteristics a dark matter particle must have. Taoso, Bertone, and Masiero [61] have detailed a "Ten-Point Test" that all dark matter candidates must obey to be considered viable. We reproduce the list here in italics and add additional comments

to each question:

1. Does it match the appropriate relic density?

Early in the history of the universe, the dark matter candidate must have existed in an abundance that would explain the current measurements of Ω_{CDM}. This abundance is called the relic density. Shortly after the Big Bang, when the temperature was still very high, all species of particles are expected to be in thermal equilibrium with their equilibrium number density given by [58]

$$n^{eq} = g\left(\frac{M_\chi T}{2\pi}\right)^{3/2} e^{-M_\chi/T}, \tag{1.14}$$

where M_χ is the mass of the particle, T is the temperature of the universe, and g is the internal degrees of freedom such as spin, isospin, color, and polarization. When the T drops below M_χ as the universe expands, interactions between the particles become less likely, and when the interaction rate of the particles becomes smaller than the expansion rate of the universe, the species of particle falls out of thermodynamic equilibrium with the expanding universe, a process called freeze out.

For dark matter, the density at which this happens can be calculated from the Boltzmann equation [58], and an approximation of the relic density is given by

$$\Omega_{CDM}h^2 \approx \frac{3\times 10^{-27}\mathrm{cm}^3\mathrm{s}^{-1}}{<\sigma v>}, \tag{1.15}$$

where $h = H_0/(100\ \mathrm{km\ s^{-1}\ Mpc^{-1}})$ is the scaled Hubble constant and $<\sigma v>$ is the thermal average of the dark matter annihilation cross section multiplied by velocity.

A single dark matter species or the contributions from a number of separate dark matter species must be able to reproduce the well-constrained value for Ω_{CDM}.

2. Is it cold?

Cold in this case refers when dark matter particles become non-relativistic. In the standard view of galaxy formation, baryons become trapped in gravitational potential wells set up by the dark matter. For this to be the case, dark matter must become non-relativistic well before baryonic matter to provide time for dark matter to clump on small scales, providing the frame work for the later formation of galactic structures. Hot dark matter, such as neutrinos, are relativistic particles and do not clump on the scales necessary to drive structure formation in the universe.

3. Is it neutral?

This arises from the fact that we are only able to infer the existence of dark matter on galactic and extra-galactic scales from purely gravitational interactions and not from interactions with electromagnetism in the form of photons. Hence, this exotic matter has been termed "dark". There are, however, some proposed dark matter particles with fractional electric or color charge. Details can be found in the literature [61].

4. Is it consistent with BBN?

Big Bang Nucleosynthesis (BBN) is the prediction of the abundances of the light elements (deuterium, helium, and lithium) within the first three minutes after the Big Bang. Currently, predictions from BBN agree with observations of the current abundances of these elements by over nine orders of magnitude [61] and therefore is a tight constraint on the contribution of dark matter to the early dynamics of the

universe.

5. Does it leave stellar evolution unchanged?

The interiors of stars are hot enough that light dark matter particles may be produced. If the dark matter escapes without interacting significantly with the star, then the dark matter will become a source of energy loss in the star. If the energy loss is great enough, the evolution of the star may be changed. Constraints on these particles would also come from their possible direct detection (similar to the case of Solar neutrinos) or the detection of their decay or annihilation products.

6. Is it compatible with constraints on self-interactions?

A striking example of the collisionless nature of dark matter comes from observations of the Bullet Cluster [62]. In Fig.1.1 the merger of two clusters of galaxies is shown. The left figure shows the visible spectrum where the galaxies that make up each cluster are seen. The right figure show the same image in the x-ray spectrum. The green contours shows the gravitational potential determined by gravitational lensing. These images are interpreted as the collision of two clusters of galaxies. The bulk of the visible mass is in the form of the hot gas, which has collided and rests in the center of the image. The galaxies, which are sparse and have a low interaction cross section with each other, have largely passed by each other as have the clouds of dark matter associated with each cluster as indicated by the gravitational lensing observations, which show that the majority of the gravitational mass is found with the galaxies and not with the hot gas.

In addition to the observations of the Bullet cluster, constraints on the self-interaction come from the relic density calculation and from the structure of galaxies.

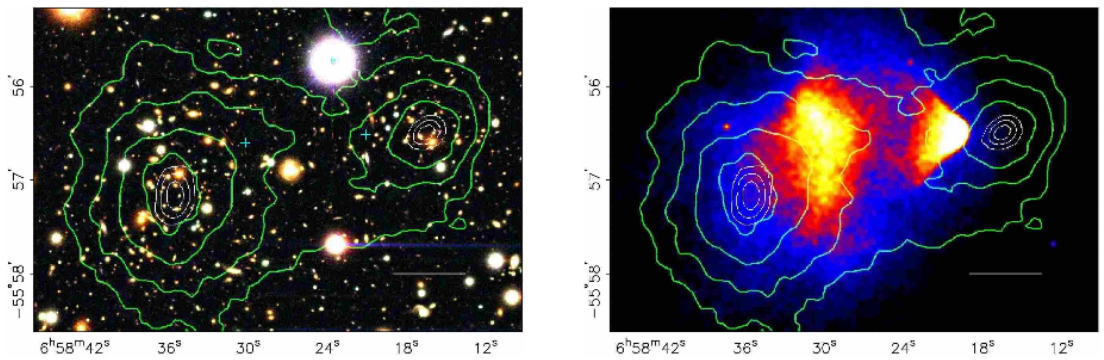

Figure 1.1: Images of the Bullet Cluster in the visible spectrum (left) and in x-ray (right) are shown along with the mass distribution from gravitational lensing (green contours). The typical interpretation is that this image shows two clusters of galaxies after they have collided. Most of the visible mass of the cluster is in the hot gas, which after interacting, is found to lag behind the visible galaxies that have passed by each other. However, most of the gravitational mass is found with galaxies, indicating that the dark matter clouds surrounding the clusters have not collided like the x-ray gas but passed through each other with little interaction. This figure is taken from [62].

If dark matter self-interactions were common, the large halos of dark matter surrounding galaxies and clusters would quickly collapse from energy lost in collisions. There is, however, some evidence that dark matter may self-interact near the center of galaxies. N-body simulations of galaxy formation often find that the density of dark matter in the centers of galaxies should increase rapidly towards the center. However observations of dwarf galaxies, which are thought to be dominated by dark matter, often show a constant dark matter density near the core. These discrepancies have been attributed to annihilation of dark matter in the galactic centers.

7. Is it consistent with direct DM searches?

The direct detection of dark matter and its current constrains on the interaction cross section for dark matter particles is discussed later in detail in Chapter 4.

8. Is it compatible with gamma-ray constraints?

The indirect detection of dark matter via gamma-ray emissions either through its annihilation or decay is discussed later in this thesis in Chapter 5.

9. Is it compatible with other astrophysical bounds?

Aside from gamma-rays, dark matter annihilation or decay may produce anti-matter or other cosmic rays. Recently, there has been much excitement in the cosmic-ray community about anti-matter in the form of positrons and anti-protons and their implications for a dark matter source of cosmic rays. In Appendix A, we discuss in detail the electronic component of cosmic rays and show that there may not be need for a dark matter explanation for the recent observations.

10. Can it be probed experimentally?

If there is no method for detecting, either directly or indirectly, a dark matter candidate, then it should be set aside in order to study those whose discovery may be possible. There are many dark matter candidates whose detection is currently beyond our technological means, but improvements to detector technology and clever new methods will allow for the testing of many dark matter candidates in the upcoming decades.

1.3.1 The Local Properties of Dark Matter

Knowing the dark matter density and velocity dispersion is essential to analyzing direct and indirect detection experiments. By modeling the mass and dynamics of the Milky Way, the local dark matter density $\rho_{DM}(R_0)$, where R_0 is the distance from the Sun to the Galactic center, has been estimated by many groups and has been constrained to the range $\sim 0.2 - 0.6$ GeV cm^{-3}: ~ 0.39 GeV cm^{-3} [63], 0.2-0.4

GeV cm^{-3} [64], 0.40 ± 0.04 GeV cm^{-3} [65], $0.43 \pm 0.11 \pm 0.10$ GeV cm^{-3} [66], 0.3±0.1 GeV cm^{-3} [67]. An isothermal dark matter halo with a $\rho_{DM}(R_0) = 0.3$ GeV/cm^3 and $< v_{DM}^2 >^{1/2} = 270$ is often referred to as the Standard Halo Model of dark matter in the Milky Way. The actual value of the dark matter velocity dispersion is quite uncertain as a large range of values ($< v_{DM}^2 >^{1/2} \approx 270 - 500$ km/s) fit the current observations of the Galactic rotation curve [32, 33].

1.3.2 Current Candidates

DM candidate	I. Ωh^2	II. Cold	III. Neutral	IV. BBN	V. Stars	VI. Self	VII. Direct	VIII. γ-rays	IX. Astro	X. Probed	Result
SM Neutrinos	×	×	✓	✓	✓	✓	✓	–	–	✓	×
Sterile Neutrinos	∼	∼	✓	✓	✓	✓	✓	✓	✓!	✓	∼
Neutralino	✓	✓	✓	✓	✓	✓	✓!	✓!	✓!	✓	✓
Gravitino	✓	✓	✓	∼	✓	✓	✓	✓	✓	✓	∼
Gravitino (broken R-parity)	✓	✓	✓	✓	✓	✓	✓	✓	✓	✓	✓
Sneutrino $\tilde{\nu}_L$	∼	✓	✓	✓	✓	✓	×	✓!	✓!	✓	×
Sneutrino $\tilde{\nu}_R$	✓	✓	✓	✓	✓	✓	✓!	✓!	✓!	✓	✓
Axino	✓	✓	✓	✓	✓	✓	✓	✓	✓	✓	✓
SUSY Q-balls	✓	✓	✓	✓	∼	–	✓!	✓	✓	✓	∼
B^1 **UED**	✓	✓	✓	✓	✓	✓	✓!	✓!	✓!	✓	✓
First level graviton UED	✓	✓	✓	✓	✓	✓	✓	×	×	✓	×[a]
Axion	✓	✓	✓	✓	✓	✓	✓!	✓	✓	✓	✓
Heavy photon (Little Higgs)	✓	✓	✓	✓	✓	✓	✓	✓!	✓!	✓	✓
Inert Higgs model	✓	✓	✓	✓	✓	✓	✓	✓!	–	✓	✓
Champs	✓	✓	×	✓	×	–	–	–	–	✓	×
Wimpzillas	✓	✓	✓	✓	✓	✓	✓	✓	✓	∼	∼

Figure 1.2: Here, several proposed dark matter candidates are shown along with how they score against the "Ten-Point Test" in Taoso, Bertone, and Masiero. A ✓ indicates agreement with the question, while an × indicates disagreement. The ∼ is used for cases where the answer is affirmative only under very specific circumstances and the ! indicates that experiments are underway which will test that question. This figure is taken from [61].

After their "Ten-Point Test", Taoso, Bertone, and Masiero [61] also provide a table of dark matter candidates indicating how each of these fare in their test (see Fig.1.2). Of those listed, the most widely studied are the axion and the neutralino as

their direct or indirect detection may be imminent. For the rest of this analysis, we will consider only neutralino dark matter and will discuss its prospects for its direct and indirect detection in detail in Chapters 4 and 5 respectively. Details of each candidate can be found in the reviews listed above or in the references in [61].

1.4 Dark Matter Detection Experiments

There are currently many experiments underway to detect dark matter both directly and indirectly. Direct detection experiments aim to detect the signatures of nuclear recoils from a dark matter particle scattering off a baryonic matter nucleus. Indirect detection looks for the products of dark matter annihilation or decay including gamma rays and antimatter. We discuss the efforts for direct and indirect detection separately.

1.4.1 Direct Detection

If a neutralino dark matter particle strikes a normal matter nucleus, it may transfer a small amount of energy $\sim 1-100$ keV to the target nucleus (see Chapter 4 for details). The current generation of dark matter detectors are sensitive to energies of this range and are either insensitive to or take care to discriminate against the recoils produced by other incident radiation. Cosmic-ray neutrons or other high-energy particles may also scatter off of nuclei with energies on the order of those expected from neutralinos. As a result, experiments for the direct detection of dark matter are located deep underground where the surrounding rock shields the detectors from cosmic rays.

However, the experiments must also be shielded from radioactivity in the surrounding bedrock and in the materials that make up the detector. While accounting for the effects of background radiation, the detectors must also have large active lifetimes. We show in Chapter 4 that the event rates based on the theoretically expect cross sections for the interaction of dark matter with normal matter corresponds to fewer than one dark matte scattering event per kilogram of detector material per decade. A combination of long active lifetimes and large active detector volumes are used in conjunction to increase the expected event rate.

Detectors such as LUX [54], XENON [68], XMASS [69], ZEPLIN [70], and ArDM [71] are large containers filled with a noble liquid such as xenon (for XENON, LUX, XMASS, and ZEPLIN) or argon (for ArDM). Noble liquids are easily purified and have a high density, and the detectors are easily scaled to large volumes. The details of a nuclear recoil event are determined by measuring its ionization and scintillation yield in the liquid. For example, in the ZEPLIN detector, the scattering of the dark matter particle off a Xenon nucleus both excites and ionizes the Xe atom [72]. In the excitation process, the excited Xe^* atom and a normal Xe atom form a metastable Xe_2^* excimer. In the ionization process, an Xe_2^* excimer is formed when an Xe_2^+ ion formed from the combination of the ionized Xe^+ atom with a normal Xe atom recombines with some of the ionized electrons. The two excimers, formed by different processes, decay with different time constants and both emit 175-nm photons, which are detected by photomultipliers. The decay constants are also found to be different depending upon the type of incident radiation (neutrons, alpha particles, gamma rays, etc.). Experiments such as ZEPLIN apply an electric field to drift the ionized

electrons out of the liquid xenon into a gaseous xenon phase and through fine wire meshes where the electrons emit scintillation photons in the strong electronic field. The ratio of the photon yield from the excited excimer to the photons produced from the scintillation in the gaseous xenon is different for nuclear recoils and electronic recoil events, allowing for discrimination against muon and gamma ray background events. In order to shield the detector from ambient neutrons and alpha particles, both of which produce nuclear recoils in the energy range expected from dark matter, and from other background particles, the detectors are surrounded by layers of paraffin and lead.

Other experiments, such as EDELWEISS [73], CDMS [51], CoGeNT [74], and DAMA/LIBRA [75] use very pure cryogenically-cooled crystals of germanium, silicon, or sodium iodide as the target material. Unlike the liquid nobel detectors where the only signals are in the form of photons, the cryogenic crystal detectors utilize multiple detection methods. The phonons from the vibrations caused by incident dark matter particles are measured by sensitive bolometers. The scintillation light and ionization charge is also detected. The combination of these signals is used to measure the recoil energy of the target nucleus.

The SIMPLE [78], COUPP [77], and PICASSO [76] experiments use heavy refrigerants in a standard bubble chamber or superheated droplet detector configuration. Dark matter experiments with bubble chambers are reviewed in great detail in Appendix B where a novel bubble chamber dark matter detector involving triggered cavitation in acoustic fields is proposed.

In Fig.1.3, the interaction cross sections excluded as a function of dark matter

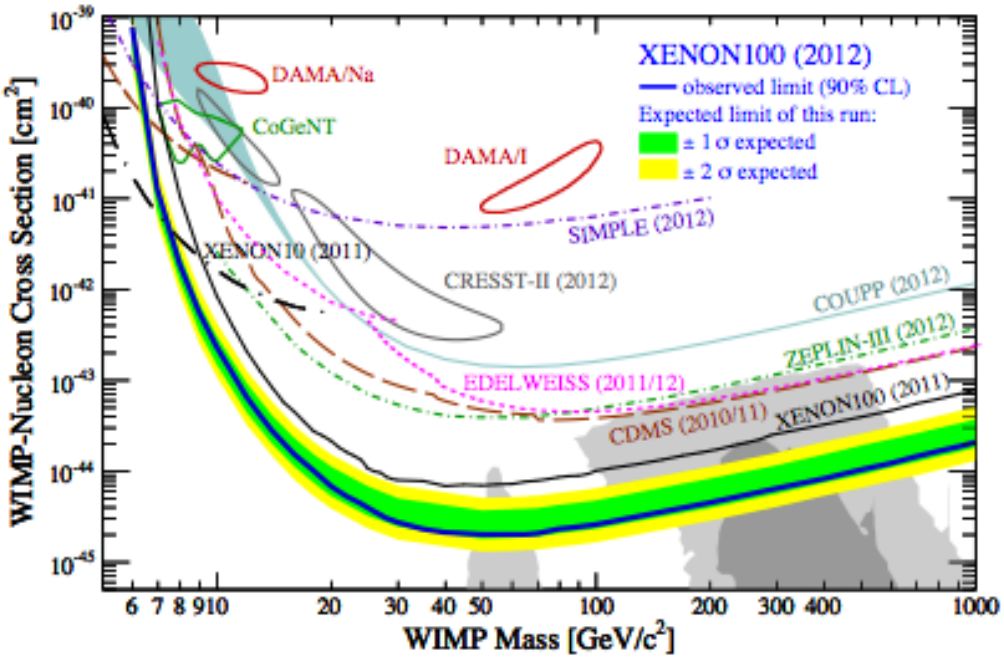

Figure 1.3: Exclusion plots for the current generation of dark matter detectors. The gray areas are predictions from supersymmetric models. This figure is taken from [68], and the lines represent the upper bounds on the interaction cross section of dark matter with normal matter as a function of mass of the dark matter particles set by various experiments.

mass by the current generation of dark matter experiments are shown. Only within the past two years have dark matter detection experiments been able to probe the parameter space predicted for particles such as the neutralino by supersymmetric extension of the standard model. Either the discovery of dark matter or the exclusion of the currently favorable candidates may be possible within the next decade.

1.4.2 Indirect Detection

Astronomical observations of the products from the annihilation or decay of dark matter such as gamma rays (egs. FERMI [79] and VERITAS [80]) or cosmic rays (egs. FERMI [79], AMS [81], PAMELA [82], and ICECUBE [83]) would constitute

an indirect detection of dark matter. Detecting these products may be possible in favorable conditions where the expected dark matter density is high. In Chapter 5, we discuss in detail the prospect of detecting gamma rays from annihilation or decay near the center of the Milky Way after putting some constraints on the central dark matter density in Chapter 3. In Appendix A, we discuss in detail the recent observations of positrons in cosmic rays in the context of whether or not the current observations necessitate a dark matter explanation.

1.5 Motivation and Outline

In this thesis, we focus on dark matter in the Milky Way since that is where most of the experimental efforts to detect dark matter are confined. In order to correctly interpret the results of the detection experiments, the phase-space distribution of dark matter must be well understood because the local properties of the dark matter including its local density and velocity distribution are needed to calculate the expected interaction rate between dark and normal matter. The understanding of the phase-space distribution of dark matter in the Galaxy depends on the distribution of the visible matter in the Galaxy. In Chapter 2, we review the current astronomical observations of the distribution of visible matter in the Milky Way and develop a two-component axisymmetric model for describing the visible matter density of the Galaxy.

In Chapter 3, we assume the phase-space distribution of dark matter follows a lowered isothermal form and self-consistently solve Poisson's equation for the density

distribution of dark matter particles moving in the gravitational potential generated by the visible matter and the dark matter particles themselves. The density distribution of dark matter depends on the densities of the various components of the visible matter of the Galaxy and the parameters characterizing the distribution function of dark matter such as the central dark matter density, the velocity dispersion parameter, and the cutoff radius of the distribution. We produce a set of models for the phase-space distribution of dark matter that are then constrained by enforcing the criteria that the rotation curves predicted by these models agree with observations and that they accurately predict the velocity distributions of tracers of the Galactic potential such as blue horizontal-brach and blue straggler stars.

In Chapters 4 and 5, we discuss the implications these constrained models of dark matter have on the direct and indirect detection of dark matter respectively, and in Chapter 6, we discuss the results of this analysis as well as prospects for future improvements.

References

[1] Weinberg, S. 2008, *Cosmology*, Oxford University Press, USA

[2] Komatsu, E. et al. 2011, ApJS, 192, 18

[3] Contaldi, C. R. , Hoekstra, H., & Lewis, S. 2003, PRL, 90, 221

[4] Carroll, S. M. 1997, arXiv:gr-qc/9712019v1

[5] Beringer, J. et al. (Particle Data Group) 2012, PRD, 86, 010001

[6] Zwicky, F. 1933, Helvet. Phys. Acta, 6, 110

[7] Cowsik, R. & McClelland, J. 1972, PRL, 29, 669

[8] Cowsik, R. & McClelland, J. 1973, ApJ, 180, 7

[9] Oort, J. 1932, Bull. Astron. Inst. Neth., 6, 249

[10] Rood, H. J., et al. 1972, ApJ, 175, 627

[11] Abell, G. 1965, Ann. Rev. Astron. Astrophys., 2, 1

[12] Omer, G. C., Page, T. L., & Wilson, A. G. 1965, AJ, 70, 440

[13] Demoulin, M. 1969, ApJ, 157, 81

[14] Humason, M. L., Mayall, N. U., & Sandage, A. R. 1956, AJ, 61, 97

[15] Seyfert, C. K. 1951, PASP, 63, 72

[16] Peebles, P. J. E. 1971, *Physical Cosmology*, Princeton University Press, Princeton

[17] Ginzburg, V. L. 1978, *Key Problems in Physics and Astronphysics*, Mir Publishers, Moscow

[18] Rubin V. C. & Ford, W. K. 1970, ApJ, 159, 379

[19] Rubin, V. C., Thonnard, N., & Ford, W. K. 1980, ApJ, 238, 471

[20] Bosma, A. 1978, *The Distribution and Kinematics of Neutral Hydrogen in Spiral Galaxies of Various Morphological Types*, PhD thesis. Groningen University

[21] Rood H. J. & Dickel, J. R. 1979, ApJ, 233, 418

[22] Cowsik R. & Ghosh, P. 1987, ApJ, 317, 26

[23] Bahcall, J. N. 1984, ApJ, 276, 156

[24] Bahcall, J. N. 1984, ApJ, 276, 169

[25] Bahcall, J. N., Flynn, C., & Gould, A. 1992, APJ, 389, 234

[26] Kuijken, K. & Gilmore, G. 1989, MNRAS, 239, 571

[27] Kuijken, K. & Gilmore, G. 1989, MNRAS, 239, 605

[28] Kuijken, K. & Gilmore, G. 1991, ApJ, 367, L9

[29] Flynn, C. & Fuchs, B. 1994, MNRAS, 270, 471

[30] Holmberg, J. & Flynn, C. 2000, MNRAS, 313, 209

[31] Holmberg, J. & Flynn, C. 2004, MNRAS, 352, 440

[32] Cowsik, R., Ratnam, C., & Bhattacharjee, P. 1996, PRL, 76, 3886

[33] Cowsik, R., et al. 2007, New Astron., 12, 507

[34] Sofue, Y., Honma, M., & Omodaka, T. 2009, PASJ, 61, 227

[35] Lee, B. W. & Weinberg, S. 1977, PRL, 39, 165

[36] Gershtein, S. S. & Zel'dovich, Ya. B. 1966, J. Exp. Theor. Phys. Lett., 4, 124

[37] Szalay, A. S. & Marx, G. 1976, A&A, 49, 437

[38] Tremaine, S. & Gunn, J. E. 1979, PRL, 42, 407

[39] Kim, J. -E. 1979, PRL, 43, 103

[40] Shifman, M. A., Vainshtein, A. I., & Zakharov, V. I. 1989, Nucl. Phys. B, 166, 493

[41] Zhitnitsk, A. R. 1980, Sov. J. Nucl, Phys., 31, 260

[42] Dine, M., Fischler, W., & Srednicki, M. 1981, Phys. Lett. B, 104, 1955

[43] Peccei, R. D. & Quinn, H. R. 1977, PRL, 38, 1440

[44] Weinberg, S. 1978, PRL, 40, 223

[45] Wilczek, F. 1978, PRL, 40, 279

[46] Jungman, G., Kamionkowski, M., & Griest, K. 1996, Phys. Rept., 267, 195

[47] Shandarin, S. F. & Zeldovich, Ya. B. 1989, Rev. Mod. Phys., 61, 185

[48] Peebles, J. 1982, ApJ, 263, L1

[49] Trimble, V. 1989, Ann. Rev. Astron. Astrophys., 25, 425

[50] Primack, J. R., Seckel, D., & Sadoulet, B. 1988, Ann. Rev. Nucl. Part. Sci., 38, 751

[51] Aghmet, Z., et al. 2011, PRL, 106, 131302

[52] Archambault, S., et al. 2012, arXiv:1202.1240

[53] Angle, J., et al. 2008, PRL, 100, 021303

[54] Akerib, D. S. et al. 2012, arXiv:1207.3665

[55] Zacek, V. 2007, arXiv:0707.0427

[56] Feng, J. L. 2010, Ann. Rev. Aston. Astrophys., 48, 495

[57] Gaitskell, R. J. 2004, Ann. Rev. Nuc. Part. Sci., 54, 315

[58] Bertone, G., Hooper, D. & Silk, J. 2005, Phys. Rept., 405, 279

[59] Bartelmann, M. 2010, Rev. Mod. Phys., 82, 331

[60] Bertone, G. ed. 2010, *Particle Dark Matter*, Cambridge University Press, Cambridge

[61] Taoso, M., Bertone, G. & Masiero, A. 2008, JCAP, 0803, 022

[62] Clowe, D. 2006, AJ, 648, L109

[63] Catena, R. & Ullio, P. 2010, JCAP, 08, 004

[64] Weber, W. & de Boer, W. 2010, A&A, 509, A25

[65] McMillan, P. J. 2011, MNRAS, 414, 2446

[66] Salucci, P. et al. 2010, A&A, 523, 83

[67] Bovy, J. & Tremaine, S. 2012, AJ, 756, 89

[68] Scotto Lavina, L. et al. 2013, arXiv:1305.0224v1

[69] Abe, K. et al. 2013, arXiv:1211.5404v3

[70] Akimon, D. Yu. et al. 2012, Phys. Lett. B, 709, 14

[71] Rubbia, André 2006, J. Phys: Conf. Ser. 39, 129

[72] Cline, D. B. et al. 2001, IEEE Nucl. Sci. Symp. Conf. Rec. 1, 417

[73] Armengaud, E. et al. 2011, arXiv:1103.4070v3

[74] Aalseth, C. E. et al. 2011, PRL, 106, 131301

[75] Bernabei, R. et al. 2010, Eur. Phys. J. C, 67, 39

[76] Archambault, S. et al., 2012, Phys. Lett. B, 711, 153

[77] Behnke et al., 2011, PRL,106, 021303

[78] Felizardo, M. et al., 2012, PRL, 108, 201302

[79] FERMI-LAT Collaboration, 2013, arXiv:1305.5597

[80] Geringer-Sameth, A. 2013, arXiv:1303.1406

[81] Aguilar, M. et al. 2013, PRL, 110, 141102

[82] Adriani et al. 2009, Nature, 458, 607

[83] Aartsen, M. G. et al. 2013, arXiv:1307.3473

Chapter 2

The Milky Way

In order to understand the distribution of dark matter in the Galaxy, the visible distribution of matter must be well understood as it is their total gravitational potential that controls the dynamics of the Galaxy. In fact, the observed kinematics of the various components of the visible matter of the Galaxy are a measure of the total potential, and by subtracting from the observed potential the contribution of visible matter, the contribution of dark matter to the total potential can be inferred. Currently, the best tools we have to probe the dark matter distribution come from the observations of the rotation curve and distribution of stars and gas in the Galaxy. In this chapter, models of the density of the various components of the Milky Way are reviewed; the model used in our analysis is constructed; and the dynamical observations of the Galaxy relevant to constraining the dark matter component are discussed.

The distribution of matter in the the Milky Way is customarily divided into several components: a dense central bulge extending from the Galactic center to 3-4 kpc, a disk of thickness $\sim$ 1 kpc that extends from the galactic center out to $\sim 13 -$

15 kpc, a sparse halo of stars and gas that may extend out to $\sim$ 100 kpc, and a spherical halo of dark matter extending out to a few hundred kpc. One of the earliest attempts to model the mass distribution of the Milky Way was by Schmidt in 1956 [1]. His model comprised four non-homogeneous spheroids, which had been extensively studied by Kuzmin in 1952 [2], representing the known stellar populations, and nine homogeneous spheroids used to account for deviations from Oort's vertical force law [3]. The spheroids were parameterized to fit the observations of the gravitational force perpendicular to the Galactic plane, the rotation speed at the Solar location, and the Oort constants.

For two decades, Galactic mass models were similar to the one by Schmidt. For example, Innanen [4, 5] used non-homogeneous spheroids to fit what were then new observations of the rotation curve within the Solar circle. In 1975, Miyamoto and Nagai [6] used a generalized combination of the thin disk described by Kuzmin and a sphere (used by Plummer to describe globular clusters) to fit the bulge and disk of the Milky Way separately instead of together as had been done in the Schmidt and Innanen models. These models often produced rotation curves that fell sharply outside the Solar circle, where no reliable observations were available, and there was no inclusion of any kind of Galactic dark matter.

Studying the mass structure of external galaxies provided much insight into the structure of the Milky Way. In 1959, DeVaucouleurs [7] showed that visible matter of spiral galaxies can be described by a central bulge surrounded by an exponential disk by studying their radial surface brightness profiles. The exponential disk was later studied in detail by Freeman [8] and is typically used to describe the disk of

the Milky Way. In the 1960's, Toomre [9] and Mestel [10] studied spiral galaxies to develop simple models where the apparent mass distribution and rotation speed of the galaxies could be reconciled. Athanassoula et al. [11] decomposed galaxies into bulge and disk components and estimated the parameters of the dark halo. It was found that in most cases, there was evidence for a maximal disk of visible matter. That is, the mass-to-light ratio of the disk was "as high as possible while requiring a halo mass distribution without a hollow core" [11].

By the 1970s, dark matter was beginning to be included into galactic mass models. Kormendy [12, 13, 14] developed models for galaxies based on photometric studies, which included a central bulge, exponential disk, and a dark matter corona. Einasto's 1989 [15] model of the Milky Way used modified exponential functions to describe the visible mass distributions of the Galaxy, which were fit to observations of the vertical force at the Solar location, the distance of the Sun from the Galactic center, the rotational speed of the Sun with respect to the Galactic center, local mass density, and other observations. The dark corona was described by a modified isothermal sphere. A summary of various three-component (inner bulge, exponential disk, and massive dark corona) models of the Galaxy by Bahcall and Soneira [16], Rohlfs and Kreitschmann [17], Caldwell and Ostriker [18] and others can be found in Schmidt's 1985 review[19] and in Rohlfs and Kreitschmann [20]. Details of the density distributions of the various components used in the most recent mass models of the Milky Way are discussed below.

2.1 The Distribution of Mass in the Galaxy

The distribution of stars and gas in the Milky Way can be well described as the combination of a central bulge and flat disk embedded in a large halo of tenuous gas and stars. There are substructures that are important to a complete understanding the Galaxy but do not contribute significantly to overall dynamics of the Galaxy in the regions of interest of this study (see Section 2.1.5 for a brief description of some of these objects). Here, we review the components of the Galaxy with particular focus on those that contribute to its dynamics beyond ~ 1 kpc. We begin with the outer reaches of the Galaxy and continue inwards towards the Galactic center. Finally, we discuss the finer structures of the Galaxy and present the mass model used in our analysis to derive the phase-space distribution of Galactic dark matter.

2.1.1 The Stellar Halo

The stellar halo, often called the spheroid, is a low-density stellar region extending from the Galactic center to the farthest reaches of the visible Galaxy. Stars have been detected out to ~ 100 kpc [21] and recently, the Chandra X-ray telescope may have detected a significant amount of hot gas ($> 10^{10} M_{\odot}$) as distances extending out to more than 100 kpc [22]. The stellar halo contains the most metal-poor and possibly oldest stars in the Galaxy [23]. Since the time needed for stars to transfer energy and momentum in the halo is much longer than the age of the Galaxy, the distribution of stars in the halo is useful in studying formation history of the Milky Way.

The stellar halo, though not as dense as the other components of the Milky Way,

contains much substructure, including the Sagittarius stream, the Virgo overdensity, and the Hercules-Aquila Cloud [21, 24, 25, 26, 27], indicating that much of the stellar halo is comprised of tidally disrupted satellites. Most models of the mass distribution of the stellar halo take care to either avoid or subtract over-densities caused by these known substructures for computational simplicity in studying the overall dynamics of the Galaxy [21]. Excellent reviews of the stellar halo are found in Helmi [23], Gilmore et al. [28], Majewski [29], and Freeman and Bland-Hawthorn [30].

There have been recent studies [31, 32, 33] (and the references within) that claim the stellar halo is not a single component but may be composed of an inner and outer halo, which rotate in opposite directions about the Galactic center . These studies also find the stellar metallicty distributions to be different for the inner and outer halo. There is no consensus currently as to whether the stellar halo is indeed composed of two components.

The stellar halo is often modeled as a single power law [23, 34] of the form

$$\rho_{SH}(r,z) = \rho_{SH,0}\frac{(r^2 + z^2/q^2)^{n/2}}{R_0^n}, \tag{2.1}$$

where $\rho_{SH,0}$ is the stellar halo density at R_0, the distance from Sun to the Galactic center, and q is the flattening of the stellar halo. Robin et al. [34, 35] find, using deep star counts at high and medium Galactic latitudes, that $n = -2.44$ and $q = 0.76$ while Siegel et al. [36] find $n = -2.75$ and $q = 0.6$. An analysis of 340 RR Lyrae and BHB stars finds $n = -3.2$ and $q = 0.5$ [37] while an analysis of 666 BHB stars finds $n = -2.5$ and $q \approx 1$ up to ~ 100 kpc from the Galactic center [38]. Morrison et al.

[39] observed turn-off halo stars to determine $n = -3$ and $q = 0.6$. Similarly, Chen et al. [40] also observed turn-off halo stars but in a panoramic survey, as opposed to the pencil-beam survey of Morrison et al. [39], to find $n = -2.3/2.5$ and $q = 0.6/0.5$. Yanny et al. [41] observed BHB and BS stars to determine $n = -3.2 \pm 0.3$ and $q = 0.65$. Analyses of RR Lyrae stars find $n \sim -3$ [42] and $n = -3.1 \pm 0.1$ [43] with a flattening q that varies with radius. Xu et al. [44] find $n = -2.8$ and $q = 0.7$ using SDSS data. These studies show that n is known to within a factor of ∼1.5 (-2.3$\lesssim n \lesssim$ -3.6) and q within a factor of ∼2 (0.5$\lesssim q \lesssim$ 1.0).

The normalization $\rho_{SH,0}$ found by studying nearby M dwarf stars is $\rho_{SH,0} = 1.5 \times 10^{-4}$ $M_\odot$ pc^{-3} [45, 46]. Robin et al.[35], using deep star counts, found the normalization to be $\rho_{SH,0} = 0.932 \times 10^{-5}$ $M_\odot$ pc^{-3}. Hubble Space Telescope counts [47, 48] find $\rho_{SH,0} = 6.4 \times 10^{-5}$ $M_\odot$ pc^{-3}. This factor ~ 7 difference among the studies hints at the difficultly in observing the faint halo populations.

Newberg and Yanny [49] find that Hernquist-like profile is a better fit to their Sloan Digital Sky Survey sample of stars once known over-densities and the thick disk component were removed. The Hernquist profile is give by

$$\rho_{SH}(r) = \frac{\rho_{SH,0}}{r^{\alpha}(r + R_{core})^{\delta}} \tag{2.2}$$

where $\alpha = 1$ and $\delta = 3$. The authors find that any combination of parameters where $\alpha + \delta \approx 4$ fits their data well. However, the Hernquist profile predicts a significantly lower local stellar halo density than is usually inferred from observations.

Deason, Belokurov, and Evans [21] find that when using a large set of photometric

data of BHB and BS stars from SDSS DR8, the stellar halo is well-described by a broken power law of the form

$$\rho_{SH}(r_q) \propto r_q^{-\alpha_{in}} \quad for\ r_q \leq r_b \tag{2.3}$$

$$\rho_{SH}(r_q) \propto r_q^{-\alpha_{out}} \quad for\ r_r > r_b, \tag{2.4}$$

where $\alpha_{in} = 2.3$, $\alpha_{out} = 4.6$, and the breaking radius $r_b = 27$ kpc. This agrees with previous analyses by Watkins et al. [50] and Sesar et al. [51].

Deason, Belokurov, and Evans also find that the stellar halo may be equally well fit by an Einasto profile [15], which has the form

$$\ln[\rho_{SH}(r_q)/\rho(r_{r_{eff}})] = -d_n[(r_q/r_{eff})^{1/n} - 1], \tag{2.5}$$

where $d_n \approx 3n - 1/3 + 0.0079/n$ for $n \geq 0.5$ [52]. The best fit parameters for the Einasto model are $q = 0.58$, $n = 1.7$, and $r_{eff} = 20$ kpc.

The contribution of the stellar halo to the visible matter density is on the order of 0.1% at R_0 [23], and it is therefore expected to contribute negligibly to dynamical indicators such as the rotation curve of the Galaxy. For this reason, the stellar halo is not included in the mass model used for our later analysis.

2.1.2 The Stellar Disk

The Galactic disk makes up the bulk of the visible mass of the Milky Way and consists of a flat, rotating population of stars and gas, which extends from inside the Galactic

bulge out to $\sim 13 - 15$ kpc from the Galactic center [53, 54] and ~ 1 kpc above and below the Galactic plane. The disk can be divided into two separate populations, a dense thin disk, which only extends about 300 pc above the Galactic plane and a sparse thick disk, extending upwards of 1 kpc from the Galactic plane. The thick disk was first speculated to be a distinct component in the early 1980s by Gilmore and Reid [55] after analyzing photometric data from a population of stars near the South Galactic Pole. While both disk components contain similar stellar populations, the stars in the thick disk are known to be older, at 8-12 Gyr, compared to < 10 Gyr for the thin disk stars [56]. Until recently it was uncertain whether the thick disk was a separate stellar population [28, 57, 58] or it was just an extension of thin disk stars with the highest velocity dispersion [59, 60]. Currently, the consensus is that there are two separate stellar components to the disk. Also contained within the thin disk are populations of HI and HII gas, whose observations are used to determine the rotation speed of the Galaxy.

Modeling the Disk

The mass density of both the thin (tn) and thick (tk) disk components are typically modeled as double-exponential functions, early evidence for which was given by Freeman [8]. Following the notation used in many recent analyses [61, 62], the densities

for the separate components may be written in cylindrical coordinates as

$$\rho_{tn}(r,z) = \frac{\Sigma_{tn,0}}{2z_{tn}} e^{-|z|/z_{tn}} e^{-r/r_{tn}}, \tag{2.6}$$

$$\rho_{tk}(r,z) = \frac{\Sigma_{tk,0}}{2z_{tk}} e^{-|z|/z_{tk}} e^{-r/r_{tk}}, \tag{2.7}$$

$$\rho_d = \rho_{tn} + \rho_{tk}, \tag{2.8}$$

$$\Sigma_d = \Sigma_{tn} + \Sigma_{tk}, \tag{2.9}$$

where ρ_d is the total density of the Galactic disk, $\Sigma_{tk/tn,0}$ is the surface density including stars and gas at the Galactic center, $z_{tk/tn}$ is the scale height, and $r_{tk/tn}$ is the scale length for the respective thick and thin components. The mass of the two components is given by

$$M_{tk/tn} = 2\pi\Sigma_{tk/tn,0} r_{tk/tn}^2. \tag{2.10}$$

This simple model does not include some of the finer structures of the disk such as the spiral arms or the warp included in other analyses [63].

Disk Parameters

The parameters for the thin disk component, due to its higher density and therefore better visibility, are better determined than those of the thick disk. Analyses of DIRBE data [64, 65] are used to constrain the scale height to $z_{tn} = 160 - 250$ pc and the scale length to $r_{tn} = 2.5 - 3$ kpc. Other NIR analyses provide similar results on the scale length and height, finding $r_{tn} = 2 - 3$ kpc [54, 66, 67, 68] and $z_{tn} = 250 - 350$ pc [68, 69, 70, 71]. Reddy [56] cites the thin disk scale height as being $z_{tn} = 300$ pc.

The density of the thick disk is much lower than that of the thin disk. Therefor, determining the scale length and height is much more difficult as the stellar populations being analyzed are sparse. A review of many early analyses of the thick disk parameters can be found in Buser et al [72]. The scale height is found to be $z_{tk} = 700 - 2000$ pc with a scale length of $r_{tk} = 2.5 - 4.5$ kpc [36, 67, 71, 72, 73, 74, 75, 76]. Reddy [56] lists some recent determinations of the the parameters of the thick disk including Carollo et al. [31], who find $z_{tk} = 510 \pm 40$ pc with $r_{tk} = 2.2 \pm 0.35$ kpc (noticeably lower than most other measurements) and Jurić et al. [25] who determine $z_{tk} = 900$ pc with $r_{tk} = 3.6$ kpc. Other recent studies prefer an exceedingly short scale length for the thin disk ~ 2 kpc [77, 78, 79]. The scale heights of both the thin and thick disks vary with Galactic longitude [80]. The effect is on the order of $\sim 10\%$ for both disks.

It is difficult to separate the contributions from the thick and think disk to the surface density. The density distribution of the disk is often parameterized in terms of the total local surface density $\Sigma_{d,\odot}$, which falls exponentially with scale length for each component [81] as given by

$$\Sigma_{tk/tn}(R) = \Sigma_{tk/tn,\odot} e^{-(r-R_0)/r_{tk/tn}}. \tag{2.11}$$

Using a Bayesian approach, which takes photometric and kinematic data into account, a recent analysis by McMillan [62] finds the central surface density for the two components to be $\Sigma_{tk}(0) = 238 \pm 110$ M$_\odot$ pc^{-2} and $\Sigma_{tn}(0) = 741 \pm 123$ M$_\odot$ pc^{-2}. This same analysis finds the total local density to be $\Sigma_{d,\odot} = 62.0 \pm 7.6$ M$_\odot$ pc^{-2}. Another

recent study by Rossetto et al. [82] uses $\Sigma_{tn,\odot} = 59$ M$_\odot$ pc^{-2} for the local surface density of the thin disk and parameterizes the thick disk in terms of the total local mass density $\rho_{tk,\odot} = 0.004$ M$_\odot$ pc^{-3}. The most commonly used value for the local surface density for the disk comes from the vertical force analysis by Kuijken and Gilmore [83], where $\Sigma_{d,\odot} = 48 \pm 8$ M$_\odot$ pc^{-2}. Romano et al. [81] provides references to other measurements of the total surface density, and we provide a compilation of many measurements of the local surface mass density in Table 2.1.

The surface density of the thick disk is often reported as the ratio of the surface density of the thick disk to that of the thin disk at the Solar location. Details on this local normalization may be found in Reddy [56]. Many studies place $\Sigma_{tk,\odot}/\Sigma_{tn,\odot} = 2 - 10\%$ [36, 67, 71, 72, 73, 74, 75, 76]. Recent analyses find $\Sigma_{tk,\odot}/\Sigma_{tn,\odot} = 15 \pm 7\%$ [31] and $\Sigma_{tk,\odot}/\Sigma_{tn,\odot} = 8.5\%$ [36].

A recent study of the thick disk by Minnitti et al. [53] uses disk clump giants as standard candles and takes data from the new UKIDSS-GPS [84] and VVV [85] NIR surveys. They find the edge of the stellar disk to be located at $R = 13.9 \pm 0.5$ kpc, which is similar to earlier findings of evidence for a cutoff at $R \sim 14$ kpc at anticenter region of the disk from the the Solar position [53, 86].

2.1.3 The Bulge

The Galactic bulge is the name given to the ellipsoidal inner region of the Galaxy extending up to 3-4 kpc from the Galactic center. Much of what is known about the Galactic bulge comes from infrared and stellar surveys. The COBE/DIRBE [65, 99, 100] and 2MASS [101] suveys (see also [102, 103, 104]) are all-sky near infrared

Table 2.1: Observations of the Local Visible Matter Surface Density

Reference	$\Sigma_{d,\odot}$ [$M_\odot$ pc^{-2}]	**Observations**
[87] (1989)	Stars: 35 ± 5	K dwarf stars
	Gas: 13 ± 3	Gas surveys
	Total: 48 ± 8	
[83] (1991)	49 ± 9	K dwarf stars
[88] (1994)	52 ± 13	K giant stars
[89] (1996)	40	M dwarf stars
[90] (2003)	42 ± 6	Red giant stars
[91] (2003)	67^{+47}_{-18}	Red clump stars
[92] (2004)	53	Stellar and gas surveys
[93] (2006)	48.7	Stellar and gas surveys
[94] (2009)	35 ± 5 [28]	Visible Stars
	27 [89]	"
	30 [95]	"
	3 ± 1 [96]	Stellar Remnants
	8 ± 5 [97]	Interstellar Gas
	13-14 [98]	"
	Total: 35-58	

maps of $2 - 4$ μm, where dust does not interfere as much as in optical surveys. These surveys show the Milky Way as a spiral galaxy with a peanut-shaped bulge in the center, which contains mainly old stars [99, 105]. While NIR surveys allow us to peer deeper towards the Galactic center, they have their own limitations. The NIR observations span the entire sky but at very low spatial resolution, and the measurements must be adjusted for the light that the dust does absorb [106]. Low spatial resolution means that the COBE/DIRBE and 2MASS surveys are not very useful for studying the properties of the innermost region of the bulge, and other methods, such as stellar surveys and gravitational microlensing must be used.

Shape of the Bulge

Infrared surveys show the presence of a bar-like structure within the bulge region, making the bulge a boxy or peanut-shaped object. This is confirmed by several

independent observations (see Kennicutt [107]) including the kinematics of atomic gas [100, 108, 109], reddening-corrected clump giant stars [110], properties of stars in Baade's Window [105, 111, 112], IRAS-identified AGB stars [113, 114, 115], and other infrared stellar sources [113, 116, 117, 118]. It is also confirmed that the bar rotates within the Galaxy with a corotation radius of 3-4 kpc [106, 117, 119, 120]. The rotation of the bar is seen from many independent observations including stellar observations, non-circular motions in atomic gas, microlensing towards the Galactic center, and the COBE/DIRBE and 2MASS surveys [121]. The speed of the rotation of the bar is seen to reach upwards of 75 km/s [24, 122, 123, 124, 125, 126] with a velocity dispersion that decreases as one looks further from the Galactic center [24, 124, 127] (see Fig.2.1).

In the inner part of the bulge, within 500 pc from the Galactic center, there is a dense region of stars and gas often referred to as the nuclear bulge. In a recent analysis of IRAS and COBE/DIRBE data, Launhardt, Zylka, and Mezger [128] found the nuclear bulge consists of an inner stellar cluster whose mass distribution follows an inverse-square law. The nuclear bulge contains stellar and molecular gas disks of equal size with a radii of 230 ± 20 pc and scale heights of 45 ± 5 pc. Reviews of the nuclear bulge [129, 130, 131, 132] and details of the inner parsec of the nuclear bulge [133, 134] may be found in the literature.

Bulge Parameters

A good summary of the observable parameters of the Galactic bulge can be found in Table I of Vanhollebeke, Groenewegen, and Girardi [135].

The orientation of the bar is denoted by ϕ_{bar}, the angle in the Galactic plane between the line connecting the Sun and the Galactic center and the bar's major axis. Integrated light measurements and models of the bulge gas dynamics find $15° \leq \phi_{bar} \leq 35°$ [100, 106]. Models based on star counts find both $6° \leq \phi_{bar} \leq 18°$ [103] and $20° \leq \phi_{bar} \leq 30°$ [105, 115]. The DIRBE L-band data analyzed with constraints from clump giant data yields $15° \leq \phi_{bar} \leq 25°$ [136]. Microlensing data yields $\phi_{bar} \approx 15°$ [137]. Mira variables find $\phi_{bar} \approx 40°$ [138]. OH/IR stars show $\phi_{bar} \approx 44°$ [117]. HIPPARCOS data shows $\phi_{bar} \approx 11.1 \pm 0.7°$ [34]. The measurements for ϕ_{bar} seem to fall into two categories: those that are $\sim 20°$ and those that are $\sim 45°$. The low values may be the result of not considering a wide enough range of longitude in stellar and gas surveys [117, 135]. The discrepancies may also reflect the variation in distribution of the different stellar populations [135, 138].

There is a better consensus on the values of the bar axis ratios than on the bar orientation angle. The bar axis ratio is defined as $10 : \eta : \zeta$, which is related to the galactocentric distance R and the rectangular coordinates (x, y, z) by $R = \sqrt{x^2/10 + y^2/\eta^2 + z^2/\zeta^2}$. DIRBE data yields 10:3-4:3 [106], which agrees with the model of Bissantz and Gerhard [136]. Star count models yield 10:4:3 [110] and 10:5.4:3.3 [103]. HIPPARCOS data analysis yields 10:2.7:2.7 [34]. A more recent analysis using OGLE-II red clump giants shows axis ratios of 10:3.5:2.6 [139]. Therefore the axis ratios values of 10:4:3 are in good agreement with the majority of observations.

It is also possible to measure the distance from the Galatic center to the end of the bar and therefore the radial extent of the Galactic bulge. This is often referred to

as the bar length R_{bar}. The DIRBE NIR data yields $R_{bar} = 3.2 \pm 0.3$ kpc [64, 65, 136], which agrees with data from OH/IR stars [117] and IRAS variables[115].

Modeling the Bulge

Vanhollebeke, Groenewegen and Girardi [135] summarize the three types of triaxial models created to agree with discovery of the bar. Exponential-type models combined with a modified spheroid are found to agree with COBE/DIRBE data [99]. Boxy Gaussian-type models [34] are able to accommodate the bar but do not model the inner part of the bulge, but perhaps the most used of the three models is an exponentially-truncated power-law [64, 136]. Bissantz and Gerhard [136] give the density function of this model as

$$\rho_b(R) = \frac{\rho_{b,0}}{(1 + R/R_0)^{1.8}} e^{-R^2/r_{cut}^2} \tag{2.12}$$

where $R = \sqrt{x^2/10 + y^2/\eta^2 + z^2/\zeta^2}$. In this model, R_0 is the inner truncation length, r_{cut} is the scale length, $\rho_{b,0}$ is the central density of the bulge, and η and ζ are the values of the scaled bar axis ratios given by $10 : \eta : \zeta$ as before.

Recently, McMillan [62] has used an axisymmetric approximation of the Bissantz and Gerhard [136] model, where the density of the bulge is given by

$$\rho_b(R') = \frac{\rho_{b,0}}{(1 + R'/R_b)^{1.8}} e^{-(R'/r_{cut})^2} \tag{2.13}$$

where $R' = \sqrt{r^2 + (z/q)^2}$, $R_b = 75$ pc, $r_{cut} = 2.1$ kpc, $q = 0.5$, $\rho_{b,0} = 9.93 \times 10^{10} \pm 10\%$

$M_\odot$ kpc^{-3}, and $r = \sqrt{x^2 + y^2}$. This results in a bulge mass of $M_b = 8.9 \times 10^{10} \pm 10\%$ $M_\odot$.

The nuclear bulge may be modeled as a power law

$$\rho_{NB}(R) \approx \rho_{NB,0} \left(\frac{R}{1\ pc} \right)^{-1.8} \tag{2.14}$$

for 1 pc$\leq r \leq$10 pc [133, 134, 140, 141] and $\rho_{NB,0} \approx 1.5 \times 10^5$ $M_\odot$ pc$^{-3} \pm 50\%$. in the inner parsec, the index flattens from 1.8 to 1.2, and the nuclear bulge has a total mass of $1.6 \pm 0.6 \times 10^6$ $M_\odot$ [133, 134].

2.1.4 The Center for the Galaxy

Currently, there is little doubt that the radio source Sgr A* is a supermassive black hole of mass $M_{BH} \approx 4 \times 10^6$ $M_\odot$ [143, 144, 145, 146, 147, 148, 149] located within 100 AU of the Galactic center. The central black hole influences the orbits of stars up to $\sim$3 pc from the Galactic center [150]. This region is filled with hot neutral and ionized gas as well as a dense cluster of stars. The stars orbiting within just a few light hours of Sgr A* travel with speeds upwards of 10^3 km/s, providing evidence for the high mass of the central black hole and the orbits of these fast stars show that Sgr A* sits relatively stationary at the center of the Galaxy [145, 146, 151, 152, 153]. The literature provides several reviews of both the evidence for the classification of Sgr A* as a black hole as well as its properties [148, 150, 154, 155]. We do not include the black hole in our mass model as it does not influence the dynamics in our region of interest.

2.1.5 Other Components

The Milky Way contains many other structures in addition than those listed above. Dwarf spheroidal galaxies are bound to the Galaxy at distances of $\sim 60 - 250$ kpc and may also be useful probes for investigating Galactic dark matter [156]. The visible halo contains ~ 150 globular stellar clusters and high density areas such as the Sagittarius stream, the Virgo overdensity, and the Hercules-Aquila Cloud [21, 24, 25, 26, 27] that are likely the results of past mergers between the Milky Way and smaller galaxies. The disk of the Galaxy contains the overdensities defining spiral arms and others which give the disk a "warped" appearance [157]. The central regions of the Galaxy also contain much substructure. Besides, the disks in the nuclear bulge described above, the inner few parsecs of the bulge contains mini spiral arms and dense regions of dust [130].

In order to fully understand the precise phase-space distribution of dark matter in the Milky Way, the densities and motions of all known substructures in the Galaxy would have to be included. However, given the uncertainty in the distribution of the visible matter in the Galaxy and for simplifying later computations, we construct a two-component mass model for the Milky Way consisting of the spherical central bulge and a double-exponential disk. The structures in the inner region of the Galaxy including such as the bar seen in the nuclear bulge and the black hole are not included since they do not contribute significantly to the dynamics of the Galaxy beyond ~ 1 kpc. Similarly, the stellar halo is neglected because of its low density. We present our mass model below.

2.2 Our Mass Model

In this study, we model the disk in the usual way, as a two-component double-exponential density distribution receiving contributions from both the young thin disk (tn) and the old thick disk (tk), given by eqs. 2.6 and 2.7. For the total local surface density from visible matter, we consider three possibilities:

$$\Sigma_{d,\odot} = 40,\ 55,\ \text{and } 70\ \mathrm{M_\odot pc^{-2}}.$$

For convenience, the ratio of the thick disk surface density to the total surface density is taken to be

$$\frac{\Sigma_{tk,\odot}}{\Sigma_{tk,\odot} + \Sigma_{tn,\odot}} = 0.1, \tag{2.15}$$

a value that is within the range found in the literature [31, 36, 67, 71, 72, 73, 74, 75, 76]. The choice of the ratio in eq. 2.15, within its observational constraints, is found to not have a significant effect on the rotation curve or other dynamical indicators.

For radial scale lengths, we consider the range r_{tn}=2.0, 2.5, 3.0, and 3.5 kpc and the value $r_{tk} = 3.5$ kpc. The scale heights are chosen to be $z_{tn} = 350$ pc and $z_{tk} = 900$ pc, close to the values determined by Jurić et al. [25]. Varying the scale heights within observational constraints was found to not significantly change the rotation curves computed for the dark matter models in Chapter 3. This agrees with the analysis of McMillan [62] who found that varying the scale heights had very little effect on the dynamics derived from his Galactic mass models. This small effect could be explored in greater detail in future work. The above parameters yield a combined

disk mass in the range $3.57 - 6.24 \times 10^{10}$ $M_\odot$. Note that this simple disk does not include the finer structures such as the spiral arms or the warp included in other analysis since an axisymmetric model is adequate to describe the overall dynamics and provides computational simplicity.

The disk potential has the form (see Appendix C for a derivation) [87, 158]

$$\begin{aligned}\Phi_d(r,z) &= -2\pi G\Bigg(\Sigma_{tn,0} r_{tn}^2 \int_0^\infty dk \frac{J_0(kr)}{[1+(kr_{tn})^2]^{3/2}} \frac{e^{-k|z|} - (kz_{tn})e^{-|z|/z_{tn}}}{1-(kz_{tn})^2} \\ &\quad + \Sigma_{tk,0} r_{tk}^2 \int_0^\infty dk \frac{J_0(kr)}{[1+(kr_{tk})^2]^{3/2}} \frac{e^{-k|z|} - (kz_{tk})e^{-|z|/z_{tk}}}{1-(kz_{tk})^2}\Bigg). \end{aligned} \tag{2.16}$$

Note the potential includes integration over Bessel functions, which slows down numerical calculations of the rotation curve for the different models. We find that using an adaptive quasi-Monte Carlo method in *Mathematica* provides the quickest calculation time without sacrificing accuracy.

The bulge, in cylindrical coordinates, is described by a Plummer density profile of the form

$$\rho_b(r,z) = \frac{3M_b}{4\pi b^3}\left(1 + \frac{r^2+z^2}{b^2}\right)^{-5/2}, \tag{2.17}$$

where, r is the distance from the Galactic center in the plane of the Galaxy, z is the height from the Galactic plane, M_b is the total mass of the bulge and b is the scale radius. To determine M_b and b, we assume the dark matter contribution to the dynamics from $\sim 0.1-1$ kpc is small (an assumption which is justified *post facto*) and subtract only the disk contribution from the inner 1 kpc of the observations of the Galactic rotation curve. The resulting points are fit with the rotation curve derived

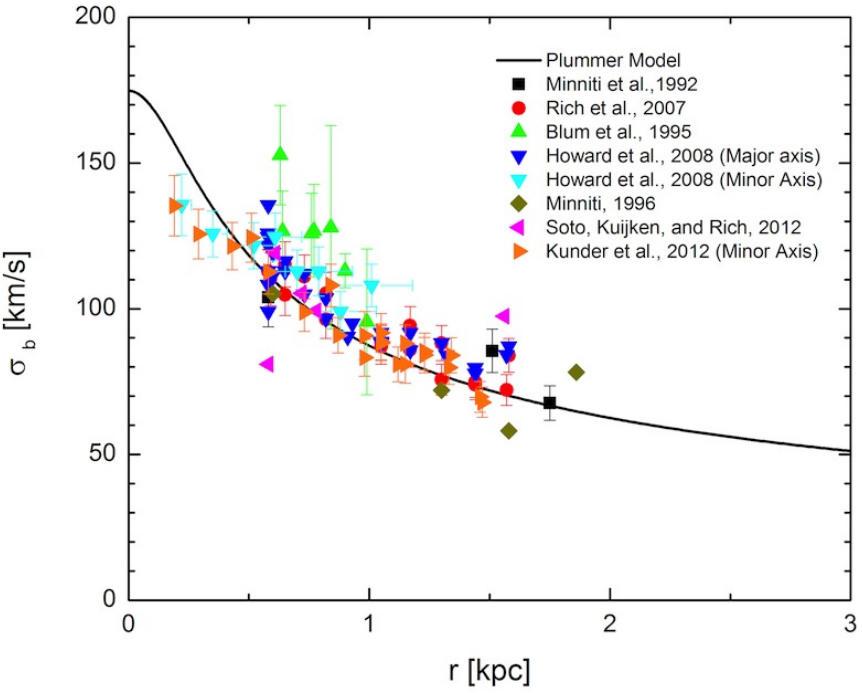

Figure 2.1: The velocity dispersion expected from the bulge alone (eq. 2.19) is plotted along with K and M giant observations [122, 126, 159]. The agreement between the observations and the prediction from the Plummer profile implies that the mass distribution of the bulge can be adequately fit by a Plummer profile in the region of interest.

from the Plummer density. The bulge parameters are found to be $M_b = 1.02\times10^{10}\ M_\odot$ and $b = 0.258$ kpc. The potential of the Plummer model has the simple analytical form

$$\Phi_b = -\frac{GM_b}{(r^2 + z^2 + b^2)^{1/2}} \tag{2.18}$$

and a velocity dispersion [142] given by

$$\sigma_b^2 = \frac{GM_b}{6(r^2 + z^2 + b^2)^{1/2}}. \tag{2.19}$$

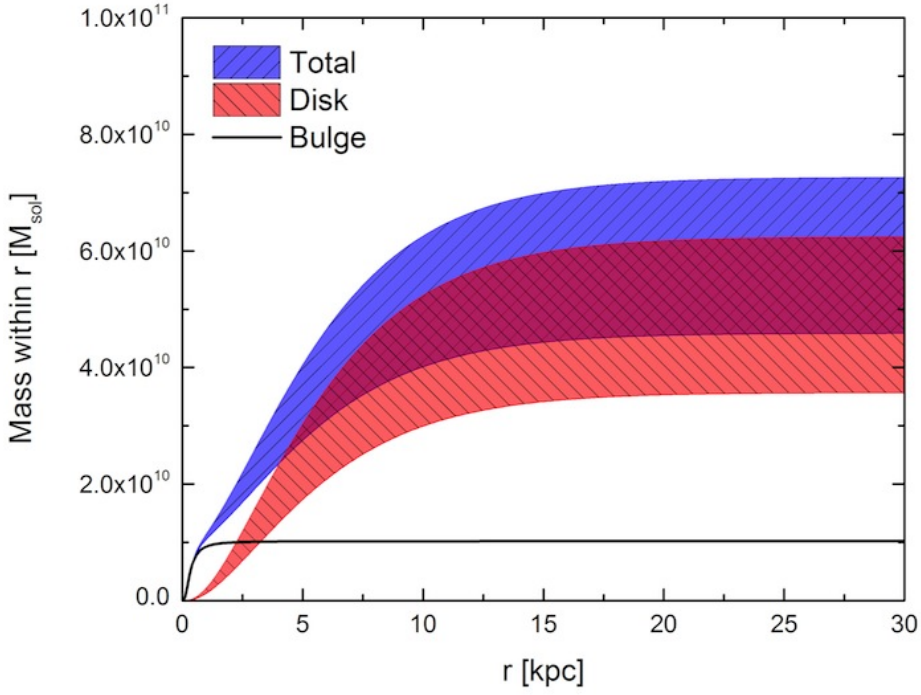

Figure 2.2: The mass profiles of the Plummer bulge (eq. 2.17) and double-exponential disk (eq. 2.8) as well as their sum are plotted as a function of distance from the Galactic center. The range of masses for the r_{tn} =3.0 kpc disk is shown for $\Sigma_{d,\odot} = 40 - 70$ $M_\odot$ pc^{-2}.

We show the velocity dispersion in Fig.2.1, along with measurements from K and M bulge giants [122, 126, 159]. Note that the dispersion expected from the Plummer model agrees with observations, implying that this region is adequately described by a bulge-dominated density profile. Including the mass contribution from the disk in this region does not noticeably increase velocity dispersion.

We show an example of the mass profiles of the Galactic disk and bulge for $r_{tn} =$ 3.0 kpc in Fig. 2.2 and a contour plot of the density distribution for the combined model of the Milky Way in Fig. 2.3.

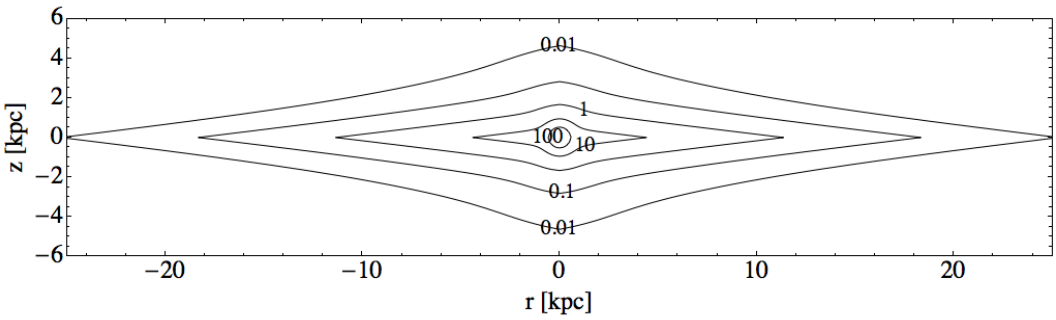

Figure 2.3: A contour plot of the edge-on density distribution (in units of GeV cm^{-3} for our model of the Milky Way is shown for $\Sigma_{d,\odot} = 55$ M$_\odot$ pc^{-2} and r_{tn}=3.0 kpc.

2.3 Dynamical Observations

Recent observations of stars, interstellar gas, and masers have been able to extend our understanding of the gravitational potential of the Galaxy beyond the Solar circle as well as near the Solar location. We present here the current state of observations of the rotation curve of the Galaxy and the details of the motion of the Sun about the Galactic center. The gravitational potential in the Galactic plane as a function of the distance from the Galactic center can be determined from the rotational speed of the Galaxy, which is related to the Galactic potential by

$$\frac{v_c^2}{r} = \left| \frac{\partial \Phi_{tot}}{\partial r} \right|, \tag{2.20}$$

where Φ_{total} includes contributions from both visible and dark matter. The best observations of the Milky Way's rotation curve now span $\sim 1-20$ kpc, and the Galactic potential can be probed up to $\sim$ 90 kpc by considering the velocity distribution of BHB and BS stars as a function of distance from the Galactic center.

Table 2.2: Observations of the Rotation Curve of the Milky Way

Reference	Range [kpc]	Observations
[162] (1978)	0.1-8	HI and CO Gas
[163] (1982)	10-17	CO Gas
[164] (1983)	4-18	Planetary Nebulae and CO Gas
[165] (1985)	2-8	CO Gas
[166] (1989)	2-17	HI and CO Gas
[167] (1993)	0.1-8	HI Gas
[168] (1993)	12-15	Young Stellar Groups
[169] (1997)	3-21	HI Gas
[170] (1997)	10-16	Cepheids
[171] (2007)	13-14	H_2O Masers
[172] (2007)	3-8	HI Gas
[173] (2010)	6-10	H_2O Masers
[174] (2011)	3-14	Masers

2.3.1 The Rotation Curve

The best estimates of the gravitational potential in the Galactic plane within $\sim$ 10 kpc of the Galactic center come from measurements of the rotation speed. We have compiled a large sample of the available observations, excluding only those with exceptionally high dispersion in the data [178] or where reproducing the data is exceptionally difficult [179]. Those data sets that were difficult to reproduce did not differ significantly from other observations in the same region. The rotation curve inside the solar circle is well-determined by observations of HI regions and CO emission associated with HII regions. Outside the Solar circle, distances to objects are much more difficult to measure accurately, so the errors in the rotation curve are correspondingly larger. We present a compilation of references to the data used in our analysis in Table 2.2, and a plot of the data can be seen in Fig.2.4 with error bars when available.

The Milky Way's rotation curve at various distances from the Galactic center

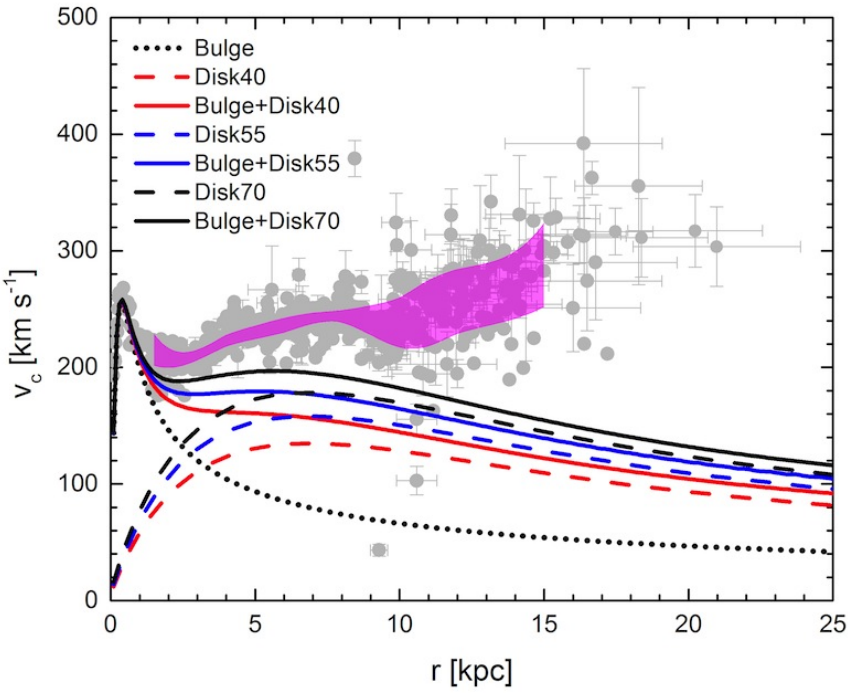

Figure 2.4: Observations of the rotation curve [162, 163, 164, 165, 166, 167, 168, 169, 170, 171, 172, 173, 174] are plotted after rescaling all the data using $R_0 = 8.3$ kpc and $\Theta_0 = 240$ km s^{-1} and adjusting for the current measurements of the peculiar motion of the Sun. The magenta band indicates there region where 2/3 of the points lie within 1 kpc radial bins. The rotation curve predicted by the visible matter components alone for the three local disk surface densities with $r_{tn} = 3.0$ kpc is shown along with the shaded observations.

can be inferred from line-of-sight observations of gas complexes, masers, planetary nebula, and other astrophysical objects. The calculation of the rotation speed is a function of R_0, the distance from the Galactic center to the Sun, and Θ_0, the rotation speed of the Sun about the Galactic center. Recently, maser observations and measurements of stellar orbits near SgrA* have been able to constrain $R_0 = 7.2-9$ kpc [144, 147, 148, 175, 176]. A summary of other recent estimates of R_0 is found in Avedisova [179] and Table 2.3. We choose $R_0 = 8.3$ kpc based on these and other stellar observations from the past decade. The ratio Θ_0/R_0 is well-constrained

from masers and stellar orbits [148, 176, 177] (see Table 2.4) and is in the range of $\Theta_0/R_0 = 28.5 - 30.3$ km/s kpc^{-1}. McMillan and Binney [180] also argue for a high value of Θ_0/R_0=29.9-31.6 km/s kpc^{-1} based on analysis of maser data from Reid et al. [148]. There are some recent studies [181, 182] that call into question the high values of Θ_0 implied by the maser observations and instead prefer values closer to ∼26 km/s kpc^{-1} . We take $\Theta_0/R_0 \approx 28.9$ km/s kpc^{-1} such that $\Theta_0 = 240$ km/s. The values we have chosen for R_0 and Θ_0 differ significantly from the IAU standard values of $R_0 = 8.5$ kpc and $\Theta_0 = 220$ km/s, which give $\Theta_0/R_0 \approx 25.9$ km/s kpc^{-1}. The IAU standard values were derived by Kerr and Lynden-Bell in 1986 [183] from the available observations. Since then observation of the Galaxy have improved, and while there is still considerable uncertainty in the values of R_0 and Θ_0, we choose to use the results of the recent maser observations in our analysis. The result of increasing Θ_0 is that the rotation curve gently rises, as is the case with several external galaxies, from $\sim 2 - 15$ kpc instead of remaining flat. We have also corrected the observations for the new measurements of the peculiar motion of the sun $(U_\odot, V_\odot, W_\odot)$ where $V_\odot$ has been updated from ~ 5 km/s to $\sim 11 - 15$ km/s [180, 184]. We take $(U_\odot, V_\odot, W_\odot) = (11, 12, 7.5)$ km/s.

2.3.2 The Vertical Force at R_0

Another estimate of the local Galactic potential comes from the gravitational force on stars within ~ 1 kpc from the Galactic plane at R_0. The most widely used formulation comes from Bahcall [201] and was used by Kuijken and Gilmore [83, 87] to calculate the widely cited surface density for visible matter at R_0. The general idea (see Kuijken

Table 2.3: Constraints on R_0

Reference	$R_\odot$ [kpc]	Observations
[185] (1988)	7.1 ± 1.5	H2O Masers in Sgr B2
[186] (1992)	7.9 ± 0.8	HI Gas
[187] (1993)	7.6 ± 0.4	Globular Clusters
[71] (1993)	6.5 ± 1.5	H2O Masers in Sgr B2
[188] (1994)	7.5 ± 1	HI Gas
[189] (1994)	7 ± 0.57	Globular Cluster Modeling
[190] (1995)	7.1 ± 0.5	Cepheids
[191] (1995)	8.3 ± 1	RR Lyrae Stars in Galactic Center
[170] (1997)	8.1 ± 0.3	Cepheids
[192] (1998)	7.66 ± 0.32	Cepheids
[193] (1998)	7.1 ± 0.4	Gas Distribution
[194] (1998)	8.4 ± 0.4	Red stars in the Galactic Bulge
[195] (1998)	8.2 ± 0.3	Red Stars in M31 and the Galactic Center
[196] (1998)	7.3 ± 0.3	Cepheids, Open Clusters, and Red Giants
[197] (2000)	7.9 ± 0.3	RR Lyrae and δ Scu Stars in the Galactic Center
[198] (2000)	7.9 ± 0.85	Cluster in the Galactic Center
[199] (2003)	7.94 ± 0.42	Orbit of S2 around the GC
[200] (2004)	8.2 ± 0.4	Open Clusters
[179] (2005)	8 ± 0.36	Star-forming Regions
[144] (2008)	8.4 ± 0.4	Stellar Orbits
[175] (2008)	8.4 ± 0.6	Masers
[147] (2009)	8.33 ± 0.34	Stellar Orbits
[148] (2009)	$7.9^{+0.8}_{-0.7}$	Masers
[176] (2011)	8.3 ± 0.23	Masers and Stellar Orbits

Table 2.4: Constraints on Θ_0/R_0

Reference	Θ_0/R_0 [km/s kpc^{-1}]
[177] (2004)	29.5 ± 0.125
[148] (2009)	29.4 ± 0.9
[176] (2011)	28.79 ± 0.26

and Gilmore [83] for details) is that near the Sun, the vertical (z-direction) motion of stars can be described by the one-dimensional collisionless Boltzmann equation. The energy in the z-direction, defined by

$$E_z = \Phi(z) + \frac{1}{2}v_z^2, \tag{2.21}$$

is an integral of motion. Therefore, by Jean's theorem, the phase-space distribution of any population of stars above the Galactic plane, which serve as tracers of Galactic potential, depends only on E_z. The spatial density of stars at a height z above the Galactic plane can be calculated by

$$\rho_z(z) = \int_{-\infty}^{\infty} f_z(z, v_z) dv_z, \tag{2.22}$$

which after parameterizing the height z in terms the potential Φ and inverting via an Abel transformation yields

$$f_z(E_z) = \frac{1}{\pi} \int_{E_z}^{\infty} \frac{-d\rho_z/d\Phi}{\sqrt{2(\Phi - E_z)}} d\Phi. \tag{2.23}$$

Therefore, given the spatial density of stars at a height z and assuming a form for the gravitational potential above the plane, the phase-space distribution of stars can be compared to observations. The vertical force above the plane,

$$F_z = \frac{d\Phi}{dz}, \tag{2.24}$$

can then be calculated from the Galactic potential. At distances z' far from the plane ($\gtrsim 1$ kpc), the vertical force is related to the total surface density of all matter within z' by

$$\Sigma_{tot}(|z| \gtrsim z') \approx \frac{|F_z(z')|}{2\pi G}. \tag{2.25}$$

Like the rotation curve, this can be used to constrain models of the Galaxy. The vertical force at R_0 must remain above the value predicted by eq. 2.25 beyond $\gtrsim 1$ kpc.

2.3.3 Blue Horizontal-Branch and Blue Straggler Stars

Xue et al. [202] have compiled an extensive list of the line-of-sight velocities of 2401 BHB stars from the Sloan Digital Sky Survey DR6 taking care to ensure their sample is pure and contains accurate data on both the distance and velocity of each star. They use this data to constrain cosmological simulations and estimate the virial mass of the Galaxy as well as derive the rotation curve up to ~ 60 kpc. We combine the compilation of 2401 BHB stars with their compilation of stars at $\sim 60 - 90$ kpc from the Galactic center. This combined compilation extends from 5-90 kpc with line-of-sight velocities spanning ± 350 km/s. After rescaling the galactocentric distances and line-of-sight velocities for each star to correspond to the values of R_0 and Θ_0 chosen above, the observations are divided into eleven radial bins (see Fig.3.17) where the velocity distribution is shown after averaging the positive and negative velocity distributions together in 50 km/s bins. Error bars are shown as $\pm\sqrt{N}$ where N is the average number of stars in each velocity bin. While this sample of BHB stars is

not complete, it is shown below that the BHB observations can be used to constrain the distribution of Galactic dark matter.

Brown et al. [203] have compiled a sample of 910 BHB and BS stars from the Hypervelocity Star Survey, which contains twice as many stars at $R \geq 50$ kpc than the Xue et al. compilation, in order to determine the velocity dispersion profile of the Milky Way out to ~ 95 kpc. While this sample is complete in color, magnitude depth, and spatial coverage, there is some ambiguity in distinguishing BHB from BS stars. To achieve the ratio of BHB to BS stars as stated in Brown et al., stars with $f_{BHB} \geq 0.6$, where f is the likelihood of a candidate star being a BHB star as reported in Table 1 of Brown et al., were taken to be BHB stars, and any star with $f_{BHB} < 0.6$ was considered to be a BS star. This reproduces the 74% to 26% BHB to BS ratio in Brown et al. As with the Xue et al. stars, this sample must also be rescaled for our adopted values of R_0 and Θ_0. We find that we are unable to reproduce the R_{BHB} and R_{BS} distances in Table 1 of Brown et al. for their choices of R_0, Θ_0 and $(U_\odot, V_\odot, W_\odot)$. We calculate the heliocentric distance for the BHB and BS stars using eq. 2 in Brown et al. and convert it to a galactocentric distance in the usual way (see eq. 4 in Xue et al. [202]). The stellar observations are then divided into eight radial bins. The line-of-sight velocities are averaged and the error bars are determined in the same manner as for the Xue et al. distribution (see Fig.3.18 for the resulting velocity distribution).

The observations reviewed briefly in this chapter for constructing a model of the visible matter in the Milky Way provides the input needed for setting up the self-consistent Poisson equation for the dark matter potential and density in the next

chapter. The observations of the Galactic rotation curve and the distributions of BHB and BS stars allow us to probe the phase-space distribution function and constrain the allowed properties of Galactic dark matter.

References

[1] Schmidt, M. 1956, Bull. Artron. Inst. Neth., 13, 15

[2] Kuzmin, G. G. 1952, Pub. Tar. Astro. Obs., 32, 211

[3] Oort, J. 1932, Bull. Astron. Inst. Neth., 6, 249

[4] Innanen, K. A. 1966, ApJ, 143, 153

[5] Innanen, K. A. 1973, Astro. Spa. Sci., 22, 393

[6] Miyamoto, M. & Nagai, R. 1975, PASJ, 27, 533

[7] deVaucouleurs, G. 1959, Hdb. d. Phys., 53, 311

[8] Freeman, K. C. 1970, ApJ, 160, 811

[9] Toomre, A. 1963, ApJ, 138, 385

[10] Mestel, L. 1963, ApJ, 126, 553

[11] Athanassoula, E., Bosma, A., & Papioannou, S. 1987, A&A, 179, 23

[12] Kormendy, J. 1977, ApJ, 214, 359

[13] Kormendy, J. 1977, ApJ, 218, 333

[14] Kormendy, J. 1977, ApJ, 217, 406

[15] Einasto, J. & Haud, U. 1989, A&A, 223, 89

[16] Bahcall, J. N. & Soneira, R. M. 1980, ApJ Sup. Ser., 44, 73

[17] Rohlfs, K. & Kreitschmann, J. 1981, Astrophys. Spac. Sci., 79, 289

[18] Caldwell, J. A. R. & Ostriker, J. P. 1981, AJ, 251, 61

[19] Schmidt, M. 1985, *The Milky Way Galaxy*; Proceedings of the 106th Symposium, Groningen, Netherlands 75

[20] Rohlfs, K. & Kreitschmann, J. 1988, A&A, 201, 51

[21] Deason, A. J., Belokurov, V., & Evans, N. W. 2011, arXiv:1104.3220v1

[22] A. Gupta et al., 2012, ApJ, 756, L8

[23] Helmi, A. 2008, Astron. Astrophys. Rev., 15, 145

[24] Ibata, R. & Gilmore, G. 1995, MNRAS, 275, 591

[25] Jurić, M., et al. 2008, ApJ, 673, 864

[26] Belokurov, V., et al. 2006, ApJ, 642, L137

[27] Belokurov, V., et al. 2007, ApJ, 657, L89

[28] Gilmore, G., Wyse, R., & Kuijken, K. 1989, ARA&A, 27, 555

[29] Majewski, S. R. 1993, ARA&A, 31, 575

[30] Freeman, K. C. & Bland-Hawthorn, J. 2002, ARA&A, 40, 487

[31] Carollo, D., et al. 2010, ApJ, 712, 692

[32] Carollo, D., et al. 2007, Nature, 450, 1020

[33] Beers, T. C., et al. 2011, arXiv:1104.2513v1

[34] Robin, A. C., et al. 2003, A&A, 409, 523

[35] Robin, A. C., Reylé, C., & Crézé, M. 2000, A&A, 359, 103

[36] Siegel, M. H., et al. 2002, ApJ, 578, 151

[37] Sluis, A. P. N. & Arnold, R. A. 1998, MNRAS, 297, 732

[38] DePropris, R., Harrison, C. D., & Mares, P. J. 2010, ApJ, 719, 1582

[39] Morrison, H. L., et al. 2000, AJ, 119, 2254

[40] Chen, B., et al. 2001, ApJ, 553, 184

[41] Yanny, B., et al. 2000, ApJ, 540, 825

[42] Ivezić, $\check{Z}$., et al. 2000, AJ, 120, 963

[43] Vivas, A. K., et al. 2004, AJ, 127, 1158

[44] Xu, Y., Deng, L. C., & Hu, J. Y. 2007, MNRAS, 379, 1373

[45] Fuchs, B. & Jahreiß, J. 1998, A&A, 329, 81

[46] Digby, A. P., et al. 2003, MNRAS, 344, 583

[47] Flynn, C., Gould, A., & Bahcall, J. N. 1996, ApJ, 466, L55

[48] Gould, A., Flynn, C., & Bahcall, J. N. 1998, ApJ, 503, 798

[49] Newberg, H. J. & Yanny, B. 2006, J. Phys. Conf. Ser., 47, 195

[50] Watkins, L. L., et al. 2009, MNRAS, 398, 1757

[51] Sesar, B., et al. 2010, ApJ, 708, 717

[52] Graham, A. W., et al. 2006, AJ, 132, 2701

[53] Minniti, D., et al. 2011, ApJ, 733, L43

[54] Ruphy, S., et al. 1996, A&A, 313, L21

[55] Gilmore, G. & Reid, N. 1983, MNRAS, 202, 1025

[56] Reddy, B. E. 2009, IAU Symp, Chemical Abundances in the Universe: Connecting First Stars to Planets, eds. Cunha, K., Spite, M., & Barbuy, B., 265, 119

[57] Gilmore, G. & Wyse, R. 1985, AJ, 90, 2015

[58] Carney, B. W., Latham, D. W., & Laird, J. B. 1989, AJ, 97, 423

[59] Norris, J. & Green, E. M. 1989, ApJ, 337, 272

[60] Norris, J. & Ryan, S. G. 1991, ApJ, 380, 403

[61] Cabrera-Lavers, A., Garzón, F., & Hammersley, P. L. 2005, A&A, 433, 173

[62] McMillan, P. J. 2011, MNRAS, 414, 2446

[63] Sofue, Y., Honma, M., & Omodaka, T. 2009, PASJ, 61, 227

[64] Binney, J., Gerhard, O., & Spergel, D. 1997, MNRAS, 288, 365

[65] Freudenreich, H. T. 1998, ApJ, 492, 495

[66] Drimmel, R. & Spergel, D. N. 2001, ApJ, 556, 181

[67] Ojha, D. K. 2001, MNRAS, 322, 426

[68] López-Corredoira, M., et al. 2002, A&A, 394, 426

[69] Bahcall, J. N. & Soneira, R. M. 1984, ApJS, 55, 67

[70] Robin, A. C. & Crézé, M. 1986, A&AS, 64, 53

[71] Reid, N. & Majewski, S. R. 1993, ApJ, 409, 635

[72] Buser, R., Rong, J., & Karaali, S. 1999, A&A, 348, 98

[73] Spagna, A., et al. 1996, A&A, 313, L21

[74] Ng, Y. K., et al. 1997, A&A, 324, 65

[75] Larsen, J. A. & Humphreys, R. M. 2003, AJ, 125, 1958

[76] Robin, A. C., et al. 1996, A&A, 305, 125

[77] Bensby, T. et al. 2011, ApJ, 735, L46

[78] Cheng, J. Y. et al. 2012, ApJ, 752, 51

[79] Bovy, J. et al. 2012a, ApJ, 753, 148

[80] Cabrera-Lavers, A., et al. 2007, A&A, 464, 565

[81] Romano, D., et al. 2000, ApJ, 539, 235

[82] Rossetto, B. M., et al. 2011, ApJ, 141, 185

[83] Kuijken, K. & Gilmore, G. 1991, ApJ, 367, L9

[84] Lucas, P. W., et al. 2008, MNRAS, 391, 136

[85] Minniti, D., et al. 2010, New Astro., 15, 433

[86] Robin, A. C., Crézé, M., & Mohan, V. 1992, ApJ, 400, L25

[87] Kuijken, K. & Gilmore, G. 1989, MNRAS, 239, 605

[88] Flynn, C. & Fuchs, B. 1994, MNRAS, 270, 471

[89] Gould, A., Bahcall, J. N., & Flynn, C. 1996, ApJ, 465, 759

[90] Korchagin, V. I., et al. 2003, ApJ, 126, 2896

[91] Siebert, A., Bienaymé, O, and Soubiran, C. 2003, A&A, 399, 531

[92] Holmberg, J. & Flynn, C. 2004, MNRAS, 352, 440

[93] Flynn, C., et al. 2006, MNRAS, 372, 1149

[94] Weber, W. & de Boer, W. 2010, A&A, 509, A25

[95] Zhen, Z., et al. 2001, ApJ, 555, 393

[96] Mera, D., Chabrier, G., & Schaeffer, R. 1998, A&A, 330, 937

[97] Dame, T. M. 1993, AIP Conf., Back to the Galaxy, eds. Holt, S. S. & Verter, F., 278, 267

[98] Olling, R. P. & Merrifield, M. R. 2001, MNRAS, 326, 164

[99] Dwek, E., et al. 1995, ApJ, 445, 716

[100] Binney, J., et al. 1991, MNRAS, 252, 210

[101] López-Corredoira, M., Cabrera-Lavers, A. & Gerhard, O. E. 2005, A&A, 439, 107

[102] López-Corredoira, M., et al. 1997, MNRAS, 292, L15

[103] López-Corredoira, M., et al. 2000, MNRAS, 313, 392

[104] Hammersley, P. L., et al. 1999, MNRAS, 308, 333

[105] Stanek, K. Z., et al. 1994, ApJ, 429, L73

[106] Gerhard, O. E. 2001, Galaxy Disks and Disk Galaxies, ASP Conf. Ser., eds. Funes, J. G., Corsini, S. J., & Corsini, E. M., 230, 21

[107] Kennicutt, R. C. 2001, Tetons 4: Galactic Structure, Stars and the Interstellar Medium, ASP Conf. Ser., eds. Woodward, C. E., Bicay, M. D., & Shull, J. M., 231, 2

[108] deVaucouleurs, G. 1964, IAU Symp 20, ed Kerr, F. J., Canberra: Aust Acad Sci, 195

[109] Liszt, H. S. & Burton, W. B. 1980, ApJ, 236, 77

[110] Stanek, K. Z., et al. 1997, ApJ, 477, 163

[111] Paczynski, B., et al. 1994, ApJ, 435, L113

[112] Alcock, C., et al. 1997, ApJ, 486, 697

[113] Weinberg, M. D. 1992, ApJ, 384, 81

[114] Weinberg, M. D. 1992, ApJ, 392, 67

[115] Nikolaev, S. & Weinberg, M. D. 1997, ApJ, 487, 885

[116] Whitelock, P. A. & Catchpole, R. 1992, IAU Symp 149, eds. Barbuy, B. & Renzini, A., Dordrecht: Kluwer, 503

[117] Sevenster, M., et al. 1999, MNRAS, 307, 584

[118] Unavane, M. & Gilmore, G. 1998, MNRAS, 295, 145

[119] Fux, R. 1999, A&A, 345, 787

[120] Englmaier, P. & Gerhard, O. E. 1999, MNRAS, 304, 512

[121] Gerhard, O. E. 1999, ASP Conf. Ser., Galaxy Dynamics, eds. Merritt, D., Selwood, J. A., & Valluri, A., 182, 307

[122] Minniti, D., et al. 1992, ApJ, 393, L47

[123] Harding, P. & Morrison, H. 1993, IAU Symp., Galactic Bulges, eds. Dejonghe, H. & Habing, H., 153, 297

[124] Minniti, D. 1996, ApJ, 459, 175

[125] Beaulieu, S. F. 2000, AJ, 120, 855

[126] Rich, M., et al. 2007, ApJ, 658, L29

[127] Terndrup, D., Sadler, E., & Rich, M. 1995, AJ, 110, 1774

[128] Launhardt, R., Zylka, R., & Mezger, P. G. 2002, A&A, 384, 112

[129] Blitz, L., et al. 1993, Nature, 361, 417

[130] Genzel, R., Hollenback, D., & Townes, C. H. 1994, Rep. Prog. Phys., 57, 417

[131] Mezger, P. G., Duschl, W. J., & Zylka, R. 1996, AAR, 7, 289

[132] Morris, M. & Serabyn, E. 1996, ARA&A, 34, 645

[133] Merritt, D. 2010, arXiv:1001.5435v3

[134] Schödel, R., et al. 2007, A&A, 469, 125

[135] Vanhollebeke, E., Groenewegen, M. A. T., & Girardi, L. 2009, A&A, 498, 95

[136] Bissantz, N. & Gerhard, O. 2002, MNRAS, 330, 591

[137] Zhao, H. & Mao, S. 1996, MNRAS, 283, 1197

[138] Groenewegen, M. A. T. & Bloomaert, J. A. D. L. 2005, A&A, 443, 143

[139] Rattenbury, N. J., et al. 2007, MNRAS, 378, 1064

[140] Genzel, R., et al. 2003, ApJ, 594, 812

[141] Oh, S., Kim, S. S., & Figer, D. F. 2009, J. Kor. Astro. Soc., 42, 17

[142] Dejonghe, H. 1987, MNRAS, 224, 12

[143] Eisenhauer, F., et al. 2005, ApJ, 628, 246

[144] Ghez, A. M., et al. 2008, ApJ, 689, 1044

[145] Ghez, A. M., et al. 2003, Astron. Nach., 324, 527

[146] Ghez, A. M., et al. 2005, ApJ, 620, 744

[147] Gillessen, S., et al. 2009, ApJ, 692, 1075

[148] Reid, M. J. 2009, Int. J. Mod. Phys. D, 18, 889

[149] Bozza, V. & Mancini, L. 2009, ApJ, 696, 701

[150] Genzel, R. & Karas, V. 2006, IAU Symp., 238, *Black Holes: from Stars to Galaxies-across the Range of Masses*, eds. Karas, V. & Matt, G., 173

[151] Ghez, A. M., et al. 2000, Nature, 407, 349

[152] Schödel, R., et al. 2002, Nature, 419, 694

[153] Schödel, R., et al. 2003, ApJ, 596, 1015

[154] Genzel, R., Eisenhauer, F., & Gillessen, S. 2010, Rev. Mod. Phys., 82, 3121

[155] Melia, F. & Falcke, H. 2001, Ann. Rev. Astron. Astrophys., 39, 309

[156] Cowsik, R. et al. 2007, New Astron., 12, 507

[157] Momany, Y. et al. 2006, A&A, 451, 515

[158] Mo, H., van den Bosch, F., & White, S. 2010, Galaxy Formation and Evolution, (Cambridge: Cambridge University Press)

[159] Blum, R. D., et al. 1995, ApJ, 449, 623

[160] Demers, S. & Battinelli, P. 2007, A&A, 473, 143

[161] Avedisova, V.S. 2005, Astron. Rep. 49, 435

[162] Burton, W. B. & Gordon, M. A. 1978, A&A, 63, 7

[163] Blitz, L., Fich, M., & Stark, A. A. 1982, ApJS, 49, 183

[164] Schneider, S. E. & Terzian, Y. 1983, ApJL, 274, L61

[165] Clemens, D. P. 1985, ApJ, 295, 422

[166] Fich, M., Blitz, L., & Stark, A. A. 1989, ApJ, 342, 272

[167] Burton, W. B. & Liszt, H. S. 1993, A&A, 274, 765

[168] Turbide, L. & Moffat, A. F. J. 1993, AJ, 105, 1831

[169] Honma, M. & Sofue, Y. 1997, PASJ, 49, 453

[170] Pont, F., et al. 1997, A&A, 318, 416

[171] Honma, M., et al. 2007, PASJ, 59, 889

[172] McClure-Griffiths, N. M. & Dickey, J. M. 2007, ApJ, 671, 427

[173] Oh, C. S., et al. 2010, PASJ, 62, 101

[174] Stepanishchev, A. S. & Bobylev, V. V. 2011, Astron. Lett., 37, 254

[175] Reid, M. J., et al. 2008, ApJ, 700, 137

[176] Brunthaler, A., et al. 2011, Astron. Nachr., 332, 461

[177] Reid, M. J. & Brunthaler, A. 2004, ApJ, 616, 872

[178] Demers, S. & Battinelli, P. 2007, A&A, 473, 143

[179] Avedisova, V.S. 2005, Astron. Rep. 49, 435

[180] McMillan, P. J. & Binney, J. J. 2010, MNRAS, 402, 934

[181] Koposov, S. E. et al. 2010, ApJ, 712, 260

[182] Bovy, J. et al. 2012b, ApJ, 759, 131

[183] Kerr, F. J. and Lynden-Bell, D. 1986, MNRAS, 221, 1023

[184] Schönrich, R., Binney, J. & Dehnen, W. 2010, MNRAS, 403, 1829

[185] Reid, M. J., et al. 1988, ApJ, 330, 809

[186] Merrifield, M. R. 1992, AJ, 103, 1552

[187] Maciel, W. J. 1993, Astrophys. Space Sci., 206, 285

[188] Nikiforov, I. I. & Petrovskaya, I. V. 1994, Astron. Rep., 38, 642

[189] Rastorguev, A. S., et al. 1994,, Astron. Lett., 20, 591

[190] Dambis, A. K., Mel'nik, A. M., & Rastorguev, A. S. 1995, Astron. Lett., 21, 291

[191] Carney, B. W., et al. 1995, AJ, 110, 1674

[192] Metzger, M. R., Caldwell, A. R., & Schechter, P. L. 1998, AJ, 115, 635

[193] Olling, R. P. & Merrifield, M. R. 1998, MNRAS, 297, 943

[194] Paczynski, B. & Stanek, K. Z. 1998, ApL, 494, L219

[195] Stanek, K. Z. & Garnavich, P. M. 1998, ApJ, 503, L131

[196] Glushkova, E. V., et al. 1998, A&A, 329, 514

[197] McNamara, D. H., et al. 2000, Publ. Astron. Soc. Pac., 112, 202

[198] Genzel, R., et al. 2000, MNRAS, 317, 348

[199] Eisenhauer, F., et al. 2003, ApJ, 597, L121

[200] Gerasimenko, T. P. 2004, Astron. Rep., 48, 103

[201] Bahcall, J. N. 1984, ApJ, 276, 156

[202] Xue, X. X., et al. 2008, ApJ, 684, 1143

[203] Brown, W. R., et al. 2010, ApJ, 139, 59

Chapter 3

The Phase-Space Distribution of Galactic Dark Matter [1]

The phase-space distribution of Galactic dark matter is currently not well determined. The density distribution of dark matter depends not only on the assumed form of its velocity distribution but also on the gravitational potential generated by the dark matter particles themselves and by the visible stellar and gaseous matter in the Galaxy. The total potential, Φ_{tot}, is the sum of both the visible and dark matter matter potentials given by

$$\Phi_{tot} = \Phi_b + \Phi_d + \Phi_{DM}, \tag{3.1}$$

where Φ_{DM} is the potential from dark matter and Φ_b and Φ_d refer to the potential contributed by the central bulge and disk respectively, representing the two major visible components of the Galaxy as defined in Chapter 2. To construct a self-consistent

[1] This work has been submitted to ApJ (Burch, B. & Cowsik, R. 2013, arXiv:1306.1920).

model for the distribution of dark matter in the Galaxy, we require a dynamical model whose phase-space distribution function represents a collisionless system that can be parameterized by the dark matter velocity dispersion, density at either the Galactic center or at R_0, and the size of the dark matter halo. A lowered isothermal (King) distribution, which is described in detail in Binney and Tremaine [1], has a finite mass and non-singular central density (unlike the isothermal sphere) and meets these requirements. Reasons for choosing the King distribution are also discussed in earlier papers [2, 3].

3.1 The King Distribution

The phase-space distribution function of the King model is given by

$$f(\varepsilon) = \begin{cases} \frac{\rho_1}{\left(2\pi\sigma_{DM}^2\right)^{3/2}}\left(e^{\varepsilon/\sigma_{DM}^2} - 1\right) & \text{for } \varepsilon > 0 \\ 0 & \text{for } \varepsilon \leq 0 \end{cases} \tag{3.2}$$

where

$$\varepsilon \equiv \Phi_0 - \left(\frac{1}{2}v^2 + \Phi_{tot}\right). \tag{3.3}$$

The total potential at $r = r_t$, the "virial" (King) radius of the Galactic dark matter halo, is denoted by Φ_0, and ρ_1 and σ are are related but not equal to the central dark matter density, ρ_{DM0} and the dark matter velocity dispersion respectively, both of which can be directly calculated from the phase-space distribution function.

The dark matter density distribution is readily calculated by integrating the phase-

space distribution function

$$\rho_{DM} = \int f \; d^3v \tag{3.4}$$

and vanishes at r_t where $\varepsilon = 0$. Defining $\Psi(r,z)$ as the scaled potential at the position (r,z) with

$$\Psi(r,z) \equiv \Phi_0 - \Phi_{tot}(r,z), \tag{3.5}$$

eq. 3.4 becomes

$$\begin{aligned}
\rho_{DM}(\Psi(r,z)) &= \frac{\rho_1}{(2\pi\sigma_{DM}^2)^{3/2}} \int_0^{\sqrt{2\Psi(r,z)}} dv \; v^2 \left[\exp\left(\frac{\Psi(r,z) - \frac{1}{2}v^2}{\sigma_{DM}^2} \right) - 1 \right] \\
&= \rho_1 \left[e^{\Psi(r,z)/\sigma_{DM}^2} \mathrm{erf}\left(\frac{\sqrt{\Psi(r,z)}}{\sigma_{DM}} \right) \right. \\
&\quad \left. - \sqrt{\frac{4\Psi(r,z)}{\pi\sigma_{DM}}} \left(1 + \frac{2\Psi(r,z)}{3\sigma_{DM}^2} \right) \right],
\end{aligned} \tag{3.6}$$

where $\sqrt{2\Psi(r,z)}$ is the Galactic escape speed.

Since ρ_{DM}, which is the source of Φ_{DM}, depends on Φ_{DM} itself, the dark matter potential is calculated iteratively by numerically solving the Poisson equation,

$$\nabla^2 \Phi_{DM}(r,z) = 4\pi G \rho_{DM}(r,z), \tag{3.7}$$

by a Legendre polynomial expansion as described in Cowsik et al. [4] and based on earlier work by Wilson [5] and Prendergast and Tomer [6]. In this way, we compute the potential for the visible matter and the potential and density distribution for the dark matter.

3.2 Solving Poisson's Equation

To solve Poisson's equation, we begin by following Wilson [5] and write the relative potential Ψ in spherical coordinates and in dimensionless units, denoted by a tilde over the variable, such that

$$\tilde{\nabla}^2\tilde{\Psi}(\tilde{R},\theta) = \lambda\tilde{\rho}(\tilde{R}\sin\theta,\tilde{\Psi}) \tag{3.8}$$

and subject to the central boundary conditions

$$\begin{aligned} \tilde{\Psi}(0,\theta) &= \tilde{\Psi}_0, \\ \frac{\partial\tilde{\Psi}}{\partial\tilde{R}}\Big|_{\tilde{R}=0} &= 0. \end{aligned} \tag{3.9}$$

The dimensionless variables can be converted to dimensional variables with the appropriate scale factors defined by

$$\begin{aligned} \tilde{\nabla}^2 &= r_*^2\nabla^2, \\ \tilde{\Psi} &= \frac{\Psi}{v_*^2}, \\ \tilde{R} &= \frac{R}{r_*}, \\ \tilde{\rho} &= \frac{\rho}{\rho_*}, \end{aligned}$$

such that

$$\lambda = 4\pi G \frac{r_*^2 \rho_*}{v_*^2}.$$

For the purposes of this study, $r_* = 1$ kpc, $v_* = 100$ km/s, and $\rho_* = 1$ GeV/cm^3, which implies $\lambda \approx 0.1423$. The potential and density can be expanded in terms the Legendre polynomials as

$$\tilde{\Psi}(\tilde{R}, \theta) = \sum_{k=0}^{2N-2} u_k(\tilde{R}) P_k(\cos\theta) \tag{3.10}$$

and

$$\tilde{\rho}(\tilde{R}, \theta) = \sum_{k=0}^{2N-2} g_k(\tilde{R}) P_k(\cos\theta), \tag{3.11}$$

where the sums are only over even values of k to enforce axisymmetric symmetry. For our analysis, we take the maximum values of k to be 16. The Poisson equation as written in eq. 3.8, subject to the above boundary conditions, can be manipulated into a set of integral equations to obtain the potential coefficients in eq. 3.10, which are given by

$$u_0(\tilde{R}) = \tilde{\Psi}_0 + \lambda \left[\int_0^{\tilde{R}} t g_0(t) dt - \frac{1}{\tilde{R}} \int_0^{\tilde{R}} t^2 g_0(t) dt \right] \tag{3.12}$$

and

$$u_k(\tilde{R}) = -\frac{\lambda}{2k+1} \left[\tilde{R}^k \int_{\tilde{R}}^{\infty} t^{1-k} g_k(t) dt + \frac{1}{\tilde{R}^{k+1}} \int_0^{\tilde{R}} t^{k+2} g_k(t) dt \right] \tag{3.13}$$

for $k = 2, 4, 6, ..., 2N-2$. The density coefficients $g_k(\tilde{R})$ are found by inverting eq.

3.11, which is given at a particular $\tilde{R}$ by

$$g_k(\tilde{R}) = \frac{1}{2}(2k+1)\int_{-1}^{1} \tilde{\rho}(\tilde{R},\mu)P_k(\mu)d\mu, \tag{3.14}$$

again for $k = 2, 4, 6, ..., 2N-2$. In this way, the visible matter potential and the dark matter potential and density is computed iteratively and self-consistently, starting from the central boundary condition until the outer regions of the Galaxy when $\Psi = 0$ (see Appendix D for the FORTRAN program which solves Poisson's equation and computes the other quantities of interest).

3.3 Comparison with the Astronomical Observations

For the above calculations, we formulate the King distribution in terms of σ_{DM}, ρ_{DM0}, and Ψ_0/σ_{DM}^2 instead of ρ_1 and Φ_0. The precise choices for σ, ρ_{DM0}, and Ψ_0/σ_{DM}^2 are made by solving eq. 3.7 for a range of values, calculating the corresponding rotation curve (eq. 3.16), and comparing the results to the observations of the rotation curve and to the velocity distribution of BHB and BS stars. We also calculate the root-mean-square velocity given by

$$< v_{DM}^2(r,z) >^{1/2} = \sqrt{\frac{\int_0^{v_{esc}} v^4 \left(e^{[\Psi(r,z)-\frac{1}{2}v^2]/\sigma^2} - 1 \right) dv}{\int_0^{v_{esc}} v^2 \left(e^{[\Psi(r,z)-\frac{1}{2}v^2]/\sigma^2} - 1 \right) dv}}. \tag{3.15}$$

Table 3.1: Models for the $r_{tn} = 2.5$ kpc disk which best fit the rotation curve.

ρ_{DM0}	σ_{DM}	Ψ_0/σ_{DM}^2	$v_c(R_0)$	$< v_{DM}^2(R_0) >^{1/2}$	$\rho_{DM}(R_0)$	$v_{esc}(0)$	$v_{esc}(R_0)$	L
$\Sigma_{d,\odot}$=40 M$_\odot$ pc^{-2}								
50	240	8	246.0	521.6	0.723	960.0	673.3	0.274
75	225	9	240.5	515.1	0.644	954.6	665.0	0.652
75	230	9	250.0	533.9	0.737	975.8	689.3	0.746
100	220	9	241.7	487.4	0.632	933.4	629.3	0.093
100	225	9	251.9	506.1	0.726	954.6	653.4	0.173
250	205	10	242.7	453.6	0.573	916.8	585.6	0

Densities are in units of GeV cm^{-3}, and velocities are in units of km s^{-1}.

Table 3.2: Models for the $r_{tn} = 3.0$ kpc disk which best fit the rotation curve.

ρ_{DM0}	σ_{DM}	Ψ_0/σ_{DM}^2	$v_c(R_0)$	$< v_{DM}^2(R_0) >^{1/2}$	$\rho_{DM}(R_0)$	$v_{esc}(0)$	$v_{esc}(R_0)$	L
$\Sigma_{d,\odot}$=40 M$_\odot$ pc^{-2}								
250	205	11	250.1	515.4	0.760	961.5	665.4	0.777
500	195	12	244.2	497.7	0.662	955.3	642.5	0.791
$\Sigma_{d,\odot}$=55 M$_\odot$ pc^{-2}								
100	220	10	251.3	546.1	0.719	983.9	705.0	1
250	200	11	241.3	489.0	0.563	938.1	631.4	0.732
250	205	11	252.2	508.3	0.654	961.5	656.3	0.834
500	195	11	244.5	442.6	0.535	914.6	571.4	0
$\Sigma_{d,\odot}$=70 M$_\odot$ pc^{-2}								
25	255	7	244	520	0.573	954.1	671.3	0.524
50	235	8	248.3	498.3	0.582	940	643.3	0.250
75	220	9	242.7	490.8	0.505	933.4	633.6	0.597
100	215	9	243.1	463.1	0.489	912.2	597.8	0.056
250	200	11	245.6	480.7	0.470	938.1	620.6	0.784
500	190	12	240.7	462.5	0.395	930.8	597.1	0.764

Densities are in units of GeV cm^{-3}, and velocities are in units of km s^{-1}.

In order to compare with the rotation curve and the BHB and BS observations, a large sample of possible dark matter models were generated, with values chosen by hand, encompassing $\rho_{DM0} = 1 - 1000$ GeV cm^{-3} (we considered 1, 5, 10, 25, 50, 75, 100, 250, 500, and 1000 GeV cm^{-3}), $\sigma_{DM} \approx 100 - 1000$ km s^{-1} (in 5 km s^{-1} intervals), and $\Psi_0/\sigma_{DM}^2 \approx 1 - 25$ (in unit intervals) for each of the three disks. For each model, $\Psi(r, z)$ for the visible and dark matter, the density distribution of the dark matter, $\rho_{DM}(R_0)$, $< v_{DM}^2(R_0) >^{1/2}$, $v_c(r)$, the escape velocity, and the King radius r_t were calculated. Bounds were first put on the parameters of the models by placing the constraint 220 km s^{-1} $\leq v_c(R_o) \leq$ 260 km s^{-1}. Then, models which agreed with the rotation curve by passing through the narrow band encompassing 2/3 of the observational were identified. The results of this analysis are shown in Tables 3.1-3.3.

Table 3.3: Models for the $r_{tn} = 3.5$ kpc disk which best fit the rotation curve.

ρ_{DM0}	σ_{DM}	Ψ_0/σ^2_{DM}	$v_c(R_0)$	$< v^2_{DM}(R_0) >^{1/2}$	$\rho_{DM}(R_0)$	$v_{esc}(0)$	$v_{esc}(R_0)$	L
$\Sigma_{d,\odot}$=40 M$_\odot$ pc^{-2}								
500	200	10	251.3	421.0	0.736	894.4	543.5	0
$\Sigma_{d,\odot}$=55 M$_\odot$ pc^{-2}								
250	205	11	254.1	515.3	0.758	961.5	665.2	0.781
500	195	11	246.0	450.3	0.631	914.6	581.4	0
$\Sigma_{d,\odot}$=70 M$_\odot$ pc^{-2}								
100	225	8	256.4	450.9	0.725	900.0	582.1	0
250	200	10	242.9	440.6	0.551	894.4	568.8	0
250	205	10	253.8	459.2	0.642	916.8	592.9	0
500	195	10	244.5	392.2	0.502	872.1	506.3	0

Densities are in units of GeV cm^{-3}, and velocities are in units of km s^{-1}.

3.3.1 Comparison with the Rotation Curve

The discovery and study of dark matter in the Galaxy comes almost entirely from measurements of rotation curve. In this section we limit the range of parameters characterizing the phase-space distribution function of the dark matter by requiring that the models we have calculated agree with the compilation of observations of the rotation curve shown in Fig. 2.4. The rotation curve predicted from the dark matter models can be calculated using the expression

$$v_c(r) = \left(\left| r \frac{\partial \Phi_{tot}(r,0)}{\partial r} \right| \right)^{1/2} = \left(\left| r \frac{\partial}{\partial r} [\Phi_b(r,0) + \Phi_d(r,0) + \Phi_{DM}(r,0)] \right| \right)^{1/2} \quad (3.16)$$

for the twelve sets of models characterized by the three choices of $\Sigma_{d,\odot} = 40$ M$_\odot$ pc^{-2}, 55 M$_\odot$ pc^{-2}, and 70 M$_\odot$ pc^{-2} and the four choices of the radial scale length of the thin disk $r_{tn} = 2.0$ kpc, 2.5 kpc, 3 kpc, and 3.5 kpc. We display in Figs. 3.1-3.3 the models which fit the rotation curve (i.e. pass through the shaded band) for each these sets of model. The corresponding of density profiles for these models are shown in Figs. 3.4-3.6. The vertical force at R_0 for each model is shown in Figs. 3.7-3.9. The local and central dark matter density, escape velocity from the R_0 and the Galactic center, and the root-mean-square velocity at R_0 for each of these models

are presented in Tables 3.1-3.3 and shown as cross plots in Figs. 3.10-3.15. All the models displayed here also satisfy the criterion that $v_c(R_0)$ lies in the range 220-260 km s^{-1}, which encompasses 2/3 of all the available measurements.

The results as presented in the tables and figures allow us to make the following statements:

1. All dark matter models with the thin disk scale length of 2.0 kpc have corresponding rotation curves which fall below the observations. For $r_{tn} = 2.5$ kpc, only the lightest disk produced dark matter models consistent with the rotation curve.

2. All the dark matter models in Tables 3.1-3.3 provide good fits to the observed rotation curve within the solar circle ($r < R_0$).

3. The larger the assumed value of the surface density of the disk, larger is the range of allowed parameters of the dark matter distributions.

4. The range in the parameters allowed by the models which best fit the rotation curve is:

   (a) 872.1 km s^{-1} $\lesssim$ $v_{esc}(0)$ $\lesssim$ 983.9 km s^{-1}

   (b) 506.3 km s^{-1} $\lesssim$ $v_{esc}(R_0)$ $\lesssim$ 705.0 km s^{-1}

   (c) 25 GeV cm^{-3} $\lesssim$ ρ_{DM0} $\lesssim$ 500 GeV cm^{-3}

   (d) 0.395 GeV cm^{-3} $\lesssim$ $\rho_{DM}(R_0)$ $\lesssim$ 0.760 GeV cm^{-3}

   (e) 392.2 km s^{-1} $\lesssim$ $< v^2_{DM}(R_0) >^{1/2}$ $\lesssim$ 546.1 km s^{-1}.

5. The local dark matter density for every model is greater than the standard value of 0.3 GeV cm^{-3}. Using a lower value of Θ_0 would correspond to a lower local dark matter density, and this effect must be considered in future study. The signals for direct detection are directly proportional to $\rho_{DM}(R_0)$ and increase at least linearly with $< v^2_{DM}(R_0) >^{1/2}$, so that the allowed rate may vary at least by a factor of ~ 8, even for detectors with very low threshold. The indirect experiments focus usually on detecting annihilation or decay products from dark matter in the central regions of the Galaxy. These rates, proportional to $\rho^2_{DM}(0)$ and $\rho_{DM}(0)$ (see Chapter 5), span a range of 400 and 20 respectively.

6. It is interesting to see if there exists any correlation between different parameters in these models that generally fit the rotation curves within the solar circle. These are shown in Figs. 3.10-3.15.

   (a) The correlation between the values of the σ_{DM} parameter and the central density ρ_{DM0} is shown in Fig. 3.10, and the value of σ_{DM} is shown to decrease with increasing ρ_{DM0} and begins to level off, but is still gently decreasing around ~ 200 km s^{-1}.

   (b) Similarly, the escape velocity from the center of the Galaxy gently decreases beyond ρ_{DM0} $\sim$200 km s^{-1} for a given set of disk parameters (see Fig. 3.11). Correspondingly, the escape from the location of the Sun shows similar behavior (see Fig. 3.12).

   (c) The root-mean-square velocities of the dark matter particles $< v^2_{DM}(R_0) >^{1/2}$ and $\rho_{DM}(R_0)$ decreases as ρ_{DM0} increases (see Fig. 3.13 and Fig. 3.14).

(d) The value of $\rho_{DM}(R_0)$ increases statistically with increasing $< v_{DM}^2(R_0) >^{1/2}$ as shown in Fig. 3.15, thereby increasing the range of expectation of event rates in direct detection experiments.

7. The solution to Poisson's equation yields the potential at every point in the Galaxy. It is therefore possible to calculate the vertical force profile. In Figs. 3.7-3.9, the vertical force profiles at the Solar location are shown for the dark matter models which best fit the observations of the rotation curve. In principle, the motions of stars above the Galactic plane at R_0 could be used to further constrain the dark matter parameters. We note here that the vertical force obtains dominant contribution from the visible matter disk for $z \ll 1$ kpc and exceeds the disk contribution of

$$F_z \geq 2\pi G\Sigma_d$$

at greater heights.

3.3.2 Comparison with the Distributions of BHB and BS Stars

The BHB and BS stars, with their distribution extending up to $\sim$ 90 kpc, serve as tracers of the gravitational potential of the Galaxy, even though they contribute negligibly to the potential. Since only their radial velocities are well determined, we will first write down their radial distribution function under the assumption that their

phase-space distribution function follows the King distribution such as that given in eq. 4.40. This is achieved by writing $\Psi(r) = \frac{1}{2}v_{esc}^2(r)$ and integrating the phase-space distribution function over the transverse velocities:

$$\begin{aligned} F_B(r, v_r) &= \frac{\rho_B}{(2\pi\sigma_B^2)^{3/2}} \int_0^{v_{esc}^2(r)-v_r^2} \left[\exp\left(\frac{v_{esc}^2(r) - v_r^2 - v_\perp^2}{2\sigma_B^2}\right) - 1\right] dv_r \pi dv_\perp^2 \\ &= \frac{\pi\rho_B}{(2\pi\sigma_B^2)^{3/2}} \left\{ 2\sigma_B^2 \left[\exp\left(\frac{v_{esc}^2(r) - v_r^2}{2\sigma_B^2}\right) - 1\right] \right. \\ &\quad \left. -(v_{esc}^2(r) - v_r^2) \right\} dv_r \end{aligned} \tag{3.17}$$

Further integration of eq. 3.17 over radial and radial velocity bins, $\Delta r(r_i)$ and $\Delta v_r(r_i, v_j)$ respectively, is carried out to facilitate comparison with the observational data, which are binned similarly. First, the radial distribution is obtained by integrating $F_B(r, v_r)$ over the radial velocities:

$$\begin{aligned} n_B(r) &= \int_0^{v_{esc}(r)} F_B(r, v_r) dv_r \\ &= \frac{\rho_B}{(2\pi\sigma_B^2)^{3/2}} \left[\frac{(2\pi\sigma_B^2)^{3/2}}{2} e^{v_{esc}^2(r)/2\sigma_B^2} \mathrm{erf}\left(\frac{v_{esc}(r)}{\sqrt{2\sigma_B^2}}\right) \right. \\ &\quad \left. -\frac{2\pi}{3} v_{esc}^3(r) - 2\pi\sigma_B^2 v_{esc}(r) \right]. \end{aligned} \tag{3.18}$$

We may now integrate $4\pi r^2 n_B(r)$ in the range Δr centered at various r_i to get $\Delta N(r_i)$ for comparison with the observations. A single choice for the parameter ρ_B should, in principle, fit the total number of stars in each radial bin when we include all the stars in each at that location irrespective of their velocities. Unfortunately, as described below, this does not happen, and the observed number of stars, especially at galactocentric distances below $\sim 20-30$ kpc, fall short of the theoretical expectation.

The most likely explanation for this is that the catalogues of the observations are incomplete in these regions. In fact, the radial distributions presented by Xue et al. [7] and Brown et al. [8] differ significantly from each other. We show in Fig. 3.16 the theoretical distribution of stars $N(r)$, where

$$N(r) = 4\pi r^2 n_B(r), \tag{3.19}$$

for the Brown et al. and Xue et al. data separately. The σ_B values were chosen to be 115 km s^{-1} and 106 km s^{-1} for fitting the Brown et al. and Xue et al. data respectively beyond ~ 25 kpc along with arbitrary normalizations to the total number of stars in the particular radial bin. It was later found that a value of $\sigma_B = 108$ km s^{-1} provides the best fit for both distributions simultaneously. For illustrative purposes, the escape velocity profile was taken from the dark matter model in the $\Sigma_{d,\odot} = 70$ M$_\odot$ pc^{-2} disk where $\rho_{DM0} = 500$ GeV cm^{-3} and $\sigma_{DM} = 200$ km s^{-1}. The escape velocity profile from any other model in Tables 3.1-3.3 would produce a similar distributions for the BHB and BS stars. In order to proceed further, we normalize $\Delta N(r_i)$ at each radial bin and compare the theoretical distribution of radial velocities with the observations in (see for example, Figs. 3.17 and 3.18). Here again, a range of parameters fit the observations.

In oder to find the best-fitting model, we define f_{ij} as the theoretical expectation for the number of stars in the radial bins at r_i and the velocity bin at v_{rj}. If n_{ij} is the actual number of stars observed in this bin, then using Poisson statistics, we may

define the likelihood function for each model to be

$$L = \prod_{ij} \frac{e^{-f_{ij}} f_{ij}^{n_{ij}}}{n_{ij}!}. \tag{3.20}$$

After the likelihoods for all the models were calculated, they were normalized to the model with the greatest likelihood, the $\rho_{DM0} = 100$ GeV cm^{-3}, $\sigma_{DM} = 220$ km s^{-1} model for the $\Sigma_{d,\odot} = 55$ M$_\odot$ pc^{-2} and $r_{tn} = 3.0$ kpc disk. The likelihood for each dark matter model which fits the rotation curve is shown in the final column in Tables 3.1-3.3.

The most probable models, according to the BHB and BS analysis, occurs for $\rho_{DM0} \gtrsim 100$ GeV cm^{-3}, and except for two specific cases, one in each of the $r_{tn} = 2.5$ and 3.5 kpc scenarios, the models with $L > 0.7$ are found for $r_{tn} = 3.0$ kpc. All models with $L > 0.8$ are found for $r_{tn} = 3.0$ kpc and $\Sigma_{d,\odot} = 55$ M$_\odot$ pc^{-2}. Most models for the $r_{tn} = 3.5$ kpc disk, though they fit the rotation curve, do not predict enough stars at large velocities to agree with the BHB and BS data as indicated by the sharply falling rotation curves in these models. Consquently, the likelihood $L = 0$ because f_{ij}=0 in one or more of the bins at large r.

If we consider only the models with $L > 0.7$, we find the following range in parameters:

$$930.8 \text{ km s}^{-1} \leq v_{esc}(0) \leq 983.9 \text{ km s}^{-1}$$

$$597.1 \text{ km s}^{-1} \leq v_{esc}(R_0) \leq 705.0 \text{ km s}^{-1}$$

$$75 \text{ GeV cm}^{-3} \leq \rho_{DM0} \leq 500 \text{ GeV cm}^{-3}$$

$$0.395 \text{ GeV cm}^{-3} \leq \rho_{DM}(R_0) \leq 0.758 \text{ GeV cm}^{-3}$$

$$462.5 \text{ km s}^{-1} \leq < v_{DM}^2(R_0) >^{1/2} \leq 546.1 \text{ km s}^{-1}.$$

We take these limits to be a conservative estimate of the allowed parameters space from our analysis of the phase-space distribution of dark matter. More robust results could be found by increasing the resolution of the model parameters investigated by using a Monte Carlo method and by better observations of the rotation curve and tracers of the Galactic potential beyond $\sim$ 20 kpc. The implication of these results for direct and indirect detection will be discussed in the next chapters.

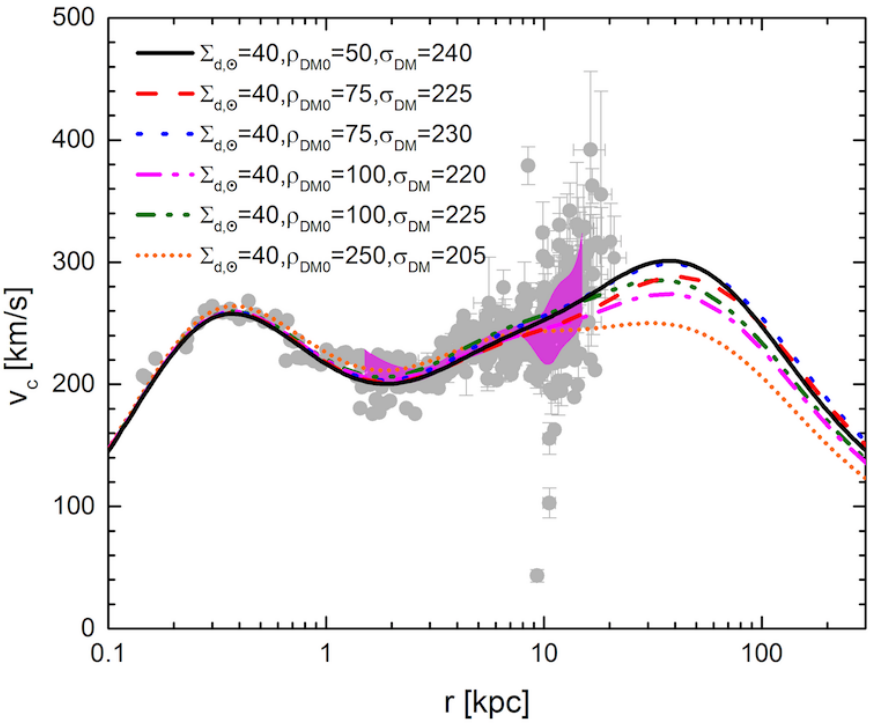

Figure 3.1: The rotation curves are shown for the dark matter models which pass through the band encompassing 2/3 of the observations for disk model with $r_{tn} = 2.5$ kpc and $\Sigma_{d,\odot} = 40$ M$_\odot$ pc^{-2}.

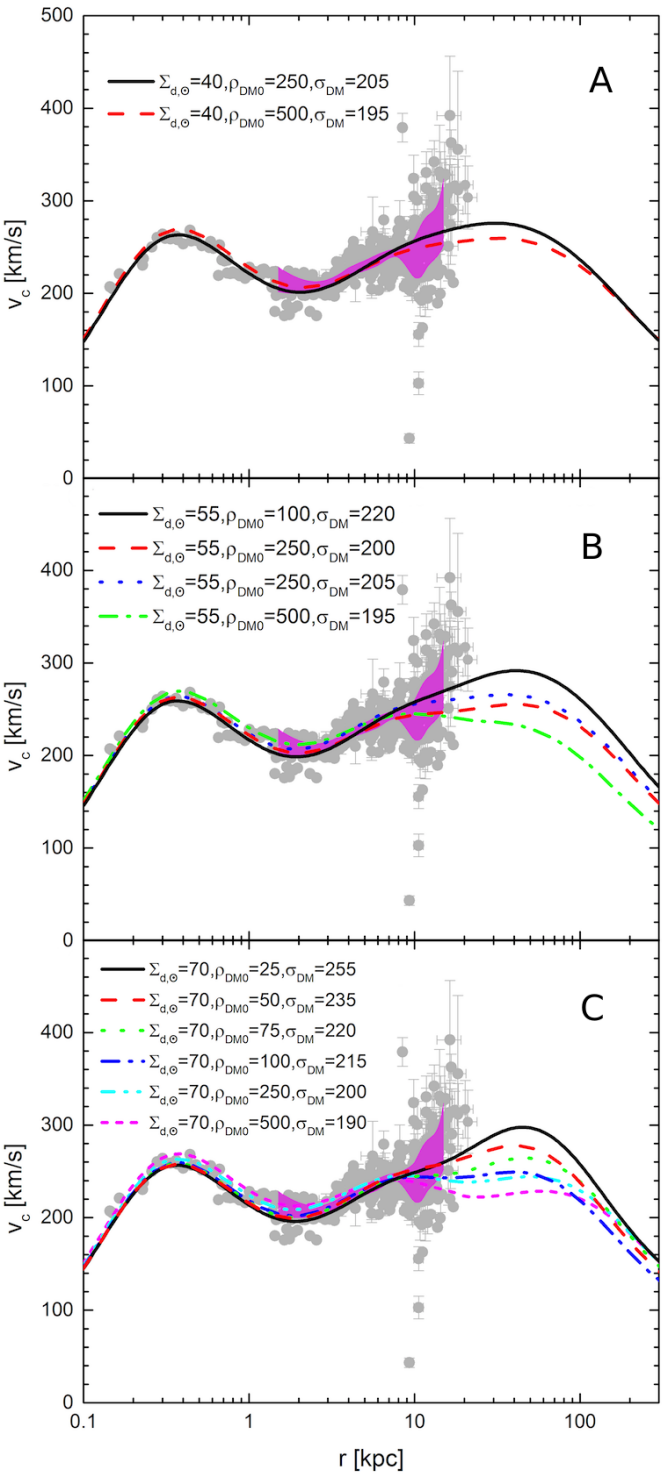

Figure 3.2: The rotation curves are shown for the dark matter models which pass through the band encompassing 2/3 of the observations for the disk models with r_{tn} = 3.0 kpc and with A) $\Sigma_{d,\odot}$ = 40 $M_\odot$ pc, B) $\Sigma_{d,\odot}$ = 55 $M_\odot$ pc^{-2}, and C) $\Sigma_{d,\odot}$ = 70 $M_\odot$ pc^{-2}.

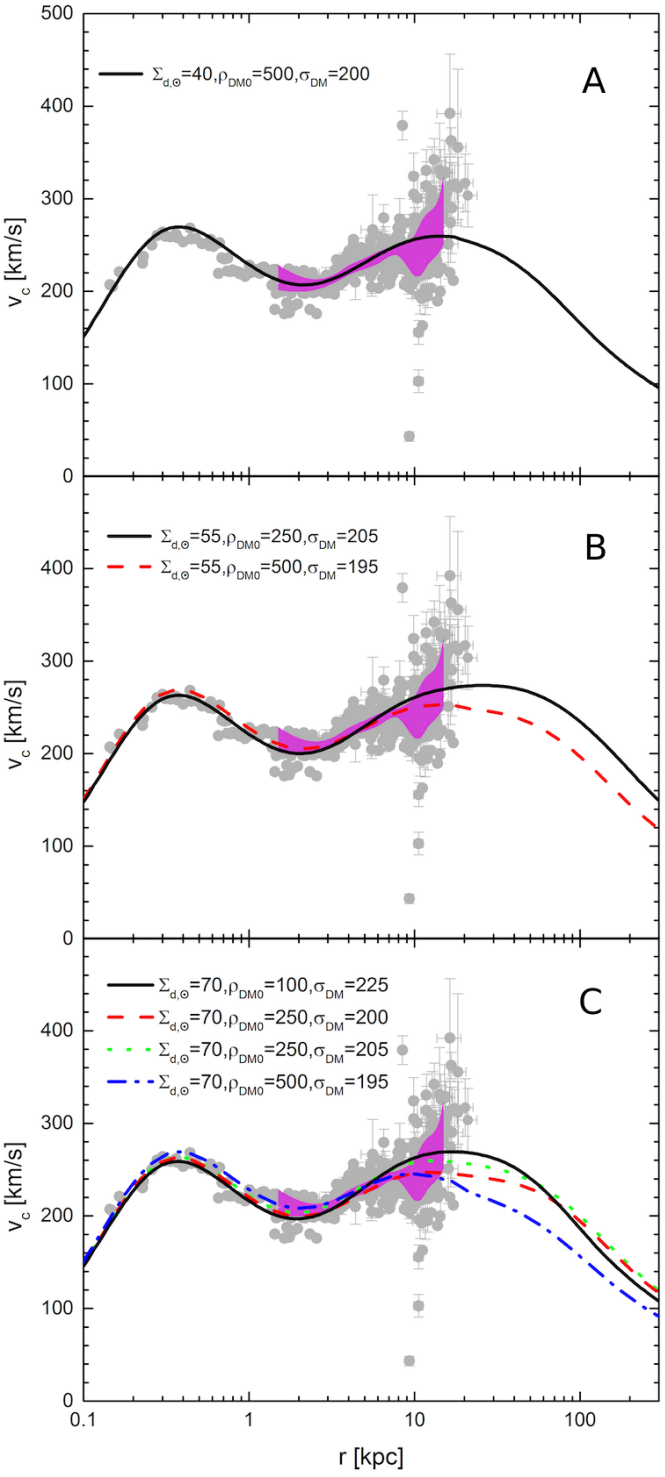

Figure 3.3: The rotation curves are shown for the dark matter models which pass through the band encompassing 2/3 of the observations for the disk models with r_{tn} = 3.5 kpc and with A) $\Sigma_{d,\odot}$ = 40 $M_\odot$ pc, B) $\Sigma_{d,\odot}$ = 55 $M_\odot$ pc^{-2}, and C) $\Sigma_{d,\odot}$ = 70 $M_\odot$ pc^{-2}.

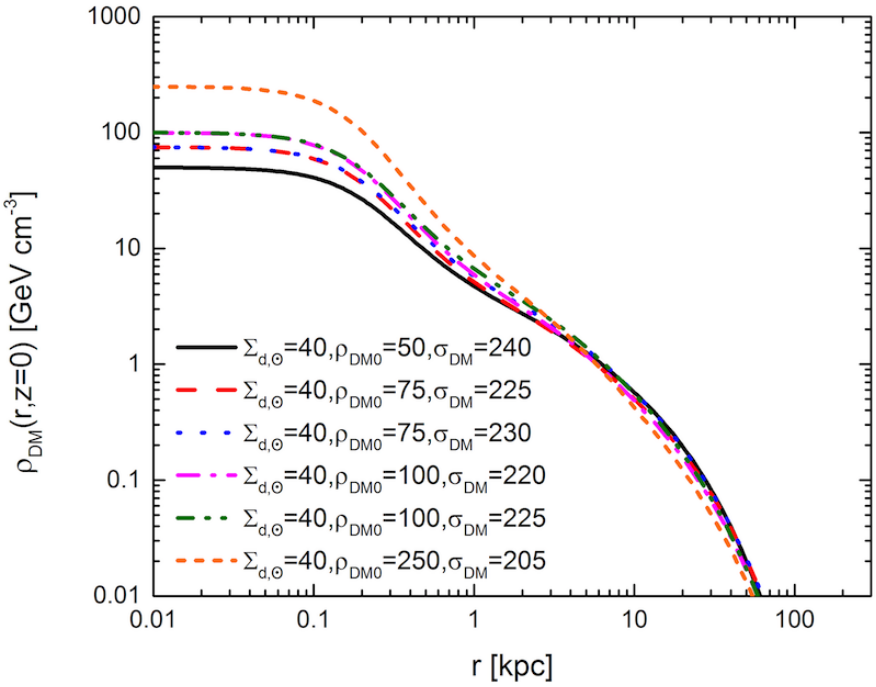

Figure 3.4: The radial density profiles of dark matter in the Galactic plane are shown for the dark matter models corresponding to the disk model with $r_{tn} = 2.5$ kpc and $\Sigma_{d,\odot} = 40$ M$_\odot$ pc^{-2}.

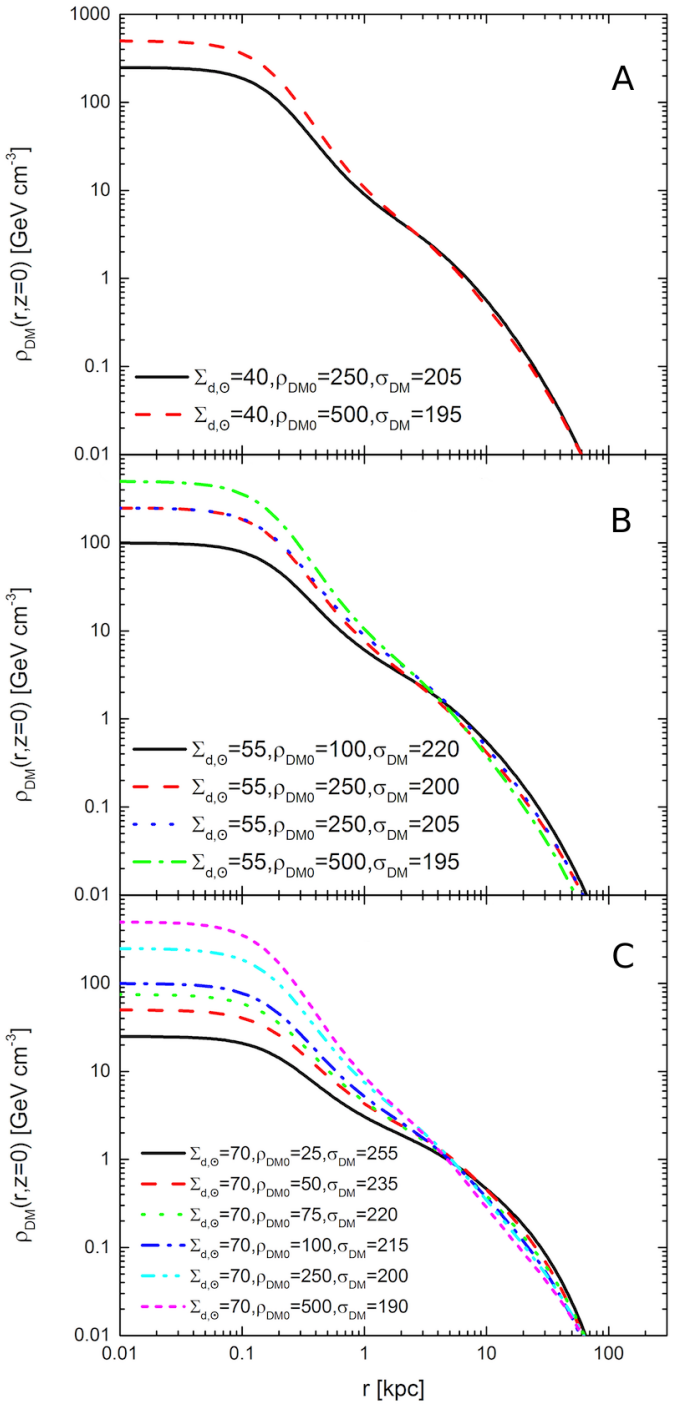

Figure 3.5: The radial density profiles of dark matter in the Galactic plane are shown for the dark matter models corresponding to the disk model with $r_{tn} = 3.0$ kpc and with A) $\Sigma_{d,\odot} = 40$ M$_\odot$ pc, B) $\Sigma_{d,\odot} = 55$ M$_\odot$ pc^{-2}, and C) $\Sigma_{d,\odot} = 70$ M$_\odot$ pc^{-2}.

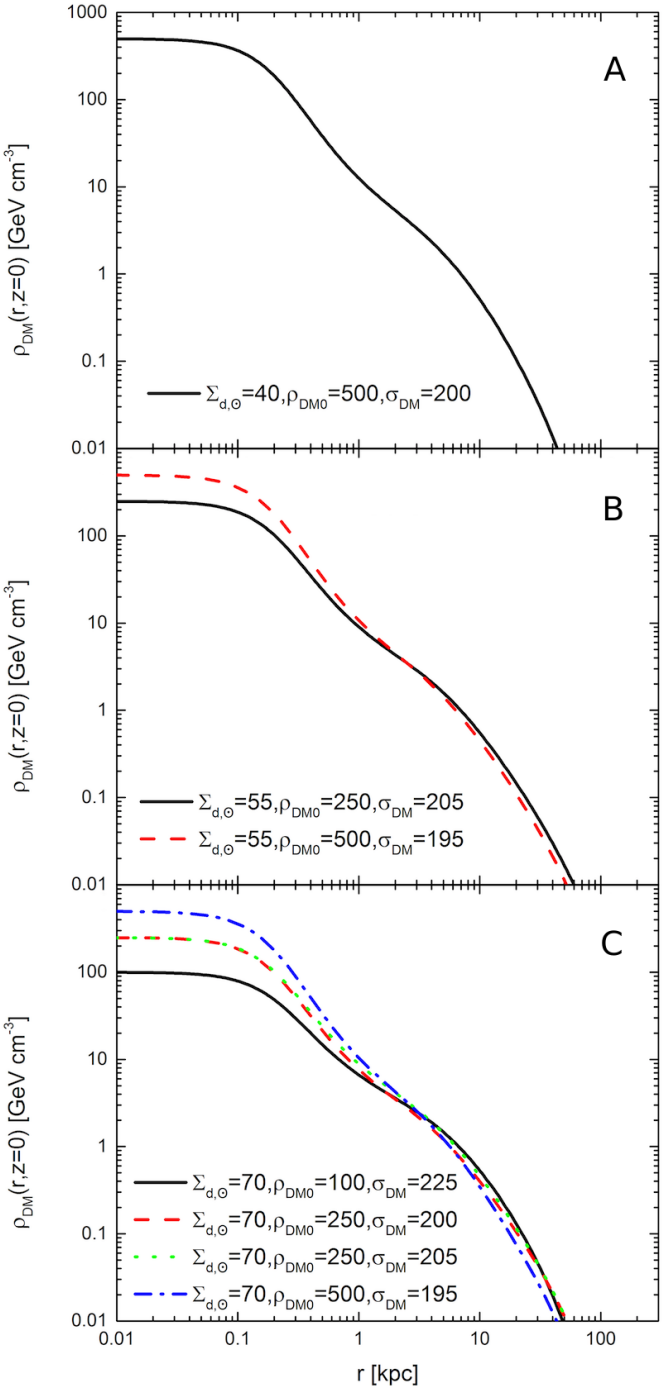

Figure 3.6: The radial density profiles of dark matter in the Galactic plane are shown for the dark matter models corresponding to the disk model with $r_{tn} = 3.5$ kpc and with A) $\Sigma_{d,\odot} = 40$ M$_\odot$ pc, B) $\Sigma_{d,\odot} = 55$ M$_\odot$ pc^{-2}, and C) $\Sigma_{d,\odot} = 70$ M$_\odot$ pc^{-2}.

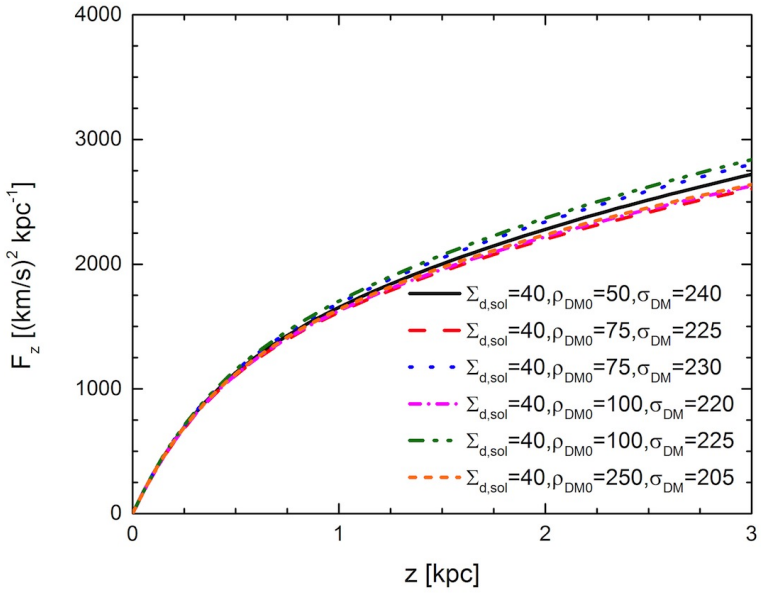

Figure 3.7: The vertical force profiles of dark matter in the Galactic plane are shown for the dark matter models corresponding to the disk model with $r_{tn} = 2.5$ kpc and $\Sigma_{d,\odot} = 40$ $M_\odot$ pc^{-2}.

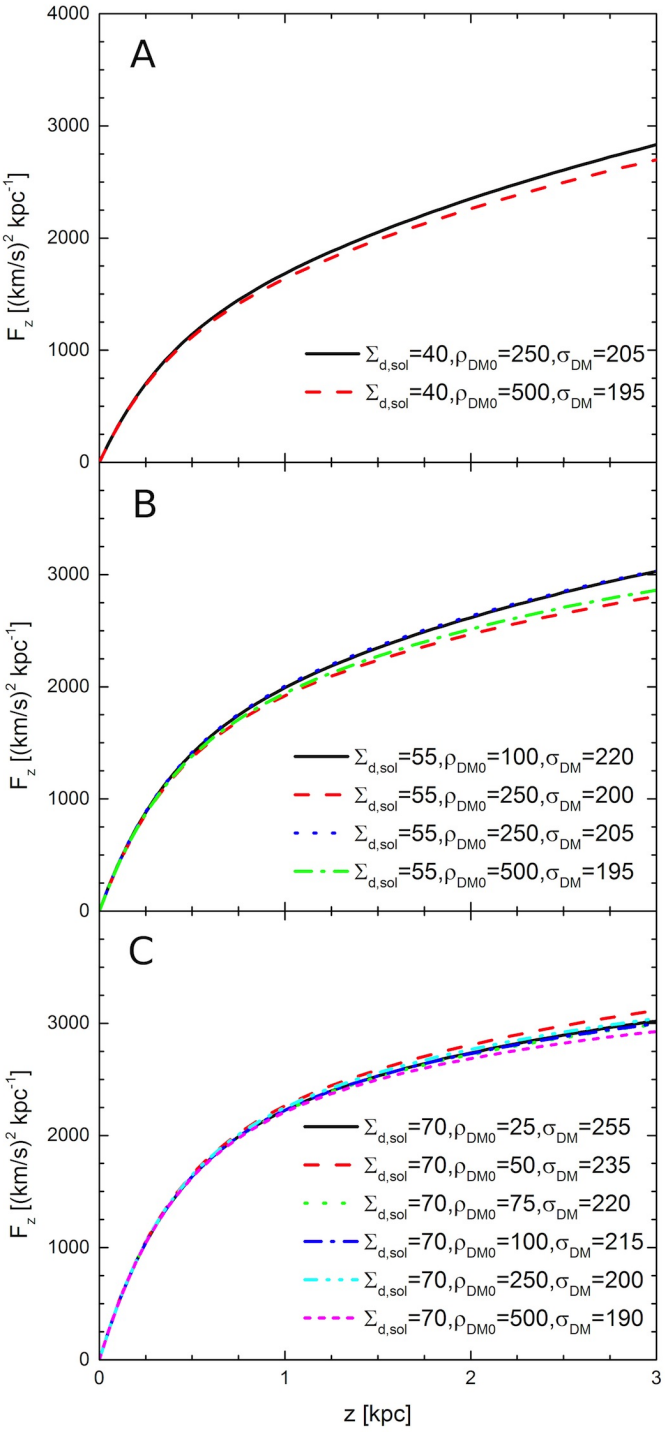

Figure 3.8: The vertical force profiles of dark matter in the Galactic plane are shown for the dark matter models corresponding to the disk model with $r_{tn} = 3.0$ kpc and with A) $\Sigma_{d,\odot} = 40$ M$_\odot$ pc, B) $\Sigma_{d,\odot} = 55$ M$_\odot$ pc^{-2}, and C) $\Sigma_{d,\odot} = 70$ M$_\odot$ pc^{-2}.

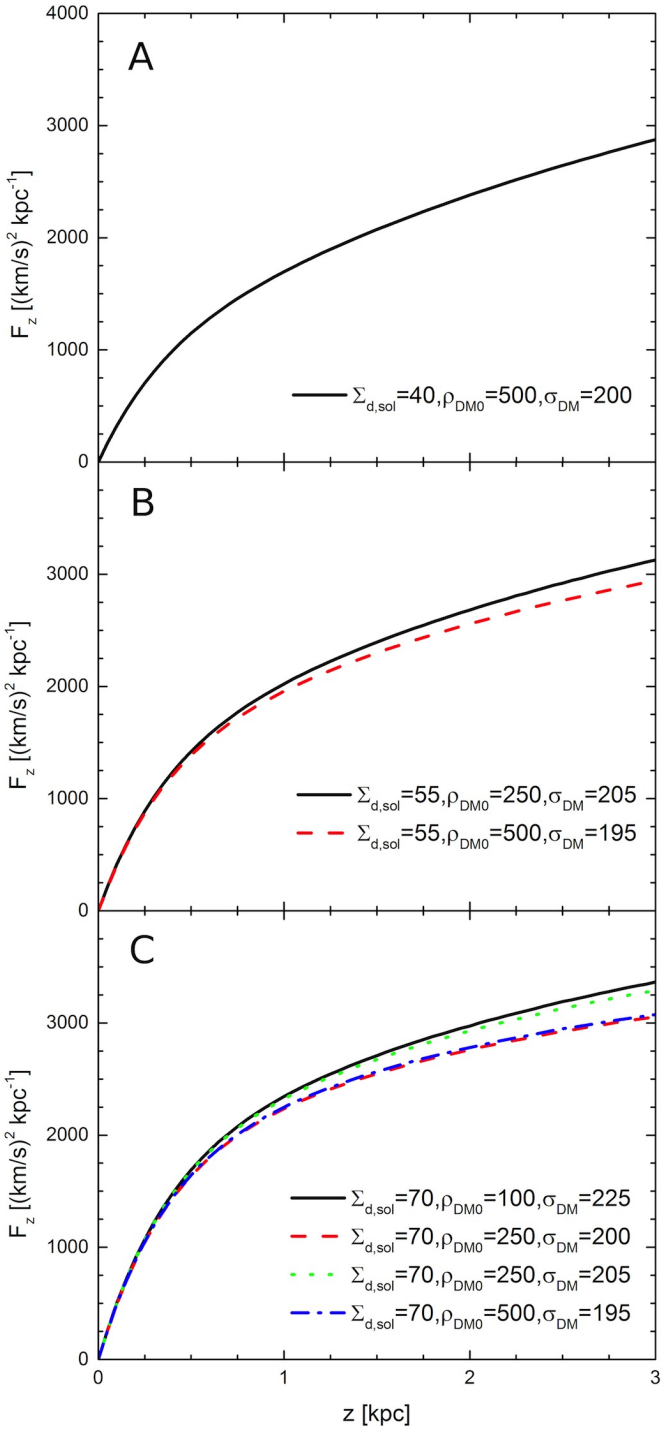

Figure 3.9: The vertical force profiles of dark matter in the Galactic plane are shown for the dark matter models corresponding to the disk model with $r_{tn} = 3.5$ kpc and with A) $\Sigma_{d,\odot} = 40$ $M_\odot$ pc, B) $\Sigma_{d,\odot} = 55$ $M_\odot$ pc^{-2}, and C) $\Sigma_{d,\odot} = 70$ $M_\odot$ pc^{-2}.

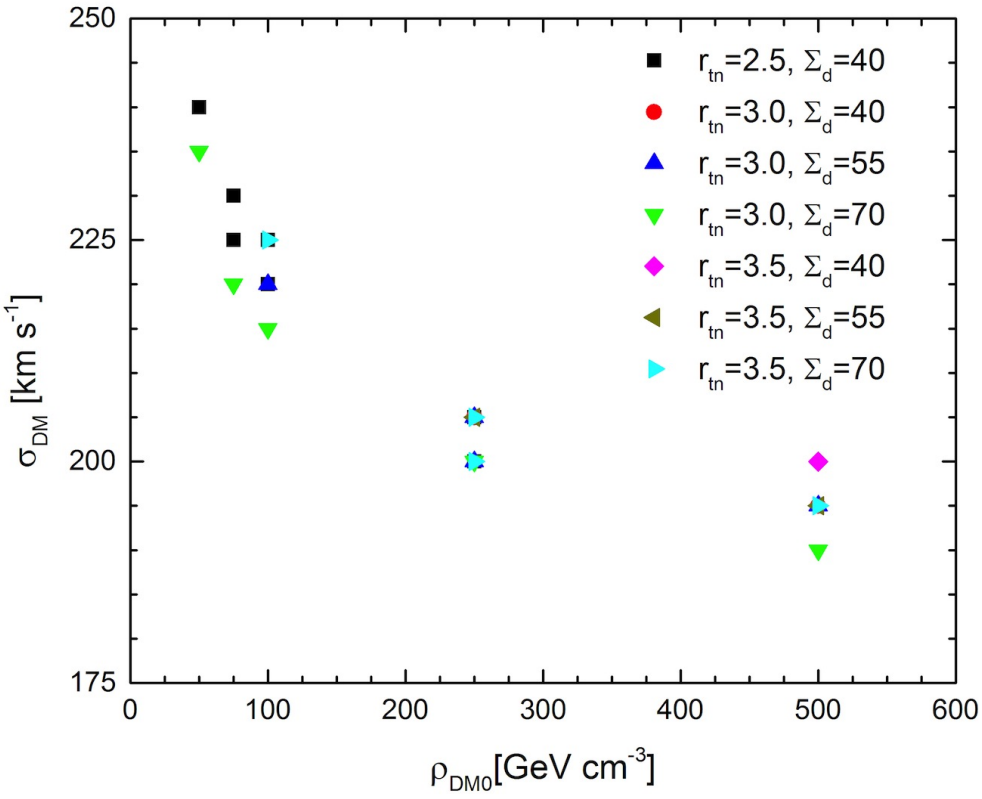

Figure 3.10: The σ_{DM} parameter is shown as a function of the central dark matter density for the dark matter models in Tables 3.1-3.3.

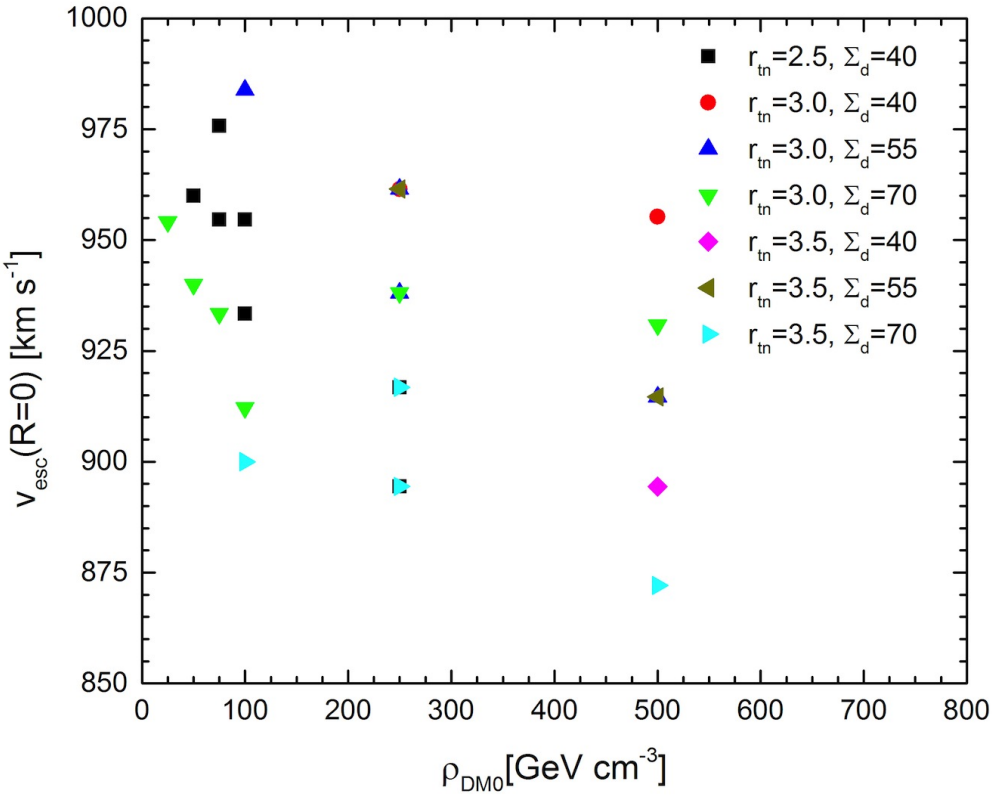

Figure 3.11: The escape speed from the Galactic center is shown as a function of the central dark matter density for the dark matter models in Tables 3.1-3.3.

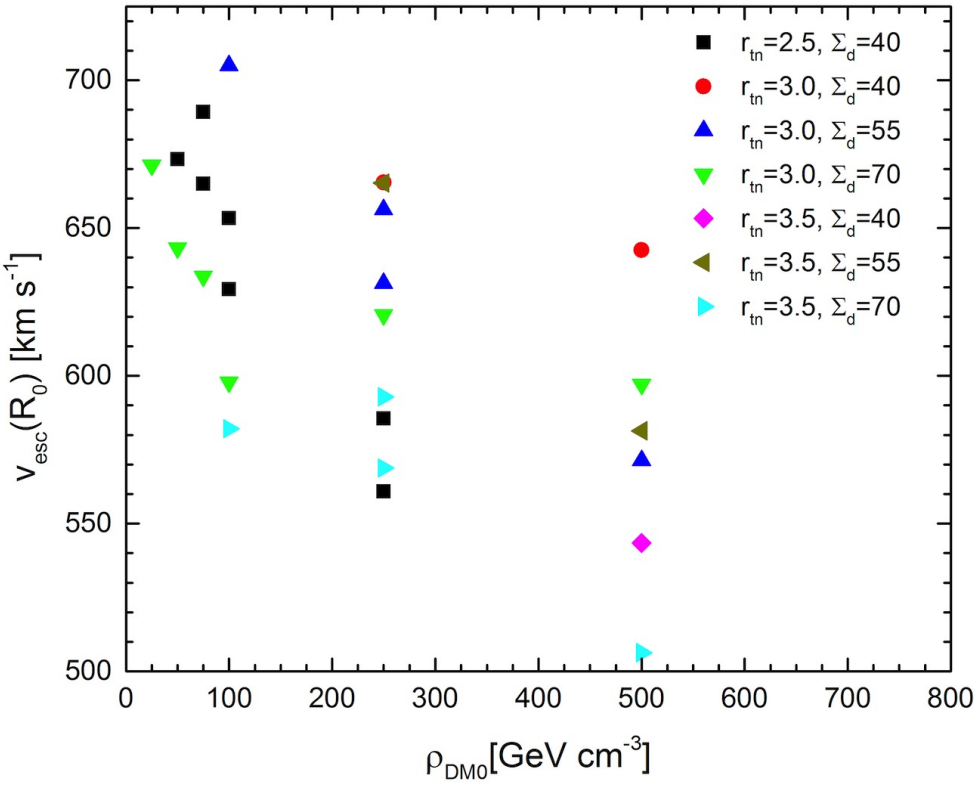

Figure 3.12: The escape speed at R_0 is shown as a function of the central dark matter density for the dark matter models in Tables 3.1-3.3.

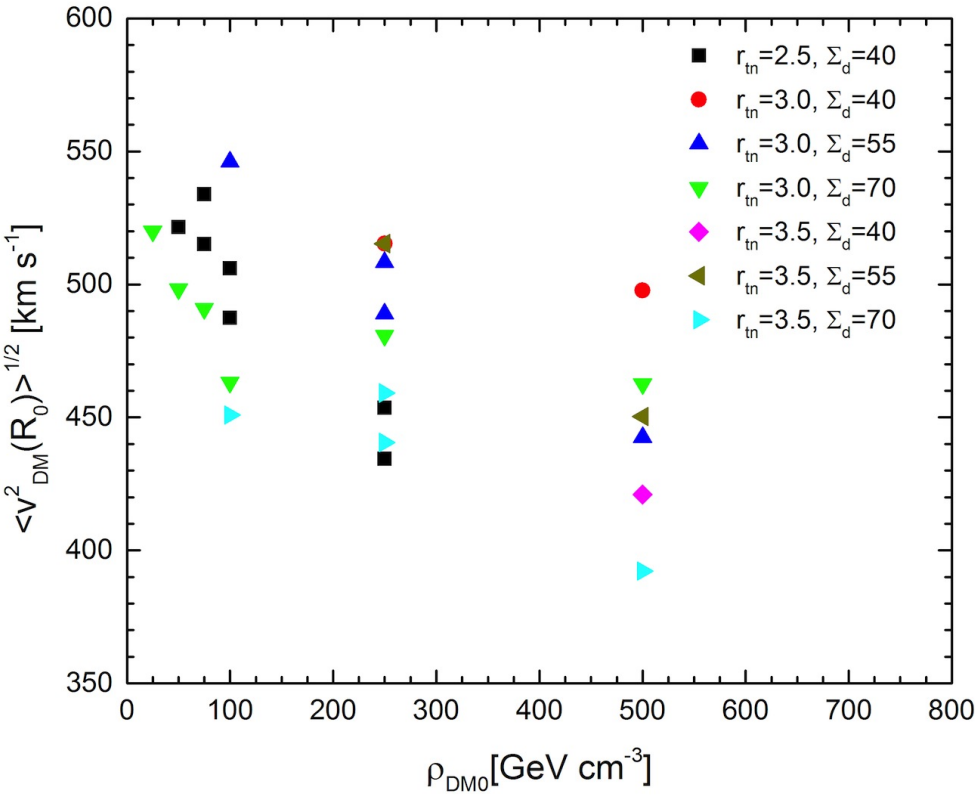

Figure 3.13: The root-mean-square velocity at R_0 is shown as a function of the central dark matter density for the dark matter models in Tables 3.1-3.3.

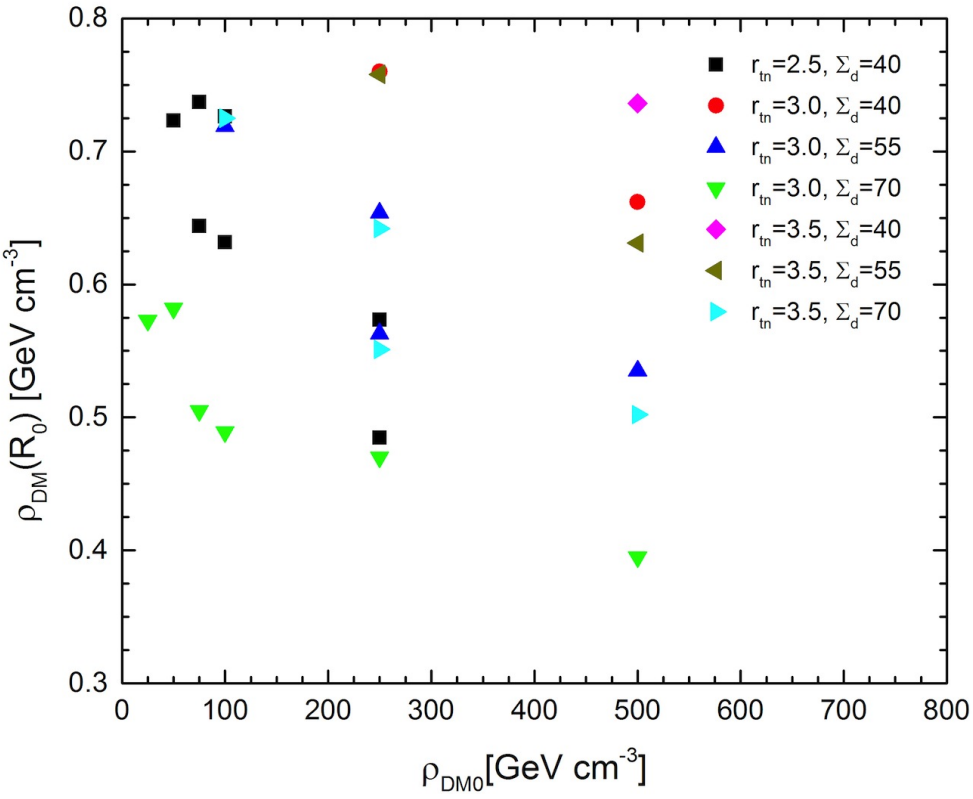

Figure 3.14: The dark matter density at R_0 is shown as a function of the central dark matter density for the dark matter models in Tables 3.1-3.3.

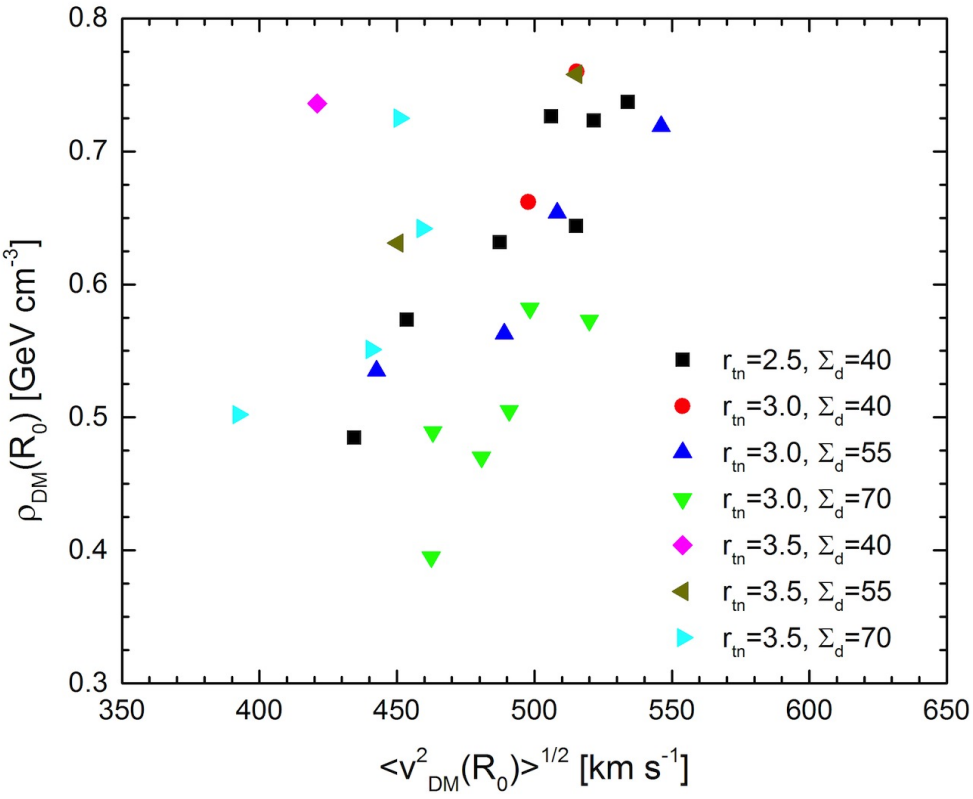

Figure 3.15: The dark matter density at R_0 is shown as a function of the root-mean-square velocity at R_0 for the dark matter models in Tables 3.1-3.3.

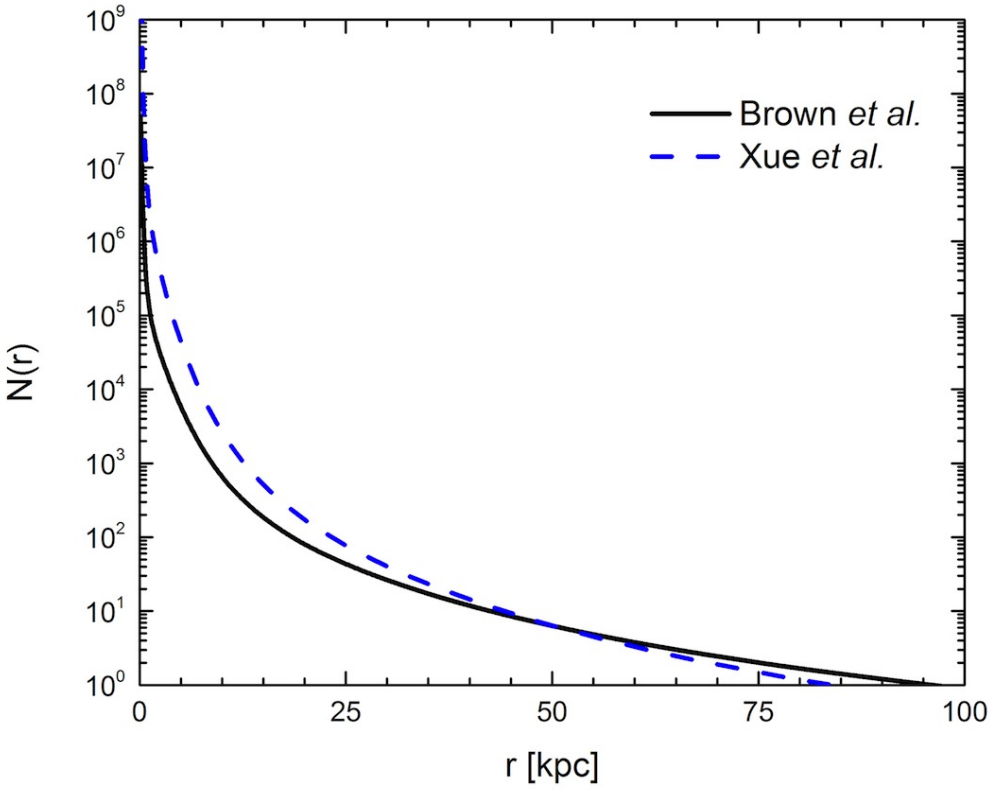

Figure 3.16: The distribution of BHB and BS stars expected from the velocity distribution measured by Brown et al. and Xue et al. The distribution is shown for the $\Sigma_{d,\odot}$=70 $M_\odot$ pc^{-2}, r_{tn} = 3.0 kpc disk with ρ_{DM0} = 500 GeV cm^{-3}, σ_{DM} = 200 km s^{-1}, and σ_B = 115 km s^{-1} for Brown et al. and σ_B = 106 km s^{-1} for Xue et al.

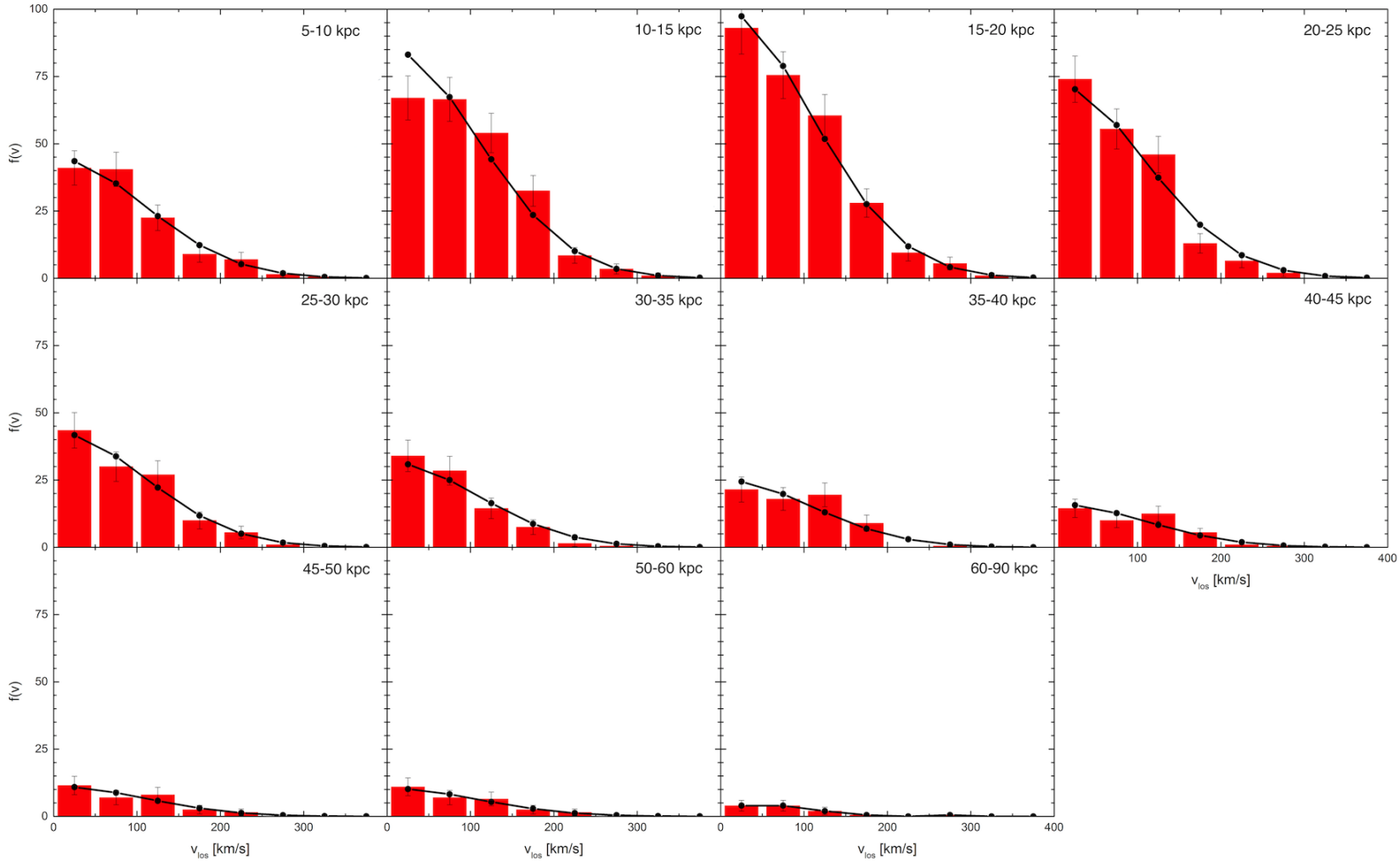

Figure 3.17: The line-of-sight velocity distribution of BHB stars from [7] is presented in radial velocity and radial bins in the red histogram with error bars. The distribution computed for the best-fit dark matter model for the $\Sigma_{d,\odot}$=55 $M_\odot$ pc^{-2}, r_{tn} = 3.0 kpc, disk is shown as points, connected for clarity. In this model, ρ_{DM0} = 100 GeV cm^{-3}, σ_{DM} = 220 km s^{-1}, Φ_0/σ^2_{DM}=10 and σ_{BHB} = 108 km s^{-1}.

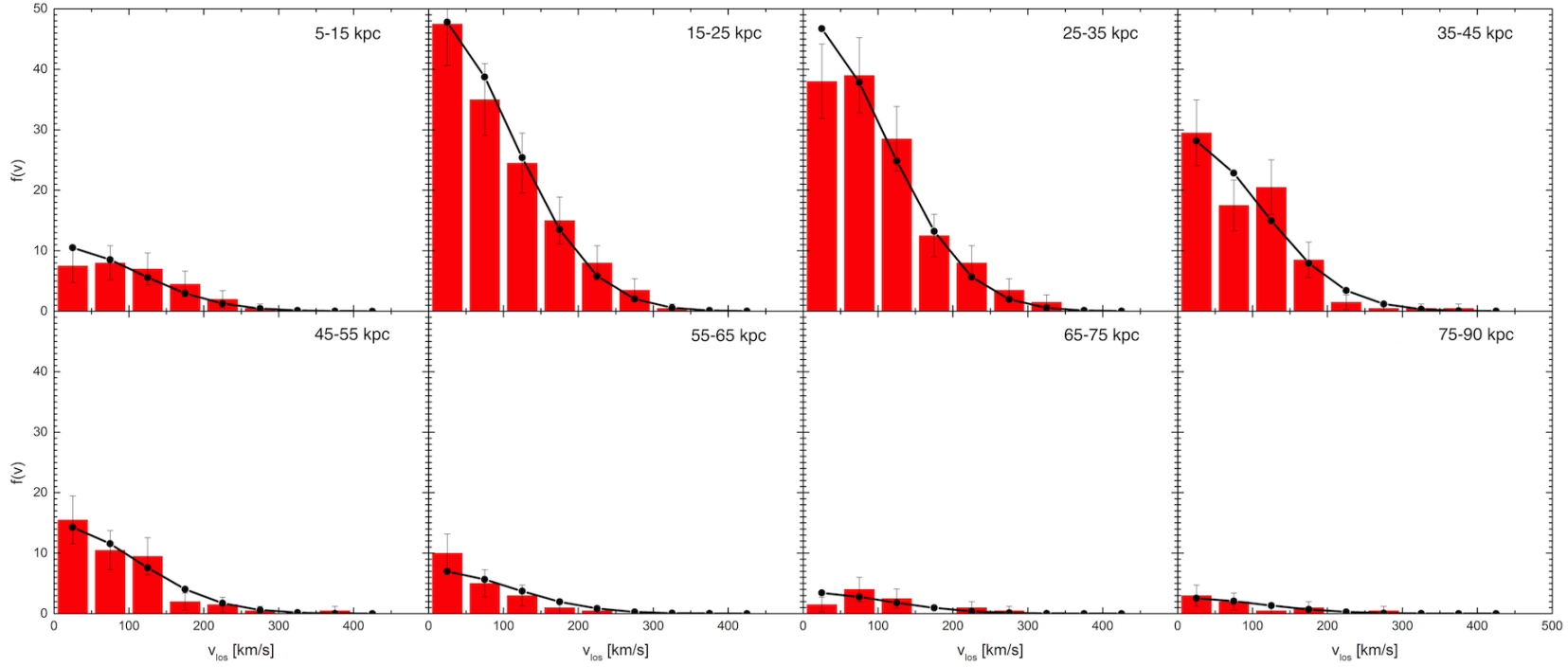

Figure 3.18: The line-of-sight velocity distribution of BHB and BS stars from [8] is presented in radial velocity and radial bins in the red histogram with error bars. The distribution computed for the best-fit dark matter model for the $\Sigma_{d,\odot}$=55 $M_\odot$ pc^{-2}, r_{tn} = 3.0 kpc disk is shown as points, connected for clarity. In this model, ρ_{DM0} = 100 GeV cm^{-3}, σ_{DM} = 220 km s^{-1}, Φ_0/σ_{DM}^2=10 and $\sigma_{BHB,BS}$ = 108 km s^{-1}.

References

[1] Binney, J. & Tremaine, S. 2008, *Galactic Dynamics*, Princeton University Press, Princeton

[2] Cowsik, R. et al. 2007, New Astron., 12, 507

[3] Chaudhury, S., Bhattacharjee, P., & Cowsik, R. 2010, JCAP, 09, 020

[4] Cowsik, R., Ratnam, C., & Bhattacharjee, P. 1996, PRL, 76, 3886

[5] Wilson, C. P. 1975, ApJ, 80, 175

[6] Prendergast, K. H. & Tomer, E. 1970, AJ, 75, 674

[7] Xue, X. X., et al. 2008, ApJ, 684, 1143

[8] Brown, W. R., et al. 2010, ApJ, 139, 59

Chapter 4

Implications for the Direct Detection of Dark Matter

The current generation of direct dark matter detectors are able to distinguish scattering of weakly-interacting massive particles (WIMPs) off of normal matter nuclei from scattering caused by cosmic rays, radioactivity from the rock surrounding the detectors, and radioactivity of the detector components. For theoretically estimating the distribution of kinetic energies and the angular distribution of of recoil nuclei, we need to know the phase-space distribution of Galactic dark matter. Such estimates will allow us to correctly interpret the data from these experiments. In the previous chapter, we showed that observations of the Galactic rotation curve and the spatial and velocity distributions of blue horizontal-branch and blue straggler stars allow for a range in the parameters describing the phase-space distribution of dark matter that are relevant to its direct and indirect detection.

The current effort to directly detect weakly-interacting massive particles via elastic

scattering off nuclei in Earth-bound detectors has its roots in the detection of neutrinos from nuclear reactors and from the Sun. Neutrino detectors were first proposed by Drukier and Stodolsky [1], and the physics was worked out in detail by Goodman and Witter [2]. Drukier, Freese, and Spergel [3] extended these studies to other cold dark matter candidates [4]. Lewin and Smith [5] worked out the mathematics of direct dark matter detection in great detail and Jungman, Kamionkowski, and Griest [6] have given the details for supersymmetric dark matter candidates. The general formalism for dark matter detection, as well as details for detecting supersymmetric neutralinos, will be reviewed here. The dark matter phase-space distribution will also be discussed below in the context of a lowered isothermal (King) model. Many excellent reviews of direct dark matter detection can be found in the literature (see [4, 5, 6, 7, 8, 9, 10]).

We begin by reviewing the concepts necessary for calculating the rates of interaction between dark matter and various nuclei as found in many of the references listed above. Then we use the phase-space distribution of dark matter particles along with the range of values for the different parameters from Chapter 3 to calculate the distribution of speeds of the dark matter particles. We also calculate the distribution of speeds of the dark matter particles as a function of the arrival angle in the laboratory frame, which is useful for the analysis of experiments with sensitivity to the recoil angle of scattered nuclei. To calculate the energy spectrum and angular distribution of nuclei scattered by dark matter in the laboratory frame, we develop a quasi-Monte Carlo method and as an example, calculate the expected event rates for a generic detector with liquid xenon as the target material.

4.1 The Basic Detection Rate

A WIMP of mass M_χ moving with a speed u in the laboratory frame and scattering elastically off a nucleus of mass M_N will transfer momentum $\mathbf{p}$ to the nucleus that depends on the scattering angle α in the center-of-mass frame (see Fig. 4.1):

$$|\mathbf{p}|^2 = 2\mu^2 u^2(1 - \cos\alpha), \tag{4.1}$$

where μ is the WIMP-nucleon reduced mass defined as

$$\mu = \frac{M_\chi M_N}{M_\chi + M_N},$$

and $|\mathbf{p}|^2$ is invariant under Galilean transformations. The energy transferred to the nucleus is then

$$E_r = \frac{|\mathbf{p}|^2}{2M_N} = \frac{\mu^2 u^2}{M_N}(1 - \cos\alpha) \tag{4.2}$$

with the maximum energy transfer occurring when $\alpha = \pi$, such that

$$E_{r,max} = \frac{2\mu^2 u^2}{M_N}. \tag{4.3}$$

Each dark matter detector has a lower threshold for the recoil energy it is able to reliably detect. The minimum velocity with respect to the detector that a dark matter particle must have to produce a recoil energy E_r can be found from inverting eq. 4.3 and has the form

$$u^2_{min} = \frac{E_r M_N}{2\mu^2}. \tag{4.4}$$

Scattering.png

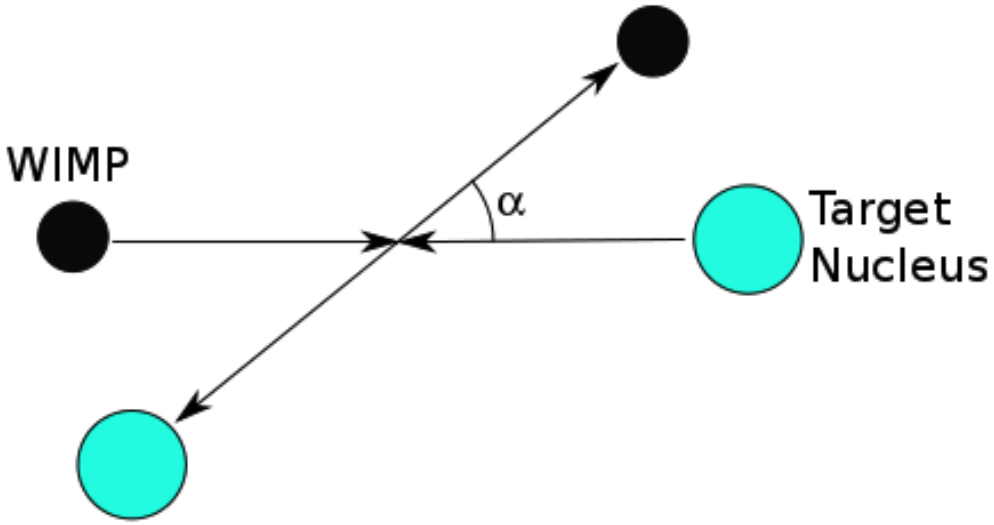

Figure 4.1: A typical collision between a WIMP and a target nucleus in the center-of-mass frame is shown. The WIMP has a typical speed of ~ 250 km/s with respect to the detector and transfers energy to the target nucleus via elastic scattering with a scattering angle α. The momentum in the center-of-mass frame is given by $\mathbf{p}_{cm} = \mu u$.

The maximum velocity that may be seen in the a dark matter detector is given by the $u_{max} = v_{\oplus} + v_{esc}$ where v_{esc} is the escape speed defined by the local potential and $v_{\oplus}$ is the speed of the Earth about the Galactic center. A typical dark matter scattering event is shown in Fig. 4.1.

The rate at which dark matter will collide with a target particle per square unit interval in momentum transfer squared depends on the WIMP-nucleon interaction cross section as well as the local dark matter density $\rho_{DM}(R_0)$ and its distribution of speeds relative to the detector $f(u)$ and may be written as

$$dR = \frac{\rho_{DM}(R_0)}{M_\chi M_N} \int_{u_{min}}^{u_{max}} \frac{d\sigma}{d|\mathbf{p}|^2} d|\mathbf{p}|^2 u f(u) du, \tag{4.5}$$

where $d\sigma/d|\mathbf{p}|^2$ is the differential WIMP-nucleon cross section. Note $d|\mathbf{p}|^2 = 2m_N dE_r$

so eq. 4.5 can be rewritten as the event rate per unit recoil energy as

$$\frac{dR}{dE_r} = \frac{2\rho_{DM}(R_0)}{M_\chi} \int_{u_{min}}^{u_{esc}} \frac{d\sigma}{d|\mathbf{p}|^2} u f(u) du. \tag{4.6}$$

The differential cross section depends on input from nuclear and particle physics, and the velocity distribution depends on astronomical observations and detailed astrophysical models of the Galaxy. It is possible, however, to roughly estimate the expected interaction rate [4]. For a WIMP mass of M_χ=100 GeV (supersymmetry allows for WIMP masses of ∼30 GeV-340 TeV [4, 11]) striking a detector of nuclei with mass $M_T = 50$ GeV and a relative velocity of $u = 240$ km/s, the expected average recoil energy is

$$< E_r >= \frac{1}{2}\frac{\mu^2}{M_T} u^2 \sim 10 \text{ keV}. \tag{4.7}$$

Current dark matter detectors are tuned to look for recoil energies of this order over a wide range of WIMP masses. The local dark matter density is currently not known precisely but is constrained by astronomical observations and numerical simulations to be in the range $\rho_{DM}(R_0) \approx 0.2-0.6$ GeV/cm^3 (see Chapter 1). Taking the standard value of $\rho_{DM}(R_0) = 0.3$ GeV/cm^3, the flux of dark matter particles on Earth is

$$F = \frac{\rho_{DM}(R_0)}{M_\chi} u \approx 7 \times 10^4 \text{ cm}^{-2}\text{s}^{-1}. \tag{4.8}$$

Electroweak elastic scatterings have a cross section $\sigma_{EW} \sim 10^{-38}$ cm^2, and we expect WIMP-nucleon interactions to behave similarly. The cross section is, in general energy dependent, and will be discussed in detail below. We take the value above for

illustrative purposes. The total elastic scattering rate in a detector of mass 1 kg (i.e. with $N = N_a/A$ atoms, where N_a is Avogadro's number and A is the atomic number of the target nucleus) is then given by

$$R \sim NF\sigma_{EW} \sim 0.07 \text{ events kg}^{-1} \text{ yr}^{-1}. \tag{4.9}$$

This simple back-of-the-envelope estimation demonstrates the needs for large detectors with long stable operational lifetimes in order to see even a few dark matter interactions.

The event rate as written in eq. 4.6 does not include several effects important for completely understanding the signal in any dark matter detector. The speed distribution $f(v)$ must include the motion of the detector with respect to the dark matter halo. Therefore the rotation of the Earth, the motion of the Earth about the Sun, and the Sun's motion about the Galactic center will play a role in determining the energy and the angular distribution of the events as well as their modulation in time. This motion of the Earth with respect to the center of mass of the Galaxy produces an annual modulation of the event rate and an anisotropy in the angular distribution of scattered nuclei in the detectors, both of which may be exploited to discriminate against background events. The differential cross section in eq. 4.6 will depend on the specific WIMP being considered as well as the type of interaction (axial or scalar) responsible for the scattering process. In the next section, we review the changes in $v_\oplus$ that give rise to the annual modulation in the interaction rate of dark matter. Then, we review the expected WIMP-nucleon cross sections for spin-dependent and

spin-independent interactions with supersymmetric neutralinos. Detailed calculations for other dark matter candidates can be found in the literature (see [6, 12, 13] and the references therein).

4.2 Annual Modulation

The Keplerian motion of the Earth about the Sun produces an annual variation in the velocity of an Earth-based dark matter detector with respect to the rest frame of the Galaxy. Following Lewin and Smith [5], the velocity vector representing this motion, $\mathbf{v}_\oplus$, can be written as the sum of the Galactic rotational velocity

$$\Theta_0 = (0, 240, 0) \text{ km/s}, \tag{4.10}$$

the peculiar motion of the Sun,

$$\mathbf{v}_\odot = (11, 12, 7.5) \text{ km/s}, \tag{4.11}$$

and the Earth's orbital velocity relative to the Sun,

$$\mathbf{v}_{orb} = \big(u_\oplus(\lambda)\cos\beta_x \sin(\lambda - \lambda_x), u_\oplus(\lambda)\cos\beta_y \sin(\lambda - \lambda_y), u_\oplus(\lambda)\cos\beta_z \sin(\lambda - \lambda_z)\big). \tag{4.12}$$

The various parameters in $\mathbf{v}_{orb}$ are defined in Lewin and Smith [5]. The ecliptic latitudes $\beta_{x,y,z}$ and longitudes $\lambda_{x,y,z}$ are

$$\beta_x = -5.5303^\circ, \quad \beta_y = 59.575^\circ, \quad \beta_z = 29.812^\circ$$

and

$$\lambda_x = 266.141^\circ, \quad \lambda_y = -13.3485^\circ, \quad \lambda_x = 179.3212^\circ.$$

The parameter $u_\oplus(\lambda)$ is defined by

$$u_\oplus(\lambda) =< u_\oplus > [1 - e\sin(\lambda - \lambda_0)], \tag{4.13}$$

where Earth's average velocity is $< u_\oplus >= 29.79$ km/s; the ellipticity of Earth's orbit is $e = 0.016722$; the longitude of Earth's orbit's minor axis is $\lambda_0 = 13 \pm 1^\circ$; and λ can be approximately calculated from

$$\lambda \approx L + 1.915\sin g + 0.020\sin 2g. \tag{4.14}$$

In the above expression, $L = 280.460^\circ + 0.9856474^\circ n$, $g = 357.528^\circ + 0.9856003^\circ n$, and n is the number of days relative to noon 31 December 1999. In Fig. 4.2, $|\mathbf{v}_\oplus|$ is shown for three years as a function of days since 31 December. The periodic nature of the annulation modulation produces an annual variation in $|\mathbf{v}_\oplus|$ of $\sim 6\%$, and the average value of $|\mathbf{v}_\oplus| \approx 253$ km/s is shown as a dotted line.

The movement of the Earth about the Sun also produces an effect useful for

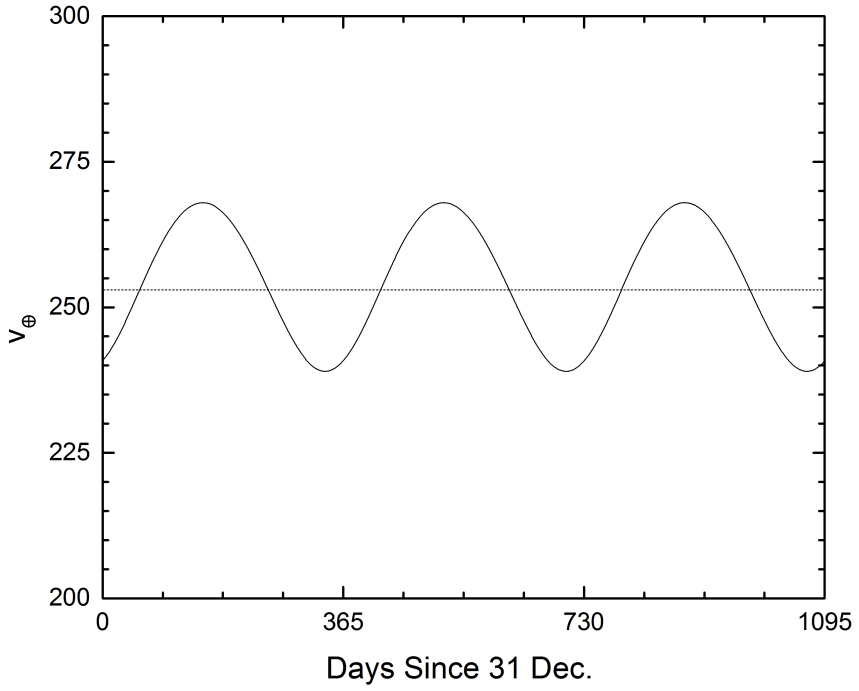

Figure 4.2: The magnitude of $\mathbf{v}_\oplus = \Theta_0 + \mathbf{v}_\odot + \mathbf{v}_{orb}$ is shown for three years as a function of days since 31 December. The periodic behavior of $v_\oplus$ is what gives rise to the expected annual modulation in direct detection experiments. Also shown is a dotted line indicating the average value of $v_\oplus$.

isolating the signal induced by dark matter in detectors that are able to discern the direction of the recoiling nuclei. As the detector travels with the motion of the Sun about the Galactic center, an effective dark matter wind is created, making the angular distribution of the velocities of dark matter anisotropic with respect to the detector. This should increase the rate of detection of dark matter traveling against the motion of the detector. By detecting this asymmetry, greater confidence may be placed in dark matter detection by detectors sensitive to the recoils direction of the scattered nucleus than that derived from the detection of recoil energy spectra exclusively, with or without the annual modulation of the signal.

4.3 The WIMP-Nucleon Interaction Cross Section

The differential cross section includes the details of the specific WIMP model being considered. The lightest stable particle in supersymmetric extensions of the standard model (often the neutralino) is a well-motivated dark matter candidate that may be seen by the current generation of dark matter detectors. Here, we will describe the details of the WIMP-nucleon cross section in the context of neutralino dark matter.

In supersymmetric models, the neutralino interacts through exchange of squarks, Z bosons, and Higgs bosons. In general, a WIMP-nucleon interaction can involve scalar, pseudo-scalar, axial, vector, or tensorial coupling. Since the neutralino is a Majorana fermion, is only acts through scalar couplings (Higgs and squark exchange) and axial couplings (Z and squark exchange) [10]. The spin-dependent (axial) and spin-independent (scalar) couplings have separately calculable cross sections. Detec-

tors have been constructed focusing on both types of coupling.

In general, the differential cross section may be written as

$$\frac{d\sigma}{d|\mathbf{p}|^2} = \frac{1}{4\mu^2 u^2}[\sigma_{scalar} F^2_{scalar}(E_r) + \sigma_{axial} F^2_{axial}(E_r)] \tag{4.15}$$

where σ_{scalar} and σ_{axial} are the spin-independent and spin-dependent cross sections at zero-momentum transfer, respectively, which depend on the particular particle physics model used to describe the WIMP-nucleon interaction and F_{scalar} and F_{axial} are nuclear form factors. The cross sections at zero-momentum transfer are defined by

$$\sigma_{scalar/axial} = \int_0^{4\mu^2 u^2} \frac{d\sigma(p=0)}{d|\mathbf{p}|^2} d|\mathbf{p}|^2 = 4G_F^2 \mu^2 C_{scalar/axial}, \tag{4.16}$$

where C is the spin dependence of the interaction and G_F is the Fermi coupling constant. The particular form of the $\sigma_{scalar/axial}$ is calculated from the effective Lagrangian L_{eff} of the WIMP-nucleon interaction. In supersymmetry, there are several models for the neutralino that produce degenerate interaction cross sections. If a neutralino were detected via elastic scattering, there may not be a way to discriminate amongst the various supersymmetric models. Here, we show the most general formulation of neutralino-nucleon interaction. The fine details can be found in the literature [6, 9, 10, 11] .

For a scalar interaction,

$$C_{scalar} = \frac{1}{\pi G_f^2}[Z f_p + (A - Z) f_n]^2 \tag{4.17}$$

where Z is the number of protons in the target and $(A - Z)$ is the number of neutrons. The couplings of neutralinos to protons and neutrons are given by f_p and f_n respectively and are calculated from the L_{eff} of the WIMP-nucleon interaction, which depends on the quark content of the target nucleus. These couplings are given by

$$f_{p,n} = \sum_{q=u,d,s} f_{Nq}^{(p,n)} a_q \frac{m_{p,n}}{m_q} + \frac{2}{27} f_{Ng}^{(p,n)} \sum_{q=c,b,t} a_q \frac{m_{p,n}}{m_q}, \tag{4.18}$$

where a_q describes the WIMP-quark coupling, f_{Nq} is the quark content of the nucleus, and f_{Ng} is the gluon content of the nucleus. In most cases, the quark-coupling dominates, which makes $f_p \simeq f_n$ and $C_{scalar} \propto A^2$. When this is not the case, the couplings must be explicitly calculated.

For axial couplings,

$$C_{axial} = \frac{8}{\pi} \Lambda^2 J(J+1), \tag{4.19}$$

where J is the the total angular momentum of the nucleus and Λ is defined by

$$\Lambda = \frac{1}{J} [\hat{a}_p < S_p > + \hat{a}_n < S_n >]. \tag{4.20}$$

The expectation values of the neutron and proton spin are given by $< N|S_n|N >$ and $< N|S_p|N >$ respectively, and $\hat{a}_p$ and $\hat{a}_n$ are nuclear spin operators. The value of C depends not only on the dark matter model but also on the detector material, and correspondingly, the theoretical cross sections have been calculated for several detector types.

Given eq. 4.16, the zero-momentum cross section for scalar and axial interactions

can now be written as

$$\sigma_{scalar} = \frac{4\mu^2}{\pi}[Zf_p + (A-Z)f_n]^2 \tag{4.21}$$

$$\sigma_{axial} = \frac{32\mu^2}{\pi}G_F^2\Lambda^2 J(J+1). \tag{4.22}$$

For the neutralino, in the case of scalar coupling, the effective coupling between the WIMP and neutron and the WIMP and proton are comparable and are often taken to be identical for simplicity. In this case, the scalar cross section may be written as

$$\sigma_{scalar} = \frac{\mu^2}{\mu_p^2}A^2\sigma_{p,scalar} \tag{4.23}$$

where μ_p is the reduced mass of the dark matter particle and proton and $\sigma_{p,scalar}$ is the WIMP-proton cross section. The dependence on A^2 shows the benefit of using heavy atoms for spin-independent dark matter detectors.

In general, for the case of a scalar interaction, the form factor $F(E_R)$ is the Fourier transform of the density distribution of the target nucleus. A simple form factor is given by the exponential form

$$F_{exp}(E_r) = e^{-E_r/2E_{r0}}, \tag{4.24}$$

where the nuclear coherence energy is $E_{r0} = \frac{3}{2M_nR_0^2}$ and the radius of the nucleus is

$$R_0 = [0.3 + 0.91(M_N/\text{GeV})^{1/3}] \times 10^{-13} \text{ cm}.$$

In this case, the radial density of the nucleus would have a Gaussian form.

For a more accurate description of the nucleus, the Helm form factor F_H is commonly used, which is an approximation of the Fourier transform of the Woods-Saxon nuclear density distribution and is given by

$$F_H^2(p) = \left[\frac{3j_1(pR_1)}{pR_1}\right]^2 e^{-(ps)^2}, \tag{4.25}$$

where the momentum $p = \sqrt{2M_N E_r}$, $R_1 = \sqrt{R^2 - 5s^2}$, $R \simeq 1.25$ fm $A^{1/3}$, $s \simeq 1$ fm, and j_1 is a spherical Bessel function. Figure 4.3 shows the Helm form factor for various atoms used in current dark matter experiments. Note the form factor suppression that happens for the heavier elements. Detection of large nuclear recoils for heavy atoms such as xenon or iodine is suppressed by five orders of magnitude at $E_r = 1$ MeV over light atoms such as fluorine.

For axial interactions, the form factor is usually defined as

$$F_{axial}^2(p) = \frac{S(p)}{S(0)}, \tag{4.26}$$

where $S(p)$ is the spin-structure function given by

$$S(p) = a_0^2 S_{00}(p) + a_0 a_1 S_{01}(p) + a_1^2 S_{11}(p), \tag{4.27}$$

where $a_0 = \hat{a}_p + \hat{a}_n$ and $a_1 = \hat{a}_p - \hat{a}_n$. The spin-dependent form factor is only relevant when the target nucleus has a non-zero spin in the ground state, which occurs for odd-even nuclei, and depends on total number of nucleons and the model used to describe

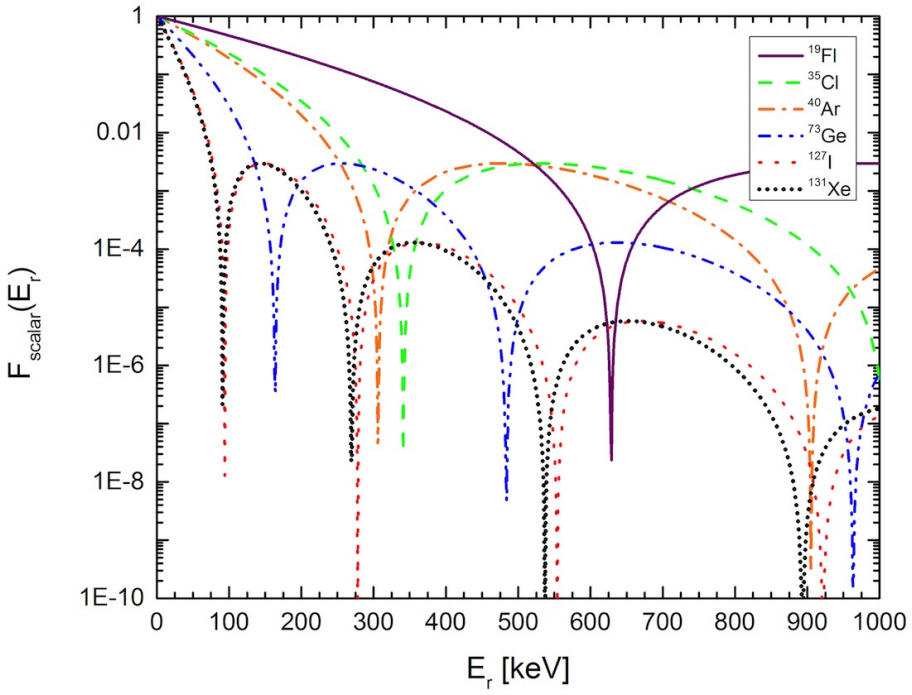

Figure 4.3: The Helm form factor (eq. 4.25) is plotted as a function of recoil energy for several elements currently being used in direct dark matter detection experiments. Note the form factor suppression for heavy elements at large nuclear recoils.

the shell structure of the nucleus and interactions between the nucleons. The nuclear form factors are, in general, calculated from detailed nuclear models, the results of which can be found in the literature (see [6] for example). Here, the spin-dependent form factors for the most commonly used elements in the current generation of dark matter detectors are given. A review of the nuclear spin structures related to dark matter searches and the details of the formulae presented below can be found in Bednyakov and Šimkovic [14, 15] and the references therein. A comparison of the form factors listed below is shown in Fig. 4.4.

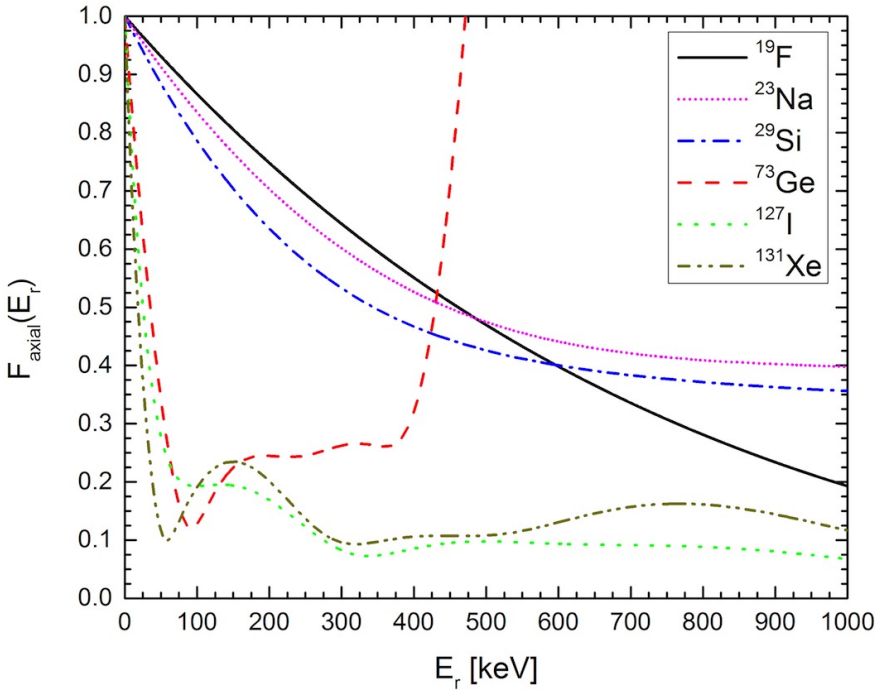

Figure 4.4: The spin-dependent form factor (eq. 4.26) is plotted for various nuclei used in current dark matter detection experiments. The lightest nuclei have the largest form factors over a wide range of recoil energies. This makes them preferable for spin-dependent dark matter detection. Note the form factor for ^{73}Ge diverges after $\sim$ 400 keV. The formulae describing the nuclear structure for germanium are only valid up to $\sim$250 keV. We plot the form factor for germanium over the full range of recoil values to illustrate the limitations of current calculations.

4.3.1 ^{19}F

Fluorine is the lightest and therefore most sensitive element of those here considered that is susceptible to spin-dependent interactions with dark matter and is currently being used in the COUPP [16], SIMPLE [17], and PICASSO [18] experiments. The spin structure of ^{19}F was first worked out by Vergados and others [19, 20, 21]. Fluroine derives its spin dependence from an unpaired proton and has $J = 1/2$. Through detailed shell-model calculations, the pure isoscalar (S^F_{00}), isovector (S^F_{11}),

and interference (S_{01}^F) structure functions can be written separately:

$$\begin{aligned} S_{00}^F(p) &= 2.610\frac{2J+1}{16\pi}e^{-q}[P_{(0,1)}^2(q)+P_{(2,1)}^2(q)], \\ S_{11}^F(p) &= 2.807\frac{2J+1}{16\pi}e^{-q}[Q_{(0,1)}^2(q)+Q_{(2,1)}^2(q)], \\ S_{01}^F(p) &= 2.707\frac{2J+1}{8\pi}e^{-q}[P_{(0,1)}(q)Q_{(0,1)}(q)+P_{(2,1)}(q)Q_{(2,1)}(q)], \end{aligned} \tag{4.28}$$

where $q=(pb)^2/2$, $b=A^{1/6}$, and

$$\begin{aligned} P_{(0,1)}(q) &= 0.1145q^2-0.6667q+1, \\ P_{(2,1)}(q) &= -0.0026q^2+0.0100q, \\ Q_{(0,1)}(q) &= 0.1088q^2-0.6667q+1, \\ Q_{(2,1)}(q) &= 0.0006q^2+0.0041q. \end{aligned}$$

For large momentum transfer, there is a correction to the nucleonic axial current, and the structure functions become more complicated [15].

4.3.2 ^{23}Na

Like ^{19}F, the spin dependence from ^{23}Na comes from an unpaired proton, but in the case of ^{23}Na, $J=3/2$. Using NaI crystals, the DAMA/LIBRA experiment has found possible evidence of dark matter in the annual modulation of their detector signal

[22]. Vergados et al. [20] give the structure functions of sodium as

$$\begin{aligned}
S_{00}^{Na}(p) &= 0.478\frac{2J+1}{16\pi}e^{-q}[P_{(0,1)}^2(q)+P_{(2,1)}^2(q)+P_{(2,3)}^2(q)+P_{(4,3)}^2(q)], \\
S_{11}^{Na}(p) &= 0.346\frac{2J+1}{16\pi}e^{-q}[Q_{(0,1)}^2(q)+Q_{(2,1)}^2(q)+Q_{(2,3)}^2(q)+Q_{(4,3)}^2(q)], \quad (4.29) \\
S_{01}^{Na}(p) &= 0.406\frac{2J+1}{8\pi}e^{-q}[P_{(0,1)}(q)Q_{(0,1)}(q)+P_{(2,1)}(q)Q_{(2,1)}(q) \\
&\quad +P_{(2,3)}(q)Q_{(2,3)}(q)+P_{(4,3)}(q)Q_{(4,3)}(q)],
\end{aligned}$$

where q and b are defined as before and

$$\begin{aligned}
P_{(0,1)}(q) &= 0.0477q^2-0.6667q+1, \\
P_{(2,1)}(q) &= -0.0177q^2+0.1048q, \\
P_{(2,3)}(q) &= -0.0767q^2+0.6092q, \\
P_{(4,3)}(q) &= 0.0221q^2, \\
Q_{(0,1)}(q) &= 0.0465q^2-0.6667q+1, \\
Q_{(2,1)}(q) &= -0.0349q^2+0.1494q, \\
Q_{(2,3)}(q) &= -0.0894q^2+0.7405q, \\
Q_{(4,3)}(q) &= 0.0287q^2.
\end{aligned}$$

Bednyakov and Šimkovic [15] also present other calculations of the ^{23}Na structure functions that are systematically lower than the Vergados calculations in the isovector and mixed components. For the sake of consistency, we choose to use the Vergados calculations throughout when available.

4.3.3 ^{29}Si

The CDMS group has studied the use of cryogenic silicon crystals as dark matter detectors [23]. Silicon is has an unpaired neutron and $J = 1/2$. The low momentum transfer structure functions can be written as

$$\begin{aligned} S_{00}^{Si}(p) &= 0.208\frac{2J+1}{16\pi}e^{-q}[P_{(0,1)}^2(q) + P_{(2,1)}^2(q)], \\ S_{11}^{Si}(p) &= 0.220\frac{2J+1}{16\pi}e^{-q}[Q_{(0,1)}^2(q) + Q_{(2,1)}^2(q)], \\ S_{01}^{Si}(p) &= -0.214\frac{2J+1}{8\pi}e^{-q}[P_{(0,1)}(q)Q_{(0,1)}(q) + P_{(2,1)}(q)Q_{(2,1)}(q)], \end{aligned} \tag{4.30}$$

with

$$\begin{aligned} P_{(0,1)}(q) &= 0.2843q^2 - 0.6667q + 1, \\ P_{(2,1)}(q) &= -0.0567q^2 + 0.4566q, \\ Q_{(0,1)}(q) &= 0.2719q^2 - 0.6667q + 1, \\ Q_{(2,1)}(q) &= -0.0621q^2 + 0.4680q. \end{aligned}$$

Like fluorine, silicon's structure functions require a correction at large momentum transfer.

4.3.4 ^{73}Ge

The current generation of the CDMS detector uses exceedingly pure cryogenic germanium crystals and has claimed to be able to exclude much of the parameter space

where the DAMA/LIBRA experiment has claimed dark matter detection [24]. Germanium has an unpaired neutron, $J = 9/2$, and has a particularly complicated nuclear structure that makes numerical calculations difficult. Dimitrov et al. [25] give sixth-order polynomial fits to the structure functions:

$$\begin{aligned} S_{00}^{Ge}(y) &= 0.1606 - 1.1052y + 3.2320y^2 - 4.9345y^3 + 4.1229y^4 \\ &\quad -1.8016y^5 + 0.3211y^6, \\ S_{11}^{Ge}(y) &= 0.1164 - 0.9228y + 2.9753y^2 - 4.8709y^3 + 4.3099y^4 \\ &\quad -1.9661y^5 + 0.3624y^6, \\ s_{01}^{Ge}(y) &= -0.2736 + 2.0374y - 6.2803y^3 + 0.0426y^3 - 8.5710y^4 \\ &\quad +3.8310y^5 - 0.6948y^6, \end{aligned} \tag{4.31}$$

where $y = (pb/2)^2$. Note, this formula is only valid for $y < 1$, with small y being more accurate. Bednyakov and Šimkovic [15] suggest $S_{ij}^{Ge} = 0$ for $y \geq 1$. With $A = 73$, $y = 1$ corresponds to $E_r \approx 274$ keV. The form factor for ^{73}Ge is plotted in Fig. 4.4 without any correction for $y \geq 1$.

4.3.5 ^{127}I

Iodine has an unpaired proton and $J = 5/2$. As stated above, the DAMA/LIBRA experiment used sodium iodide crystals as their detector material [22]. Iodine is also used in the COUPP bubble chamber experiment [16]. Ressell and Dean [26] created separate eighth-order polynomial fits based on the Bonn A and Nijmegen II

Hamiltonians. For ^{127}I and for ^{131}Xe we choose the Bonn A calculation for purposes of illustration. The structure functions are given by

$$\begin{aligned} S^I_{00}(y) &= e^{-2y}(0.0983 - 0.4891y + 1.1402y^2 - 1.4717y^3 + 1.1717y^4 \\ &\quad -0.5646y^5 + 0.1583y^6 - 0.0239y^7 + 0.0015y^8), \\ S^I_{11}(y) &= e^{-2y}(0.1199 - 0.6184y + 1.5089y^2 - 2.0737y^3 + 1.7731y^4 \\ &\quad -0.9036y^5 + 0.2600y^6 - 0.0387y^7 + 0.0024y^8), \\ S^I_{01}(y) &= e^{-2y}(0.0366 - 0.1950y + 0.5049y^2 - 0.7475y^3 + 0.7043y^4 \\ &\quad -0.3930y^5 + 0.1219y^6 - 0.0192y^7 + 0.0012y^8), \end{aligned} \tag{4.32}$$

where y is defined as before. The differences between the Bonn A and Nijmegen II calculations are non-trivial [15], but it is beyond to scope of this analysis and the expertise of the author to comment on the details. These structure functions also neglect the inelastic interactions that may occur at large recoil energies.

4.3.6 ^{131}Xe

Xenon liquid and gas is used by the appropriately named XENON project [27] and the LUX experiment [28]. For these experiments and others that use Xenon, the spin structure of both ^{129}Xe and ^{131}Xe must be considered. For illustrative purposes and because ^{131}Xe is the isotope with the greatest abundance in the experiments, we show only ^{131}Xe, which has an unpaired neutron and $J = 3/2$. As in the case of ^{121}I, Ressell and Dean [26] provide fits for the Bonn A and Nijmegen II calculations. The Bonn

A fit is given as

$$
\begin{aligned}
S_{00}^{Xe}(y) &= e^{-2y}(0.02964 - 0.13343y + 0.37799y^2 - 0.57961y^3 + 0.57890y^4 \\
&\quad -0.34556y^5 + 0.11595y^6 - 0.02012y^7 + 0.00142y^8), \\
S_{11}^{Xe}(y) &= e^{-2y}(0.0251 - 0.13772y + 0.36661y^2 - 0.53851y^3 + 0.49255y^4 \\
&\quad -0.26990y^5 + 0.08369y^6 - 0.01340y^7 + 0.00087y^8), \\
S_{01}^{Xe}(y) &= e^{-2y}(-0.05455 + 0.27176y - 0.72302y^2 + 1.0545y^3 - 0.97133y^4 \\
&\quad +0.53842y^5 - 0.16899y^6 + 0.02742y^7 - 0.00181y^8).
\end{aligned}
\tag{4.33}
$$

The details of the ^{129}Xe structure functions can be found in Bednyakov and Šimkovic [15].

The spin-dependent form factors (eq. 4.26) for all the above nuclei are plotted in Fig. 4.4. For purposes of illustration, we take $a_p = 0.32$ and $a_n = -0.1$ [29] for spin-dependent interactions, which is well within the allowed parameter space for these values as constrained by current experiments [18]. It is immediately clear that the lightest nuclei offer the greatest chance of spin-dependent detection as the form factor remains much greater over a large range of recoil energies. Given a specific target material, one needs to either look up or calculate the expected WIMP-nucleon interaction parameters for either scalar or axial couplings. Then the total detection rate can be found by integrating eq. 4.5 (and hence, eq. 4.15) over all possible recoil energies. In addition to uncertainty in the structure of the various nuclei, there is still much uncertainty in the cross section calculations that comes from uncertainty

in the collider physics that constrains the supersymmetric models.

We now turn to the distribution of speeds of dark matter in the Milky Way. In eq. 4.6, the product of the differential WIMP-nucleon cross section and the distribution of speeds for the WIMPs must be integrated over the full range of velocities which may produce a recoil energy E_r. We first compute the normalized distribution of dark matter speeds in the rest frame of the laboratory for dark matter particles whose phase-space distribution is described by a King distribution. Then, we calculate the distribution of speeds as a function of the arrival angle with respect to $\mathbf{v}_\oplus$. Finally, we compute the spectral intensity and angular distribution of the nuclei scattered by dark matter in the rest frame of the laboratory.

4.4 The WIMP Speed Distribution

In general, the local differential dark matter particle density can be written as

$$dn = \frac{\rho_{DM}(R_\odot)}{kM_\chi}\mathscr{F}(\mathbf{v}, \mathbf{v}_\oplus)d^3\mathbf{v} \tag{4.34}$$

where $\mathscr{F}(\mathbf{v}, \mathbf{v}_\oplus)$ is the dark matter phase-space distribution, k is a normalization constant defined by

$$k = \int \mathscr{F}(\mathbf{v}, \mathbf{v}_\oplus)d^3\mathbf{v}, \tag{4.35}$$

$\mathbf{v}$ is the WIMP velocity in the detector's rest frame, located on Earth, and $\mathbf{v}_\oplus$ is the velocity of Earth with respect to the Galactic rest frame, subject to an annual modulation as shown in Section 4.2 [5, 30].

Most studies assume dark matter follows a simple Maxwell-Boltzman (MB) distribution, where the dark matter distribution is smooth, having reached a steady state. While some numerical simulations [31] agree that the dark matter distribution near the Sun is well-approximated by a MB distribution, it is generally known that the full Galactic dark matter phase-space distribution is not well-described by a MB distribution [32]. The King distribution provides an alternative to the sharp cutoff usually found in a truncated MB distribution and has been well-studied by Binney and Tremaine [33]. We first review the method for normalizing the MB distribution before proceeding to the King distribution.

4.4.1 The Maxwell-Boltzman Speed Distribution

With a sharp cutoff at the local escape speed from the Galaxy, v_{esc}, the MB distribution is given by

$$\mathscr{F}_{MB}(\mathbf{v}, \mathbf{v}_{\oplus}) = \begin{cases} e^{[v_{esc}^2 - (\mathbf{v}+\mathbf{v}_{\oplus})^2]/2\sigma_{MB}^2} & \text{for } |\mathbf{v}| < v_{esc} \\ 0 & \text{for } |\mathbf{v}| \geq v_{esc} \end{cases} \tag{4.36}$$

where it is assumed that $\sigma_{MB} \approx \sqrt{\frac{3}{2}}\Theta_0$ is the velocity dispersion, and Θ_0 is the velocity of the Sun about the Galactic center. This result arises when the Galactic dark matter distribution is approximated as a single-component isothermal sphere, which has the property that $v_{esc} = \infty$ and the mass of the $M(r)$ tends linearly to infinity as $r \to \infty$. In order to avoid this divergence, the MB distribution is usually truncated at $v = v_{esc}$.

For illustrative purposes and for comparison with the lowered isothermal/King distribution, we show the procedure for normalizing the MB distribution for two cases. The normalization was worked out in great detail for the MB distribution by Lewin and Smith [5]. In the simplest case, the escape velocity is taken to be infinite and $v_\oplus = 0$, the "stationary Earth" approximation. Since the speed of the Earth around the Sun ($\sim$ 30 km/s) is significantly less than the speed of the Sun around the Galactic center ($\Theta_0 \sim 240$ km), taking $v_\oplus = 0$ will give a rough estimate of the normalization factor k.

$$\begin{aligned} k_{\{MB,v_{esc}=\infty\}} &= \int e^{-(\mathbf{v}+\mathbf{v}_\oplus)^2/\sigma_{MB}^2} d^3\mathbf{v} \\ &= \int_0^\infty dv v^2 e^{-v^2/\sigma_{MB}^2} \int_{-1}^{1} d(cos\theta) \int_0^{2\pi} d\phi \\ &= (\pi\sigma_{MB}^2)^{3/2}. \end{aligned} \tag{4.37}$$

Since $v_\oplus$ is small compared to the velocity of light, the number density of particles represented by k_{MB} is independent of $v_\oplus$. This can be checked by expanding $(\mathbf{v} + \mathbf{v}_\oplus) = v^2 + 2vv_\oplus \cos\theta + v_\oplus^2$ and proceeding as in eq. 4.37. Indeed the resulting normalization [5] is the same as in eq. 4.37 and independent of $v_\oplus$.

Realistically, dark matter particles traveling faster than the escape velocity leave the Galaxy and therefore they do not interact in dark matter detectors. Lewin and Smith [5] have also calculated the MB normalization for a finite escape velocity in the stationary Earth approximation, and it is given by

$$k_{\{MB,v_{esc}\neq\infty\}} = (\pi\sigma_{MB}^2)^{3/2} \left[\mathrm{erf}\left(\frac{v_{esc}}{\sigma_{MB}}\right) - \frac{2}{\pi^{1/2}} \frac{v_{esc}}{\sigma_{MB}} e^{-v_{esc}^2/\sigma_{MB}^2} \right]. \tag{4.38}$$

This normalization is calculated by setting the upper limit of the velocity integral in eq. 4.37 equal to v_{esc}. Lewin and Smith also work out the normalizations for $v_\oplus \neq 0$ and the results can be found in their paper [5]. We now turn to the King distribution, which deals with the finite values of v_{esc} and mass of the dark matter in the Galaxy in a self-consistent way.

4.4.2 The King Speed Distribution

The King distribution provides an alternative to a the sharp cutoff to the MB distribution in eq. 4.36. The phase-space distribution function for the King distribution is given in its simplest form by

$$\mathscr{F}_K(\varepsilon) = \begin{cases} e^{\varepsilon/\sigma_K^2} - 1 & \text{for } \varepsilon > 0 \\ 0 & \text{for } \varepsilon \leq 0, \end{cases} \tag{4.39}$$

where σ_K is related but not equal to the velocity dispersion, $\varepsilon = \Phi_0 - \left[\frac{1}{2}v^2 + \Phi_{tot}(r,z)\right]$, $\Phi_0 = \frac{1}{2}v_{esc}^2$, the gravitational potential at the "virial" radius of the Galaxy, and Φ_{tot} is the total Galactic potential from both visible and dark matter at any point in the Galaxy. If we define a scaled potential $\Psi(r,z) = \Phi_0 - \Phi_{tot}(r,z)$ and note that the escape velocity can be written as $v_{esc}(r,z) = \sqrt{2\Psi(r,z)}$, then the King *velocity* distribution can be written written as

$$\mathscr{F}_K(\mathbf{v}) = \begin{cases} e^{(v_{esc}^2 - \mathbf{v}^2)/2\sigma_K^2} - 1 & \text{for } |\mathbf{v}| < v_{esc} \\ 0 & \text{for } |\mathbf{v}| \geq v_{esc}. \end{cases} \tag{4.40}$$

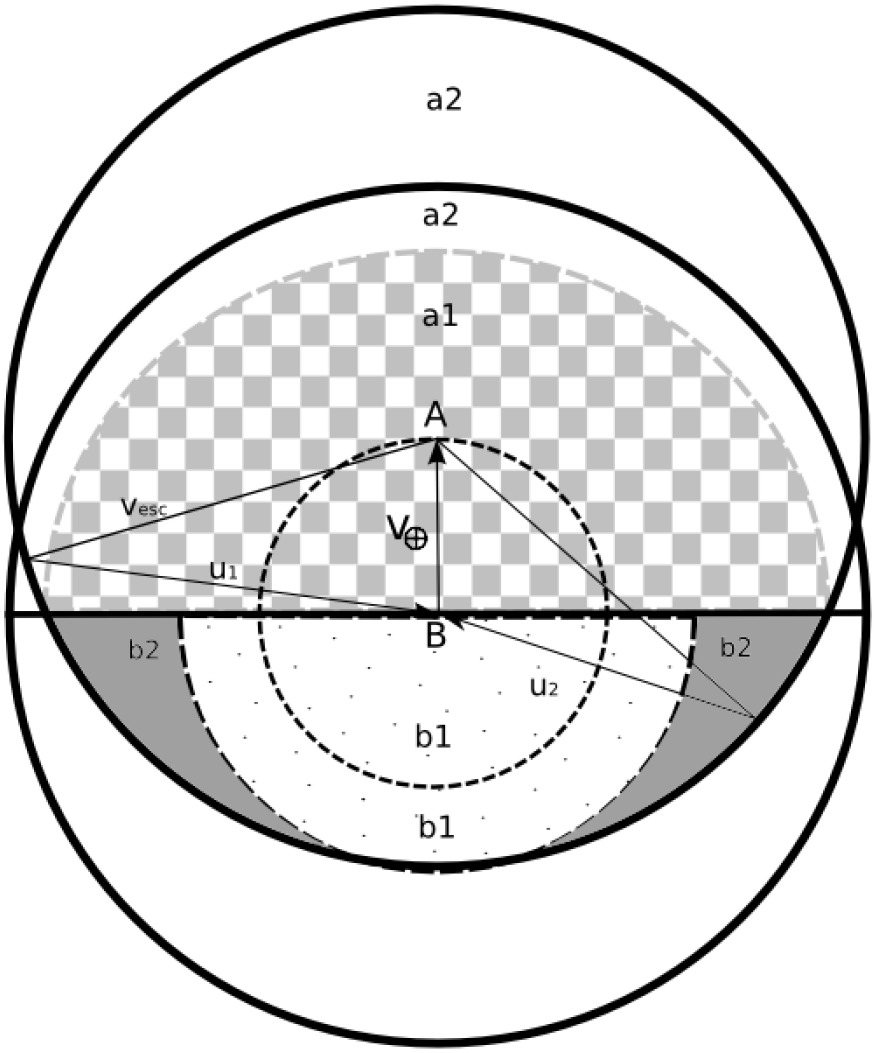

Figure 4.5: A diagram of the limits on the speeds of head-on ($a1$ and $a2$) and overtaking ($b1$ and $b2$) dark matter in the rest frame of the laboratory situated at B and moving with a velocity $\mathbf{v}_\oplus$ with respect to the Galactic rest frame. The region $a1$ includes the grey checkered region. The $a2$ region is the two topmost solid white crescent-shaped regions. Region $b1$ is represented by the dotted region, and $b2$ is the solid gray region. Any dark matter in the bottom-most white crescent would have an velocity greater than the escape velocity from the Galaxy and will leave the Galaxy. The $u1$ vector represents an example of head-on dark matter while the u_2 vector represents overtaking dark matter.

In order to compute the dark matter detection rates, the normalized one-dimensional distribution of dark matter particle *speeds* per unit interval must first be derived.

To normalize the speed distribution for the King phase-space distribution, we take a different approach from that taken with the MB distribution [5]. Since some detectors such as DM-TPC [34] and DRIFT [35] are capable of measuring the direction of the recoil nuclei, we would also like to compute the directional dependence of the distribution of speeds of dark matter particles as seen in the laboratory frame.

We begin by constructing a spherical polar coordinate system in velocity space (see Fig. 4.5) with the polar axis pointing in the positive direction ($\overrightarrow{BA}$) of $\mathbf{v}_\oplus$, with A representing the Galactic rest frame and B the velocity of the terrestrial dark matter detector (located at B) with respect to the Galactic rest frame. As noted earlier, $\mathbf{v}_\oplus = \overrightarrow{BA}$ is subject to an annual modulation because of the Keplerian motion of the Earth. We divide our consideration of the dark matter velocities into two cases, which are treated separately. In the first case, dark matter travels head-on towards the detector and $\mathbf{u} \cdot \mathbf{v}_\oplus < 0$, where $\mathbf{u}$ is the velocity of dark matter in the lab frame. The vector $\mathbf{u}_1$ in Fig. 4.5. is an example of head-on dark matter. Conversely, dark matter with $\mathbf{u} \cdot \mathbf{v}_\oplus > 0$ must overcome $\mathbf{v}_\oplus$ to interact in the detector. This second case is termed overtaking dark matter, an example of which is shown as $\mathbf{u}_2$ in Fig. 4.5.

We write the dark matter velocity in the Galactic rest frame in terms of orthogonal longitudinal (v_l) and transverse ($v_\perp$) components, measured in the Galactic rest frame, such that

$$v^2 = v_l^2 + v_\perp^2. \tag{4.41}$$

In the laboratory rest frame, the longitudinal and transverse components are written as $u_l = v_l - v_\oplus$ and $u_\perp = v_\perp$ respectively. The speed u of a dark matter particle in the laboratory rest frame is then

$$u^2 = u_l^2 + u_\perp^2 = (v_l - v_\perp)^2 + v_\perp^2, \tag{4.42}$$

implying the longitudinal velocity in the Galactic rest frame is

$$v_l = v_\oplus \pm \sqrt{u^2 - u_\perp^2} \tag{4.43}$$

and

$$\left|\frac{\partial v_l}{\partial u}\right| = \frac{u}{\sqrt{u^2 - u_\perp^2}}. \tag{4.44}$$

In the Galactic rest frame, the *speed* distribution can then be written as

$$f_{DM}(v)d^3v = \frac{\pi}{k}\Big[e^{(v_{esc}^2 - v_l^2 - v_\perp^2)/2\sigma_{DM}^2} - 1\Big]dv_l dv_\perp^2, \tag{4.45}$$

and the corresponding distribution in the rest frame of the laboratory is

$$f_{DM}(u)d^3u = \frac{\pi}{k}\left[e^{(v_{esc}^2 - \left[v_\oplus \pm \sqrt{u^2-u_\perp^2}\right]^2 - u_\perp^2)/2\sigma_{DM}^2} - 1\right]\frac{u}{\sqrt{u^2 - u_\perp^2}}dudu_\perp^2. \tag{4.46}$$

To compute the normalization constant k in either frame, the integral over $u_\perp = v_\perp$ must be taken over all possible transverse velocities. In the next two sections, we derive the limits on $u_\perp$ for head-on (corresponding to the minus sign before the radical in the exponent in eq. 4.46) and overtaking dark matter (corresponding to

the plus sign before the radical in the exponent in eq. 4.46) separately.

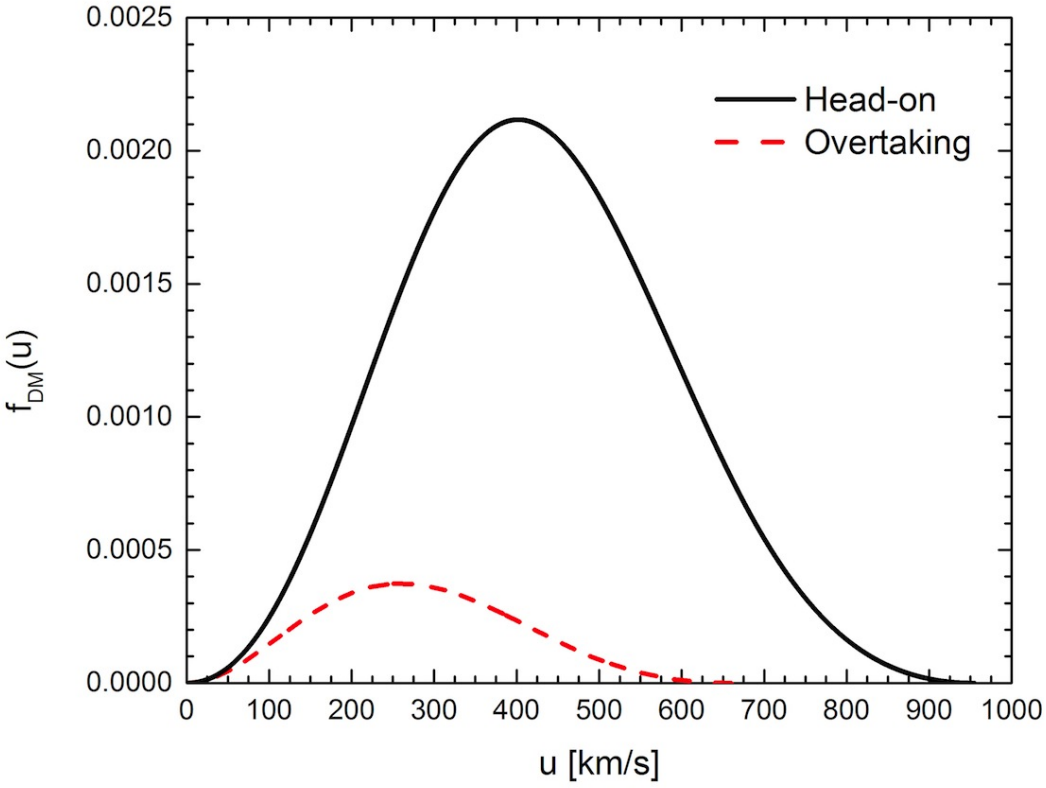

Figure 4.6: The normalized speed distribution of head-on and overtaking dark matter for the dark matter model that best fits both the rotation curve and the BHB and BS stars: ρ_{DM0} = 100 GeV cm^{-3} and σ_{DM} =220 km s^{-1} for the 55 M$_{\odot}$ pc^{-2} disk with r_{tn}=3.0 kpc.

Head-on Dark Matter

For head-on (downwards in Fig. 4.5) dark matter, we illustrate the upper limit of the speed of the dark matter particle in the rest frame of the detector by drawing a circle of radius v_{esc} with its origin at A. The speed of the dark matter particles cannot exceed v_{esc} or else they would not be bound to the Galaxy. In this case, the detector is experiencing an effective dark matter wind and the maximum dark matter speed

that the detector can see in its rest frame is $v_{esc} + v_{\oplus}$. The head-on dark matter case is divided into two regions, a_1 and a_2, as shown in the Fig. 4.5.

In the a_1 region,

$$|u| < \sqrt{v_{esc}^2 - v_{\oplus}^2},$$

and the dark matter speed u may lie anywhere in this region. The upper and lower limits on $u_\perp$ are the limits on the transverse component of the dark matter velocity vector, which are given by

$$\begin{aligned} u_{\perp,min}^{a_1} &= 0 \\ u_{\perp,max}^{a_1} &= |u|. \end{aligned} \tag{4.47}$$

In the a_2 region the dark matter speed lies in range

$$\sqrt{v_{esc}^2 - v_{\oplus}^2} < |u| < v_{esc} + v_{\oplus},$$

and the limits on $u_\perp$ are correspondingly

$$\begin{aligned} u_{\perp,min}^{a_2} &= 0 \\ u_{\perp,max}^{a_2} &= \left| v_{esc} \left[1 - \frac{(v_{esc}^2 + v_{\oplus}^2 - u^2)^2}{4 v_{\oplus}^2 v_{esc}^2} \right]^{1/2} \right|. \end{aligned} \tag{4.48}$$

Overtaking Dark Matter

In the case of overtaking (upwards in Fig. 4.5) dark matter, the limits on the dark matter speed are illustrated by a circle of radius v_{esc} centered at B. As in the case of

head-on dark matter, overtaking dark matter is divided into two regions, b_1 and b_2.

The limits on u in b_1 are

$$|u| < |v_{esc}| - |v_{\oplus}|,$$

which leads to the limits on $u_\perp$,

$$\begin{aligned} u^{b_1}_{\perp,min} &= 0 \\ u^{b_1}_{\perp,max} &= |u|. \end{aligned} \tag{4.49}$$

For b_2,

$$|v_{esc}| - |v_{\oplus}| < |u| < \sqrt{|v^2_{esc}| - |v^2_{\oplus}|},$$

and the corresponding limits on $u_\perp$ are

$$\begin{aligned} u^{b_2}_{\perp,min} &= \left| v_{esc}\left[1 - \frac{(v^2_{esc} + v^2_{\oplus} - u^2)^2}{4v^2_{\oplus}v^2_{esc}}\right]^{1/2}\right|. \\ u^{b_2}_{\perp,max} &= |u|. \end{aligned} \tag{4.50}$$

In Fig. 4.6 we show the normalized speed distributions computed by integrating eq. 4.46 over $u_\perp$ for head-on and overtaking dark matter respectively for the dark matter model in Table 3.2 that best fits both the rotation curve and BHB and BS observations and take an approximate average value for $v_{\oplus}$=250 km s^{-1}. To compute the normalization constant k, the speed distributions for both head-on and overtaking dark matter must be integrated over all u and added together. Note that k depends on the local value of the escape speed and therefore depends on the distribution of visible

matter in the Galaxy. Given a model for the interaction between the dark matter and normal nuclei, eq. 4.6 can then be integrated to calculate the expected event rates for a given experiment. In the next section, we use the formalism developed for normalizing the dark matter speed distribution to compute the angular distribution of dark matter at various speeds.

4.4.3 The Angular Distribution of Dark Matter

With the same method used to calculate the distribution of speeds for head-on and overtaking dark matter, we calculate the distribution of dark matter as a function of arrival angle with respect to $\mathbf{v}_\oplus$ at any given speed both for head-on and overtaking dark matter particles. Knowing the angular distribution is essential for interpretation the results of detectors that are sensitive to the recoils direction of scattered nuclei.

Let θ be the arrival angle of the dark matter particle with respect to $\mathbf{v}_\oplus$. The transverse velocity can then be written as

$$u_\perp^2 = u^2(1 - \cos^2\theta), \tag{4.51}$$

implying

$$\left|\frac{du_\perp^2}{d\cos\theta}\right| = |2u^2\cos\theta|. \tag{4.52}$$

The dark matter speed distribution (eq. 4.46) can then be rewritten as

$$f_{DM}(u,\cos\theta)dudcos\theta = \frac{2\pi}{k}\left[e^{(v_{esc}^2-[v_\oplus \pm |u\cos\theta|]^2-u^2(1-\cos^2\theta))/2\sigma_{DM}^2} - 1\right]u^2 dudcos\theta. \tag{4.53}$$

Again, limits are derived separately for the head-on and overtaking dark matter. Using eq. 4.51 to convert from limits on $w_\perp$ to limits on $\cos\theta$ yields:

$$\begin{aligned} \cos\theta^{a_1}_{min} &= -1 \\ \cos\theta^{a_1}_{max} &= 0 \end{aligned} \tag{4.54}$$

$$\begin{aligned} \cos\theta^{a_2}_{min} &= -1 \\ \cos\theta^{a_2}_{max} &= -\left|\left\{1 - \frac{v_{esc}^2}{u^2}\left[1 - \frac{(v_{esc}^2 + v_\oplus^2 - u^2)^2}{4v_\oplus^2 v_{esc}^2}\right]\right\}^{1/2}\right| \end{aligned} \tag{4.55}$$

$$\begin{aligned} \cos\theta^{b_1}_{min} &= 0 \\ \cos\theta^{b_1}_{max} &= 1 \end{aligned} \tag{4.56}$$

$$\begin{aligned} \cos\theta^{b_2}_{min} &= 0 \\ \cos\theta^{b_2}_{max} &= \left|\left\{1 - \frac{v_{esc}^2}{u^2}\left[1 - \frac{(v_{esc}^2 + v_\oplus^2 - u^2)^2}{4v_\oplus^2 v_{esc}^2}\right]\right\}^{1/2}\right|. \end{aligned} \tag{4.57}$$

In Fig. 4.7, the angular distribution of speeds is shown for the velocities $u = 100 - 900$ km s^{-1} for the dark matter model in Table 3.2 that best fits both the rotation curve and the BHB and BS stars. Note that for speeds greater than v_{esc} only head-on dark matter contributes to the velocity distribution. Similarly, only overtaking dark matter contributes for $u < v_\oplus$. Now that we know the distribution of dark matter particles as a function of angle, the event rate as a function of $\cos\theta$ for a given experiment can be found by integrating eq. 4.6 for a given dark matter

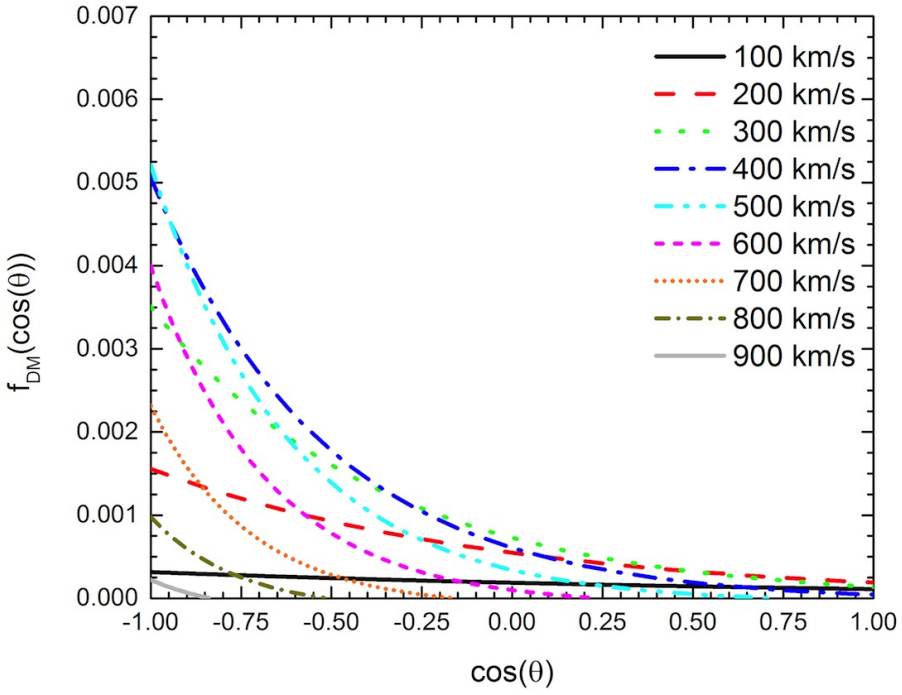

Figure 4.7: The angular speed distribution of dark matter is plotted against the cosine of the arrival angle for several dark matter speeds, as measured in the rest frame of the laboratory, for the $\rho_{DM0} = 100$ GeV cm^{-3} and σ_{DM} =220 km s^{-1} dark matter model for the 55 M$_\odot$ pc^{-2} disk with $r_{tn} = 3.0$ kpc.

candidate. We now proceed to calculate the spectral intensity of the scattered nuclei as a function of scattering angle in the rest frame of the laboratory.

4.5 The Energy Spectrum and Angular Distribution of Nuclei Scattered by Dark Matter

For dark matter detectors with sensitivity to the recoil direction of the scattered nuclei, it is important to know the expected energy and angular distribution of target nuclei scattered by dark matter particles. This has been worked out analytically for

the MB distribution [36, 37] and the Michie distribution [38]. We take a different approach than was used above to calculate the angular velocity distribution and develop a semi-Monte Carlo approach to calculate these spectral intensities.

Consider a dark matter particle arriving at an Earth-bound detector with a speed u in the lab frame and making an angle ξ with respect to the direction of the motion of the Earth with $v_\oplus$ chosen as the z-axis (see Fig. 4.8 for a detailed illustration of the coordinate system used in this calculation). Upon impact, the incoming WIMP will scatter a target particle P in the (η', ψ') direction with respect to the arrival direction of the dark matter particle $\hat{u}$ that defines the z' reference frame. Directional detection experiments look to record the recoil energy T (This is equivalent to the recoil energy E_r defined above, but we change notation for computational clarity.) and the recoil direction η (and possibly ψ) in the lab frame with respect to the $v_\oplus$ direction.

We postulate the phase-space distribution of dark matter in the center-of-mass system of the Galaxy,

$$f_{DM}(v)d^3v = \frac{1}{k}\Big(e^{\left[v_{esc}(r)^2 - v^2\right]/2\sigma_{DM}^2} - 1\Big)d^3v \quad \text{for } v_{esc}^2 > v^2 > 0, \tag{4.58}$$

is isotropic, allowing for the separation of its the angular dependence,

$$f_{DM}(v)d^3v = \frac{1}{k}\Big(e^{\left[v_{esc}(r)^2 - v^2\right]/2\sigma_{DM}^2} - 1\Big)2\pi v^2 dcos\xi dv \quad \text{for } v_{esc}^2 > v^2 > 0, \tag{4.59}$$

and create a semi-Monte Carlo method to compute the energy and angular distribu-

tion of recoil events. Speed values v_i in the Galactic rest frame are chosen such that they randomly sample the dark matter distribution. In order to achieve this, consider the probability distribution $F(x)$, which satisfies the equation

$$\frac{dF}{dx} = \frac{dF}{dv}\frac{dv}{dx} = C, \tag{4.60}$$

where

$$\frac{dF}{dv} = f_{DM}(v),$$

and C is a constant. Then

$$\int C dx = \int_0^v f_{DM}(v')dv' \equiv G(v), \tag{4.61}$$

with x defined as

$$x \equiv \frac{G(v)}{C}. \tag{4.62}$$

The probability distribution $F(x)$ is uniform in x from $x = 0$ to $x = G(v_{esc})/C$ and integrates to unity for $C = 1/2$ when $f_{DM}(v)$ is interpreted as the number per unit solid angle at a given polar angle over all azimuths. Points are chosen equally spaced in x ($dx = 0.002$), and $G(v)$ is inverted to find the corresponding v values. Similarly, equally spaced values of $\cos\theta_j$ ($\Delta\cos\theta_j$=0.1) from $-1 \leq \cos\theta_j \leq 1$ are chosen, where θ_j is the angle between $\mathbf{v}$ and $\mathbf{v}_\oplus$. The components of the velocity distribution in the

reference frame of the laboratory and the incident angle ξ can then be written as

$$u_{||} = v_i \cos\theta_j - v_\oplus \tag{4.63}$$

$$u_\perp = v_i \sin\theta_j \tag{4.64}$$

$$u_{ij} = \sqrt{u_{||}^2 + u_\perp^2} \tag{4.65}$$

$$\cos\xi_{ij} = u_{||}/u_{ij} \tag{4.66}$$

$$\sin\xi_{ij} = u_\perp/u_{ij}. \tag{4.67}$$

We have chosen 21 values of $\cos\theta_j$ and 501 values of v corresponding to 10,521 dark matter particles distributed evenly in x space.

If the particles collide with a target nucleus of mass M_N, then the velocity of the center of mass is

$$v_{cij} = \frac{M_\chi}{M_N + M_\chi} u_{ij} \equiv \frac{\mu}{M_N} u_{ij}. \tag{4.68}$$

Let the target particle scatter through an angle θ_k^* in the center-of-mass frame. Noting that the laboratory angle

$$\eta_k' = \frac{1}{2}(\pi - \theta_k^*), \tag{4.69}$$

we write

$$\cos\theta_k^* = 1 - 2\cos^2\eta_k'. \tag{4.70}$$

We choose 21 values of $\cos\eta_k'$ for an equally spaced set in $\cos\theta_k^*$ from 0-π because the scattering is isotropic in the center of mass frame. This allows us to write the square

of the momentum transfer as

$$q_{ijk}^2 = 4\mu^2 u_{ij}^2 \cos^2 \eta'_k \tag{4.71}$$

and the kinetic energy carried by the target nucleus

$$T_{ijk} = \frac{q_{ijk}^2}{2M_N}. \tag{4.72}$$

The differential WIMP-nucleon cross section $d\sigma/d\Omega$ is a function of q_{ijk}^2 only (see eqs. 4.15 and 4.25), allowing us to define weight functions

$$W_{ijk} = n_{DM}\rho_T u_{ij} \frac{d\sigma}{d\Omega}(q_{ijk}^2)\frac{A}{A_t}, \tag{4.73}$$

where n_{DM} is the number density of dark matter particles, ρ_T is the density of the target nuclei, A is Avogardo's Number, and A_t is atomic weight of the target nucleus.

We choose 21 equally spaced values of the azimuthal angle of the scattered particles, ψ', in the interval $0 - 2\pi$ and calculate

$$\cos \eta_{ijkl} = \sin \xi_{ij} \sin \eta'_{jk} \sin \psi'_l + \cos \xi_{ij} \cos \eta'_{jk}, \tag{4.74}$$

the scattering angle in the lab frame. There are $501 \times 21^3 = 4,639,761$ values of $\cos \eta_{ijkl}$, which are ordered in ascending order from -1 to 1 and bunched together, with the corresponding kinetic energies, in intervals of 0.1 in $\cos \eta_{ijkl}$. The recoil energies T_{ijk} in each $\cos \eta_{ijkl}$ bin are binned in 1 keV intervals. Keeping track of

indices in each bunch, the weight factors in each kinetic energy bin are summed to give the number of recoil events per second per unit volume in each recoil energy and lab-frame scattering angle bin. We show in Figs. 4.9 and 4.10 the event rates calculated in this manner for two dark matter models from Table 3.2. We also assume the detector is a spin-independent liquid xenon detector with a density of $\sim$3 g cm^{-3} and that the dark matter mass is 50 GeV.

Here, we have only shown the calculated spectra for two dark matter models that represent the range allowed in the local dark matter density and escape velocity. The expected rate of interaction between dark matter and a terrestrial detector depends significantly on the distribution of dark matter speeds with respect to the detector as well as the details of the WIMP-nucleon scattering cross section, which varies greatly depending on the assumed dark matter candidate. A full analysis of the constraints on direct detection would involve considering the full range of models for the phase-space distribution of dark matter constrained in Chapter 3 as well as considerations of the annual modulation in $v_{\oplus}$. For each of the dark matter detectors currently in operation, the range in expected event rates could then be calculated for each of the numerous candidates. As a rough estimate, the range in the local dark matter density (about a factor of 2) allowed by the analysis in Chapter 3 of a factor allows for a variation in the expected event rate by the same factor. The spectral intensities have been plotted for several of the dark matter models from Chapter 3 (not shown here) and are found not to differ significantly from Fig. 4.9 and 4.10. The main difference between Figs. 4.9 and 4.10 is seen in the tails of the spectra for each bin in recoil angle $\cos\eta$. The dark matter model in Fig. 4.10 has a greater escape speed from R_0

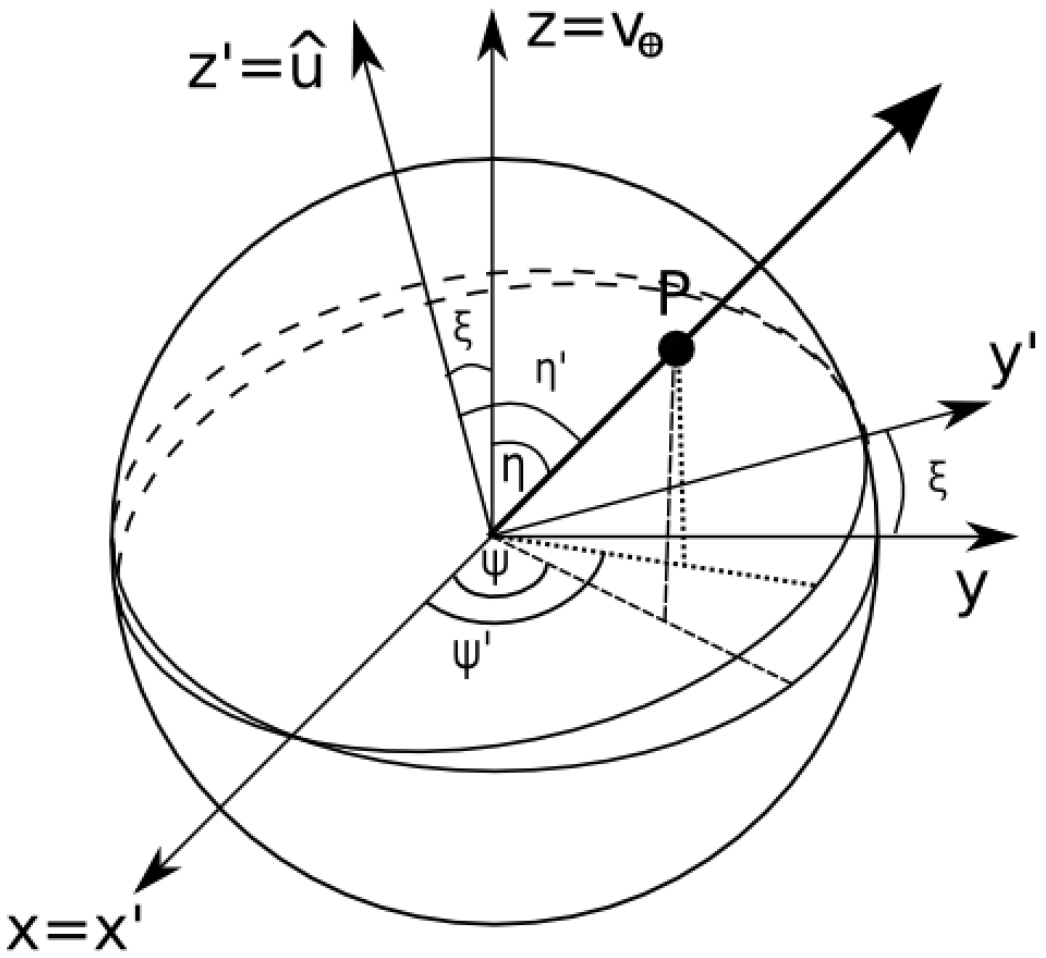

Figure 4.8: Coordinate system for calculating the spectral intensity of scattered target particles in the lab frame.

and a higher velocity dispersion for the dark matter particles. Correspondingly, there are more dark matter events predicted at higher energies in each bin than for the dark matter model in Fig. 4.9. Dark matter detectors sensitive to the recoils direction of scattered nuclei may be able to discriminate amongst the dark matter models is there is high enough sensitivity at the largest recoil energies. The dark matter density at R_0 in Fig. 4.10 is greater than in Fig. 4.9 so Fig. 4.10 has a correspondingly higher normalization.

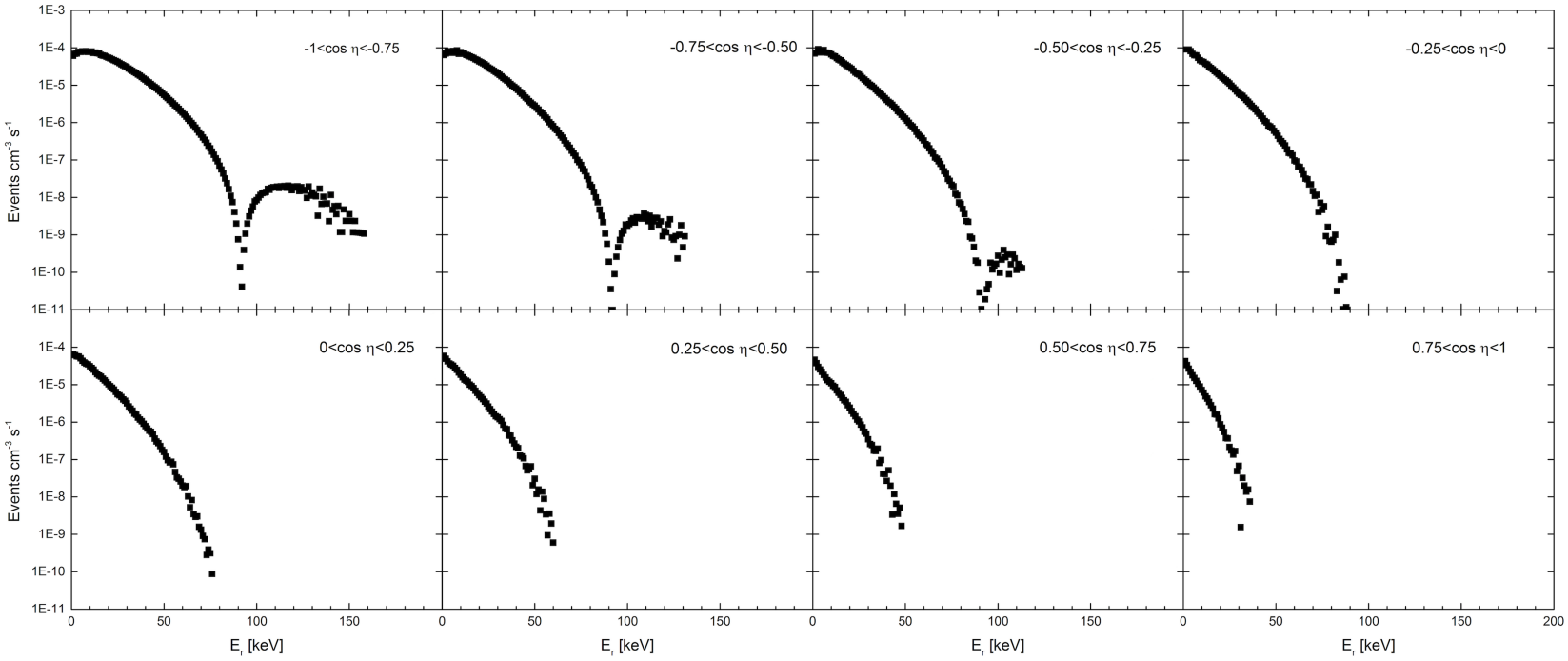

Figure 4.9: The spectral intensity and angular distribution of nuclei scattered by dark matter in the laboratory frame are shown in 1 keV energy bins for ranges in the lab frame scattering angle η. In this figure, $\cos\eta_{ijkl}$ is binned in units of 0.25. The dark matter is assumed to have the properties $\rho_{DM0} = 500$ GeV cm^{-3} and σ_{DM}=190 km s^{-1} for the 70 M$_\odot$ pc^{-2} disk with r_{tn} =3.0 kpc and a mass M_χ=50 GeV. The detector material is assumed to be liquid xenon with a density of ~ 3 g cm^{-3}.

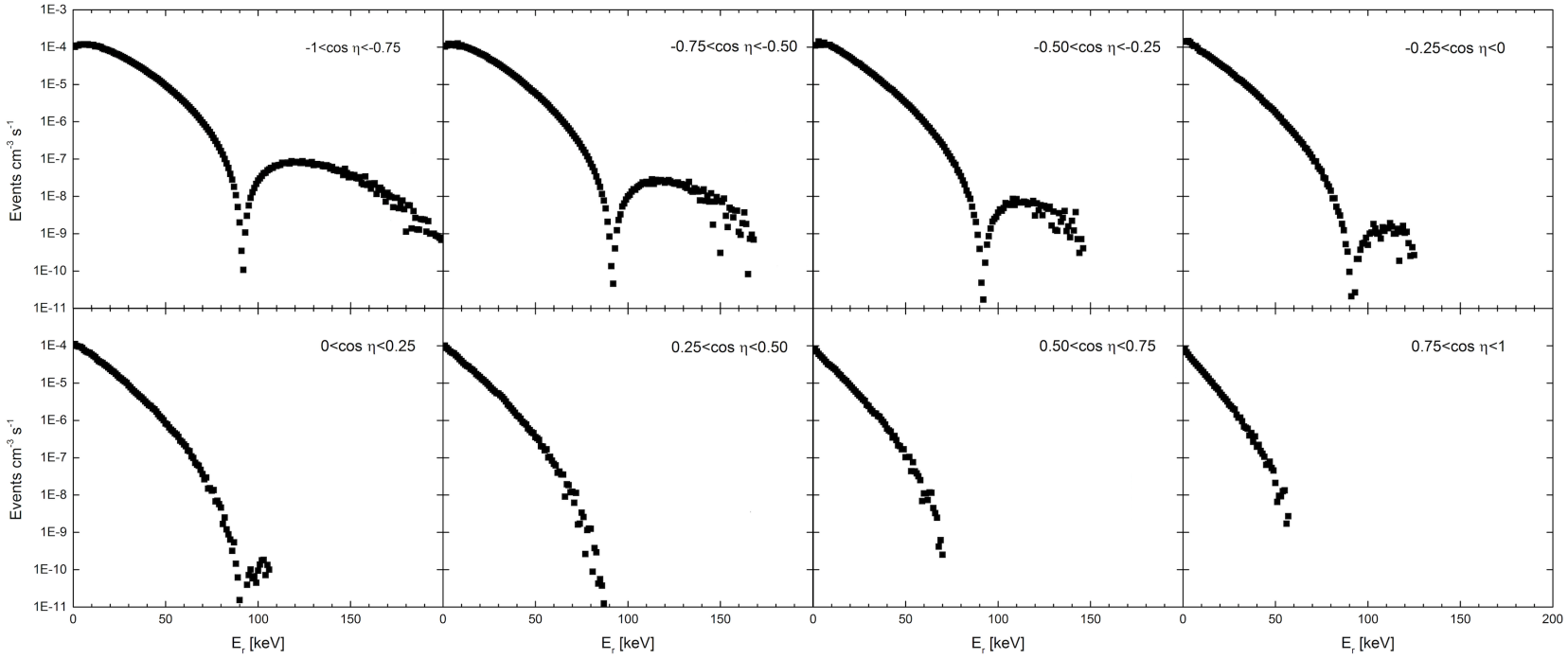

Figure 4.10: The spectral intensity and angular distribution of nuclei scattered by dark matter in the laboratory frame are shown in 1 keV energy bins for ranges in the lab frame scattering angle η. In this figure, $\cos\eta_{ijkl}$ is binned in units of 0.25. The dark matter is assumed to have the properties $\rho_{DM0} = 100$ GeV cm^{-3} and σ_{DM}=220 km s^{-1} for the 55 M$_\odot$ pc^{-2} disk with r_{tn} =3.0 kpc and a mass M_χ=50 GeV. The detector material is assumed to be liquid xenon with a density of $\sim$ 3 g cm^{-3}.

References

[1] Drukier, A. & Stodolsky, L. 1984, PRD, 30, 2295

[2] Goodman, M. W. & Witten, E. 1985, PRD, 31, 3059

[3] Drukier, A., Freese, K. & Spergel, D. 1986, PRD, 33, 3495

[4] Baudis, L. 2012, arXiv:1211.7222v1

[5] Lewin, J. D. & Smith, P. F. 1996, Astropart. Phys., 6, 87

[6] Jungman, G., Kamionkowski, M. & Griest, K. 1996, Phys. Rep., 267, 195

[7] Gaitskell, R. J. 2004, Annu. Rev. Nucl. Part. Sci., 54, 315

[8] Saab, T. 2012, arXiv:1203.2566v1

[9] Hooper, D. & Baltz, E. A. 2008, Annu. Rev. Nucl. Part. Sci., 58, 293

[10] Armengaud, R. 2010, arXiv:1003.2380v1

[11] Vergados, J. D. 2003, PRD, 67, 103003

[12] Oikonomou, V. K., Vergados, J. D., & Moustakidis, Ch. C. 2007, Nuc. Phys. B, 773, 19

[13] Bertone, G., Hooper, D. & Silk, J. 2005, Phys. Rep. 405 279

[14] Bednyakov, V. A. & Šimkovic, F. 2004, arXiv:0406218v1

[15] Bednyakov, V. A. & Šimkovic, F. 2006, arXiv:0608097v1

[16] Behnke, E. et al. 2011, PRL, 106, 021303

[17] Felizardo, M. et al. 2010, PRL, 105, 211301

[18] Archambault, S. et al. 2009, Phys. Lett. B, 682 185

[19] Vergados, J. D. 1996, J. Phys. G., 22, 253

[20] Divari, P. C. et al. 2000, PRC, 61, 054612

[21] Vergados, J. D. 2003, Phys. Atom. Nucl., 66, 481

[22] Bernabei, R. et al. 2010, arXiv:1002.1028v1

[23] Wang, G. 2010, J. Appl. Phys., 107, 094504

[24] Ahmed, Z. et al. 2011, PRL, 106, 131302

[25] Dimitrov, V., Engel, J. & Pittel, S. 1995, PRD, 51, 291

[26] Ressell, M. T. & Dean, D. J. 1997, PRC, 56, 535

[27] Aprile, E. et al., 2012 arXiv:1207.5988v1

[28] Akerib, D. S. et al. 2013, Nucl. Inst. Meth. Phys. Res. A, 704, 111

[29] Ellis, J. & Karliner, M. 1994, arXiv:9407287v2

[30] Freese, K., Lisanti, M., & Savage, C. 2012, arXiv:1209.3339

[31] Vogelsberger, M. et al. 2009, MNRAS, 395, 797

[32] Kuhlen, M. et al. 2010, JCAP, 02, 030

[33] Binney, J. & Tremaine, S. 2008, Galactic Dynamics, (2nd ed; Princeton, NJ: Princeton, University Press)

[34] Ahlen, S. et al. 2011, Phy. Lett. B, 695, 124

[35] Daw, E. et al. 2010, arXiv:1010.3027

[36] Alenazi, M. S. & Gondolo, P. 2008, PRD, 77, 043532

[37] Gondolo, P. 2002, PRD, 66, 103513

[38] Alves, D. S. M., Hedri, S. E. & Wacker, J. G. 2012, arXiv:1204.5487v1

Chapter 5

Implications for the Indirect Detection of Dark Matter

In this chapter, we will only consider gamma rays from dark matter annihilation or decay. In principle, dark matter could produce other cosmic rays including antimatter in the form of positrons and anti-protons. In Appendix A, the electronic component of cosmic rays is discussed to show that the current understanding of propagation models of cosmic rays does not yet require exotic processes such as dark matter annihilation or decay to explain the observations.

Gamma rays travel through the Galaxy in straight lines from their source and are mostly unabsorbed in the Galaxy. For some dark matter candidates, such as the neutralino, which is its own antiparticle, it may be possible to detect the gamma rays from their annihilation or decay [1, 2]. This makes neutralinos an ideal indirect detection candidate, and their detection may be able to provide information about the structure and location of the dark matter in the Galactic center, where its density

is the greatest. Gamma rays also offer a smoking-gun scenario for dark matter detection. If dark matter particles annihilate directly into a pair of photons, these will be monochromatic with an energy $E_\gamma = M_\chi$ resulting in a high-energy spectral line that is not known to be produced by any standard physical process. Current experiments are searching for such lines from the Galactic center [3].

The spectral flux of gamma rays expected per unit solid angle from the decay of dark matter is given by

$$\frac{d\Phi_{\gamma,d}(\Upsilon)}{dE_\gamma} = \frac{1}{4\pi M_\chi \tau_\chi} \frac{dN}{dE_\gamma} \int_{los} \rho_{DM}(l) dl(\Upsilon), \tag{5.1}$$

where dN/dE_γ is the photon spectrum per annihilation, τ_χ is the dark matter decay time, M_χ is the dark matter mass, and Υ symbolically represents the Galactic coordinates of the line of sight $\vec{l}$. The spectral flux of gamma rays from the annihilation of dark matter depends quadratically on ρ_{DM} and is given by

$$\frac{d\Phi_{\gamma,a}(\Upsilon)}{dE_\gamma} = \frac{dN}{dE_\gamma} \frac{< \sigma_a v >}{4\pi M_\chi^2} \int_{los} \rho_{DM}^2(l) dl(\Upsilon), \tag{5.2}$$

where $< \sigma_a v >$ is the dark matter annihilation rate and depends on the specific dark matter candidate being considered. Correspondingly, the flux from dark matter annihilation is expected to have a much greater concentration towards the Galactic center than that from dark matter decay (see Figs. 5.3 and 5.4). In the above formulae, the dark matter particle is assumed to be its own antiparticle. If this is not the case, eq. 5.2 should be multiplied by a factor of 1/2. The photon multiplicity

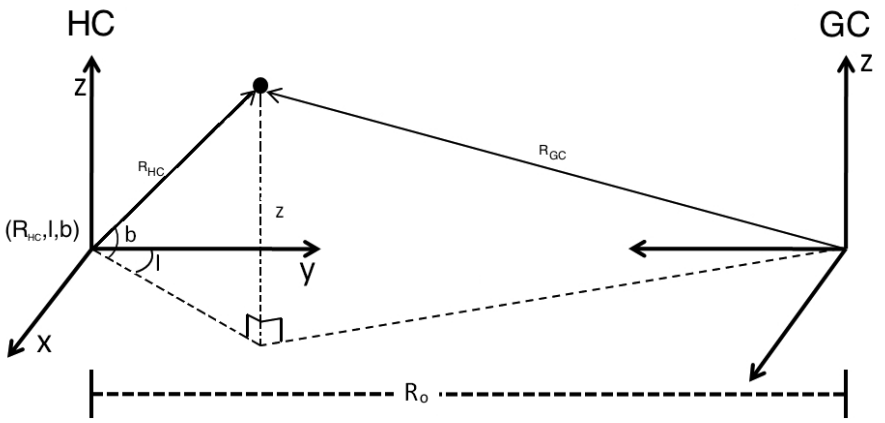

Figure 5.1: The relationship between the Sun-centered spherical coordinate system (left) defined by (r', l, b) and the galactocentric coordinate system (right) defined by (r, z).

dN/dE_γ is specific to the WIMP candidate being considered and depends on the WIMP mass as well as the specific annihilation channels and branching fractions. Details on the photon multiplicity be found in the literature [4, 5]).

The Galactic dark matter density distribution, as calculated in Chapter 3, is distributed axisymmetrically throughout the Galaxy, and the three-dimensional density profile is specified by two coordinates, the distance from the Galactic center R_{GC} and the height from the Galactic plane z (see Fig. 5.1). The integral in eq. 5.2 is taken along the line-of-sight from a point near the Galactic center to the Sun's position at R_0. Accordingly, we define the coordinate transformation between the galactocentric (GC) system defining the dark matter distribution and the heliocentric (HC) coordinate system used in the line-of-sight integration.

Consider the point (R_{HC}, l, b) in the HC coordinate system in Fig. 5.1, where l and b are the Galactic longitude and latitude respectively. The transformation to

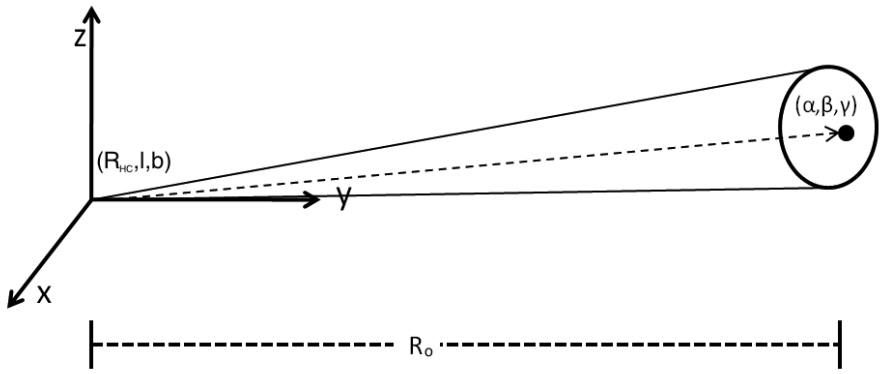

Figure 5.2: Illustration of the line of sight to a point near the Galactic Center. Note that the equation of a line from the Sun-centered coordinate system to a point (α, β, γ) is a parametric equation in one variable, t. The contribution from every point within the solid angle defining the Galactic center must be considered.

R_{GC} and z may be written as

$$R_{GC} = \sqrt{R_{HC}^2 + R_0^2 - 2R_0 R_{HC} \cos b \cos l} \tag{5.3}$$

$$z = R_{HC} \sin b. \tag{5.4}$$

The equation for a line in rectangular coordinates from the Sun $(0, 0, 0)$ to a point (α, β, γ) (see Fig. 5.2) near the Galactic center may be written parametrically as

$$\begin{aligned} x &= \alpha t \\ y &= \beta t \\ z &= \gamma t, \end{aligned} \tag{5.5}$$

where $0 \leq t \leq 1$ and converted into the parametric equations for the spherical HC

coordinate system:

$$\begin{aligned} R_{HC}\cos b\sin l &= \alpha t \\ R_{HC}\cos b\cos l &= \beta t \\ R_{HC}\sin b &= \gamma t. \end{aligned} \tag{5.6}$$

In GC coordinates, the parametric equation becomes

$$R_{GC}(t) = \sqrt{R_0^2 + (\alpha^2+\beta^2+\gamma^2)t^2 - 2R_0\beta t} \tag{5.7}$$

$$z(t) = \gamma t. \tag{5.8}$$

To complete the line-of-sight integral, the differential $dl = \sqrt{dr^2+dz^2}$ is first written in terms of dt:

$$dr = \frac{(\alpha^2+\beta^2+\gamma^2)t - \beta R_0}{\sqrt{R_0^2 - 2\beta R_0 t + (\alpha^2+\beta^2+\gamma^2)t^2}}dt \tag{5.9}$$

$$dz = \gamma dt. \tag{5.10}$$

Therefore,

$$\begin{aligned} dl &= \left(\frac{[(\alpha^2+\beta^2+\gamma^2)t - \beta R_0]^2}{R_0^2 - 2\beta R_0 t + (\alpha^2+\beta^2+\gamma^2)t^2} + \gamma^2\right)^{1/2} dt \\ &= C dt, \end{aligned} \tag{5.11}$$

where

$$C = \Big(\frac{[(\alpha^2+\beta^2+\gamma^2)t - \beta R_0]^2}{R_0^2 - 2\beta R_0 t + (\alpha^2+\beta^2+\gamma^2)t^2} + \gamma^2 \Big)^{1/2}.$$

The line-of-sight integral has therefore been transformed in the following way:

$$\int_{los} \rho(l) dl = \int_0^1 \rho(r(t), z(t)) C dt. \tag{5.12}$$

To find the total contribution from the Galactic center from decaying dark matter, the dark matter density function (or its square, for the case of annihilating dark matter) must also be integrated over the solid angle subtended by the Galactic center as illustrated in Fig. 5.2. The line-of-sight integral over and patch in the Galaxy is given by

$$\int_\Omega \rho(l) dl = \int_{l_{min}}^{l_{max}} \int_{b_{min}}^{bmax} \int_0^1 \rho_{DM}\big(r(t,l,b), z(t,l,b)\big) C \cos(b)\ dt\ dl\ db. \tag{5.13}$$

In Figs. 5.3-5.4 we show contour plots for the line-of-sight integrals per unit solid angle over the linear (left) and squared (right) dark matter density distributions for 7° in l and b around the Galactic center for two dark matter models from Table 3.2 in Chapter 3. The most striking difference among the figures is that for the $\Sigma_{d,\odot} = 55$ $M_\odot$ pc^{-2} disk model (Fig. 5.3), more dark matter is found at a larger radial extent than for the $\Sigma_{d,\odot} = 70$ $M_\odot$ pc^{-2} disk models (Fig. 5.4), meaning that the average radii of the oblate contours are larger in Figs. 5.3 than in Fig. 5.4. The wide range in the parameters of the dark matter models allowed from our previous analysis allow for a correspondingly wide range in the gamma-ray flux from annihilation or

decay of dark matter. The line-of-sight integrals per unit solid angle at the Galactic center $(l, b) = (0, 0)$ span $\sim 90 - 230$ GeV cm^{-3} kpc for decaying dark matter and $\sim 0.3 - 6.8 \times 10^4$ GeV^2 cm^{-6} kpc for annihilating dark matter.

The analysis done here is to demonstrate the method for calculating the flux of gamma rays from the Galactic center from dark matter annihilation or decay. The calculated integrals for the gamma-ray flux can only be compared to the observations from satellites such as FERMI [3] after assuming a beam size, integrating the flux over a solid angle, and assuming a form for the photon spectrum dN/dE_γ. In principle, this method could be used with the gamma-ray observations to further constrain the dark matter models calculated in Chapter 3. There is currently much debate as to whether or not dark matter should have a higher density (a cusp) at the center of the Galaxy as this feature appears in many numerical simulations. However, observations of dwarf spheroidal galaxies, whose dynamics are expected to be dominated by dark matter, show that the dark matter is expected to have a flat distribution near the center, similar to the density profiles calculated for the Milky Way in Chapter 3. A cuspy distribution would show an enhancement in the gamma-ray signal relative to what our dark matter models predict.

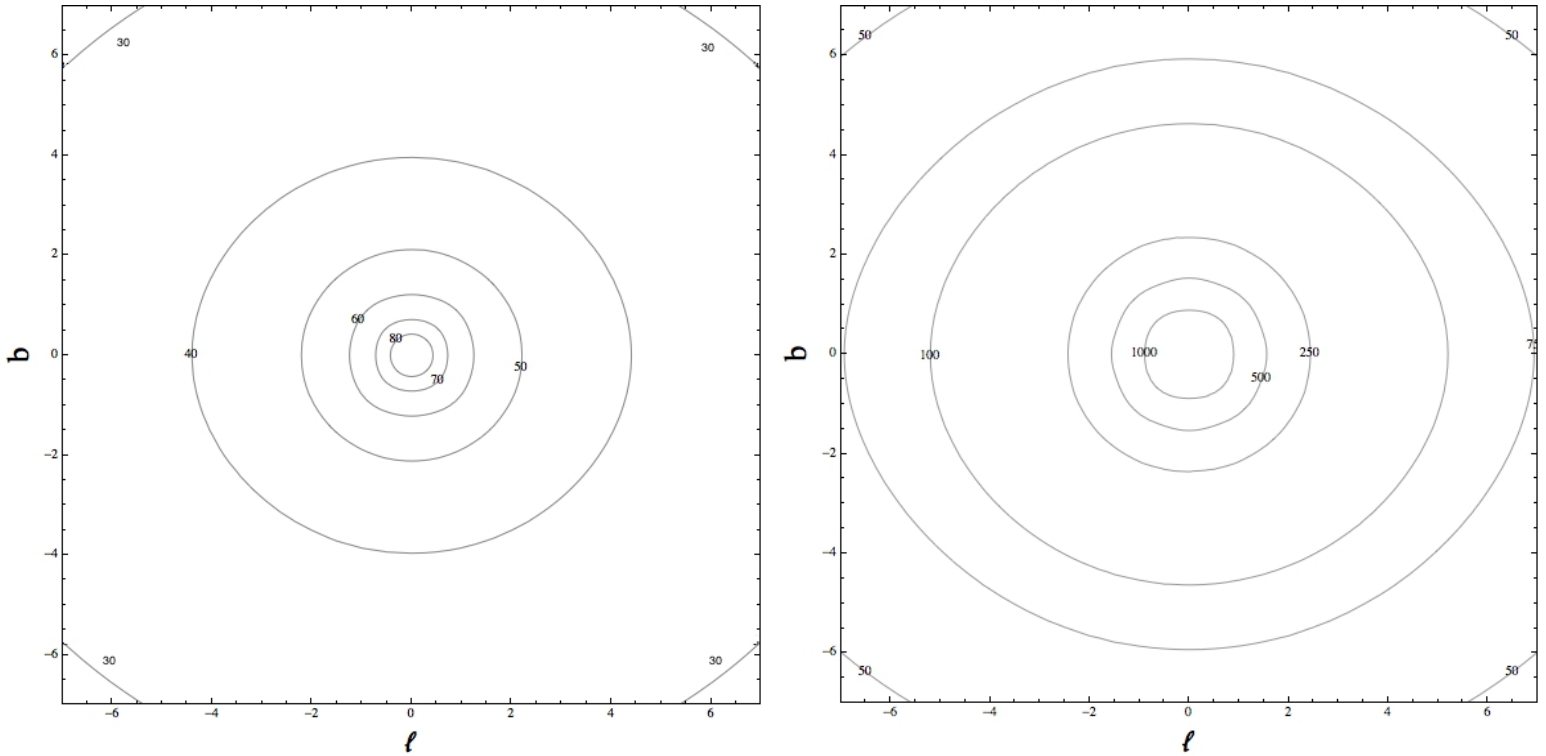

(a) $\int_{los} \rho_{DM} dl$ for decaying dark matter. The value at the Galactic center is ~ 90 GeV cm^{-3} kpc.

(b) $\int_{los} \rho_{DM}^2 dl$ for annihilating dark matter. The value at the Galactic center is $\sim 3.1 \times 10^3$ GeV^2 cm^{-6} kpc.

Figure 5.3: The line-of-sight integrals per unit solid angle over the linear (a) and squared (b) dark matter distribution, in units of GeV cm^{-3} kpc and GeV^2 cm^{-6} kpc respectively, for the 7° in l and b around the Galactic center are shown for the dark matter model $\rho_{DM0} = 100$ GeV cm^{-3} and $\sigma_{DM} = 220$ km s^{-1} for the $\Sigma_{d,\odot} = 55$ M$_\odot$ pc^{-2} disk.

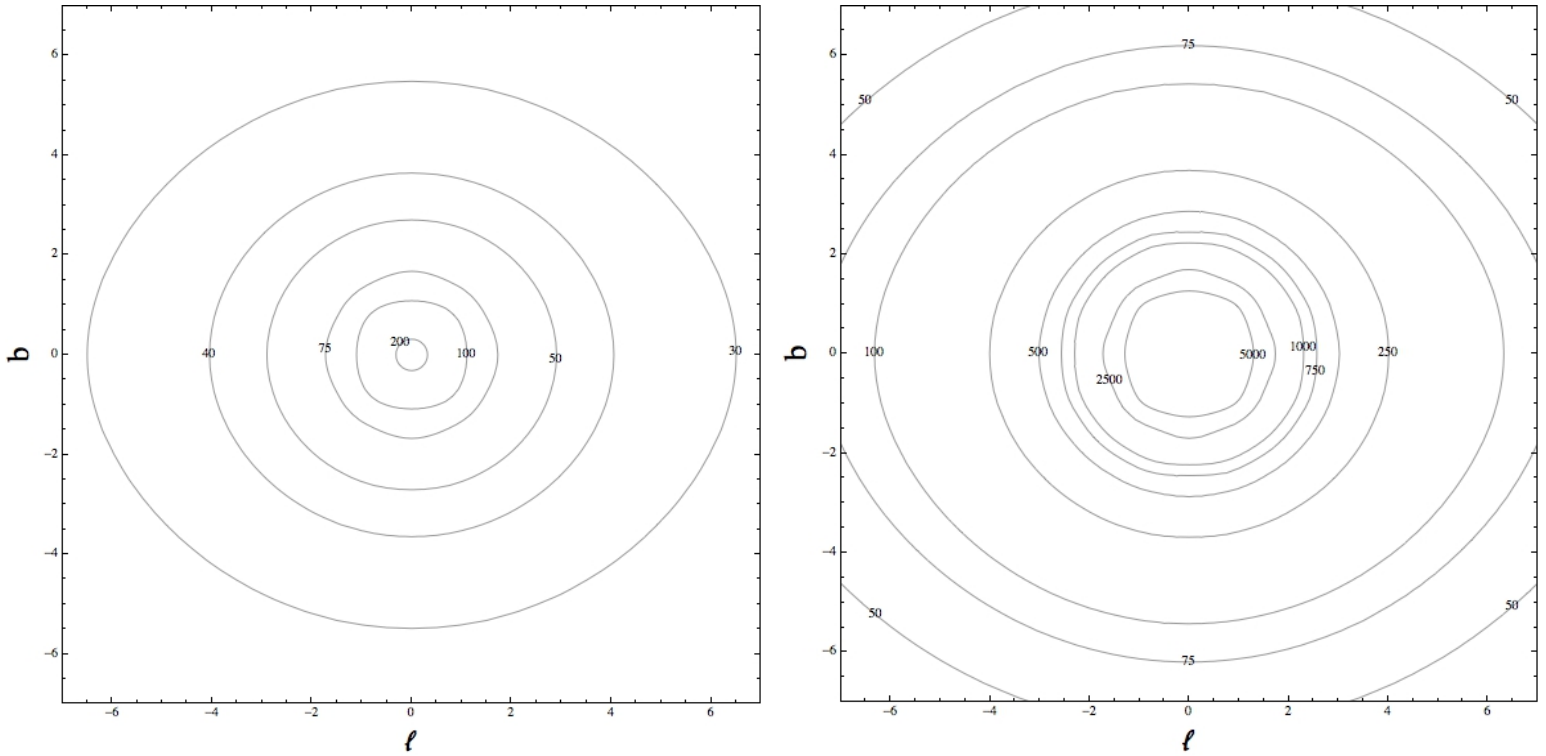

(a) $\int_{los} \rho_{DM} dl$ for decaying dark matter. The value at the Galactic center is ~ 230 GeV cm^{-3} kpc.

(b) $\int_{los} \rho_{DM}^2 dl$ for annihilating dark matter. The value at the Galactic center is $\sim 6.8 \times 10^4$ GeV^2 cm^{-6} kpc.

Figure 5.4: The line-of-sight integrals over the linear (a) and squared (b) dark matter distribution, in units of GeV cm^{-3} kpc and GeV^2 cm^{-6} kpc respectively, for the 7° in l and b around the Galactic center are shown for the dark matter model $\rho_{DM0} = 500$ GeV cm^{-3} and $\sigma_{DM} = 190$ km s^{-1} for the $\Sigma_{d,\odot} = 70$ M$_\odot$ pc^{-2} disk.

References

[1] Jungman, G., Kamionkowski, M. & Griest, K. 1996, Phys. Rep., 267, 195

[2] Bergstrom, L., Ullio, P., & Buckley, J. 1998, Astropart. Phys., 9, 137

[3] The FERMI-LAT Collaboration 2010, arXiv:1002.2280v1

[4] Fornengo, N., Pieri, L. & Scopel, S. 2004, PRD, 70, 103529

[5] Morselli, A., Cañadas, C. & Vitale, V. 2010, arXiv:1012.2292v1

Chapter 6

Conclusions and Prospects for Future Work

Discovering the true nature of dark matter is one of the central problems in astrophysics today. Studies range from extragalactic astronomy, where the dynamics of clusters of galaxies are analyzed to map the distribution of dark matter, to the studies at particle colliders, where signatures of dark matter are looked for in the high-energy collisions of particles. In this thesis, we have focused on the properties of dark matter within the Milky Way and found that much work is needed on all scales before the true nature of dark matter is discovered.

In Chapter 1, we reviewed the evidence for the existence and suspected properties of dark matter. Many lines of evidence including the rotation curves of galaxies, the cosmic microwave background, and gravitational lensing of galaxy clusters point to the existence of non-luminous, non-baryonic matter whose abundance in the universe is greater than that of baryonic matter by a factor of ~ 5. Several candidates,

including the supersymmetric neutralino, meet the criteria that this exotic matter is dark, cold, and agrees with constraints from Big Bang nucleosynthesis, stellar evolution, and structure formation in the universe. The efforts to detect the dark matter either directly from nuclear recoils produced by WIMP-nucleon collisions or indirectly from its annihilation or decay products may prove successful in the coming decades as the experiments become progressively more sensitive to the dark matter candidates predicted by theoretical extensions to the standard model.

Before we are able to fully understand the distribution of dark matter in our Galaxy, we must first know the distribution of visible matter. In Chapter 2, we extensively reviewed the observations and models for visible matter in the Milky Way. We then constructed an axisymmetric model for the Milky Way consisting of a spherical bulge and double-exponential disk that is consistent with current observations. This model can be refined and made more complex as observations of the Galaxy improve. Immediate improvements would involve including models for the stellar halo and the innermost parts of the Galaxy. There is much uncertainty in the mass and extent of the Galactic disk, and a more robust model of the Milky Way should take these uncertainties into account with better resolution than the three choices of surface densities and four choices of scale lengths used in our model.

In Chapter 3, we posited that the phase-space distribution of dark matter has a lowered isothermal form, and with the mass model of the Milky Way constructed in Chapter 2, we proceeded to self-consistently solve Poisson's equations to derive the density distribution of dark matter and the gravitational potential of both visible and dark matter. We repeated this procedure for numerous dark matter models

parameterized by the central dark matter density, the velocity dispersion, and the truncation radius of the distribution. The parameters of the models were determined by the requirement that the theoretical predictions fit the current observations of the rotation curve and the velocity distributions of blue horizontal-branch and blue straggler stars. It was found that even after these requirements, a wide range in the dark matter parameters was allowed.

To improve upon the analysis in Chapter 3, a Monte Carlo method could be developed to better sample the parameter space of the dark matter models. The present method involved choosing parameters by hand and while this method was able to sample the entirety of the parameter space allowed for the dark matter models, the parameter space could be studied with higher resolution. Additionally, if the mass model of the Milky Way were made more realistic by including the substructure in the Milky Way, the Legendre polynomial expansion for solving Poisson's equations would no longer apply, and a different, more complicated, method of solving Poisson's equation would need to be developed. In addition to improving upon the current methods, the assumption of a King distribution for dark matter could also be relaxed and a program could be developed which compares different assumptions for the phase-space distribution of Galactic dark matter.

In Chapter 4, we discussed the direct detection of dark matter. First, we reviewed the formalism for calculating direction-independent detection rates for spin-dependent and spin-independent WIMP-nucleon interactions. Then we considered dark matter with a King phase-space distribution and derived the distribution of speeds as would be seen in an Earthbound laboratory, including their angular distribution. We then

proceeded to develop a quasi-Monte Carlo method for deriving the spectral intensity and angular distribution of recoil energies from the scattering of WIMPs in a King distribution off of target nuclei in the laboratory rest frame. These spectra were computed for two of the dark matter models derived in Chapter 3 and displayed for a generic xenon detector. These calculations could be improved by considering a range of dark matter masses and detector materials. In principle, the expected event rates for each of the current generation of dark matter detectors could be calculated.

The implications of the dark matter models on the indirect detection of dark matter, specifically from gamma rays, was discussed in Chapter 5. There, we reviewed the formulae for the expected flux of gamma rays from the decay and annihilation of dark matter. Then we derived the coordinate transformation needed to compute the gamma-ray flux from the axisymmetric dark matter models from Chapter 3. We then showed the expected contribution to the gamma-ray flux at the Galactic center from the density distribution of dark matter for the same dark matter models used in Chapter 4. To compare the calculation with observations, a specific model for the dark matter particles must be assumed which defines the photon spectrum and the annihilation rate. Further study would include comparing our calculations to observational data for many dark matter candidates.

In Appendix A, we discussed the recent observations of the rising positron fraction and of the total electronic component of cosmic rays and found that using a nested-leaky box model to describe the propagation of positrons and electrons may obviate the need for a dark matter explanation for these observations. A nested leaky-box model is found to be consistent with the observations of the positron fraction, the

ratio of secondary to primary nuclei such as B/C, and the anisotropy. To fully develop this model, the predictions for other observations such as the ratio of antiprotons to protons must also be calculated and compared to observations.

In Appendix B, we reviewed bubble chamber dark matter detection experiments and discussed in detail the theory behind bubble chambers superheated in the standard way by a bellows system. We then discussed the theoretical developments in deriving the energy needed to nucleate bubbles in bubble chambers where the liquid is superheated by an acoustic field created by piezoelectric elements. The experimental setup for these ultrasonic bubble chambers is the same as that which produces sonoluminescence, and corresponding, we discussed in detail the parameter space and optical signals from a bubble undergoing sonoluminescence. Finally, we discussed the construction of an ultrasonic bubble chamber at Washington University for the detection of dark matter and the work that is still needed for its completion. In order to create a working bubble chamber, the filling and draining mechanism for the chamber must be improved. Once that is done, the chamber can be calibrated using water where sonoluminescence has been widely studied. To be able to detect dark matter, a heavy refrigerant such a Freon can be used. The response of the Freon-filled detector to radiation such as neutrons and alpha particles must first be characterized. Finally, to be sensitive to the small WIMP-nucleon cross sections expected for dark matter, an array of large ultrasonic bubble chamber can be installed in an underground lab, properly shielded from ambient radiation, and run for several years.

Appendices

Appendix A

Cosmic-Ray Propagation Models and The Electronic Component of Cosmic Rays [1]

Recently, many experiments including PAMELA [1], FERMI [2], HESS [3], ATIC [4], and AMS [5] have, with unprecedented accuracy, provided new observations of cosmic-ray electrons and positrons. It is possible that some of these particles are the products of dark matter annihilation or decay. However, it is imperative that the mechanisms of cosmic-ray generation and propagation be well understood before evoking such exotic phenomena. Here, the positron fraction measured by PAMELA and AMS, among others, is analyzed in terms of models of cosmic-ray propagation. We show

[1] This work closely follows R. Cowsik and B. Burch arXiv:0908.3494 with some extensions and has been published as: R. Cowsk and B. Burch, PRD, 82 (2010) 023009; R. Cowsik and B. Burch, arXiv:0906.2365, Proc. 31st ICRC, Łódź, Poland (2009); B. Burch and R. Cowsik, arXiv:1009.1361, Proc. ISVHECRI2010, Batavia, IL, USA (2010); R. Cowsik, B. Burch and T. Madziwa-Nussinov, arXiv:1305:1242, Submitted to PRL.

that, generally, the positron fraction is expected to reach ~ 0.7 at energies beyond $\sim$1 TeV and that the positron fraction is connected to other cosmic-ray observations such as the ratio of nuclear secondaries to primaries like B/C. The currently observed positron fraction can be fit in a model that assumes a significant fraction of the secondaries such as boron below ~ 10 GeV is generated through the spallation of the cosmic-ray primary nuclei in high density cocoon-like regions surrounding the sources such as molecular clouds. The positrons of an energy higher than a few GeV would be produced exclusively though interactions in the interstellar medium. This model, termed the nested leaky-box model, is also consistent with the bounds on cosmic-ray anisotropies and other observations. We also derive the spectral shape of the electrons and positrons expected from the annihilation of dark matter in the Galaxy and show that the spectral shape of the peak will provide important information regarding the mass of the dark matter and its spatial distribution.

A.1 Introduction

The electronic component of cosmic rays interacts with the microwave background, starlight, and magnetic fields in the Galaxy and is therefore useful in understanding the origins and propagation of cosmic rays throughout the Galaxy [6], both of which are still not well understood. Early models of the transport of the cosmic-ray electrons, described within the framework of a leaky-box model [7], considered a smooth distribution cosmic-ray sources in the Galaxy and a cosmic-ray residence time in the Galaxy that was independent of energy for $E \gg 1$ GeV. However, sub-

sequent observations of the ratio of secondary nuclei to their parent nuclei, such as B/C or (Sc+Ti+V)/Fe, showed a decrease with increasing energy beyond $\sim$ 1 GeV, indicating that the residence time of cosmic rays may also decrease with increasing energy. Consequently, if the propagation of cosmic rays followed the simple leaky-box model with a energy-dependent leakage time from the Galaxy, the anisotropy of cosmic rays would increase with energy and exceed experimental bounds at high energies (see Fig. A.3). To address this problem, the nested-leaky box model was developed, which considered the cosmic rays suffering interactions in cocoon-like regions around the cosmic-ray sources [8, 9]. In this model, the leakage time from the cocoon is taken to be energy-dependent, but the subsequent residence time of the cosmic ray in the general interstellar medium is taken to be independent of the energy. This reconciles the energy dependence of the ratio of secondary to primary nuclei with the high degree of isotropy in cosmic rays up to high energies. It is this nested-leaky box model that will be explored in this appendix.

Originally, the leaky-box model only considered a continuous distribution of cosmic ray sources. In order to discuss the electronic component of cosmic rays, Cowsik and Lee [10] also considered a discrete distribution of cosmic-ray sources within the context of a diffusion model. It was shown that cosmic-ray sources within a few hundred parsecs were needed in order to reproduce the cosmic-ray electron spectrum up to $\sim$1 TeV. In this model, the cosmic-ray sources were randomly distributed in a thin disk embedded in a thick disk signifying the diffusion region. To signify escape from the Galaxy, the density of cosmic rays was taken to vanish at the upper and lower boundaries of the thick disk. Nishimura and others [11, 12] later reiterated the need

for nearby sources of cosmic rays to explain the total electron spectrum at high energies. In this analysis, the diffusion volume is assumed to have an infinite thickness to avoid the complexities of intruding boundary conditions to the thick disk, and the effect of leakage from the Galaxy is modeled by a distributed loss term.

In this work, we use a Green's function simpler in form than that used by Cowsik and Lee [10] but also include the leakage of cosmic rays from the Galaxy by adding a leakage term similar to that in the leaky-box model. This model is found to reproduce the energy spectra from the cosmic-ray sources, and the Green's function integrates to the leaky-box model for a uniform distribution of sources surrounding the observation points. This model fits the ratio of the secondary to primary nuclei, the positron fraction, the upper bounds on the anisotropy, and the total electron spectrum. The full details of this model are available in the papers cited here [7, 8, 9], but in this work, only the details necessary to address the recent observations of the total electronic component of cosmic rays and the positron fraction are discussed.

The recent observations of cosmic-ray electrons and positrons can be divided into two categories, those that measure the total electronic component ($e^+ + e^-$) and those that measure the positron fraction $e^+/(e^+ + e^-)$. The FERMI, HESS, and ATIC collaborations have recently provided new measurements of the total electronic component while the PAMELA and AMS collaborations measured the positron fraction. Both sets of observations have caused significant excitement in the scientific community. The measurement of the spectrum of the total electronic component by the ATIC experiment showed a narrow excess around $\sim$ 600 GeV, agreeing with some earlier measurements (see Fig. A.1). The subsequent observations by the FERMI

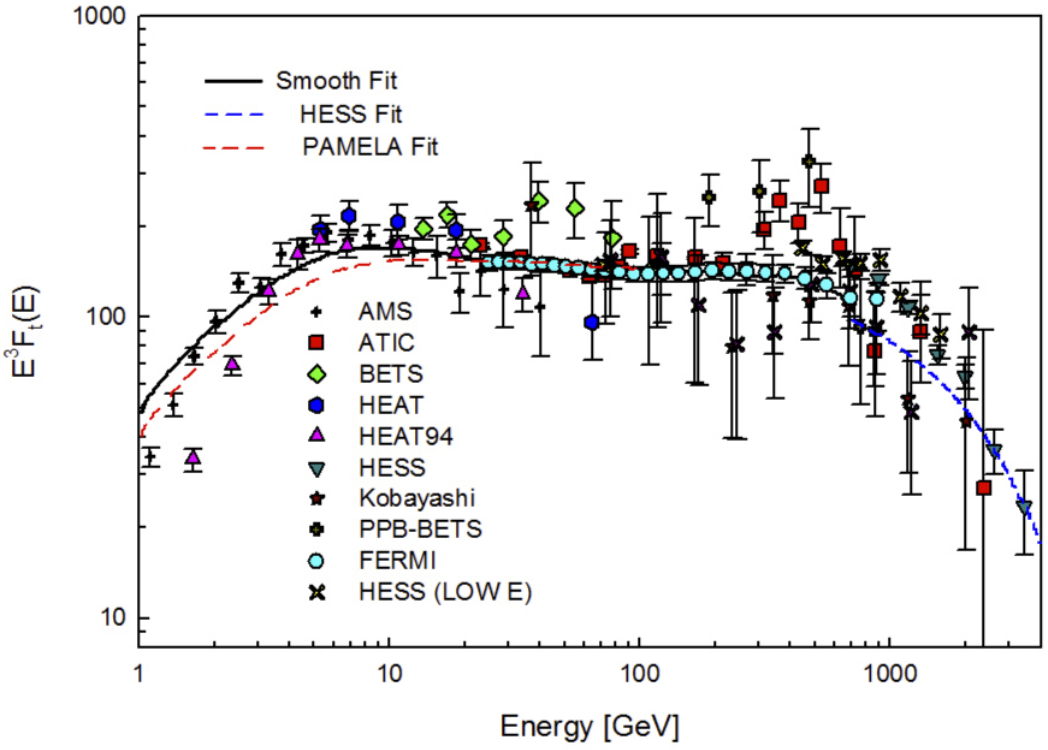

Figure A.1: The compilation of measurements of the total electron spectrum $F_t(E)$ is shown with the red dashed line representing the total spectrum of the electronic component calculated using the positron fraction measured by PAMELA. The blue dashed line is a fit to the HESS data, and the solid line is a smooth fit to the total electron spectrum.

experiment showed only a mild enhancement. The measurements of the positrons fraction by the PAMELA and AMS experiments show a monotonically increasing positron fraction beyond $\sim$ 7 GeV. These observations directly contradict the predictions of the standard model of cosmic-ray propagation developed by Moskalenko and Strong [13], which predicts a monotonic decrease at all energies. The theoretical expectation that the positron fraction should level off or gently decrease with energy is specific to the assumption that the ratio of secondary to primary nuclei, like B/C, will continue to decrease up to very high energies. From the available data (see Fig. A.2), the behavior of the ratio of secondary to primary nuclei beyond 30-40 GeV is

unclear.

In efforts to explain the positron fraction and the "bump" in the total electron spectrum observed by ATIC around 600 GeV, it was suggested that astrophysical objects such as a nearby gamma ray burst source [14], one or more pulsars [15, 16, 17, 18, 19, 20], or a few nearby supernova remnants [21, 22, 23] may be the cause of the "anomaly". Many studies focused on finding a dark matter explanation for these observations. Supersymmetric dark matter such as the neutralino may explain the excess in the observed total electron spectrum, but there may be a need for excessive clumping or an exceedingly local source [24, 25]. This clumping can be avoided if one considers Kaluza-Klein dark matter [26]. An interesting dark matter explanation comes from the introduction of new force carriers [27] which allows for a Somerfeld enhancement and boosts the annihilation rate to leptons. The new particles may even be able to explain the annual modulation of the signal seen in the DAMA experiment [28]. A kinematic cutoff in the positron spectrum at $E \sim (1/2 - 1/4)M_\chi$, where M_χ is the dark matter mass, is generally viewed as an indication for dark matter. We refer the reader to [19] and [29] for more extensive reviews of the proposed solutions to these cosmic ray "anomalies".

In this appendix, we aim to show that that: 1) the increase in the positron fraction beyond ~ 6 GeV is not anomalous, and in fact, it is expected to have an asymptotic value of $\sim 0.6 - 0.7$ at very high energies; 2) the rise in the positron fraction can be explained entirely by cosmic-ray secondaries if positrons have a residence time of 1-2 Myr in the general interstellar medium; 3) if a fraction of the boron-to-carbon ratio below ~ 10 GeV is generated in a dense cocoon-like region surrounding the soures,

then the contribution from spallation in this general interstellar medium would have a flat or weak energy dependence; 4) this model, which takes into account spallation reactions in the cocoon fits both PAMELA and AMS data and is also consistent with the high degree of isotropy seen in cosmic rays at high energies; and 5) the spectral shape of the narrow enhancement of the total electron spectrum by the as seen by the ATIC experiment provides information regarding both the mass and spatial distribution of dark matter particles. We begin in Section A.2 with a brief review of cosmic-ray propagation models, and in Section A.3, we discuss the observations of the positron fraction. In Section A.4, the secondary positron and electron spectra predicted from our propagation model is subtracted from the observations of the total electronic spectrum of cosmic rays to obtain the spectrum of primary electrons due to input from the discrete cosmic ray sources in the Galaxy. Then, in Section A.5, the "bump" in the total electron spectrum is addressed by considering a δ-function input spectrum and the spectrum expected from shock acceleration. In Section A.6, the the main results of this section are discussed.

A.2 The Propagation of Cosmic Rays

The current view of cosmic-ray propagation is that cosmic rays are produced and accelerated in discrete sources distributed throughout the Galaxy. The cosmic rays travel from these sources in random directions and interact with matter surrounding the sources, the interstellar medium, radiation, and magnetic fields before leaking from the Galaxy. Any charged secondary particles produced in these interactions,

such as electrons or positrons, will be confined by the interstellar magnetic fields and will also follow random trajectories similar to the parent particles before leaking from the Galaxy.

Models of cosmic-ray propagation are typically characterized by the *vacuum path length distribution* [7], which describes the probability $P(t)$ that the cosmic rays will spend time in a given region, such as a high-density area surrounding the source or the general interstellar medium before escaping from the Galaxy. The term *vacuum* signifies that the probability $P(t)$ assumes the cosmic rays do not undergo any subsequent interactions or lose energy during propagation since these effects are included later in a consistent way.

Here, we will focus on two classes of cosmic-ray propagation models developed to explain the observations of the ratios of secondary to primary nuclei. In leaky-box models (which are an approximation of the most widely used models of cosmic-ray propagation [13, 30]), the production of secondary particles is distributed throughout the Galaxy. In the nested leaky-box model, most secondary production takes place in a cocoon-like region surrounding the cosmic ray sources. These two models make significantly different predictions regarding the ratios of primary to secondary cosmic rays as well as for the behavior of the positron fraction and anisotropy.

A.2.1 The Leaky-Box Model

Originally [7], the probability $P(t)$ was assumed to be a simple exponential function

$$P(t) = e^{-t/\tau}, \tag{A.1}$$

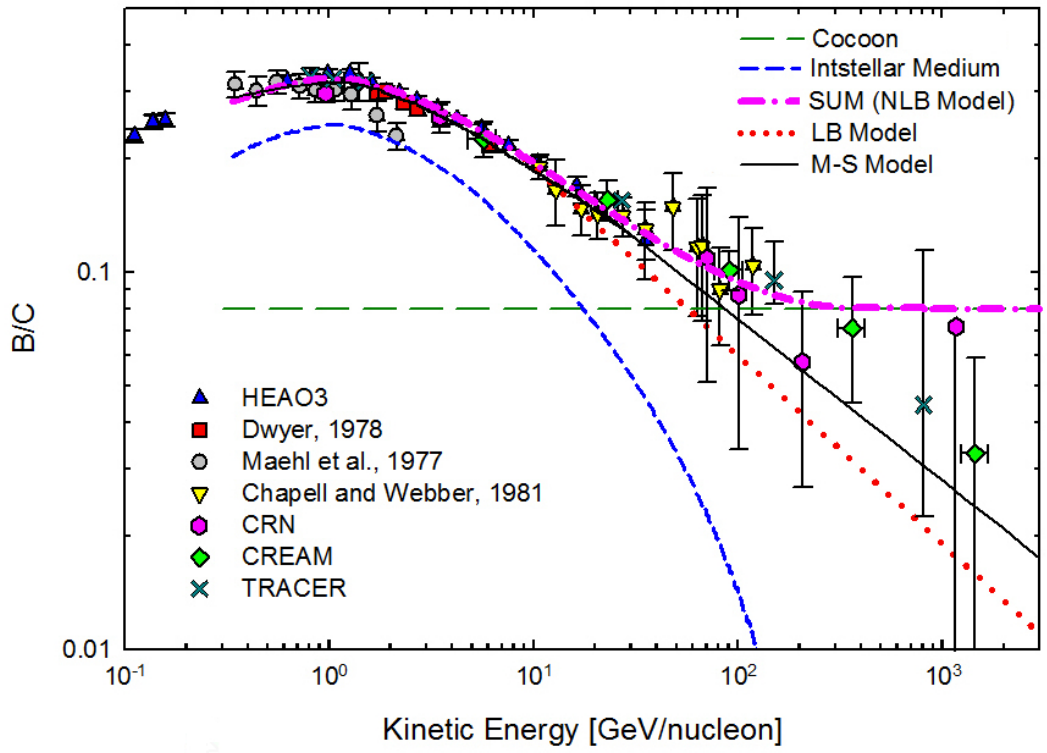

Figure A.2: The observed B/C ratio is plotted along with the spectra expected from the M-S model and nested leaky-box model. The B/C data is taken from HEAO3 [34], Dwyer [35], Maehl et al. [36], Chapell and Webber [37], as well as the Tracer [38], CRN [39] and CREAM [40] experiments.

where τ is the escape lifetime of the cosmic rays and based on the available observational data was assumed to be independent of energy beyond $\sim 1-2$ GeV. Subsequent observations of the ratio of the fluxes of secondary nuclei to primary nuclei showed that it decreases as a function of energy from $\sim 1-200$ GeV and possibly beyond. Accordingly, the escape lifetime τ was then considered to also decrease with increasing energy. The precise behavior of the secondary to primary ratios is currently uncertain beyond ~100-200 GeV where the statistical significance of the observations is low, or observations are non-existent.

Currently, most conventional models of cosmic-ray propagation, such as that by Moskalenko and Strong (M-S)[13, 30], assume production of cosmic-ray secondaries

occurs throughout the Galaxy during the transport of cosmic rays from the source, and the decrease in the secondary to primary ratio of cosmic rays is explained by an residence time τ_{LB} that decreases with increasing energy. Beyond a few GeV/nucleon, the residence time can be parameterized by

$$\tau_{LB} \sim \tau_{LB,0}(E)^{-\Delta}, \tag{A.2}$$

where $\tau_{LB,0} = 0.4$ in units of T_0 and $\Delta \approx 0.5$ to represent the range of $0.33 \leq \Delta \leq 0.7$ discussed for M-S models in the literature.

To compute the B/C ratio at $E \gg 1$ GeV/nucleon, where the loss of energy due to ionization may be neglected, we write the rate that carbon is injected into the Galaxy per unit volume per unit energy interval per unit time as

$$S_{LB,C}(E) = K_C E^{-\beta_C}. \tag{A.3}$$

Assuming loss of carbon from the Galaxy is dominated by leakage, the equilibrium spectrum in the interstellar medium is given by

$$\begin{aligned} F_{LB,C}(E) &\approx S_{LB,C}(E)\frac{\tau_{LB}\tau_{spallation}}{\tau_{LB}+\tau_{spallation}} \\ &\approx S_{LB,C}(E)\tau_{LB} \\ &\approx K_C\tau_{LB,0}E^{-\beta_C+\Delta} \\ &\approx I_C E^{-\Gamma_C}. \end{aligned} \tag{A.4}$$

Since our focus is on the spectral forms, we have approximated

$$\frac{\tau_{LB}\tau_{spallation}}{\tau_{LB}+\tau_{spallation}} \approx \tau_{LB}$$

because $\tau_{spallation} \gg \tau_{LB}$. To match the observed spectrum of carbon nuclei, where $\Gamma_C \approx 2.65$,

$$\beta_C = \Gamma_C - \Delta \approx 2.15.$$

Secondary nuclei such as boron are generated with the same energy per nucleon as the primary nuclei (carbon in this case) at a rate given by

$$S_{LB,B}(E) = cN_H\sigma_{B,C}(E)F_{LB,C}(E), \tag{A.5}$$

where c is the speed of light, N_H is the density of target nuclei in interstellar space, and the boron production cross section $\sigma_{B,C}(E)$ is taken to be nearly independent of energy. Equation A.5 can then be rewritten as

$$S_{LB,B}(E) = K_B E^{-\Gamma_C}, \tag{A.6}$$

where

$$K_B = cN_H\sigma_{B,C}K_C\tau_{LB,0} = cN_H\sigma_{B,C}I_C.$$

The equilibrium spectrum for boron is then given by

$$\begin{aligned} F_{LB,B}(E) &= S_{LB,B}(E)\tau_{LB,0}E^{-\Delta} \\ &= K_B\tau_{LB,0}E^{-(\Gamma_C+\Delta)} \\ &= cN_H\sigma_{B,C}K_C\tau_{LB,0}^2E^{-(\beta_C+2\Delta)}, \end{aligned} \tag{A.7}$$

where we have neglected the spallation of Boron and assumed that its loss is dominated by leakage from the Galaxy. The ratio of the secondary to primary spectra is then just

$$\frac{F_{LB,B}}{F_{LB,C}} = cN_H\sigma B, C\tau_{LB,0}E^{-\Delta}, \tag{A.8}$$

which shows that for the leaky-box (and M-S) model, the B/C ratio follows the energy dependence of the leakage lifetime.

An extrapolation of leaky-box model and of the M-S model to high energies for the B/C ratio is shown in Fig. A.2 as a dotted line and a solid black line respectively, indicating that the M-S model can be well-approximated in its spectral shape by a leaky-box model. It is currently unclear whether the B/C data or the (Sc+Ti+V)/Fe data [41] support the leaky-box and M-S models.

A.2.2 The Nested Leaky-Box Model

An alternative to the leaky-box and M-S models is the nested leaky-box model [8, 9] where it is assumed that prior to injection into the general interstellar medium, cosmic rays reside in a high-density region surrounding the source, interacting with matter

and generating secondaries, mostly at low energies. The leakage lifetime inside the cocoon-like region surrounding the source, τ_c, is assumed to be energy dependent, decreasing with increasing energy. Once the cosmic rays escape into the interstellar medium, their leakage time from the Galaxy τ_G is assumed to be energy independent up to several hundred TeV. The boron nuclei seen in Galactic cosmic rays is equal to the sum of their production in the cocoon and in the interstellar medium. These residence times can be parameterized as

$$\begin{aligned} \tau_c(E) &\sim \tau_{c,0} E^{\epsilon - \delta \log E} \\ \tau_G &\sim \text{constant} \\ \tau_{NLB} &= \tau_c(E) + \tau_G, \end{aligned} \tag{A.9}$$

where $\tau_{c,0} \approx 0.24$, $\epsilon = -0.01$, $\delta = 0.13$, and $\tau_G \approx 0.08$. Following the procedure for deriving the spectral forms for B and C in A.2.1, the B/C ratio for the nested leaky-box can also be calculated.

Let the rate at which cosmic-ray sources inject primary nuclei such as C into a cocoon surrounding the source be given by

$$s_{NLB,C}(E) = q_C E^{-\alpha_C}. \tag{A.10}$$

The equilibrium spectrum inside the cocoon is then

$$f_{NLB,C}(E) = s_{NLB,C}(E)\tau_c(E) = q_C E^{-\alpha_C}\tau_c(E). \tag{A.11}$$

Since the nuclear component leaks out of the cocoon with a rate inversely proportional to the residence time τ_c, each source injects cosmic-ray nuclei into the interstellar medium at a rate given by

$$\frac{f_{NLB,C}(E)}{\tau_c(E)} = s_{NLB,C}(E), \tag{A.12}$$

the same rate at which cosmic rays are injected into the cocoon. If the spatial number density of the cosmic-ray sources is given by ν, then the injection rate per unit volume may be written as

$$S_{NLB,C}(E) = \nu q_C E^{-\alpha_C}. \tag{A.13}$$

Note that q_C should decrease slightly due to interaction with material inside the cocoon (details can be found in Cowsik and Wilson [8, 9]). Here, since we are mostly interested in the spectral form for the B/C ratio, q_C has been kept unchanged. Also note that the spectral index α_C for the injection of nuclei into the interstellar medium is identical to that for the injection of nuclei from the sources into the cocoons surrounding the sources. The equilibrium spectrum of primary nuclei in the interstellar medium can then be written as

$$F_{NLB,P}(E) = S_{NLB,C}(E)\tau_G = \nu q_C \tau_G E^{-\alpha_C} \equiv I_C E^{-\Gamma_C}, \quad \text{i.e } \alpha_C = \Gamma_C. \tag{A.14}$$

The source function for the secondary nuclei generated in the cocoon by spallation

of the primary nuclei is then given by

$$s_{NLB,B}(E) = cN_H\sigma_{B,C}f_{NLB,C}(E) = cn_H\sigma_{B,C}q_C\tau_c(E)E^{-\alpha_C}. \quad (A.15)$$

The equilibrium spectrum for the secondary nuclei inside the cocoon is then

$$f_{NLB,B}(E) = s_{NLB,B}(E)\tau_c = cn_H\sigma_{B,C}q_C\tau_c^2(E)E^{-\alpha_C}. \quad (A.16)$$

As before, the injection rate per unit volume into the interstellar medium is inversely proportional to the residence time and for the secondary nuclei can be written as

$$S_{NLB,S1}(E) = \frac{\nu f_{NLB,B}(E)}{\tau_c(E)} = cn_H\sigma_{B,C}\nu q_C\tau_c(E)E^{-\alpha_c}. \quad (A.17)$$

In addition to the secondaries produced from spallation within the cocoons surrounding the sources, secondary nuclei are also produced in the collision of primaries with interstellar matter at a rate given by

$$S_{NLB,S2}(E) = cN_H\sigma_{B,C}F_{NLB,P}(E) = cN_H\sigma_{B,C}\nu q_C\tau_G E^{-\alpha_c}. \quad (A.18)$$

The total equilibrium spectrum for the secondaries is the sum of these two spectra

$$\begin{aligned} F_{NLB,B} &= [S_{NLB,S1}(E) + S_{NLB,S2}(E)]\tau_G \\ &= c\sigma_{B,C}q_C\nu\tau_G[n_H\tau_c(E) + N_H\tau_G]E^{-\Gamma_C}. \end{aligned} \quad (A.19)$$

Figure A.2 shows the B/C ratio produced inside the cocoon and in the interstellar medium separately where $[n_H\tau_c(E) + N_H\tau_G]$ is chosen to normalize the ratio of the nested leaky-box equilibrium spectra to the data of B/C ratio. The chain-dotted line in Fig. A.2 shows the total B/C ratio expected from the nested leaky-box model. The main difference between the ratios in the spectra of primary to secondary nuclei in the leaky-box and nested leaky-box models is in the constant ratio at high energies for the nested leaky-box model compared to the monotonically decreasing ratio for the leaky-box and M-S models.

A.2.3 Anisotropy

Even though, to date, both the leaky-box and nested leaky-box models provide adequate fits to the nuclear secondary to primary ratios, they require drastically different spectral forms for the injection spectrum of cosmic rays — $E^{-2.1}$ for the leaky-box model and $E^{-2.65}$ for the nested leaky-box model. The leaky-box (and M-S) model has a residence time that decreases with increasing energy, which corresponds to cosmic-ray anisotropies that increase with energy (see Fig. A.3), which does not agree with the available observations [30, 31, 32, 33]. The nested leaky-box, in contrast, due to its constant residence time in the interstellar medium, predicts a constant anisotropy up to several hundred TeV, consistent with the observations. To see this, we can rescale the predictions for the anisotropy in the M-S model [30] to conform to the nested leaky-box model. The anisotropy $\delta(E)$ is inversely proportional to the resi-

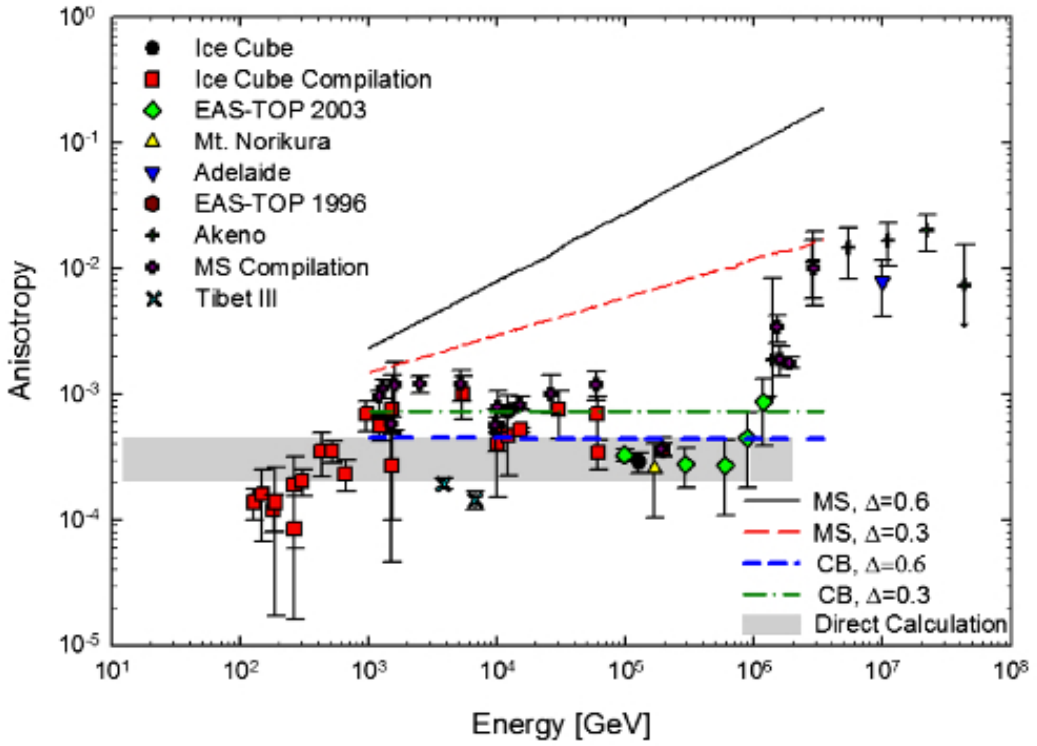

Figure A.3: Measurements of the cosmic-ray anisotropy from various compilations [30, 31, 32, 33]. Also plotted are the predictions from models in Moskalenko and Strong (MS) [30] and the results from eq. A.20, which are labeled as CB. The gray region shows the predicted anisotropy from eq. A.21.

dence time. We can therefore write the nested leaky-box anisotropy as

$$\delta_{NLB}(E) = \frac{\tau_{LB}(E)}{\tau_G}\delta_{M-S}(E) \approx \left(\frac{100\text{ GeV}}{E}\right)^{\Delta}\delta_{M-S}(\Delta, E), \tag{A.20}$$

where $\delta_{M-S}(\Delta, E)$ is the anisotropy in the M-S model calculated for $\Delta \approx 0.3$ and $\Delta \approx 0.6$ [30] and the 100 GeV is where the leaky-box and nested leaky-box residence times intersect. Figure A.3 shows that after this rescaling, the expected anisotropy becomes consistent with the observations.

The anisotropy can also be directly estimated [30]

$$\delta_{NLB} = \frac{3\kappa\nabla\rho}{c\rho} \approx \frac{3\kappa}{h_0 c} \approx 3 \times 10^{-4}, \tag{A.21}$$

where $h_0 \approx 1$ kpc is the scale height of cosmic rays in the Galactic plane and $\kappa \approx 10^{28}$ cm s^{-2} is the diffusion constant. In Fig. A.3 this direct calculation is shown as a grey band with an uncertainty of 200%. This estimate matches the form of the rescaled M-S predictions. Above ~ 1 PeV, particles escape the Galaxy with increasing rapidity causing an increase in the anisotropy. Along with the difference in predictions of the anisotropy, the leaky-box and nested leaky-box models also show a difference in predictions in the spectra of secondary electrons and positrons.

A.2.4 Secondary Electrons and Positrons

Electrons and positrons generated by cosmic-ray nucleons occurs through the production of mesons, mostly pions, which then decay into muons, which in turn decay

into electrons or positrons and transfer, on average, a fraction of the energy (about 5%) per nucleon of the primary. This is very different from the production of secondary nuclei, which, as stated above, carry away almost the same energy per nucleon as the parent nucleus. This difference in production leads to the source spectra for secondary positrons and electrons being nearly identical for both the leaky-box and nested leaky-box models, with both being proportional to $E^{-\Gamma_n}$. To see this, recall that the rate of generation of secondary positrons and electrons is proportional to the collision rate and the flux density of the nucleonic component at $E_n \approx E/0.05 \approx 20E$. Then, in both models, the production rate of positrons S_{n+} and electrons S_{n-} in the interstellar medium is given by

$$S_{n\pm} \propto f_n(20E) \sim E^{-\Gamma_n}, \tag{A.22}$$

where $f_n(E)$ is the equilibrium spectrum for a parent nucleus n.

For the nested leaky-box model, there is also a contribution from the secondary electrons and positrons produced in the cocoon surrounding the sources, which is given by

$$S_{n\pm c} \propto f_n(20E) \sim q_n E^{-\alpha_n} \tau_c(20E) \to 0 \quad \text{for } E \gg 1 \text{ GeV}. \tag{A.23}$$

In eq. A.23, f_n is defined by eq. A.11, and we note that $\tau_c(20E)$ becomes very small compared to τ_G after ~ 1 GeV. Therefore, the source spectra for secondary positrons and electrons are essentially the same for the leaky-box model and the nested leaky-box model beyond ~ 1 GeV.

On the other hand, the equilibrium spectrum for secondary positrons and electrons

are different. For energies less than $\sim$ 100 GeV, where energy losses due to inverse Compton scattering and synchrotron radiation can be neglected, the leaky-box and nested leaky-box positron equilibrium spectra are given by

$$F_{n+,LB} \sim S_{n+}(E)\tau_{LB}(E) \sim \tau_{LB,0}E^{-(\Gamma_n+\Delta)} \quad \text{for all } E \tag{A.24}$$

$$F_{n+,NLB} \sim S_{n+}(E)\tau_G \sim E^{-\Gamma_n} \quad \text{for } E > 1 \text{ GeV}. \tag{A.25}$$

The spectrum for secondaries for the nested leaky-box model is derived more explicitly in section A.4.

The equilibrium spectrum for electrons is similar to that for positrons, except that because of the dominance of protons in cosmic rays, the production rate of electrons is lower than that of positrons by

$$\frac{S_{n-}(E)}{S_{n+}(E)} = \eta. \tag{A.26}$$

The ratio η can be estimated from the characteristics of high energy interactions to be $\sim$ 0.5 [13]. However, direct observations of the ratio μ^-/μ^+ indicates $\eta \sim 0.8$ [42]. In both cases, η is expected to be energy-independent beyond a few GeV. Understanding the difference in the secondary equilibrium spectra for electrons and positrons is necessary for understanding the positron fraction.

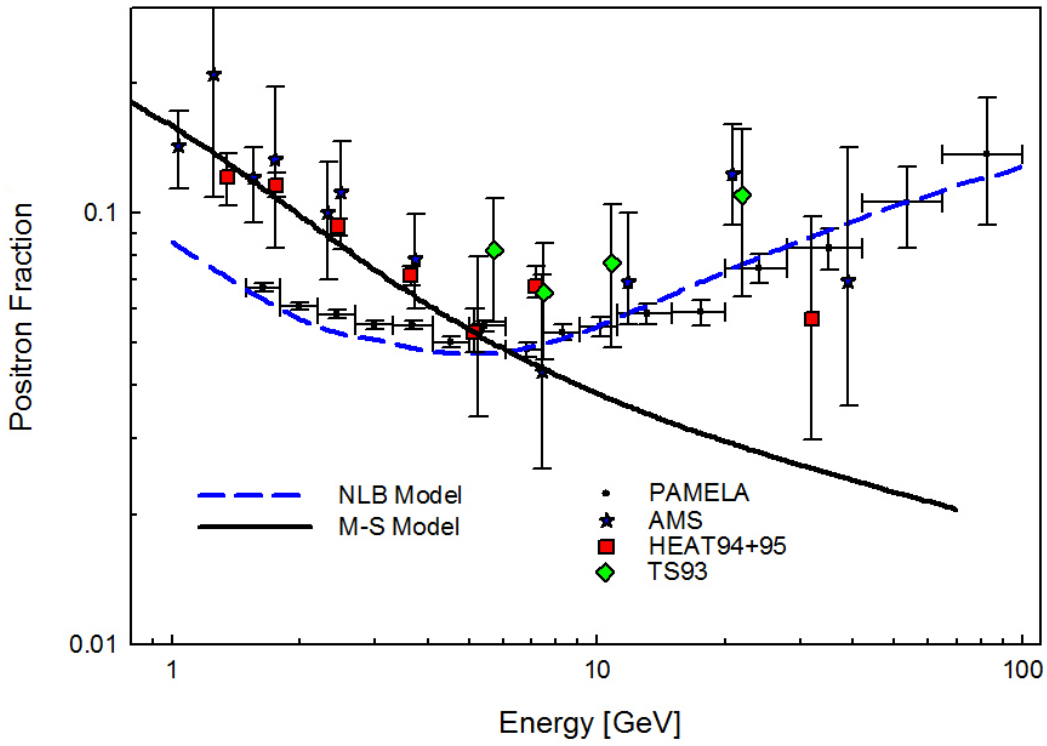

Figure A.4: The positron fraction measured by PAMELA along with the earlier measurements are shown. The effects of gradient drifts in solar modulation may account for some of the difference in the data sets at $E < 10$ GeV [1]. The energy dependence of the positron fraction expected in the M-S model [30] is shown as a solid line and in the nested leaky-box model as a dashed line.

A.3 The Positron Fraction

The positron fraction $R(E)$ is the ratio of the equilibrium spectrum of positrons to the combined spectrum of positrons and electrons and may be written as

$$R(E) = \frac{F_{n+}(E)}{F_{n+}(E) + F_{n-}(E) + F_{e^-}(E)}, \tag{A.27}$$

where $F_{e^-}(E)$ is the spectrum of primary electrons directly accelerated from the sources, and $F_{n+}(E)+F_{n-}(E)$ are the secondary positron and electron spectra defined above. Note that the positrons are secondary particles only and therefore there is no

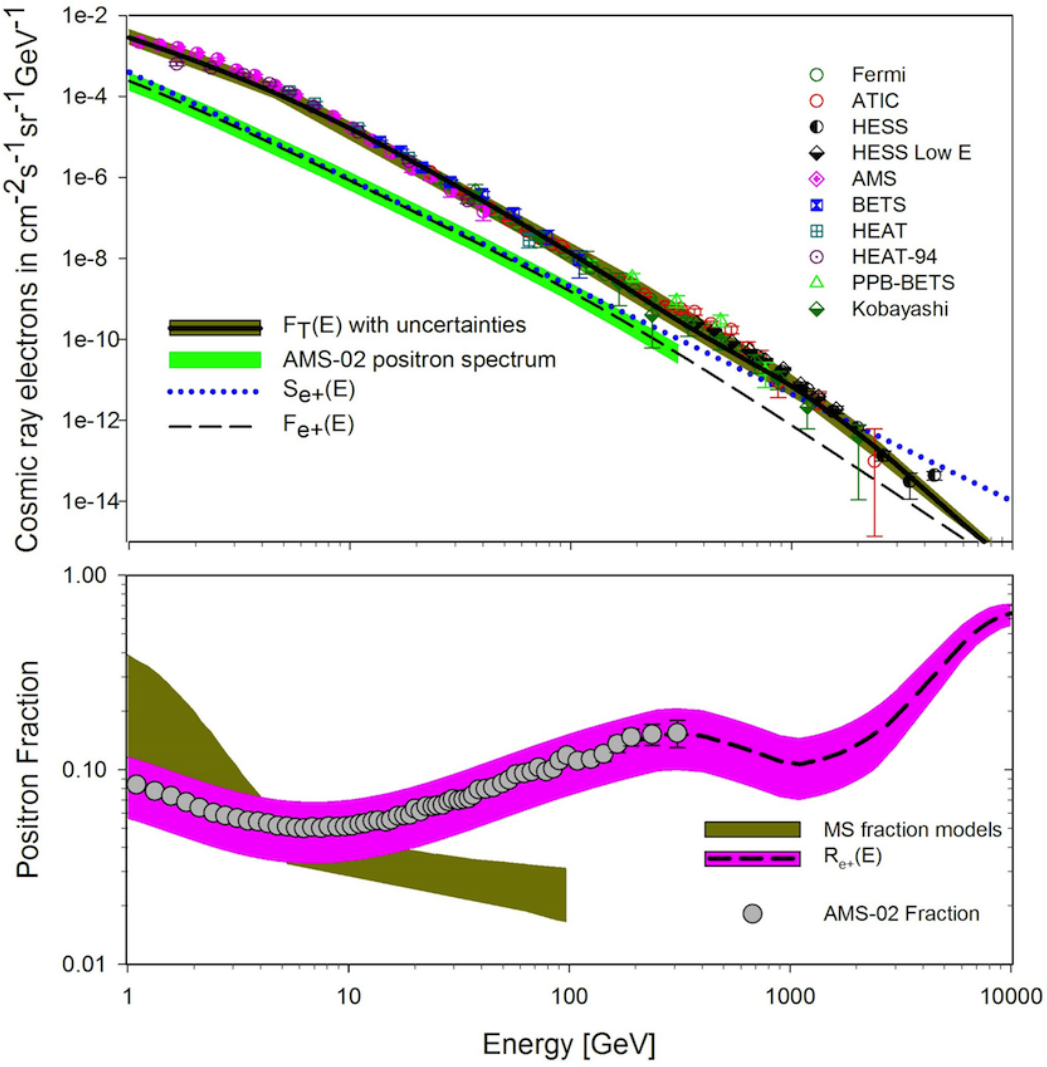

Figure A.5: Upper panel: The solid black line represents our fit, $F_t(E)$, to the spectrum of the total electronic component observed in cosmic rays, the dotted line shows the source function $S_{e^+}(E)$, with $n_H = 1$ cm^{-3} and $\tau_G = 1$ Myr, which fortuitously lies very close to the data points representing the observed positron spectrum F_{AMS} obtained by multiplying AMS-02 data on positron fraction by $F_t(E)$. The dashed line represents $F_{e^+}(E)$ the theoretical equilibrium spectrum with $S_{e^+}(E)$ as the source function, including propagation effects during a residence time $\tau = 2$ Myr and $n_H = 0.5$ cm^{-3}. Lower panel: Our predicted positron fraction, $R_{e+}(E) = F_{e+}/F_T$, with uncertainties is shown; the shaded steeply falling region is due to MS models [13].

primary positron source function. In order to work with the positron fraction, we write its inverse $P(E)$ such that

$$P(E) = \frac{1}{R(E)} = [P(E) - (1 + \eta)]F_{n+(E)}. \tag{A.28}$$

In Fig. A.6, the net secondary spectrum $F_{n\pm}(E) = (1 + \eta)F_{n+}(E)$ is shown for the nested leaky-box model along with the spectrum of primary electrons F_{e^-} obtained by subtracting $F_{n\pm}(E)$ at the corresponding energy from each data point in the total electronic spectrum shown in Fig. A.1. The positron fraction may be calculated by dividing the functional form of $F_{n+}(E)$ for the leaky-box or nested leaky box model by a smooth fit to $F_t(E)$ (see Fig. A.1). The result for the nested leaky-box model is the rising positron fraction seen as a dashed line in Fig. A.4. The leaky-box model and the M-S model predict a monotonically falling positron fraction (the solid line in Fig. A.4). Note as we are only interested in the functional form of the positron fraction at present, its normalization has not been explicitly calculated, but instead has been normalized to fit the PAMELA data. The normalization can, in principle, be explicitly calculated from the density of matter through which the cosmic rays have traversed, the spectral flux of the nuclear component, the cross section for meson production, kinematics of meson decay, and other factors. In these calculations, the effects of radiative energy losses at high energies have been included, as shown in section A.4.

When comparing the nested leaky-box model with the leaky-box model and the M-S model, the leaky-box/M-S class of models are a poor fit to the PAMELA data,

while the nested leaky-box has a functional form consistent with the observations. A similar analysis has also been done for the new AMS data [44] (see Fig. A.5), and again, the nested leaky-box provides an adequate fit to the newest observations.

The behavior of the positron fraction at high energies, beyond a few TeV, can be derived from considerations of the form of the primary electron spectrum generated by the cosmic-ray sources, $F_{e^+,i}(E)$, where the index i corresponds to the discrete cosmic-ray sources. The discrete nature of the sources impacts the form of the electron spectrum from each source [10, 11]. There is a minimum propagation time for the bulk of the cosmic rays to arrive at the Earth from the discrete sources. This results in a sharp cutoff in the $F_{e^+,i}(E)$ spectrum at high energies due to radiative losses [45]. However, since the high-energy particles are produced mostly in the interstellar medium, the source function for the secondary electrons and positrons is distributed smoothly in space resulting in a simple steepening of the spectrum at high energies to $\sim E^{-(\beta+1)}$. Therefore, at the highest energies, the equilibrium spectra of the secondaries will dominate over that of the primary electrons, such that

$$R(E \gtrsim 5 \text{ TeV}) \sim \frac{f_{n+}(E)}{f_{n+}(E) + f_{n-}(E)} = \frac{1}{1+\eta} \approx 0.6 - 0.7. \tag{A.29}$$

Thus, the positron fraction is expected to increase at high energies and to level off at $\sim 0.6-0.7$. This value comes from the ratio of protons to neutrons in cosmic rays and the nature of nuclear interactions at high energies. In the next section, by deriving an explicit form for the primary electron spectrum, we show that the positron fraction reaches this asymptotic value beyond several TeV.

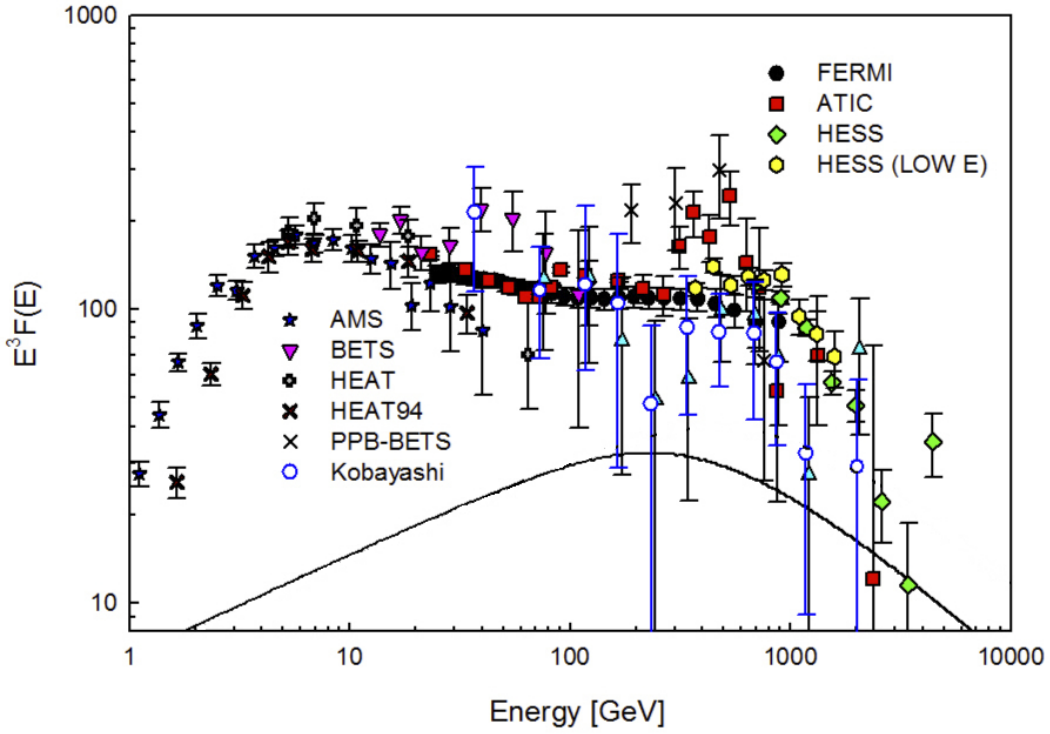

Figure A.6: We display here the primary spectrum of cosmic ray electrons $F_{e^-}(E)$ generated exclusively through acceleration of electrons in the cosmic-ray sources obtained by subtracting the secondary positrons and electron (solid line) from the measurements of the total electronic component $F_t(E)$ by HESS, ATIC, FERMI and other experiments. The sum of the secondary component and $F_{n\pm}(E)$ the primary component will add up to $F_t(E)$ shown in Fig. A.1.

A.4 The Primary Electron Spectrum Generated by Cosmic-Ray Sources

To derive the primary electron spectrum for the nested leaky-box model, we begin by writing a simple transport equation for cosmic rays [43]

$$\frac{dN}{dt} - \kappa \nabla^2 N + \frac{N}{\tau_G} = Q, \tag{A.30}$$

where N is the number density of cosmic-ray particles at a distance r from the source at time t, κ is the diffusion constant, and Q is the source term. Setting $Q = \delta(t)\delta(r)$, we get the Green's function for the cosmic-ray transport,

$$G(r,t) = (4\pi\kappa t)^{-3/2} \exp\left(- \frac{r^2}{4\kappa t} - \frac{t}{\tau_G} \right). \tag{A.31}$$

When writing eq. A.30, the term representing the energy loss for electrons $\nabla \cdot (bE^2 N)$ has not been included because the energy loss due to synchrotron and Compton processes take away energy from the electrons in such a way that the energy loss may be treated continuously. These energy losses can be described by

$$\frac{dE}{dt} = -bE^2, \tag{A.32}$$

or

$$t = \frac{E(0) - E(t)}{bE(0)E(t)}, \tag{A.33}$$

allowing for energy losses to be completely taken into account [10]. The parameter b describes the effects energy loss due to the cosmic microwave background and synchrotron radiation in the Galactic magnetic fields. For energies $E \gg 100$ GeV, the scattering cross section of starlight by the electrons is small so it is neglected in this analysis. The value of b is then given by

$$\begin{aligned} b &= 3.22 \times 10^{-3} W_{ph} + 7.9 \times 10^{-5} H^2 \\ &\approx 1.56 \times 10^{-3} \text{ GeV}^{-1} \text{ Myr}^{-1}, \end{aligned} \tag{A.34}$$

where $W_{ph} = 0.25$ eV cm^{-3} and $H = 3$ μG. Note also that for a uniform distribution of sources surrounding the point of observation, the Green's function leads to the leaky-box model with the expected exponential path length distribution,

$$P(t) = \int G(r,t) 4\pi r^2 dr \sim e^{-t/\tau}. \tag{A.35}$$

For a discrete cosmic-ray source located at a distance r_1, which continuously accelerates particles to a spectrum of the form

$$Q_1(E) = Q_e E^{-\beta} \quad \text{for } E < E_x, \tag{A.36}$$

where E_x is the maximum energy up to which the source accelerates cosmic rays, the observed spectrum is given by

$$F_1(E, r_1) = \int_0^{\frac{1}{bE} - \frac{1}{bE_x}} Q_e E^{-\beta} (1 - bEt)^{\beta - 2} G(r_1, t) dt. \tag{A.37}$$

Equations A.32 and A.33 imply that initially (t=0) positrons and electrons are produced with an energy given by

$$E(t = 0) = \frac{E}{1 - bEt}. \tag{A.38}$$

This also implies that a unit bandwidth of energy gets compressed to $(1 - bEt)^2$, which enhances the flux density per unit energy interval. The upper limit of the integral in eq. A.37 corresponds to $E(t = 0) = E_x$. In this analysis, we take $E_x \sim \infty$.

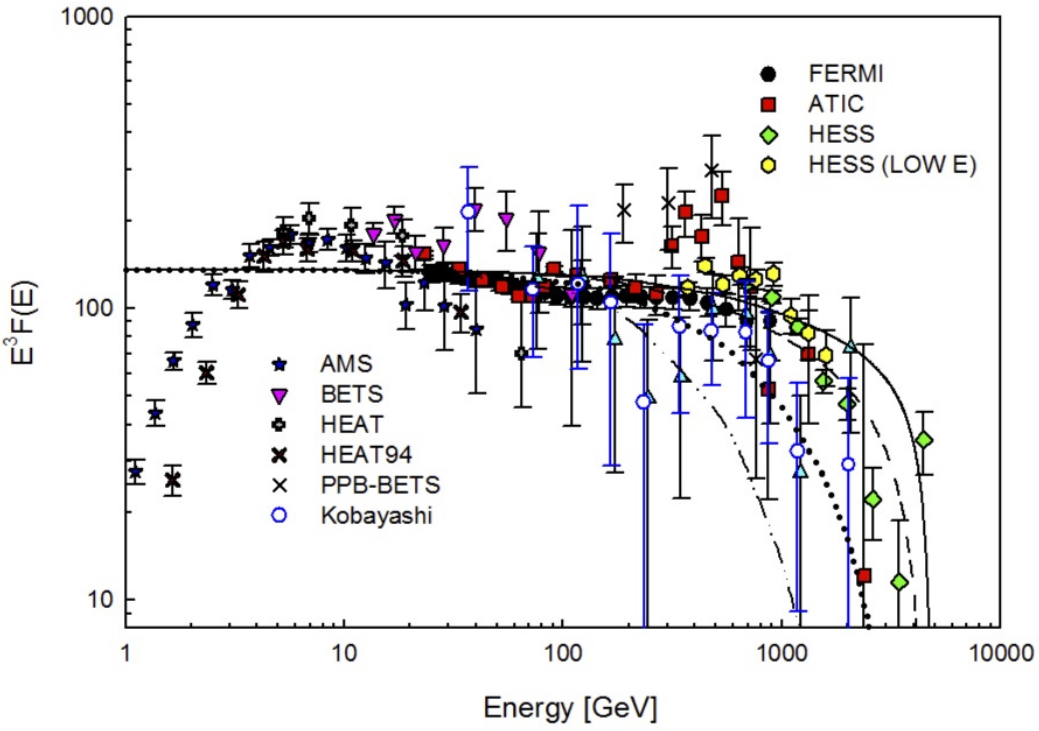

Figure A.7: The primary electron spectra due to a single source at various distances from the source with $E_x = 5$ TeV compared to the primary electron spectrum. [$r_1 = 0.1$ kpc (solid line), $r_1 = 0.2$ kpc (dashed line), $r_1 = 0.5$ kpc (dotted line), $r_1 = 1.0$ kpc (dot-dashed line)].

For a smooth distribution of sources, such as the secondary positrons and electrons in the nested leaky-box model, the equilibrium spectra are given by

$$\begin{aligned} F_{n\pm}(E) &= \int_0^{1/bE} K_\pm E^{-\Gamma}(1-bEt)^{\Gamma-2} e^{-t/\tau} dt \qquad \text{(A.39)} \\ &\sim K_\pm \tau E^{-\Gamma} \qquad \text{for } E \ll \frac{1}{b\tau} \\ &\sim K_\pm b^{-1} E^{-(\Gamma+1)} \quad \text{for } E \gg \frac{1}{b\tau} \end{aligned}$$

and agree with the spectral forms used in section A.2.4.

To understand the distribution of cosmic-ray electron sources, we first show the spectrum (eq. A.37) for single cosmic-ray sources at various distance r_1 and with a

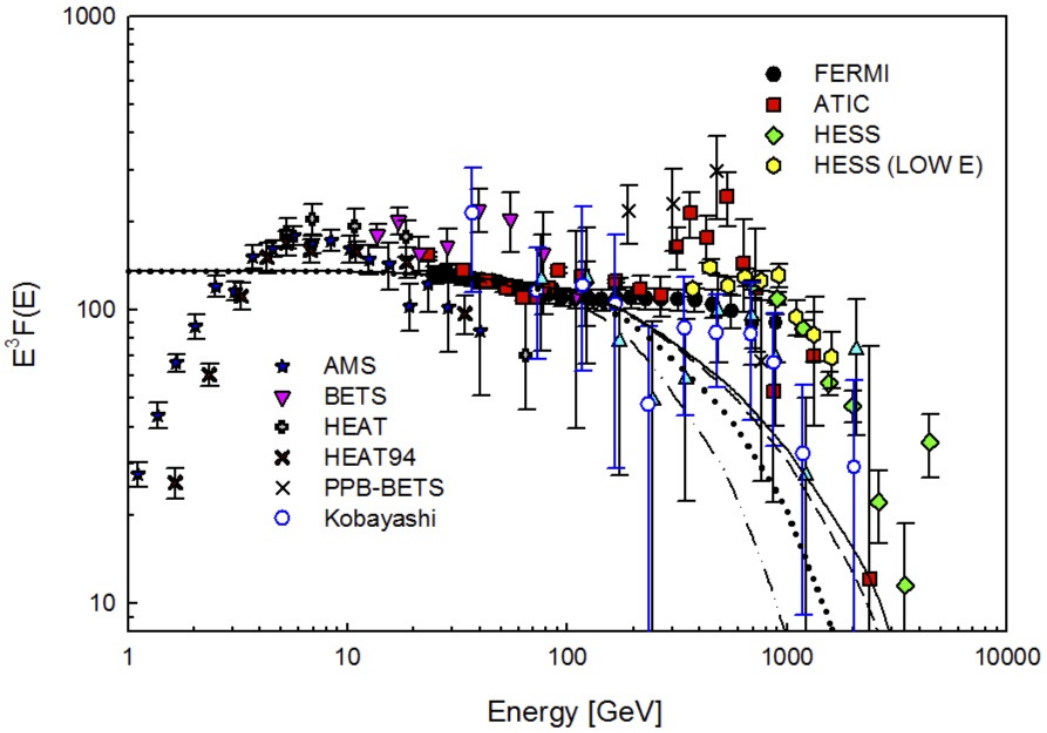

Figure A.8: The theoretical primary electron spectra resulting from an ensemble cosmic ray sources for various values of the mean spacing and $E_x = 5$ TeV is compared with the primary electron spectrum $F_{e-}(E)$. The mean spacing between the sources is taken to be $< r >= 0.1$ kpc (solid line), $< r >= 0.2$ kpc (dashed line), $< r >= 0.5$ kpc (dotted line), and $< r >_1 = 1.0$ kpc (dot-dashed line).

power law index of $\Gamma = 3$ in Fig. A.7. These spectra are similar to those calculated by Cowsik and Lee [10] and seem to fit the data for $r_1 \sim 100$ pc. Since there is no reason *a priori* to believe that all cosmic rays we observe are from a single source, we must consider an ensemble of cosmic ray sources. We assume that the cosmic-ray sources located at distances r_i are randomly distributed within the Galaxy with a mean spacing equal to the distance to the nearest source, i.e.

$$< r_i > \approx r_1 \sqrt{i}, \tag{A.40}$$

where r_1 is the distance to the nearest source. The equilibrium spectrum for an

ensemble of N cosmic-ray sources for a power-law input is given by

$$F_D(E) = \sum_{i=1}^{N} F_1(E, r_i) = \sum_{i=1}^{N} \int_{t=0}^{1/bE} K_i E^{-\Gamma} (1 - bEt)^{\Gamma - 2} G(< r_i >, t) dt. \qquad \text{(A.41)}$$

In Fig. A.8, the spectrum from eq. A.41 is shown for various values of r_1 along with the primary electron spectrum. From Figs. A.7 and A.8, we see that a distance to the nearest source of $\sim 100 - 200$ pc and a typical separation between the sources of $\sim 100 - 200$ pc fits the observations reasonably well, confirming earlier analyses [10, 11], which showed that the electronic component of cosmic rays at high enemies necessitates sources at ~ 100 pc with a similar typical spacing between the sources. We note also that this analysis does not predict the narrow enhancement seen by the ATIC experiment and others at ~ 600 GeV.

A.5 The Narrow Enhancement in the Primary Electron Spectrum

The ATIC experiment [4] reported an excess of cosmic-ray electrons at ~ 600 GeV, which has been ascribed to dark matter annihilation and other exotic processes. Subsequent observations by the FERMI experiment showed only a mild enhancement in this region, but we will investigate here what may cause such enhancement. The enhancement may be isolated by subtracting from the data of the primary electron spectrum, the expected spectrum from power-law inputs (eq. A.41). This is shown as the data points and as a smooth fit in Fig. A.9. In this section, we discuss the

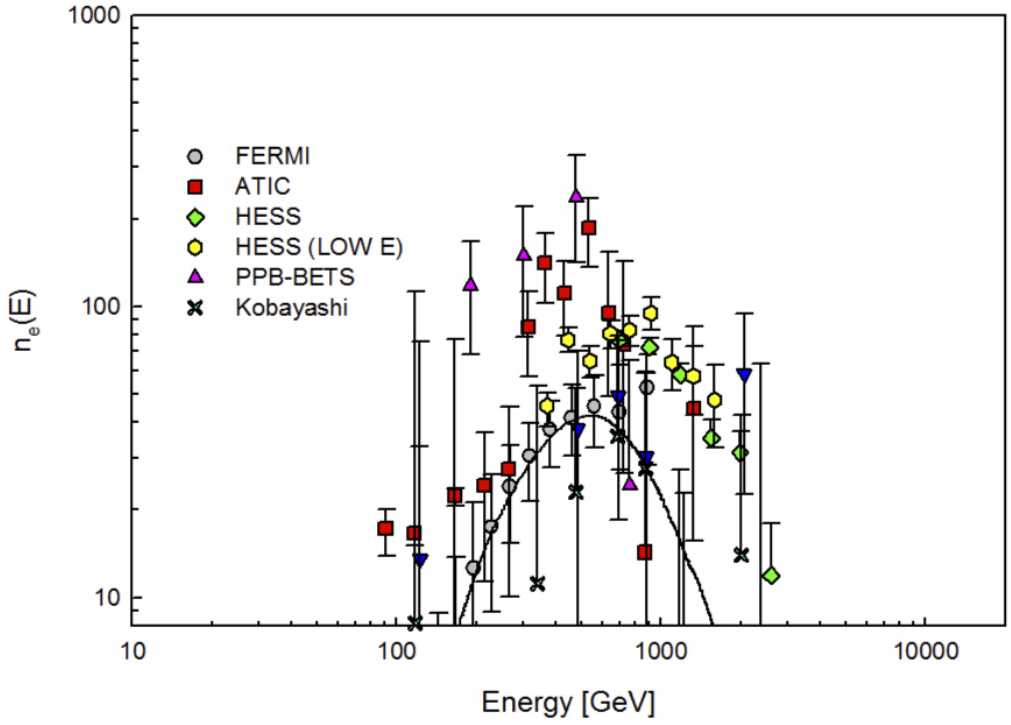

Figure A.9: The excess primary electrons obtained after subtracting the expected contribution from discrete sources estimated with a mean spacing of ~ 0.1 kpc from the primary electron spectrum $F_{e-}(E)$. This is shown both as data points and as a smooth fit through the data.

narrow enhancement in terms of two different sources: 1) a δ-function input such as that expected from the decay or annihilation of dark matter and 2) a flat spectrum $\sim E^{-2}$ such as may be expected from the acceleration of cosmic rays in planar shocks of high Mach number.

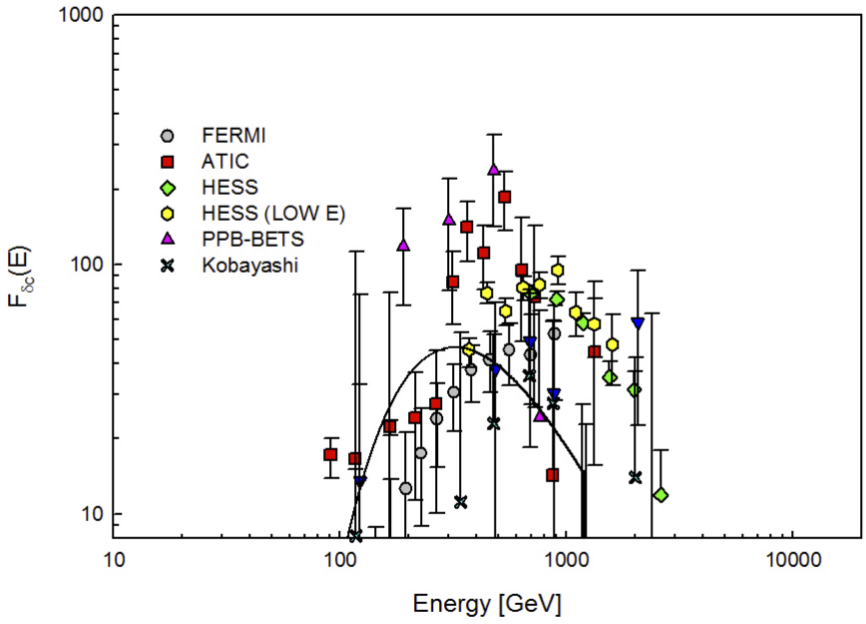

Figure A.10: The spectrum for a δ-function input from continuous distribution of sources with $E_a = 1200$ GeV . Note the peak at ~ 300 GeV$\approx E_c/2$ is expected for all $E_a > 300$ GeV (see Fig. A.11).

A.5.1 A δ-function Input

The annihilation of dark matter may produce cosmic rays at a single energy resulting in the injection spectrum

$$Q_\delta(t = 0, E_a) = \delta(E(t = 0) - E_a), \tag{A.42}$$

where E_a is the energy of the injected particles, and for dark matter with a mass M_χ, $E_a = (1/2 - 1/4)M_\chi$. From a single injection source, the corresponding equilibrium spectrum is

$$F_{\delta 1}(E, t) = \frac{E_a^2}{E^2}\delta\left(\frac{E}{1 - bEt} - E_a\right), \tag{A.43}$$

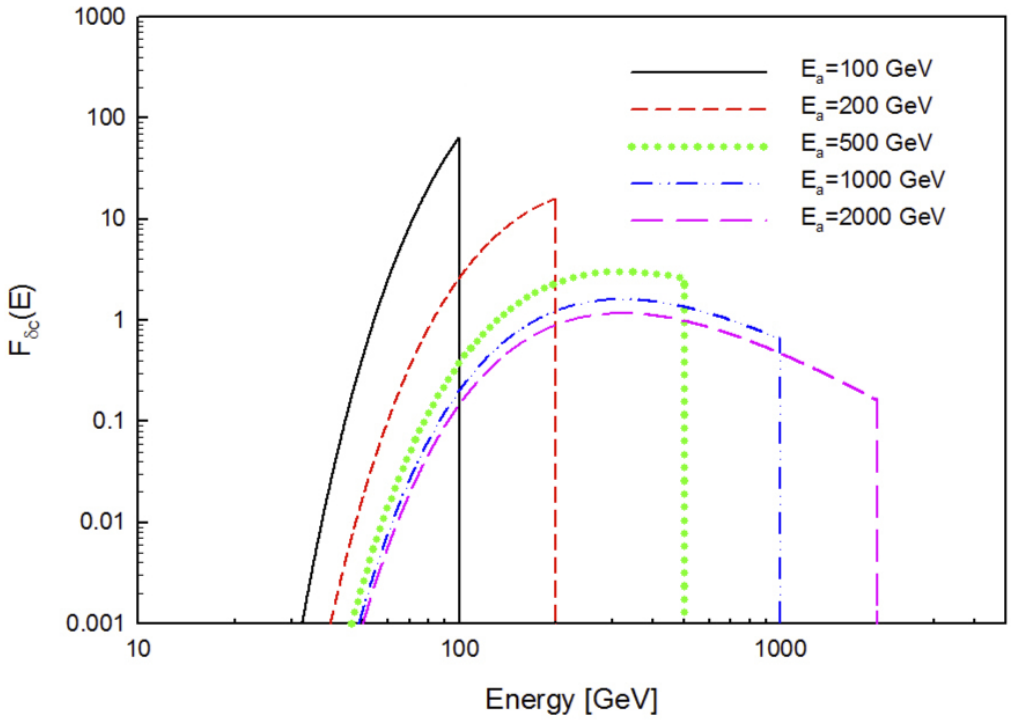

Figure A.11: Further examples of the spectra of electrons expected for δ-function inputs from a continuous spatial distribution of sources. For all $E_a > \frac{1}{b\tau}$, the peak in the intensity always occurs at $E \approx \frac{1}{b\tau}$.

which integrates to unity over E for all t. For a continuous injection of Q_δ with an energy-independent leakage, the equilibrium spectrum becomes

$$F_{\delta c}(E, E_a) = \frac{1}{bE^2} \exp\left[\left(-\frac{E_a - E}{bE_a E \tau_G}\right)\right]. \tag{A.44}$$

The equilibrium spectrum for a continuous distribution of sources is shown in Fig. A.10 for E_a =1200 GeV and for other values of E_a in Fig. A.11. We note here that $\frac{dF_{\delta c}}{dE}$ is positive for $E < \frac{1}{2b\tau_G}$ and negative for $E > \frac{1}{2b\tau_G}$. Here $\frac{1}{2b\tau_G} \approx 300$ GeV. Therefore, for a single continuous δ-function input, there is no peak at 600 GeV, and the narrow enhancement seen by ATIC is not likely the result of a spatially extended

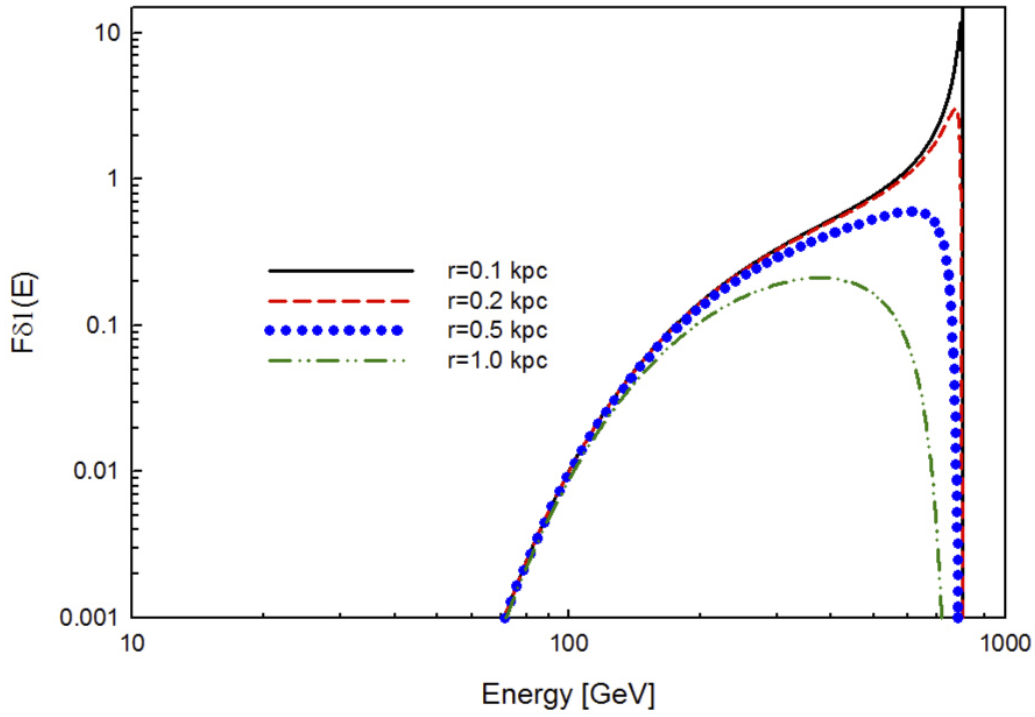

Figure A.12: The spectrum of electrons expected for a δ-function input, diffusing spatially from a single source situated at various distances.

and smoothly distributed δ-function source. If the value of b is taken to produce a peak at 600 GeV, then secondary electrons and positrons become over-produced at high energies and will be inconsistent with current data.

We can also consider a δ-function input from a single discrete source at a distance r_i. The observed equilibrium spectrum would then be

$$F_{\delta D}(E, r_i) = \frac{E_a^2}{E^2}\left[\frac{bE_aE}{4\pi\kappa(E_a - E)}\right]\exp\left[-\frac{br_i^2EE_a}{4\kappa(E_a - E)} - \frac{E_a - E}{bE_aE\tau_G}\right]. \qquad \text{(A.45)}$$

In Fig. A.12, examples of $F_{\delta D}$ are shown for different r_i. The peak in the spectrum

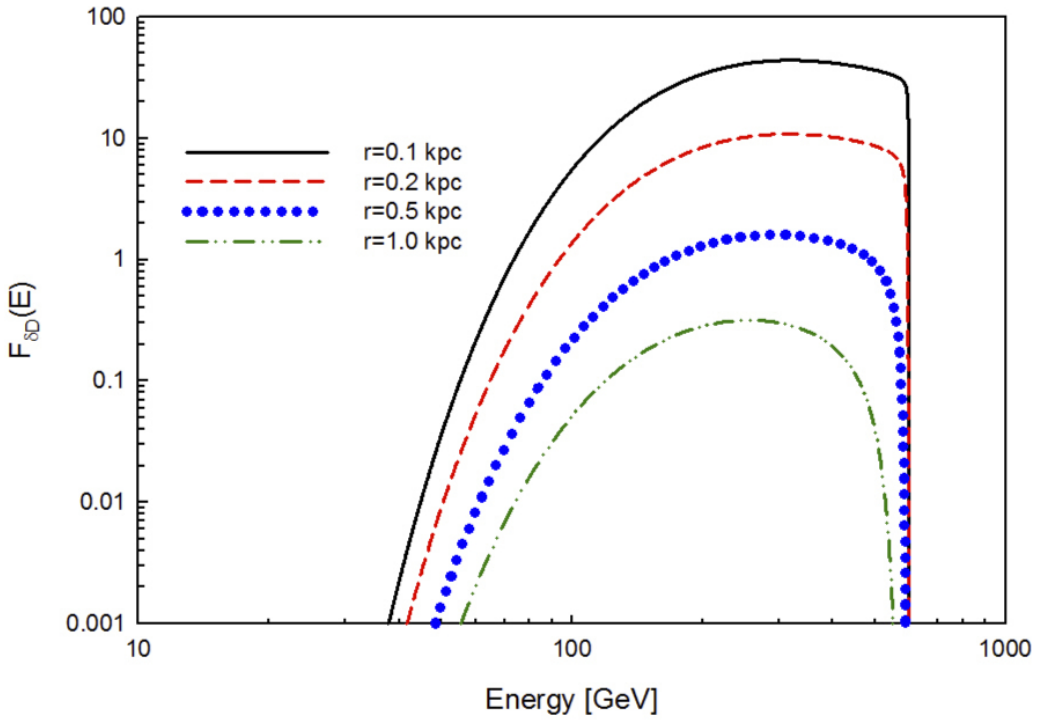

Figure A.13: The spectrum of electrons arising due to a δ-function input from a discrete set of sources located at various distances with mean spacing as indicated, and calculated assuming diffusive transport.

occurs at

$$E_{peak} \approx \frac{6\kappa E_a}{6\kappa + b r_i^2 E_a}, \tag{A.46}$$

and for small r_i, the peak is very narrow. As r_i is increased, the peak shifts to lower energies and broadens. In Fig. A.13, we show the the sum $F_{\delta D}$ over many sources at various distances and show their net contribution. These spectra are broad with a maximum around 200 GeV and do not fit well the narrow enhancement.

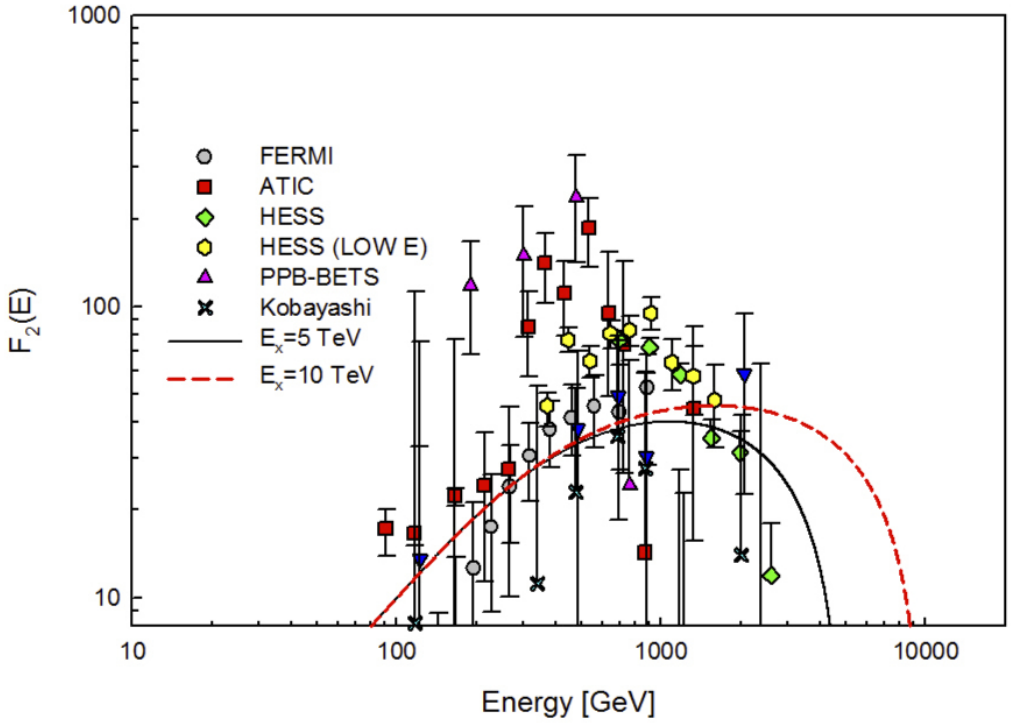

Figure A.14: The equilibrium spectrum of electrons arising from shocks has an input spectra $\sim E^{-2}$. For to various cutoff energies between $5 - 10$ TeV, this is compared with the narrow feature in the observed spectrum.

A.5.2 Shock Acceleration

Planar shocks of high Mach number will accelerate cosmic rays such that their spectra are power laws of index ~ 2, i.e.

$$Q_{shock}(E) \sim Q_0 E^{-2} \quad \text{for } E < E_x \tag{A.47}$$

for a cutoff energy E_x, and produces an equilibrium spectrum

$$F_{shock}(E) = \frac{\tau Q_0}{E^2}\left[1 - \exp\left(-\frac{E_x - E}{bEE_x\tau}\right)\right]. \tag{A.48}$$

This spectrum is shown in Fig. A.14 for $E_x = 5$ and 10 TeV and seems to be able to produce the narrow enhancement.

A.6 Discussion

This analysis has shown that the nested leaky-box model provides a good fit not only to the positron fraction observed by PAMELA and AMS but also to the cosmic-ray anisotropy and obviates the needed for exotic sources of positrons. Before precise measurements of the positron fraction, it was difficult to decided which propagation model best fit the observations. This is because, in the case of the nuclei, the secondaries carry away nearly the same energy per nucleon as the primary nuclei. As we showed, the leaky-box and nested leaky-box models both adequately fit the B/C data. However, the positrons only carry away a small percentage of the energy per nucleon of the parent nucleus, which gives rise to the behavior of the positron fraction that allows us to choose amongst the propagation models. Models that attribute a substantial fraction of the observed positrons to sources other than the high-energy interactions of cosmic rays in the interstellar medium necessitate a much smaller residence time for cosmic rays in the Galaxy corresponding to an increase in the predicted anisotropy. Improvements to the B/C and other nuclear secondary to primary ratios will help fix the parameters of the nested leaky-box model. The nested leaky-box model also makes predictions for the antiproton to proton ratio and for gamma rays generated by cosmic rays inside the cocoons. These must also be studied to fully develop the nested leaky-box model.

We have also shown that the narrow enhancement in the total electron spectrum may be due to electrons accelerated in planar shocks and that the spectral shape of a δ-function input, which would be produced by annihilating dark matter, does not fit the observed electron excess in most cases.

References

[1] Adriani, O. et al. 2009, Nature, 458, 607

[2] Abdo, A.A. et al. 2009, PRL, 102 181101

[3] Aharonian, F. et al. 2008, arXiv:0811.3894v2

[4] Chang, J. et al. 2008, Nature, 456, 362,

[5] Aguilar, M. et al. 2013, PRL, 110, 141102

[6] Cowsik, R. et al. 1966, PRL, 17 1298

[7] Cowsik, R. et al. 1967, Phys. Rev., 158, 1238

[8] Cowsik, R. & Wilson, L. W. 1973, Proc. 13th ICRC, Denver, 1, 500

[9] Cowsik, R. & Wilson, L. W. 1975 Proc. 14th ICRC, Munich, 1, 74

[10] Cowsik, R. & Lee, M. A. 1979, AJ, 228, 297

[11] Nishimura, J. et al. 1997, Adv. Space Res., 19, 767

[12] Atoyan, A. M. et al. 1995, PRD, 52, 3265

[13] Moskalenko, I.V. &Strong, A. W. 1998, ApJ, 493, 694

[14] Ioka, K. 2008, arXiv:0812.4851v2

[15] Hooper, D. et al. 2008, arXiv:0810.1527v2

[16] Kawanaka, N. et al. 2009, arXiv:0903.3782v1

[17] Malyshev, D. et al. 2009, arXiv:0903:1310v1

[18] Pohl, M. 2009, PRD, 79, 041301

[19] Profumo, S. 2008, arXiv:0812.4457v2

[20] Yüksel et al. 2008, arXiv:0810.2784v2

[21] Dado, S. &. Dar, A. 2009, arXiv:0903.0165v1

[22] Fujita, Y. et al. arXiv:0903.5298v1, 2009.

[23] Shaviv, N. et al. arXiv:0902:0376v1, 2009.

[24] Hooper, D. et al. 2008, arXiv:0812.3202v1

[25] Ishiwata, K. et al. 2009, arXiv:0903.0242v1

[26] Hooper, D. et al. 2009, arXiv:0902.0593v1

[27] Arkani-Hamed, N. et al. 2009, arXiv:0810.0713v3

[28] Bernabei, R. et al. 2008, Eur. Phys. J., C56, 333

[29] Mertsch, P. & Sarkar, S. 2009, arVix:0905.3152v2

[30] Strong, A. W., Moskalenko, I. V., & Ptuskin, V. S. 2007, Ann. Rev. Nucl. Part. Sci., 57, 285

[31] Antoni, T. et al. 2004, AJ, 604, 687

[32] Abbasi, R. U. et al. 2009, arXiv:0907.0498v1

[33] Amenomori, M. et al. 2003, Proc. 28th ICRC, Tsukuba, 1, 143

[34] Engelmann, J. J. et al. 1990, AA, 233, 96

[35] Dwyer, R. 1978, AJ, 322, 981

[36] Maehl, R. C. et al. 1977, Astrophys. Space Sci., 47, 163

[37] Chapell, J. H. & Webber, W. R. 1981, Proc. 17th ICRC, Paris, 2, 59

[38] Müller, D. et al. 2009, Proc. 31st ICRC, Łódź

[39] Swordy, S. P. et al. 1990, AJ, 349, 625

[40] Ahn, H. S. et al. 2008, Astropart. Phys., 30, 122

[41] Cowsik, R. & Burch, B., 2009, arXiv:0908.3494v1

[42] Hayakawa, S. 1969, *Cosmic Ray Physics*, Wiley Interscience, p. 380

[43] Syrovatskii, S. I. 1959, Sov. Astron., 3, 22

[44] Cowsik, R., Burch, B., & Madziwa-Nussinov, T. 2013, arXiv:1305.1242

[45] Cowsik, R. and Lee. M. A. 1977, AJ, 216, 635

Appendix B

A Novel Dark Matter Detector Using Triggered Cavitation in Acoustic Fields

Several experiments for directly detecting dark matter use bubble chamber technologies where bubbles are created by the collision of dark matter particles with the molecules of a heavy liquid inside the chamber. The bubble are then either detected acoustically or imaged directly. These experiments currently require long compression times to drive absorbed gases out of the detection liquid. In this appendix, we review these experiments and the underlying physics. We then propose a novel dark matter detector, where the heavy liquid used for detection is driven ultrasonically and gives rise to a continuously active chamber devoid of any need for lengthy compression and may provide alternative methods of discerning the properties of the incident dark matter.

B.1 Introduction

A bubble chamber is a device for detecting ionizing particles that deposit energy in a superheated liquid, creating either single bubbles or tracks of bubbles whose size and path provide information about the radiation. Early bubble chambers consisted of very large volumes of liquids such as H_2 or C_3H_8 that were superheated via a quick drop in pressure provided by a bellows system. Radiation passing through the chamber deposits energy either among the nuclei in the case of neutrons, alpha particles or dark matter or among the electrons in the case of γ-rays, x-rays, and muons. If enough energy is deposited, bubbles are formed along the trajectory of the incident particles. When the bubbles expand to macroscopic size due to the low pressure in the liquid, they are photographed, and the charge, mass, and decay lifetimes of the incident particle are often able to be discerned from the spacing between subsequent bubbles and, if the bubble chamber is placed in a magnetic field, the curvature of the particle's path. After these events, the liquid bubble chamber is compressed for several hours to drive out gasses dissolved in the liquid. Before the invention of large particle detectors such as CMS and ATLAS, bubble chambers were the standard method for measuring the results of collisions in particle accelerators.

Currently, there are several dark matter detectors looking for bubbles produced by the collisions of dark matter particles in superheated liquids including, the PICASSO [1], COUPP [2], and SIMPLE [3] experiments. Unlike most direct detection experiments, where the detector medium is either a supercooled nobel liquid or an exceedingly pure crystal of germanium, silicon, or sodium iodide operating at a few

Kelvin, the bubble chambers developed for the detection of dark matter are able to operate near room temperature and use technologies that have been refined since Glaser's invention of the bubble chamber in 1952 [4]. These bubble chambers can be "tuned" to only respond to the signatures expected from weakly interacting massive particles (WIMPs), one of the most promising dark matter candidates, and to have minimal sensitivity to background radiation.

Within the current generation of bubble chamber dark matter detectors, there are two distinct methods being employed. The PICASSO and SIMPLE experiments are superheated droplet detectors (SDDs), where the heavy liquid used for dark matter detection is suspended in tiny micron-sized droplets distributed evenly thoughout a gel matrix that is insensitive to all expected signals. This method minimizes the effects of surface defects in the detection vessel, which may cause unwanted nucleation. The COUPP experiment, instead, aims at achieving a high level of purity in their detector to be able to keep a large volume of heavy liquid (upwards of 500 L) superheated for the long times (on the order of months) needed for dark matter detection.

In both chamber designs, long compression times (on the order of several hours) are needed to drive absorbed gasses out of the detector liquid before slowly dropping the pressure in the liquid back to a state sensitive to dark matter or nuclear recoils. In this appendix, we present a case for designing a new dark matter detector where the pressure is controlled by ultrasonic transducers attached to the chamber. We propose that such a chamber may obviate the need for long compression times. This design also has the possible benefit of additional signals of bubble formation. The current experiments listen for a "pop" caused by the vibration of a transducer affixed to the

chamber by the incident particle. The COUPP experiment is also able to directly image the bubbles as they rapidly expand. In an ultrasonic bubble chamber, bubbles greater than a critical radius r_c migrate to an anti-node in the driving acoustic field and for specific pressures and temperatures may undergo single-bubble sonoluminescence. Even if sonoluminescence is not possible in the liquid, the trapped bubble may be studied via Mie scattering, acoustic oscillations, or other techniques, which will provide information about the energy of the incident radiation.

We begin by reviewing the current bubble chamber dark matter detectors in Section B.2. Then in Section B.3, the formalism for standard bubble chamber physics is reviewed and is extended to ultrasonic bubble chambers in Section B.4. In Section B.5, we briefly discuss spectrum of photons expected from bubbles undergoing sonoluminescence. Finally, in Section B.6, we discuss the prospect of designing an ultrasonic bubble chamber for the purposes of dark matter detection and the work that has been done to date.

B.2 The Current Generation of Bubble Chambers Developed for the Detection of Dark Matter

There are currently two types of bubble chamber dark matter detectors. The PICASSO and SIMPLE experiments are superheated droplet detectors in which small volumes of heavy refrigerant are suspended in small droplets within a gel matrix. The COUPP experiment, on the other hand, focuses on superheating a large continuous volume of heavy refrigerant by creating exceedingly clean bubble chamber

devoid of surface defects and by exceptional purification of the refrigerant. We begin by discussing the SDDs.

B.2.1 Superheated Droplet Detectors

First envisioned by Apfel [5] in 1979 and currently commercially produced as neutron dosimeters, superheated droplet detectors are emulsions of small droplets ($\sim 10-100$ μm in radius) of heavy refrigerant such as C_2ClF_5, C_4F_{10}, CF_3Br, CF_3I, XeF_6, etc. dispersed in a hydrogenated gel (usually glycerol). The density of the gel is matched to that of the refrigerants to ensure a homogeneous distribution of droplets within the gel. The gel and heavy refrigerant are mixed under pressure to maintain the liquid phase for the refrigerant throughout the mixing process. When the external pressure is removed, the heavy liquid becomes superheated, and radiation exceeding an energy threshold set by the thermodynamic properties of the liquid will produce an explosive liquid-to-vapor phase transition that results in the formation of a bubble. In the current generation of SDDs used for the direct detection of dark matter, SIMPLE uses C_2ClF_5, which is highly sensitive to spin-dependent interactions through fluorine. PICASSO uses C_4F_{10} and is therefore also a spin-dependent detector. To extend sensitivity into the spin-independent sector, heavier refrigerants such as CF_3Br or CF_3I may be used. These refrigerants, however, are currently unavailable to SDDs because of the challenge of matching the density of the gel to these higher density liquids. The usual method of adding salts such as CsCl to the gel to increase the density results in unwanted radioactivity within the chamber [6, 7].

The purpose of the gel matrix is to isolate the metastable superheated droplets

from surface defects in the chamber walls as well as to mitigate the effects of vibrations and convection currents in the chamber, which cause unwanted nucleation. Suspended within the gel, the detection liquid acts as a collection of individual microscopic bubble chambers instead of one continuous sensitive volume. This extends the lifetime of the superheated state of the chamber from that of a conventional bubble chamber where the aforementioned effects of vibration, convection currents, and surface events quickly produce unwanted nucleation events, necessitating the repressurization of the chamber to drive the introduced gasses out of the liquid. The downside of using the gel matrix is that it drastically reduce the active volume of the detector as it is only the heavy refrigerant and not the gel matrix that is sensitive to the incident radiation.

Aside from the gases introduced into the chamber via nucleation, SDDs are also susceptible to fractures, spurious nucleations and depletion of the superheated volume by engorged bubbles resulting from the solubility of the hydrogen-free heavy refrigerants in the water-based gels [8]. To mitigate this problem, heavy refrigerants with the lowest solubility are chosen, and additional pressure is applied to the emulsion to prevent fracturing. In addition, the heavy refrigerants must be purified to minimize spontaneous nucleations caused by impurities. For the SIMPLE experiment, when these effects are addressed, a lifetime of more than a month is claimed before recompression is needed [8].

Bubbles nucleated in the chamber are detected acoustically via a piezoelectric transducer affixed to the chamber, and their response to neutrons and background radiation is explored through extensive calibration procedures. At moderate superheat, the SDDs are only sensitive to particles with stopping powers of $dE/dx \gtrsim 200$

keV/μm, which is expected for fast neutrons, alpha particles, and some classes of WIMPs. In was shown by the PICASSO experiment [9] that the species of the incident particle may be discerned from the acoustic signal alone. Alpha particles were found to be consistently louder than the signals from neutrons or expected from dark matter. SDDs combine this discrimination technique with proper shielding of the detector from ambient neutrons to be able to run the detectors for the long times needed to account for the weak signal expected from dark matter.

Both the SIMPLE and PICASSO experiments have been able to set stringent limits on the spin-dependent cross section of dark matter. We now discuss the specifics of each experiment and their results.

SIMPLE

The SIMPLE [3, 10] experiment is currently located in the Low Noise Underground Laboratory in southern France and consists of 15 SDDs, each filled with 11-19 g of C_2ClF_5, giving a total active mass of 215 g. The C_2ClF_5 is suspended in drops of radius $\sim$ 30 μm dispersed evenly throughout 900 ml of viscoelastic glycerol gel matrix. To date, they have completed two runs, one for 14.1 kg days, with the initial data reported in the literature [10], and another another run for 13.67 kg days on a different set of 15 SDDs was completed after improving the neutron shielding [3].

In Figs. B.1 and B.2, we show the exclusion contours from SIMPLE and other direct dark matter detectors. For spin-dependent interactions, SIMPLE had been able to rule out WIMP-nucleon cross sections greater than 5.7×10^{-3} pb at a WIMP mass of 35 GeV/c^2, the energy at which the detector is most sensitive. The SIMPLE

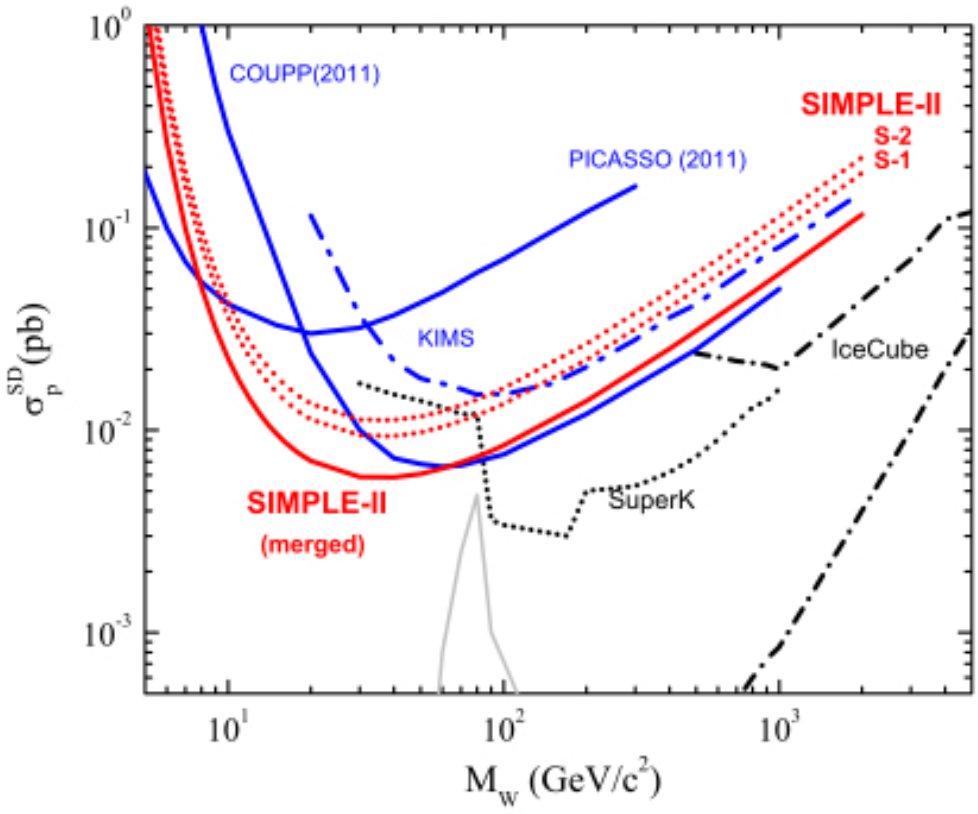

Figure B.1: The exclusion contours for spin-dependent WIMP-nucleon interactions are shown for the SIMPLE, PICASSO, COUPP, and other experiments, where M_W corresponds to the WIMP mass. This plot was taken from the SIMPLE Phase II results [3].

experiment has put the tightest constrains on spin-dependent interactions to date between $\sim 7 - 60$ GeV/c^2. The deficiency in spin-independent sensitivity is clearly seen in Fig. B.2 where the exclusion contours for the bubble chamber experiments lie far above those of the liquid nobel (XENON100, ZEPLIN-III, etc.) and cryogenic crystal (CDMS-II, EDELWEISS, etc.) chambers. SIMPLE is able to constrain the spin-independent cross section to less than 4.7×10^{-6} pb at 35 GeV/c^2 (see Fig. B.2), which is several orders of magnitude larger than the best limits by XENON100, which at its minimum excludes cross sections greater than 2×10^{-9} pb at 35 GeV/c^2.

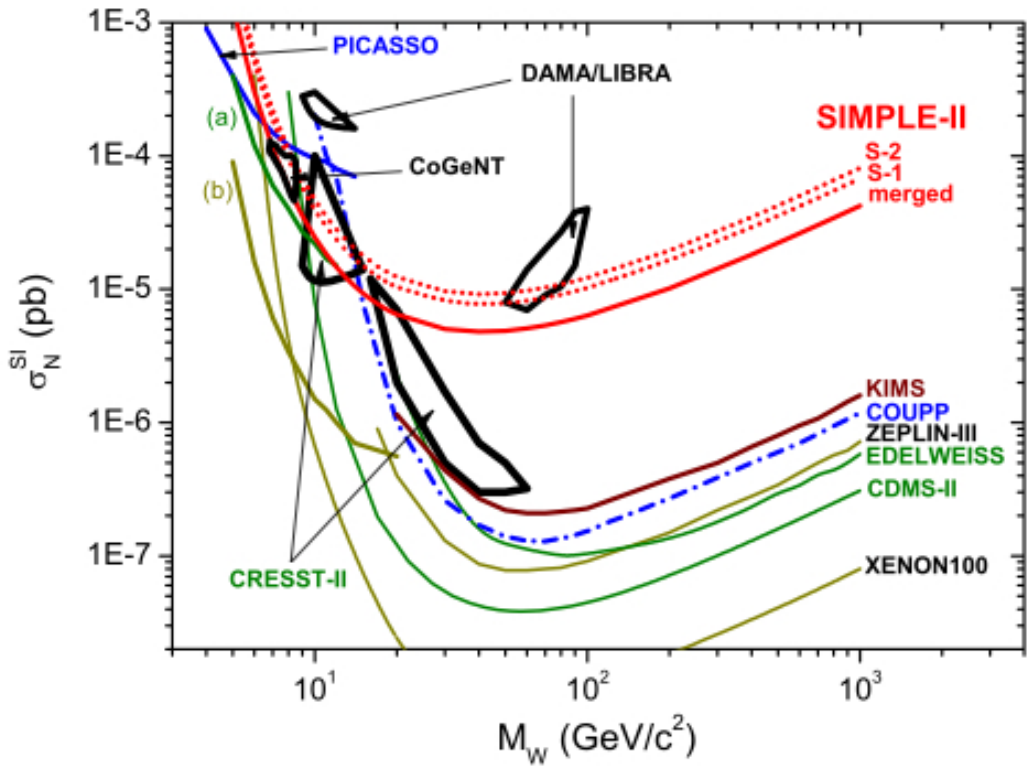

Figure B.2: The exclusion contours for spin-dependent WIMP-nucleon interactions are shown for the SIMPLE, PICASSO, COUPP, and other experiments, where M_W corresponds to the WIMP mass. This plot was taken from the SIMPLE Phase II results [3].

PICASSO

The PICASSO experiment is located in SNOLAB in Canada, and the most recent results are from a subset of 10 detectors filled with a total mass of 720 g of C_4F_{10}. The C_4F_{10} emulsion consists of ~ 200 μm diameter drops in polymerized water saturated acrylamide [1]. The current experimental setup consists of 32 cylindrical chambers each filled with 4.5 liters of emulsion. Affixed to each cylinder are 9 piezoelectric transducers capable of detecting the sharp "pop" of the violent phase change induced by WIMP-like recoils. The PICASSO detector is capable of detecting recoil energies smaller than 1.7 keV, putting the detector sensitive to WIMP masses below 15

GeV/c^2.

Figure B.1 shows that the most recent data from PICASSO excludes WIMP-nucleon cross sections greater than 3.2×10^{-2} pb at 20 GeV/c^2. In the spin-independent channel, PICASSO's strength lies in its constraints for the lightest WIMPs. Figure B.2 shows that PICASSO is the only experiment to date to put constants, albeit weak for spin-independent interactions, on WIMP masses below 5 GeV/c^2.

B.2.2 COUPP

COUPP [2] uses CF_3I, a refrigerant not currently available to SDDs due to the aforementioned problem of density matching. The iodine in the detector liquid makes COUPP far more sensitive to spin-independent interactions than the SIMPLE and PICASSO experiments. The liquid CF_3I was chosen because it can be put in a weakly superheated state at near atmospheric temperature and pressure. Whereas the SDDs negate the effects of nucleation from surface defects and impurities by suspending the detector liquid in a gel matrix, the COUPP experiment aims to remove all surface defects from the chamber and all impurities from the liquid. Once the liquid is thoroughly purified, it is put into a large quartz bell jar that is manufactured to be free of surface defects. The only other component of the chamber is a stainless steel seal that is attached to the diaphragm that controls the pressure in the chamber. Presently, the COUPP experiment is able to achieve active lifetimes in the chamber of $\sim$ 40 days before the need for recompression due to dissolved gases from nucleation events.

The bubbles created within the chamber are detected with piezoelectric transducers and and are photographed with two cameras in a stereoscopic configuration. This

allows the COUPP experiment to distinguish between slow ambient neutrons, which nucleate multiple bubbles, from WIMP-like events that would produce only a single bubble due to the exceedingly small WIMP-nucleon cross section. The cameras are placed in a stereoscopic configurations to measure the precise location of the bubble within the chamber in order to discriminate against edge events.

The latest results (Figs. B.1 and B.2) are from a 4 kg detector [11] that was run at SNOLAB for $\sim$ 550 kg days at three different recoil energy thresholds between 8 and 16 keV. A 30 L (60 kg) version of COUPP, far exceeding the $<$ 1 kg active masses of SDDs, is currently installed at SNOLAB, and there are plans to develop a 500 L chamber with a 1 ton detector mass.

B.3 The Energetics of Standard Bubble Chambers

The process of bubble nucleation by energy deposited by incoming radiation was first described by Seitz's "heat spike" theory [12] in 1958. Here there are two crucial steps: 1) the energy deposited by incident radiation must be great enough to vaporize a bubble of a critical radius r_c, defined by balancing the internal vapor pressure with the surface tension and the fluid pressure and 2) enough energy must be deposited in a small enough volume to grow the bubble from the critical radius to a macroscopic size. Here we follow derivations of the critical radius and the energy needed to nucleate a stable bubble found in the literature [12, 13, 14].

B.3.1 Deriving the Critical Radius

Assume that an initial energy deposited among the nuclei of the detector liquid vaporizes a spherical region in the liquid with a radius r. The conditions for thermodynamic equilibrium require the Gibb's potential be equal for both the gas in the initial bubble and the surrounding liquid at a pressure p and temperature T:

$$g_f(p_f, T_f) = g_v(p_v, T_v). \tag{B.1}$$

Here, the subscripts f and v refer to the fluid and vapor phases respectively. For thermal equilibrium,

$$T_f = T_v, \tag{B.2}$$

and for mechanical equilibrium, the internal vapor pressure must balance the external pressure of the liquid and the pressure resulting from the surface tension of the growing bubble:

$$p_v = p_f + \frac{2\sigma}{r}, \tag{B.3}$$

where σ is the coefficient of surface tension of the liquid. This can be easily derived by balancing the forces acting on the bubble surface. The only force pushing outwards F_{out} on the bubble surface comes from the difference in pressure inside and outside the bubble:

$$F_{out} = (p_v - p_f)\pi r^2. \tag{B.4}$$

The force pushing inwards at the bubble surface some from the surface tension and is given by

$$F_{in} = \sigma(2\pi r). \tag{B.5}$$

Equating F_{out} and F_{in} immediately leads to eq. B.3 and lets us define a critical radius in terms of the pressure of vapor inside the bubble p_v and the pressure of the surrounding fluid p_v:

$$r_c = \frac{2\sigma}{p_v - p_f}. \tag{B.6}$$

When the gas is at some initial equilibrium pressure with the external pressure p_e,

$$p_v(r \to \infty) = p_e = p_f.$$

Then eq. B.1 can be rewritten as

$$g_f(p_f, T_f) = g_v(p_f, T_f). \tag{B.7}$$

To determine the critical radius when the vapor is not at the equilibrium pressure, we consider the variation of the Gibb's potential

$$dg = -sdT + Vdp \tag{B.8}$$

where $s = -\left(\frac{\partial g}{\partial T}\right)_p$ is the specific entropy, and $V = \left(\frac{\partial g}{\partial p}\right)_T$ is the specific volume.

This can be integrated along the isothermal path to yield

$$g_f(p_f, T_f) = g_f(p_e, T_f) + \int_{p_e}^{p} V_f dp \tag{B.9}$$

for the fluid and

$$g_v(p_f + \frac{2\sigma}{r}, T_f) = g_v(p_e, T_f) + \int_{p_e}^{p_f + \frac{2\sigma}{r}} V_v dp \tag{B.10}$$

for the vapor. Combining eqs. B.9 and B.10 yields

$$g_f(p_f, T_f) = g_f(p_e, T_f) + \int_{p_e}^{p_f} V_f dp = g_v(p_e, T_f) + \int_{p_e}^{p_f + \frac{2\sigma}{r}} V_v dp, \tag{B.11}$$

which reduces to

$$\int_{p_e}^{p_f} V_f dp = \int_{p_e}^{p_f + \frac{2\sigma}{r}} V_v dp \tag{B.12}$$

under the condition of thermodynamic equilibrium. For a constant temperature,

$$V_v(p_v) = V_v(p_e)\frac{p_e}{p_v} \tag{B.13}$$

so eq. B.12 yields

$$\begin{aligned} V(p_f - p_e) &= V_v(p_e) \ln \frac{p_e}{p_f + \frac{2\sigma}{r}} \\ \frac{2\sigma}{r} &= p_e e^{-\frac{V_f}{V_v}\frac{p_e - p_f}{p_f}} - p_f. \end{aligned} \tag{B.14}$$

This defines the critical radius away from equilibrium conditions that needs to be met

or exceeded to nucleate a bubble:

$$r_c = \frac{2\sigma}{p_e e^{-\frac{V_f}{V_v}\frac{p_e - p_f}{p_f}} - p_f}. \tag{B.15}$$

For T far from the critical temperature (as is the case in bubble chambers), $\frac{V_f}{V_v} \ll 1$ so that

$$r_c = \frac{2\sigma}{(p_e - p_f)(1 - \frac{V_f}{V_v})}, \tag{B.16}$$

and for large superheat $(p_e - p_f)$, this reduces to

$$r_c = \frac{2\sigma}{p_e}. \tag{B.17}$$

To investigate the stability of a bubble at this critical radius, consider the change in the total thermodynamic potential

$$\begin{aligned} \Delta G &= [g_f(p_f, T)M_f + g_v(p_f, T)M_v + 4\pi r^2\sigma] - (M_f + M_v)g_f(p_f, T) \\ &= (g_v - g_f)M_v + 4\pi r^2\sigma \end{aligned} \tag{B.18}$$

where M_f and $M_v \equiv \frac{4}{3}\pi\frac{r^3}{V_v}$, the amount of fluid and vapor respectively. When $r = r_c$, the equilibrium condition

$$\begin{aligned} g_f(p_f, T) &= g_v(p_f + \frac{2\sigma}{r_c}, T) - g_v(p_f, T) + V_v\frac{2\sigma}{r_c} \\ g_v - g_f &= -V_v\frac{2\sigma}{r_c} \end{aligned} \tag{B.19}$$

holds, as shown in eq. B.11. Combined with the definition of M_v, the change in the thermodynamic potential becomes

$$\Delta G = 4\pi r^2 \sigma \left(1 - \frac{2r}{3r_c}\right), \tag{B.20}$$

which has a maximum value of

$$\Delta G_{max} = \frac{4}{3}\pi r_c^2 \sigma \tag{B.21}$$

at $r = r_c$. Therefore, for a critical bubble of radius r_c, perturbation towards a smaller radius will cause the bubble to collapse while perturbation towards a larger radius will cause it to expand uncontrollably.

B.3.2 Time Scale for Nucleation

A bubble of radius r_c is formed by the rapid expansion from the vaporized volume V_0 to the critical volume $V_c = \frac{4}{3}\pi r_c^3$. This vaporization occurs on a time scale of 10^{-12} sec, from when the energy is deposited on the first liquid molecule until is it transferred among the entire volume V_0. We can express the initial volume as

$$V_0 = \frac{4}{3}\pi r_0^3 \frac{\rho_v}{\rho_f} \tag{B.22}$$

where

$$r_0 = r_c \left(\frac{\rho_v}{\rho_f}\right)^{1/3}. \tag{B.23}$$

The initial vapor bubble must contain enough energy to expand to a bubble of the critical radius quicker than the time required for the heat to diffuse from the bubble. If τ_e is the expansion constant and τ_c is the diffusion constant (i.e. cooling time), then the condition on the expansion constant is

$$\tau_e \leq \tau_c = \frac{r^2}{4D} \sim 10^{-10} \text{ sec.}, \tag{B.24}$$

where D is the spatial diffusion constant. The energy required for this rapid expansion depends upon both the reversible processes needed for bubble formation including work done against the surface tension, external liquid pressure, and the energy needed to evaporate liquid as well as irreversible energy loses due to viscosity, inertia, and thermal conductivity.

B.3.3 Reversible processes

The energy required for reversible bubble formation includes the work done to expand the bubble against the surface tension and the external pressure from the liquid as well as the thermal energy needed for the initial vaporization of the bubble. The change in internal energy from bubble formation is given by

$$W_{rev} = (u_v - u_f)\frac{4}{3}\pi r_c^3 \rho_v + 4\pi r_c^2 \left(\sigma - T\frac{d\sigma}{dT}\right) + \frac{4}{3}\pi r_c^3 p_f \left(1 - \frac{\rho_v}{\rho_f}\right), \tag{B.25}$$

where u_v and u_f are, respectively, the specific internal energies of the vapor and the fluid. The first term in B.25 represents the energy needed to vaporize the initial

bubble; the second term represents the energy needed to overcome the surface tension of the liquid; and the third term describes the energy needed to overcome the fluid pressure. In order to write W_{rev} in a more useful manner, note that the heat of vaporization is the sum of the change in internal energy and the work done against the equilibrium pressure during the phase transition, which is given by

$$H = u_v - u_f + p_e\left(\frac{1}{\rho_v} - \frac{1}{\rho_f}\right). \tag{B.26}$$

Plugging eq. B.26 into eq. B.25, and using the definition of r_c as given in eq. B.16, we can write the work for reversible bubble formation as

$$W_{rev} = \frac{32\pi\sigma^3}{3(p_e - p_f)^2(1 - \frac{\rho_v}{\rho_f})^2}\left[\frac{\rho_v H}{(p_e - p_f)(1 - \rho_v/\rho_f)} + \frac{1}{2} - \frac{3}{2}\frac{T}{\sigma}\frac{d\sigma}{dT}\right]. \tag{B.27}$$

We will now consider the irreversible processes.

B.3.4 Irreversible Energy Losses

The irreversible energy losses during the formation of a critical bubble includes inertial effects, viscous effects, and the effects from the emission of sound waves and thermal conductivity. Therefore, in order to nucleate a bubble of radius r_c, an energy greater than W_{rev} is required.

Energy Lost to Inertia of the Liquid

During the expansion from the initial vaporized volume V_0 to the critical volume V_c some energy is transferred from the expanding vapor to the kinetic energy of the molecules of the liquid in order to overcome the inertia of the liquid. To derive this energy loss, we must consider the dynamics of the fluid.

Since the expansion of the bubble is subsonic, the liquid can be treated as incompressible and the velocity at a point R in liquid can be derived. The continuity equation

$$\vec{\nabla} \cdot \vec{w} = 0 \tag{B.28}$$

with the boundary conditions

$$w(r) = \dot{r} \qquad \text{and} \qquad w(\infty) = 0 \tag{B.29}$$

has the solution

$$w(R) = \dot{r}\frac{r^2}{R^2}, \tag{B.30}$$

where r is the bubble radius and R is a point in the liquid.

Now, consider the Navier-Stokes equation, the equation of motion for an incompressible fliud,

$$\frac{\partial \vec{w}}{\partial t} + (\vec{w}\nabla)\vec{w} = -\frac{1}{\rho_f}\nabla p + \frac{r}{\rho_f}\nabla^2 w. \tag{B.31}$$

Considering each term separately and using w found in eq. B.30, we find

$$\frac{\partial \vec{w}}{\partial t} = \ddot{r}\frac{r^2}{R^2} + \frac{2\dot{r}^2 r}{R^2}, \tag{B.32}$$

$$(\vec{w}\nabla)\vec{w} = \dot{r}\frac{r^2}{R^2}\frac{\partial}{\partial R}\frac{\dot{r}r^2}{R^2} = -\frac{2\dot{r}^2 r^4}{R^5}, \tag{B.33}$$

$$\frac{1}{\rho_f}\nabla p = \frac{1}{\rho_f}\frac{\partial p}{\partial R}, \tag{B.34}$$

and

$$\frac{r}{\rho_f}\nabla^2 w = 0 \tag{B.35}$$

from the continuity equation. Therefore, the equation of motion becomes

$$\frac{1}{\rho_f}\frac{\partial p}{\partial R} + \ddot{r}\frac{r^2}{R^2} + \frac{2\dot{r}^2 r}{R^2} - \frac{2\dot{r}^2 r^4}{R^5} = 0. \tag{B.36}$$

Eq. B.36 can be integrated, enforcing the boundary condition $p(\infty) = p_f$, to yield

$$p(R) = p_f + 2\rho_f \dot{r}^2 \frac{r}{R} - \frac{1}{2}\rho_f \dot{r}^2 \frac{r^2}{R^4} + \rho_f \ddot{r}\frac{r^2}{R}. \tag{B.37}$$

At the bubble's surface, $R = r$ so

$$p_s = p_f + \frac{3}{2}\rho\dot{r}^2 + \rho\ddot{r}r. \tag{B.38}$$

The effective pressure due to the inertia of the liquid is given by the difference between

the surface pressure and the liquid pressure

$$p_i = p_s - p_f = \frac{3}{2}\rho_f \dot{r}^2 + \rho_f \ddot{r} r. \tag{B.39}$$

The work done by the vapor against the liquid is turned into kinetic energy W_{KE}, which can be easily calculated by substituting eq. B.30 in for w:

$$W_{KE} = \frac{1}{2}\int_r^\infty 4\pi\rho_f w^2 R^2 dR = 2\pi\rho_f r^3 \dot{r}^2. \tag{B.40}$$

The corresponding work, calculated by the change in kinetic energy, is given by

$$\frac{dW_{KE}}{dt} = \frac{d}{dt} 2\pi\rho_f r^3 \dot{r}^2. \tag{B.41}$$

Alternatively, the change in kinetic energy can be directly written as

$$\frac{dW_{KE}}{dt} = (p_s - p_f) 4\pi r^2 \dot{r}, \tag{B.42}$$

which when combined with eq. B.41, yields the expression for p_i found in eq. B.40. Therefore, the expression for the work done against inertia derived in eq. B.41 is consistent with what we expect from the fluid equations.

Energy Lost through Viscosity

In the previous section, the continuity equation implied $\nabla^2 w = 0$, which would seem to imply that viscosity can be neglected in considering the energetics of bubble for-

mation. However, there are energy losses due to friction acting on the bubble wall, which results in a non-negligible viscosity. To calculate the effect this has on the vapor pressure, consider the equation for mechanical equilibrium at the bubble surface including the viscous term

$$p_v = p_f + \frac{2\sigma}{r} + p_i - 2\eta\frac{\partial w}{\partial R}, \tag{B.43}$$

which yields, after the making substitutions for w and p_i,

$$p_v = p_f + \frac{2\sigma}{r} + \frac{3}{2}\rho_f\dot{r}^2 + \rho\ddot{r}r + 4\eta\frac{\dot{r}}{r}. \tag{B.44}$$

To determine the energy lost, we need to consider the expansion time of the bubble. Recall that the bubble must expand faster than the time needed for heat to escape from the bubble. Assume the vapor is polytropic with a form

$$p_v = p_{v_0}\left(\frac{r_0}{r}\right)^{3\gamma}. \tag{B.45}$$

Then, eq. B.44 becomes

$$p_{v_0}\left(\frac{r_0}{r}\right)^{3\gamma} = p_f + \frac{2\sigma}{r} + \frac{3}{2}\rho_f\dot{r}^2 + 4\eta\frac{\dot{r}}{r} + \rho_f\ddot{r}r. \tag{B.46}$$

This can be examined for the limiting cases. When viscosity is small compared to

inertial effects, the terms involving η can be ignored. For $\gamma = 4/3$ (like in H_2),

$$\tau_{i,4/3} = r_0\sqrt{2\frac{\rho_f}{p_{v_0}}\left(\frac{r_c}{r_0}-1\right)}\left[1+\frac{2}{3}\left(\frac{r_c}{r_0}-1\right)+\frac{1}{5}\left(\frac{r_c}{r_0}-1\right)^2\right]. \tag{B.47}$$

For $\gamma = 1$ (like C_3H_8),

$$\tau_{i,1} = \sqrt{\frac{2}{25}\frac{\rho_f r_c}{p_{v_0} r_0^3 \ln\left(\frac{r_c}{r_0}\right)}}. \tag{B.48}$$

If the viscosity is large, eq. B.46 may be written as

$$p_{v_0}\left(\frac{r_0}{r}\right)^{3\gamma} = p_f + \frac{2\sigma}{r} + 4\eta\frac{\dot{r}}{r}, \tag{B.49}$$

which yields

$$\tau_\eta = \frac{4\eta}{3\gamma p_{v_0}}\left[\left(\frac{r_c}{r_0}\right)^{3\gamma}-1\right]. \tag{B.50}$$

From the condition that the expansion time must not be greater than the cooling time as given in eq. B.24, the following limits may also be placed on the initial vapor pressure:

$$p_{v_0,i,4/3} \geq \frac{2\rho r_0^2}{\tau_c^2}\left(\frac{r_c}{r_0}-1\right)\left[1+\frac{2}{3}\left(\frac{r_c}{r_0}-1\right)\frac{1}{5}\left(\frac{r_c}{r_0}-1\right)^2\right]^2, \tag{B.51}$$

$$p_{v_0,i,1} \geq \frac{4}{25}\frac{\rho_f r_c^5}{r_0^3\tau_c^2 \ln\left(\frac{r_c}{r_0}\right)}, \tag{B.52}$$

and

$$p_{v_0,\eta} \geq \frac{4\eta}{3\gamma\tau_c}\left[\left(\frac{r_c}{r_0}\right)^{3\gamma}-1\right]. \tag{B.53}$$

If the inertial and viscous terms are of the same order of magnitude, then

$$p_{v_0} \geq p_{v_0,i} + p_{v_0,\eta}, \tag{B.54}$$

which for $\gamma = 4/3$, yields

$$p_{v_0,4/3} \geq 6\rho_f \frac{r_0^2}{\tau_c^2} + \frac{\eta}{\tau_c}\left(\frac{r_c}{r_0}\right)^4 \tag{B.55}$$

and for$\gamma = 1$, yields

$$p_{v_0,1} \geq \frac{2}{25}\rho_f \frac{r_c^5}{r_0^2\tau_c^2} + \frac{4}{3}\frac{\eta}{\tau_c}\left(\frac{r_c}{r_0}\right)^3. \tag{B.56}$$

The internal energy of the vapor is given by

$$W_v = p_{v_0} V_{v_0} \frac{c_p \mu}{R_g} \tag{B.57}$$

where c_p is the specific heat capacity of the vapor, μ is the molar weight, and R_g is the gas constant. Then, for $\gamma = 4/3$,

$$W_{v,4/3} = \frac{c_p\mu}{R_g}\frac{4}{3}\pi r_c^3\left[6\rho_f\frac{r_c^2}{\tau_c^2}\left(\frac{\rho_v}{\rho_f}\right)^{5/3} + \frac{\eta}{\tau_c}\left(\frac{\rho_f}{\rho_v}\right)^{1/3}\right] \tag{B.58}$$

and for $\gamma = 1$,

$$W_{v,1} = \frac{c_p\mu}{R_g}\frac{4}{3}\pi r_c^3\left[\frac{2}{25}\rho_f\frac{r_c^2}{\tau_c^2} + \frac{4}{3}\frac{\eta}{\tau_c}\right]. \tag{B.59}$$

Energy Lost as Sound

During expansion, energy is lost as sound waves are emitted. The energy lost is given by

$$W_s = \frac{4\pi\rho_f r_c^6}{c\tau_e^3} \tag{B.60}$$

where c is the sound speed in the liquid.

If we compare the magnitudes of the inertial, viscous, and sonic losses, it is seen that in liquids with few internal degrees of freedom (H_2 for example), the inertial and viscous energy losses each account for $\sim 45\%$ of the energy lost with the sonic losses making up the other $\sim 10\%$. For liquids with many internal degrees of freedom (C_3H_8 or heavy refrigerants for example), viscous energy losses make up $\sim 77\%$ of the energy lost while inertia accounts for $\sim 22\%$ and sound wave emission the remaining $\sim 1\%$. The energy lost as sound waves can therefore be ignored when calculating the energy threshold for the types of liquids used in the bubble chambers looking for dark matter.

Energy Lost by Thermal Conductivity

The energy lost by thermal conductivity of the vapor can be modeled as

$$W_T = W_{v_0}\left(1 - e^{-\tau_e/\tau_c}\right) \tag{B.61}$$

where W_{v_0} is the thermal energy of the vapor just before expansion. Inertial and viscous effects (eqs. B.58 and B.59) can be added such that

$$W_{v_0} = W_T + W_{v,\gamma}. \tag{B.62}$$

In order to proceed in a clear manner, let us first decompose eqs. B.58 and B.59 each into two components, one containing the inertial effects X_i and the other containing the viscous effects X_η. These can be readily written for the given factor of γ as

$$X_{i,4/3} = 8\pi\rho_f r_c^5 \frac{c_p\mu}{R_g}\left(\frac{\rho_v}{\rho_f}\right)^{5/3}, \tag{B.63}$$

$$X_{i,1} = \frac{8}{75}\pi\rho_f r_c^5 \frac{c_p\mu}{R_g}, \tag{B.64}$$

$$X_{\eta,4/3} = \frac{4}{3}\pi r_c^3 \eta \frac{c_p\mu}{R_g}\left(\frac{\rho_f}{\rho_v}\right)^{1/3}, \tag{B.65}$$

and

$$X_{\eta,1} = \frac{16}{9}\pi r_c^3 \eta \frac{c_p\mu}{R_g}. \tag{B.66}$$

We can now rewrite eq. B.62 as

$$W_{v_0} = \left(\frac{X_\eta}{\tau_e} + \frac{X_i}{\tau^2}\right) e^{\tau_e/\tau_c}, \tag{B.67}$$

which has a minimum at $\tau_{min} = a\tau_c$, where

$$a = \frac{1}{2}\left(1 - \frac{X_i}{X_\eta\tau_c}\right) + \sqrt{\frac{1}{4}\left(1 - \frac{X_i}{X_\eta\tau_c}\right)^2 + \frac{2X_i}{X_\eta\tau_c}}. \tag{B.68}$$

Therefore, in order to compensate for the energy losses, at the beginning of expansion the internal energy available must be at least

$$W_{v_0,min} = \left(\frac{X_i}{a^2 \tau_c^2} + \frac{X_\eta}{a \tau_c} \right) e^a. \tag{B.69}$$

B.3.5 Total Energy required for nucleation

The total energy required for bubble formation is the sum of the energy needed for the reversible processes and the energy needed to overcome the irreversible energy losses:

$$W_{bubble} \geq W_{rev} + W_{v_0,min}. \tag{B.70}$$

This energy may be written as the sum of energy required to vaporize the liquid, the energy stored as surface energy, and the energy loss to irreversible processes. Then,

$$W_{bubble} = A \frac{p_e^3}{(p_e - p_f)^3} + B \frac{p_e^2}{(p_e - p_f)^2} + C \frac{p_e}{p_e - p_f} \tag{B.71}$$

where

$$A = \frac{32 \pi \sigma^3 \rho_f H}{3 \left(1 - \frac{\rho_f}{\rho_v}\right)^3 p_e^3}, \tag{B.72}$$

$$B = \frac{16 \pi \sigma^3 \left(1 - \frac{T}{\sigma} \frac{d\sigma}{dT}\right)}{3 \left(1 - \frac{\rho_v}{\rho_f}\right)^2 p_e^2}, \tag{B.73}$$

$$C_{4/3} = \left[800 \frac{\rho_f D^2}{a^2 q^4} \left(\frac{\rho_v}{\rho_f} \right)^{5/3} + 33.5 \frac{\eta D}{a q^2} \left(\frac{\rho_f}{\rho_v} \right)^{1/3} \right] \frac{\sigma c_p \mu}{p_e R_g \left(1 - \frac{\rho_v}{\rho_f}\right)} e^a, \tag{B.74}$$

and

$$C_1 = \left(10.7\frac{\rho_f D^2}{a^2 q^4} + 44.6\frac{\eta D}{aq^2}\right)\frac{\sigma c_p \mu}{p_e R_g\left(1 - \frac{\rho_v}{\rho_f}\right)}e^a \tag{B.75}$$

where q is defined by

$$\tau_c = \frac{(qr_c)^2}{4D}. \tag{B.76}$$

It is readily seen that W_{bubble} is very sensitive to the amount of superheat ($p_e - p_f$) and decreases rapidly with increasing superheat. For H_2 and C_3H_8, the energy required is on the order of a few hundred eV. For refrigerants like those used in the COUPP, PICASSO, and SIMPLE experiments, the required deposited energy for nucleation is $\sim 10 - 100$ keV [1, 2], which of the order expected from WIMP-nucleon scattering.

B.4 Ultrasonic Bubble Chambers

To create an ultrasonic bubble chamber, an external pressure is applied to a bubble chamber filled by piezoelectric transducers affixed to part of the chamber. The transducers vibrate in response to a sinusoidal driving current with an angular frequency ω and voltage corresponding to a driving pressure p_0 and can be used to set up a standing acoustic field in the liquid, where the pressure at an antinode in the liquid with an equilibrium pressure p_f is given by

$$p(t) = p_f + p_0 \sin(\omega t). \tag{B.77}$$

For a driving large driving amplitude ($p_0 > p_f$), the nodes in the standing acoustic field are put under negative pressures for part of the driving cycle. It was shown in 1959 by Lieberman that liquid under acoustic tension can be sensitive to radiation-induced cavitation [15]. This was later confirmed by experiments throughout the 1960s and into the early 1980s where it was also noticed that Seitz's theory drastically underestimated pressure at which nucleation would occur from radiation of a given energy (see [16] and the references therein). This is equivalent to the theoretical energy needed to nucleate a bubble at a given negative pressure being far less than the actual energy needed from incoming radiation. In the table in Fig. B.3, the results from several ultrasonic cavitation experiments are shown along with the predictions from Seitz's theory for the expected negative pressures for α-particle nucleation. In many of the liquid, the calculated critical radius is exceptionally small, making it difficult for incoming radiation of low energy to deposit enough energy within r_c to nucleate a bubble. The relative importance of the different terms (surface energy, viscosity, etc.) is also different in bubble chambers operating under negative pressures. In 1998 West reviewed the experiments on ultrasonic cavitation and produced a report wherein he detailed several extensions to Seitz's theory [16]. In this section, we review his findings and discuss the results relevant to developing an ultrasonic dark matter detector.

The first extension of Seitz's theory was named mT theory and relied on two additional assumptions: 1) the Seitz condition

$$p_{int}(r) - p_{ext} \geq \frac{2\sigma}{r}, \tag{B.78}$$

Material	H_{ca} kJ/mol	Recoil energy, keV	Calculated threshold (bars) for different models		Measured threshold (bars)
			Seitz/Reipe[a]	Eq. (17)	
Isopentane	39.78	101	1.13	1.99	3.34
Freon 113	44.97	166	1.20	2.05	4.49
Freon 113	44.97	101	1.49	2.63	5.21
n-hexane	59.25	101	1.43	3.22	6.89
Acetone	39.87	101	2.26	4.06	8.31
Trichloroethylene	47.07	101	2.22	5.40	11.75
Ethylene bromide	63.88	101	2.64	8.94	22.19
Acetophenone	112.61	101	2.53	12.13	22.23
Cyclohexanol[b]	99.95	101	2.00	9.81	48.74

[a]Using only the three static energy terms (W_{sl}, W_e, W_v) of the Riepe and Hahn bubble chamber calculations.
[b]This liquid has a very high viscosity compared with the others.

Figure B.3: Experimental results from ultrasonic bubble chambers for many liquids are shown. The expected negative pressure threshold expected from Seitz's theory is shown in the third column. The fourth column shows the expectation from eq. B.84, the heated mass extension. The final column shows the measured negative pressure threshold. Neither the Seitz's theory nor the heated mass theory agree with the experimental data. This table is taken from West [16].

where p_{int} and p_{ext} represent the pressure inside and outside the bubble respectively, is met for all stages of bubble growth, and 2) the vapor inside the bubble is treated like an ideal gas with the products of the mass and temperature of vapor inside the bubble assumed to be constant at all radii. The Seitz condition then becomes

$$\frac{3m(r)T(r)R_g}{4\pi r^3} + p_{neg} \geq \frac{2\sigma}{r}, \tag{B.79}$$

where R_g is the gas constant. The mT extension has the curious feature of a magic radius

$$r^\star = \frac{2\sigma}{p_{neg}} \tag{B.80}$$

where a bubble will grow even if it is empty ($m(r) = 0$). The negative pressure threshold for this model is given by solving eq. B.79 for r in the case of the equality under the condition that the roots are real and the internal pressure always exceeds the sum of the internal pressure and surface tension effects. This leads to the minimum negative pressure to cause cavitation

$$p_{neg} = \sqrt{\frac{128\pi\sigma}{81mTR_g}}. \tag{B.81}$$

The product mT can be estimated from the available recoil energy used to raise M_0 moles of liquid from the ambient temperature to the critical temperature T_{crit}. This is termed the heated mass extension of the mT theory. We replace the product R_gT by p_{crit}/ρ_{crit} and define

$$M_0 = \frac{E_{rec}}{H_{ca}} \tag{B.82}$$

and

$$V_0 = \frac{M_0}{\rho_{crit}}, \tag{B.83}$$

where E_{rec} is the available recoil energy and H_{ca} is the difference in enthalpy per mole between the liquid at the ambient temperature and at the critical temperature. The negative pressure threshold then becomes

$$p_{neg} = \sqrt{\frac{128\pi\sigma^3}{81p_{crit}V_0}}. \tag{B.84}$$

The table in Fig. B.3 shows that the heated mass extension (the fifth column) also

Material	Recoil energy, keV	Calculated threshold, bars		Measured threshold (bars)
		$Td\sigma/dT$ included	$Td\sigma/dT$ not included	
Isopentane	101	2.316	2.060	3.344
Freon 113	101	2.336	2.115	4.490
Freon 113	166	2.994	2.711	5.207
n-hexane	101	3.547	3.031	6.890
Acetone	101	4.544	4.188	8.309
Trichloroethylene	101	6.031	5.587	11.754
Ethylene bromide	101	9.664	9.197	22.190
Acetophenone	101	12.619	12.322	33.235

Figure B.4: The theoretical expectation for the variable mT theory is shown with and without the $Td\sigma/dT$ term. As with the other theories, the calculated negative pressure threshold underpredicts the experimental observations. This figure is taken from West [16].

consistently underestimates the negative pressure threshold.

The constraint of constant $m(r)T(r)$ is not realistic for a rapidly expanding bubble nucleated by explosive vaporization. A constant $m(r)T(r)$ implies a constant internal energy, but the bubble growth is assumed to be adiabatic, which implies that the difference between the surface energy and the pV work done by the negative pressure must be drawn from the internal energy. This would cause $m(r)T(r)$ to decrease as the bubble expands. The internal energy U is equal to the difference between the enthalpy and the product pV. The initial internal energy at the center of nucleation is then given by

$$U_0 = E_{rec} - p_{crit}V_0. \tag{B.85}$$

As the bubble grows, the internal energy decreases from the work done by the ex-

panding bubble to overcome the surface tension and to create a volume $V(r) = \frac{4}{3}\pi r^3$:

$$\begin{aligned} U(r) &= U_0 - W_{surface} - W_{expansion} \\ &= U_0 - 4\pi r^2\sigma - p_{neg}V(r). \end{aligned} \tag{B.86}$$

In a perfect gas, the pressure is directly proportional to the internal energy per unit volume so the internal pressure can be written as

$$p_{int}(r) = p_{crit}\frac{U(r)/V(r)}{U_0/V_0}, \tag{B.87}$$

and substituting this into eq. B.86 yields

$$p_{int}(r) = \frac{p_{crit}V_0}{U_0V(r)}[U_0 - 4\pi r^2\sigma + p_{neg}V(r)]. \tag{B.88}$$

To derive the negative pressure threshold, we substitute eq. B.88 into eq. B.78 and solve for r for the equality as before. The resulting negative pressure threshold is

$$p_{neg} = \sqrt{\frac{128\pi\sigma^3 H_{ca}}{81E_{rec}p_{crit}/\rho_{crit}}}\frac{[1 + (3/2)(p_{crit}V_0/U_0)]^{3/2}}{(1 + p_{crit}V_0/U_0)}. \tag{B.89}$$

The results of this calculation are shown in the fourth column of the table in Fig. B.4. Again, the theoretical expectation consistently predicts pressure thresholds about a factor of two smaller than the observations. The table in Fig. B.4 also shows the expectations for including a temperature-dependent surface tension. We refer the reader to West [16] for the details and for a discussion on dealing with liquids with

high viscosity such as cyclohexanol.

In the above models, the entire recoil energy of the incident radiation was assumed to be available for nucleation. This may not be the case if the distance over which the energy is deposited is much greater than the size of the critical bubble. An approximation of the rate of energy loss by a heavy particle striking a nucleus is given by the Bohr formula

$$\frac{dE}{dx} = \frac{\pi\hbar^2}{\mu} Z_n^{2/3} Z_l N_a \rho_l, \tag{B.90}$$

where μ is the mass of the electrons, $\hbar$ is Planck's constant, Z_n os the charge number for the recoil nucleus, Z_l is the charge number for the molecules in the liquid, N_a is Avogadro's number, and ρ_l is the molar density of the liquid. To determine the energy available, West posited that the deposited energy creates a cylinder of radius d at the critical temperature and pressure where d is defined

$$\begin{aligned} \frac{\pi}{4} d^2 \rho_{crit} H_{ca} &= \frac{dE}{dx} \\ d &= \sqrt{\frac{4\frac{dE}{dx}}{\pi \rho_{crit} H_{ca}}}. \end{aligned} \tag{B.91}$$

If the recoil length is much smaller than the diameter d, then the bubbles formed in the cylinders will be close together and will overlap and coalesce, forming a critical bubble. However, if the recoil length is large, then the separate bubbles will not touch and may not form the critical volume V_0. In the limiting case, where the edges of the

bubbles in the cylinders touch, the recoil length l is given by

$$\begin{aligned} \frac{\pi d^2}{4} l &= \frac{4\pi}{3}\left(\frac{l}{3}\right)^3 \\ l &= \sqrt{\frac{3}{2}} d. \end{aligned} \tag{B.92}$$

The energy limited by the loss rate available for nucleating a bubble of volume

$$V_0 = \pi \frac{d^2}{4} l = \sqrt{\frac{6}{\pi}\left(\frac{dE/dx}{\rho_{crit} H_{ca}}\right)^3} \tag{B.93}$$

is then

$$E_{available} = l \frac{dE}{dx} = \sqrt{\frac{6(dE/dx)^3}{\pi \rho_{crit} H_{ca}}}. \tag{B.94}$$

The energy available in a bubble chamber experiment is the minimum between the recoil energy of the incident particle and the energy available after the energy loss rate is considered (eq. B.94).

West also calculated the algebraically complicated negative pressure threshold including including dynamical and viscous terms (eq. 62 in [16]) and compared the results to the observations (see the table in Fig. B.5). The theoretical calculations are in reasonable agreement with the experiments, being within a factor of 2 in all cases. There is still theoretical work to be done to completely understand ultrasonic bubble chambers. For example, the equation of state for the vapor in the bubble should represent a real gas under the conditions of nucleation.

The recoil energy from a WIMP-like particle is expected to be in the range of $\sim 10 - 100$ keV. Note that all the liquids in Figs. B.3-B.5 respond to cavitation

Material	Available energy (keV)	Negative pressure thresholds, bars			
		$P_{neg}(62)$	$P_{neg}(63)$	$P_{neg}(64)$	Exptl.
Isopentane	47	**3.42**	12.46	**3.42**	3.34
Freon 113	139	**2.66**	10.49	**2.66**	4.49
Freon 113	101	**3.21**	11.68	**3.21**	5.21
n-hexane	47	**5.81**	16.60	**5.81**	6.89
Acetone	52	**6.87**	21.69	**6.87**	8.31
Trichloroethylene	101	**6.54**	21.31	**6.54**	11.75
Ethylene bromide	101	**13.06**	30.92	**13.06**	22.19
Acetophenone	58	45.51	**40.44**	**40.44**	33.23
Cyclohexanol	56	8925.87	**35.35**	**35.35**	48.74

Figure B.5: The theoretical calculations including the dynamic and viscous terms (62) is compared to the high-viscosity limit (63). Column (64) shows the minimum between (62) and (63). The energy available for nucleation is also given after considering the linear energy loss rate. The predictions are in good agreement for liquids with low negative energy thresholds. This figure is taken from West [16].

from alpha particles within this energy range. Many of these liquids may indeed be ideal candidates for a dark matter detection liquid. In section B.6, we discuss the application of ultrasonic bubble chambers to dark matter detection.

B.5 Single-bubble Sonoluminescence

Once a bubble is formed in an ultrasonic bubble chamber, it is subject to the driving pressure provided by the transducers

$$p(t) = p_f + p_0 \sin(\omega t), \tag{B.95}$$

where p_0 is the amplitude of the driving pressure and ω is the driving frequency that depends on the geometry of the chamber and the properties of the liquid. The

behavior of the bubble in this scenario is much more complex than the behavior of a bubble in a traditional bubble chamber, which grows until it breaks apart or the liquid undergoes recompression. The dynamics of bubbles trapped in an acoustic field are given by the Rayleigh-Plesset equation, and in this section, we will discuss the behavior of the bubble and the spectrum of the light that is produced by single-bubble sonoluminescence when the sinusoidal driving pressure causes the bubble to undergo a violent collapse. This section summarizes parts of the excellent reviews by Brenner et al. [22, 23], with several mathematical steps added for transparency. Single-bubble sonoluminescence has been well-studied in water so the examples here are given for water. The existence of sonoluminescence have yet to be shown for any heavy refrigerant used in a bubble chamber dark matter detector, and such a liquid may have to be doped with an inert gas, the presence of which is essential to sonoluminescence.

B.5.1 A Derivation of the Rayleigh-Plesset Equation

As in section B.3, the sound waves in the fluid can be described by the Navier-Stokes equations. Unlike in the previous section, we will use the equations for a compressible fluid because it has not yet been determined whether shock waves, which compress the liquid are an important part of the bubble dynamics of an acoustically-driven bubble. For an isothermal fluid, the Navier-Stokes equations for a compressible fluid are

$$\rho_f\left(\frac{\partial w}{\partial t} + w\cdot\nabla w\right) = -\nabla p_f + \eta_s\nabla^2 w + \eta_b\nabla(\nabla\cdot w) \tag{B.96}$$

where η_s is the shear viscosity, and η_b is the bulk viscosity, and

$$\frac{\partial \rho}{\partial t} + \nabla \cdot (\rho w) = 0. \tag{B.97}$$

We assume the sound field around the bubble is purely radial meaning that the viscous terms are negligible, and the velocity can be characterized by the gradient of a potential

$$w = \nabla \phi. \tag{B.98}$$

The Navier-Stokes equations can then be simplified, and eq. B.96 becomes

$$\begin{aligned}
\rho_f(\partial_t w + w \cdot \nabla w) &= -\nabla p_f \\
\rho_f[\partial_t \nabla\phi + \nabla\phi \cdot \nabla(\nabla\phi)] &= -\nabla p_f \\
\nabla\rho_f \left[\partial_t \phi + \frac{1}{2}(\nabla\phi)^2\right] &= -\nabla p_f \\
\rho_f \left[\partial_t \phi + \frac{1}{2}(\partial_r\phi)^2\right] &= -p_f
\end{aligned} \tag{B.99}$$

while eq. B.97 becomes

$$\partial_t \rho_f + \partial_r \phi \partial_r \rho_f + \rho_f \partial_r^2 \phi = 0. \tag{B.100}$$

Now, let the enthalpy be defined as $dH \equiv dp_f/\rho_f$ and note $dp_f = (dp_f/d\rho_f)d\rho_f =$

$c^2 d\rho_f$ where c is the sound speed in the liquid. Then, eq. B.100 becomes

$$\begin{aligned}
\partial_t \rho_f + \partial_r \phi \partial_r \rho_f + \rho_f \partial_r^2 \phi &= 0 \\
\frac{1}{\rho_f}\partial_t \rho_f + \frac{w}{\rho_f}\partial_r \rho_f + \partial_r^2 \phi &= 0 \\
\frac{1}{c^2 \rho}\partial_t p_f + \frac{w}{c^2 \rho}\partial_r p_f + \partial_r^2 \phi &= 0 \\
\frac{1}{c^2}(\partial_t H + w \partial_r H) + \partial_r^2 \phi &= 0, \qquad \text{(B.101)}
\end{aligned}$$

and eq. B.99 can be rewritten as

$$\begin{aligned}
\rho_f \left[\partial_t \phi + \frac{1}{2}(\partial_r \phi)^2 \right] &= -p_f \\
\partial_t \phi + \frac{1}{2} w^2 &= -p_f / \rho_f \\
\partial_t \phi + \frac{1}{2} w^2 &= -H \\
\partial_t^2 \phi + w \partial_t w &= -\partial_t H. \qquad \text{(B.102)}
\end{aligned}$$

Combining eq. B.101 and B.102 yields

$$\begin{aligned}
0 &= \frac{1}{c^2}(-\partial_t^2 \phi - w \partial_t w + w \partial_r H) + \nabla^2 \phi \\
\nabla^2 \phi &= \frac{w}{c^2}(\partial_t w - \partial_f H) + \frac{1}{c^2}\partial_t^2 \phi \qquad \text{(B.103)}
\end{aligned}$$

Near the bubble, the velocity potential obeys the Laplace equation $\nabla^2 \phi = 0$ subject to the boundary condition $\partial \phi (r = R) = \dot{R}$, and therefore has the solution

$$\phi = -\frac{\dot{R} R^2}{r} + A(t) \qquad \text{(B.104)}$$

where $A(t)$ is determined by matching the solution to the pressure at large r. Note that in this section, this definitions of r and R as switched compared to the previous section to be consistent with sonoluminescecne literature and the figures used in this section. The radius of the bubble is now given by R. Since the sound wavelength is much larger than the size of the bubble, the sound field is essentially independent of r so $\phi = \phi_\infty(t)$ and $A(t) = \phi_\infty(t)$. Therefore, the fluid velocity around the bubble is

$$w = \partial_r \phi = \frac{\dot{R} R^2}{r^2} \tag{B.105}$$

as before.

Now, as in the case of bubble nucleation, to derive the motion of the bubble wall, where $r = R$, the forces on the surface of the bubble must be balanced. This yields

$$\begin{aligned} P_g(t) + \Sigma_{rr}(R) &= p_v(t) = p_f(R) + 2\eta \partial_r w(R) \\ &= p_v(t) - p_f(R) + 4\eta \frac{\dot{R}}{R} = \frac{2\sigma}{R}, \end{aligned} \tag{B.106}$$

where Σ_{rr} is the radial component of the stress tensor in the liquid. Then, this

equation can be rewritten using the solution from the Laplace equation and eq. B.99.

$$\begin{aligned}
\frac{2\sigma}{R} &= p_v(t) - p_f R - 4\eta\frac{\dot{R}}{R} \\
\frac{2\sigma}{R} &= p_v(t) - \rho_f\left[\partial_t\phi + \frac{1}{2}(\partial_r\phi)^2\right] - 4\eta\frac{\dot{R}}{R} \\
\frac{2\sigma}{R} &= p_v(t) - \rho_f\left\{\frac{\partial}{\partial_t}\left[-\frac{\dot{R}R^2}{r} + \phi_\infty\right]_{r=R}\right. \\
&\quad \left. + \frac{1}{2}\left[\frac{\partial}{\partial r}\left(-\frac{\dot{R}R^2}{r}\right)^2\right]_{r=R}\right\} - 4\eta\frac{\dot{R}}{R} \\
\frac{2\sigma}{R} &= p_v(t) + \rho_f\left\{-R\ddot{R} - 2\dot{R}^2 - \frac{1}{\rho_f}p_f(t) + \frac{1}{2}\dot{R}^2\right\} - 4\eta\frac{\dot{R}}{R} \\
\rho_f\left(-R\ddot{R} - \frac{3}{2}\dot{R}^2\right) - p_f(t) &= -p_v(t) + 4\eta\frac{\dot{R}}{R} + \frac{2\sigma}{R} \\
R\ddot{R} + \frac{3}{2}\dot{R}^2 &= \frac{1}{\rho_f}\left[p_v(t) - p_0 + p_d\sin(\omega t) - 4\eta\frac{\dot{R}}{R} - \frac{2\sigma}{R}\right]. \quad \text{(B.107)}
\end{aligned}$$

This is the Raleigh-Plesset equation, which describes the motion of the bubble wall in an acoustic field.

There are many limiting cases and extensions to the Rayleigh-Plesset equation. The velocity field can be modified to include the effects of damping due to sound waves radiated from the bubble. In this case, the eq. B.107 will also include the term $\frac{\rho_f}{c}\frac{d^2}{dt^2}(R^2\dot{R})$ added to the righthand side, which clearly negligible when the bubble wall speed is small compared to the sound speed c. It should be noted that errors accumulate very rapidly when expanding the Rayleigh-Plesset equation in the limit of small bubble wall speed. Including the damping effects, the Rayleigh-Plesset equation

is given by

$$\rho_f\left(R\ddot{R}+\frac{3}{2}\dot{R}^2\right)=p_v(t)-p_0+p_d\sin(\omega t)-4\eta\frac{\dot{R}}{R}-\frac{2\sigma}{R}+\frac{R}{c}\frac{d}{dt}p_v. \tag{B.108}$$

Solutions to this equation for different driving pressures are shown in Fig. B.6.

The Rayleigh-Plesset equation describes a bubble motion that can be divided into three distinct stages:

1. Expansion: The negative pressure during half the driving cycle causes the bubble to expand. This lasts on the order of 20 μs and may increase the radius by an order of magnitude.

2. Rayleigh Collapse: The driving pressure becomes positive and the bubble undergoes a violent collapse over a time scale of $\sim$ 1 ns. At the end of the Rayleigh collapse, light may be emitted. It is this light that is termed single-bubble sonoluminescence.

3. Afterbounces: The driving pressure is still positive at this point, and the bubble again expands (to a smaller maximum radius each time) and collapses, oscillating at its natural (resonant) frequency until the driving pressure becomes negative.

The responses of the bubble to weak and strong driving, viscous effects, and inhomogeneous pressure fields within the bubble can be explored through the Rayleigh-Plesset equation. It is found that when comparing to experiment, eq. B.108 always overestimates the afterbounces of the bubble if the peak is fit.

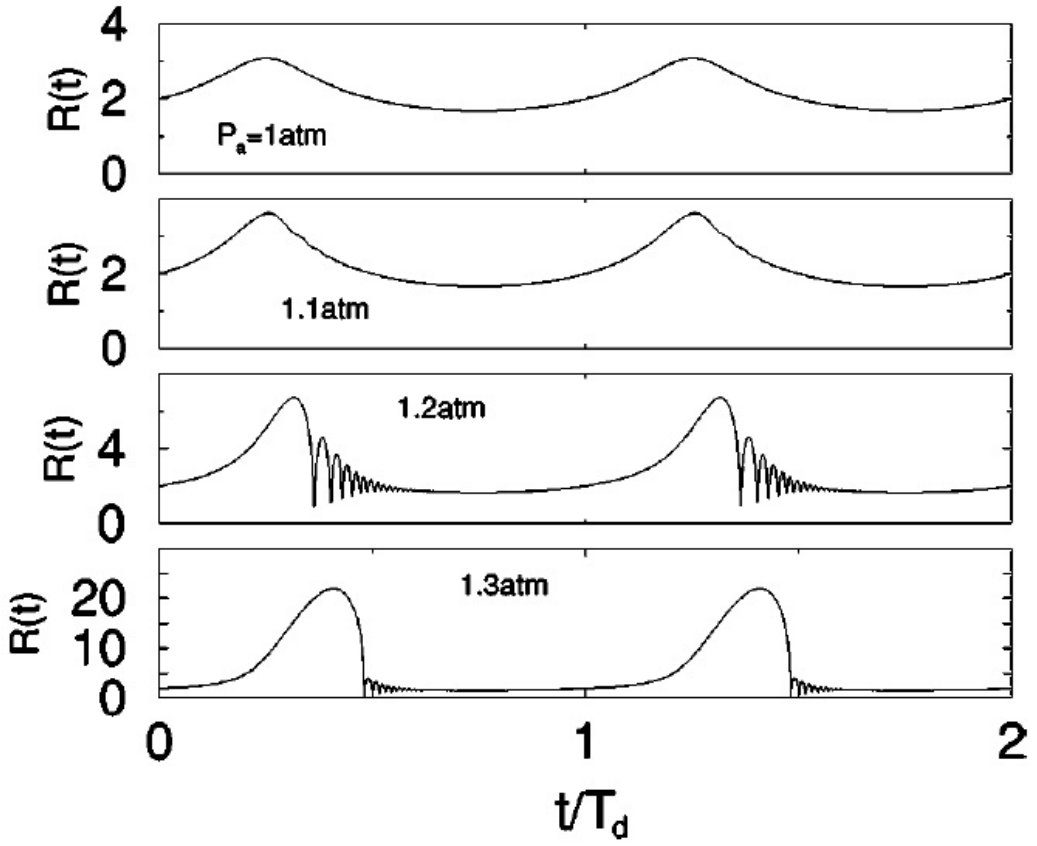

Figure B.6: Solution to eq. B.108 for different driving pressures with $R_0 = 2$ μm and $f = 26.5$ kHz. This figure is taken from [22].

B.5.2 The Parameter Space of Sonoluminescence

Sonoluminescence occurs only in a very small parameter space limited by several processes. During each each oscillation cycle, the bubble must be driven strongly enough to undergo Rayleigh collapse, and the surface tension and viscous processes must be able to stop the bubble from breaking apart. The bubble must be in a diffusive equilibrium so that the bubble may remain intact for many cycles, and the forces on the bubble must be able to keep it at an anti-node in the standing acoustic field.

Bjerknes Forces

In order for sonoluminescence to occur continuously, the bubble's center must be more or less stationary. If viscosity is neglected, the force on the bubble by the fluid pressure is given by

$$\vec{F}_{p_f} = -\int p_f \vec{n} \cdot d\vec{S}. \tag{B.109}$$

If we multiply this expression by $\hat{b}$, a unit vector pointing from the origin to the bubble center and average over driving period, we find

$$F_{Bj} = \left\langle \hat{b} \cdot \vec{F}_{p_f} \right\rangle = \left\langle -\frac{4}{3}\pi R^3 |\nabla p_f| \right\rangle, \tag{B.110}$$

which is called the primary Bjerknes force. The primary Bjerknes force must vanish if the bubble's center is to remain stationary. It can be shown that when a bubble's natural resonance frequency f_0, given by

$$2\pi f_0 = \sqrt{\frac{1}{\rho_f R_0^2}\left(2\gamma p_f + (3\gamma - 1)\frac{2\sigma}{R_0}\right)}, \tag{B.111}$$

where γ is the adiabatic exponent, the bubble is attracted to antinodes in the sound field and repelled by nodes even though at the nodes or antinodes $\nabla p_f = 0$ and the primary Bjerknes force vanishes. The bubble is also subject to a small buoyant force which causes the equilibrium position of the bubble to be located slightly above an antinode. Instabilities caused by Bjerknes forces are typically caused by driving pressures greater than upper limits found for sonoluminescence.

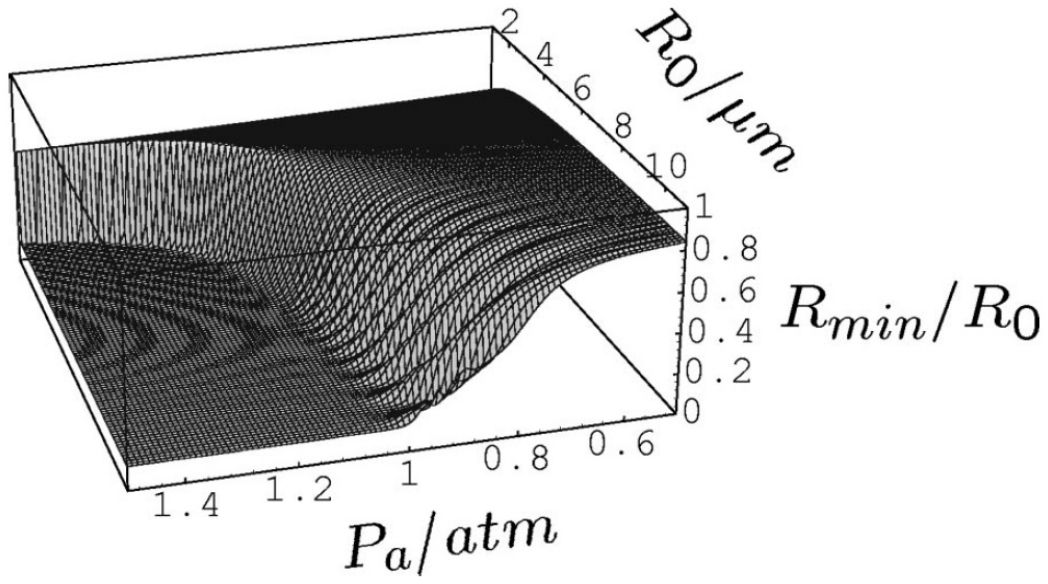

Figure B.7: The minimum bubble radius is plotted as a function of R_0 and P_a for a frequency $f = 26.5\ kHz$ Note the sudden transition where R_{min} increases, indicating where Rayleigh collapse occurs. This figure is taken from [22].

Rayleigh Collapse and the Blake Threshold

Consider the collapse of a bubble where viscosity, gas pressure, and surface tension are negligible, i.e. the collapse of a void. The solution to the Rayleigh-Plesset equation in this regime indicates that the velocity of the bubble wall should become infinite as the bubble collapses. If the viscous and surface tension terms are included, we see that inertial forces overwhelm the viscous and surface forces and the bubble wall velocity still diverges. However, including the effects of the gas pressure leads to a bubble wall velocity that halts at collapse. At the last moments of collapse, emission of sound waves plays the largest role in halting the bubble wall.

When studying the behavior of the bubble collapse as a function of the driving pressure and the ambient radius, there is a clear delineation between the parameters that lead to Rayleigh collapse, the sudden inward acceleration of the bubble wall

that may result in sonoluminescence and those that do not. This is called the Blake threshold and is given

$$R_0^{Blake} = \frac{4\sqrt{3}}{9}\frac{\sigma}{p_a - p_0}. \tag{B.112}$$

Only bubbles with $R_0 > R_0^{Blake}$ are capable of sonoluminescence. A plot of the parameter space for the Blake threshold can be seen in Fig. B.7

Diffusive Stability

Sonoluminescence depends strongly on R_0, the radius of the bubble at p_f, which changes through gas diffusion and the evaporation and condensation of water vapor. Therefore, it is important that the bubble remain diffusively stable so that the mass content of the bubble, and therefore R_0 does not change on average. We wish to determine the parameter space for this stability. Consider the transport equation for the mass concentration $q(r,t)$ for the gas around a spherical bubble

$$\partial_t q + w\partial_r q = D\frac{1}{r^2}\partial_r(r^2\partial_r q) \tag{B.113}$$

where the fluid velocity w is given by eq. B.105. If it is assumed that the gas in the bubble is in equilibrium with the gas at the bubble wall, then by the Henry-Dalton law (that the concentration of gas dissolved in a liquid is directly proportional to the partial pressure of the gas above the liquid, assuming the gas and liquid are in equilibrium and at constant temperature), the gas concentration at the bubble wall is

$$q(R,t) = c_0\frac{p_v(R,t)}{p_0}. \tag{B.114}$$

The change in mass of gas in the bubble is then given by

$$\dot{m} = 4\pi R^2 D \partial_r q|_{R(t)}, \tag{B.115}$$

which is valid where the Rayleigh-Plesset equation is valid and excludes radii near collapse where the motion of the bubble wall is fast and equilibrium cannot be guaranteed. Sound waves, chemical reactions, and boiling of the surrounding liquid play a significant role in the gas transfer near collapse.

To further explore the mass diffusion, we define the coordinates

$$l(r,t) = \frac{1}{3}[r^3 - R^3(t)]. \tag{B.116}$$

Then, the transport equation (eq. B.113) may be written as

$$\partial_t q = D \partial_l (r^4 \partial_l q), \tag{B.117}$$

which reduces to the diffusion equation

$$\partial_\tau q = \partial_{ll} q \tag{B.118}$$

at the boundary $r \approx R$, and $\tau \equiv \int R^4 dt$. Equation B.118 has the solution

$$q(l,\tau) = q_\infty + q_{osc}(l,\tau) + q_{long}(l,\tau) \tag{B.119}$$

where q_∞ is the ambient gas concentration, q_{osc} describes the gas transport on the time scale of the ultrasonic oscillations, which is negligible, and q_{long} describes the gas exchanged over long time scales compared to the driving period. In order for the bubble to be diffusively stable, the average of $q(l,\tau)$ over the time τ must be equal to the ambient concentration q_∞. This average, waited by R^4 (denoted by the subscript),is given by

$$< q >_4 = q_0 \frac{\int R^4 p_v(R,t)dt}{P_0 \int R^4 dt} \equiv q_0 \frac{< p_v >_4}{P_0} = q_\infty. \tag{B.120}$$

The change in mass over long periods can then be written as

$$\dot{m} = -4\pi R_0^2 D \frac{< q >_4 - q_\infty}{\delta}, \tag{B.121}$$

where δ is the boundary layer thickness given by

$$\delta = R_0^2 \left(\int_0^\infty \frac{dh}{T_d^{-1} \int [3l + R^3(t)]^{4/3} dt} \right)^{-1}. \tag{B.122}$$

The time integral in eq. B.122 is taken over one period of oscillation, T_d. The boundary layer thickness can also be approximated as R_0^2/R_{max}, and the corresponding time scale for mass diffusion is given by

$$\tau_{MD} \approx \frac{R_0^3 \rho_v}{R_{max} D q_0} \sim 0.1 \text{ s}. \tag{B.123}$$

This approximation holds as long as the diffusion time scale is significantly longer

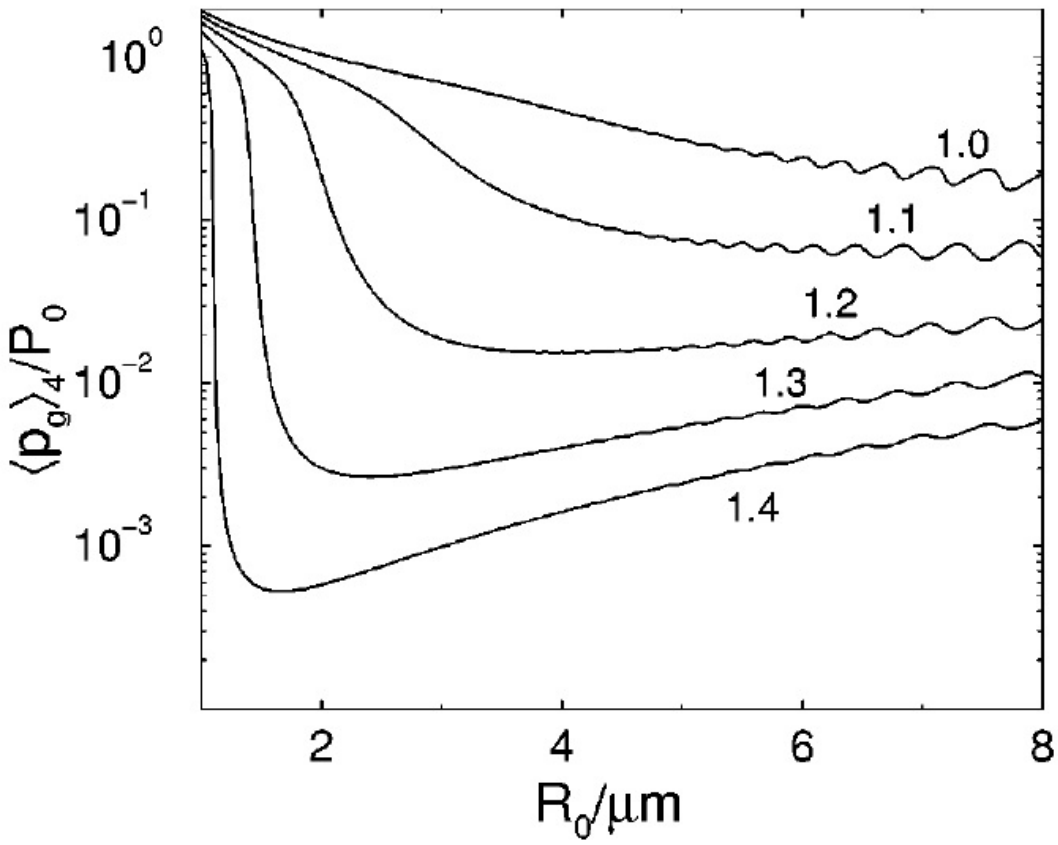

Figure B.8: $< p_v >_4 / p_0$ ($p_g = p_v$) as a function of the ambient radius R_0 for small forcing pressure amplitudes, $p_a = 1.0$ atm to $p_a = 1.4$ atm. This figure is taken from [23].

than the time scale of oscillation.

Since the bubble spends a significant amount of time near the maximum radius (see Fig. B.6), eq. B.120 can be approximated as

$$\frac{p_v(R_{max})}{p_0} = \left(\frac{R_0}{R_{max}} \right)^3 = \frac{q_\infty}{q_0}. \tag{B.124}$$

This approximation leads to the phase diagrams seen in Figs. B.8 and B.9. Note that low gas concentrations in the liquids ($q_\infty/q_0 \sim 0.001 - 0.02$) are needed to needed stable bubbles. In water, the concentration of nobel gasses is at this level, but the

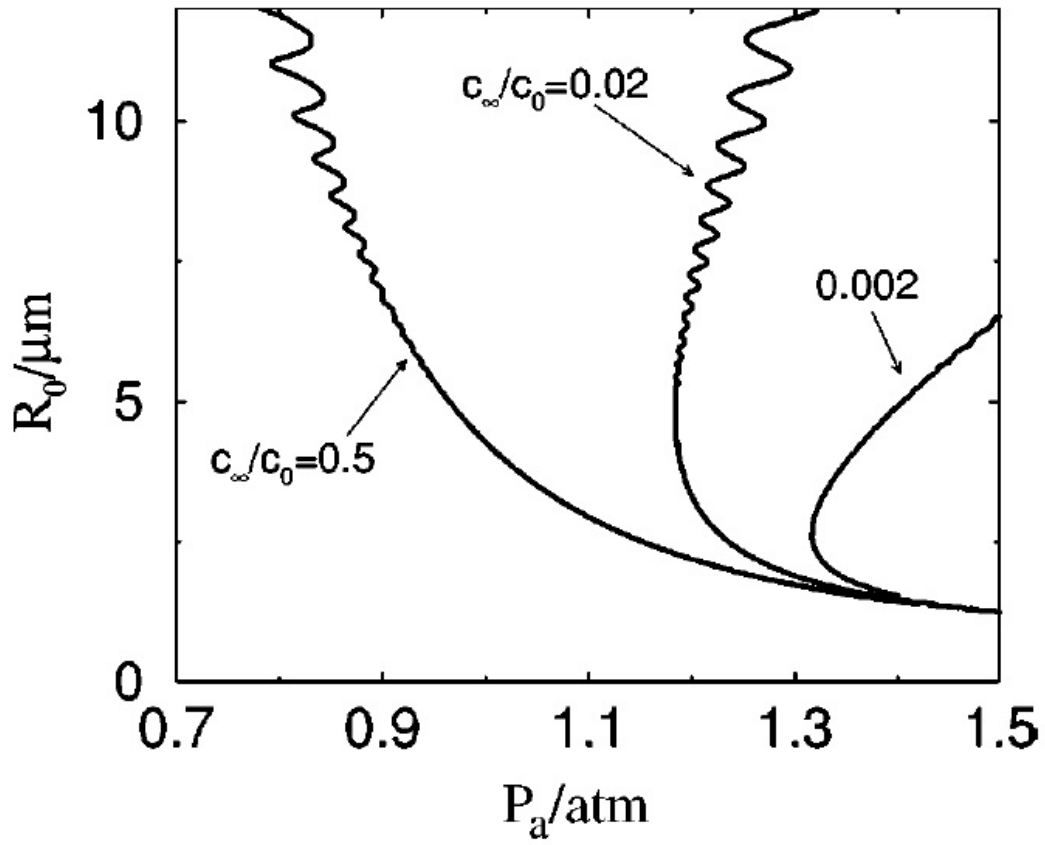

Figure B.9: The $R_0 - p_a$ parameter space. Stable regions are those with positive slope. To the left of the curves, bubbles dissolve, and to the right, bubbles grow by rectified diffusion. Note that the only stable bubbles have low gas concentrations. This figure is taken from [23] and we have changed notation from c to q in the text to avoid confusion with the speed of sound in the liquid.

concentration of air (N_2, O_2, etc.) is much greater.

To explain how stable sonoluminescence in water can occur with such a high concentration of air, we consider the chemical reactions occurring in the bubble. At maximum compression, the temperature in the bubble is high enough to dissociate both the O_2 and N_2 present in the vapor bubble. Most of the reaction products from the dissociated oxygen and nitrogen dissolve readily in water and will therefore quickly leave the bubble. The bubble then contains only inert argon. Since, in air, argon comprises only 1%, an air concentration of $q_\infty/q_0 \sim 0.2 - 0.4$ corresponds to an argon

concentration of $q_\infty/q_0 \sim 0.002 - 0.004$, which is needed for stable sonoluminescence. In order to achieve these gas concentrations in liquids other than water, it may be necessary to dissolve inert gases into the liquid.

Shape Stability

The shape of the bubble must also remain near spherical in order to not fracture upon the rapid collapse and subsequent expansion. We investigate the stability of the the spherical shape of the bubble (a summary of Plesset [24]), and begin by consider a small, first-order, perturbation in the radius $R(t)$ such that

$$r = R(t) + a_n(t)Y_n(\theta, \phi) \tag{B.125}$$

where Y_n is a spherical harmonic of degree n weighted by $a_n(t)$. The parameter $a_n(t)$ is termed the distortion amplitude, and controls the shape stability. To investigate the behavior of $a_n(t)$, as in the derivation of the Rayleigh-Plesset equation, we impose the boundary condition that the bubble wall velocity is given by

$$w = \dot{R} + \dot{a}_n Y_n. \tag{B.126}$$

The corresponding velocity potential is given by

$$\phi_{r<R} = \frac{R^2\dot{R}}{r} - \frac{r^2}{nR^{n-1}}Y_n\left(\dot{a} + 2a\frac{\dot{R}}{R}\right) \tag{B.127}$$

$$\phi_{r>R} = \frac{R^2\dot{R}}{r} + \frac{R^{n+2}}{(n+1)r^{n+1}}Y_n\left(\dot{a} + 2a\frac{\dot{R}}{R}\right). \tag{B.128}$$

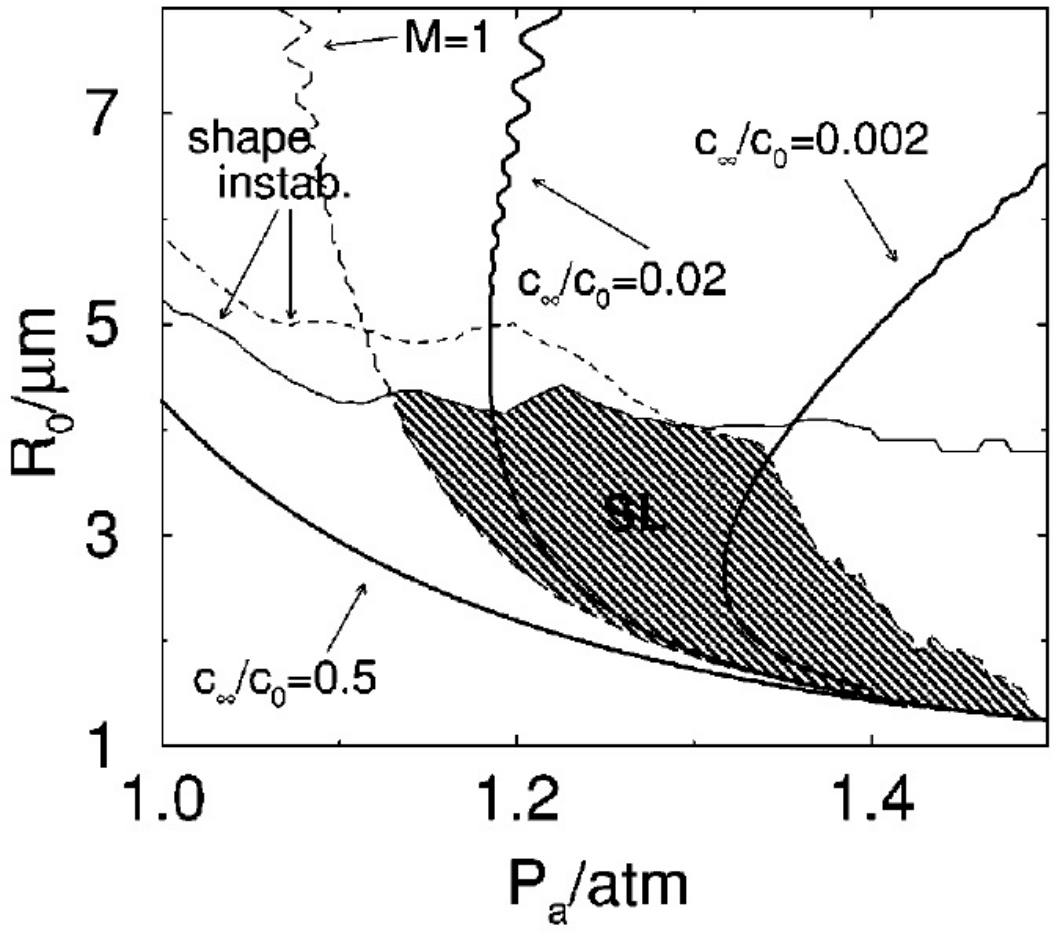

Figure B.10: Parameter space restrictions for sonoluminescing argon bubbles in water. The $M = 1$ curve (long-dashed) characterizes the onset of Rayleigh collapse and heating. The bubble grows thanks to rectified diffusion to the right of the diffusive stability curves (heavy lines, shown for q_∞/q_0 =0.5, 0.02, and 0.002, left to right, signified by c_∞/c_0 in this figure). The thin solid line marks the onset of the parametric instability and the short-dashed line combines the threshold of Rayleigh-Taylor instability and afterbounce instabilities. These lines are calculated within the simplified theory of [23], which slightly underestimates the shape stability. This figure is taken from [22].

If viscous effects are neglected, an equation for a_n may be written as

$$\ddot{a_n} + \frac{3\dot{R}}{R}\dot{a}_n - \left[(n-1)\frac{\ddot{R}}{R} - \frac{(n-1)(n+1)(n+2)\sigma}{\rho_f R^3}\right]a_n = 0. \tag{B.129}$$

Including viscosity, with vorticity is limited a thin layer of thickness δ, the dynamics of the distortion amplitude are then

$$\begin{aligned} 0 \;=\; & \ddot{a_n} + \left\{\frac{3\dot{R}}{R} + \frac{2\nu}{R^2}\left[-(n-1)(n+1)(n+2) + \frac{n(n+2)^2}{1+\frac{2\delta}{R}}\right]\right\}\dot{a}_n \\ & -\left\{(n-1)\frac{\ddot{R}}{R} - \frac{(n-1)(n+1)(n+2)\sigma}{\rho_f R^3}\right. \\ & \left. +\frac{2\nu\dot{R}}{R^3}\left[-(n-1)(n+1)(n+2) + \frac{n(n-1)(n+2)}{1+\frac{2\delta}{R}}\right]\right\}a_n, \end{aligned} \tag{B.130}$$

where ν is the kinematic viscosity. The second $\dot{a}_n$ term is responsible for exponentially dampening shape modulations. The equation governing shape instabilities is contingent on the highly non-linear Rayleigh-Plesset equation and therefore difficult to solve. However, it leads to shape instabilities on different time scales:

1. *Parametric instabilities:* These instabilities act on the time scale of the oscillation period. However, even though this time period is long, perturbations over this time period may eventually lead to the destruction of the bubble. When analyzing the parametric stability for eq. B.130, it is found that for the typical parameter range for sonoluminescence ($p_a \approx 1.2 - 1.5$ atm and $f = 26.5$ kHz), instability occurs for ambient radii greater than $R_0 \approx 4 - 5$ μm and depends weakly on p_a.

2. *Aferbounce instabilities:* After Rayleigh collapse, the bubble goes through a period of afterbounces that oscillate at the bubbles natural resonance frequency (~ 0.3 μs). The characteristic period for shape oscillations about the bubble are given by

$$\sqrt{\frac{\rho_f R_0^3}{\gamma(n-1)(n+1)(n+2)}} \approx 3 \ \mu\text{s} \qquad \text{for } n = 2, \tag{B.131}$$

which is close to the resonance frequency of the bubble and thus a cause of instability. It is possible that this instability is great enough to destroy the bubble at the first afterbounce. The afterbounces may also exacerbate an initial distortion to the point of bubble destruction.

3. *Rayleigh-Taylor instabilities:* These instabilities may occur whenever a less dense fluid is accelerated into a dense fluid. During the bubble cycle, this happens at the point of Rayleigh collapse. Therefore, any Rayleigh-Taylor instabilities will occur over a very short time scale, on the order of nanoseconds. Calculation of the Rayleigh-Taylor instability is difficult because the Rayleigh-Plesset equation does not hold for the point of Rayleigh collapse. Initial considerations point to Rayleigh-Taylor instabilities becoming important at very high driving pressures where the Bjernkes forces also come into play.

If all the above considerations of the parameter space of sonoluminescence are taken into account, the parameter space of stable sonoluminescence can be derived and is shown in Fig. B.10. This does not include the effects of temperature dependence, where lower temperatures allow for stronger driving pressures and result in a higher

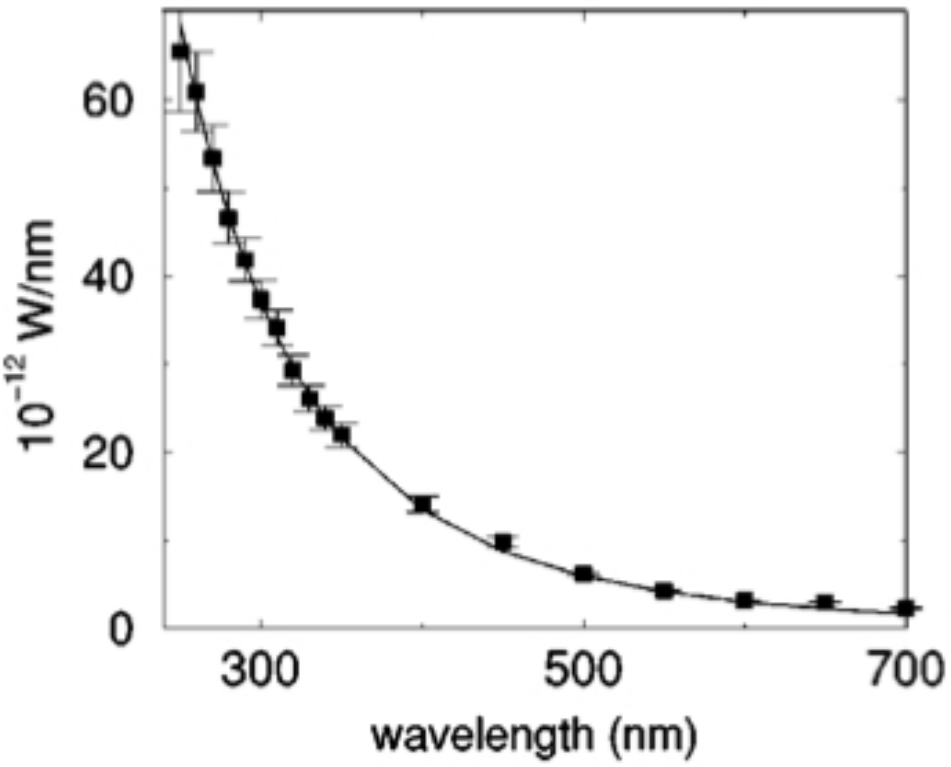

Figure B.11: Spectrum of single-bubble sonoluminescence, for water at 22 °C is shown from [22].

intensity from a bubble undergoing sonoluminescence.

B.5.3 Light Emission

At the point of Rayleigh collapse sonoluminescence may occur. This produces light pulses in phase with the driving pressure from the transducers attached to the bubble chamber. The spectrum of single-bubble sonoluminescence is smooth and continuous without the appearance of any spectral lines. From Brenner et al. [22], this can be seen in Fig. B.11 for sonoluminescence in water and Fig. B.12 for a 0.1 M sodium chloride solution. In the case of water, there is evidence for emission lines (see Fig. B.13) from excited OH at 310 nm and 337 nm during unstable sonoluminescence

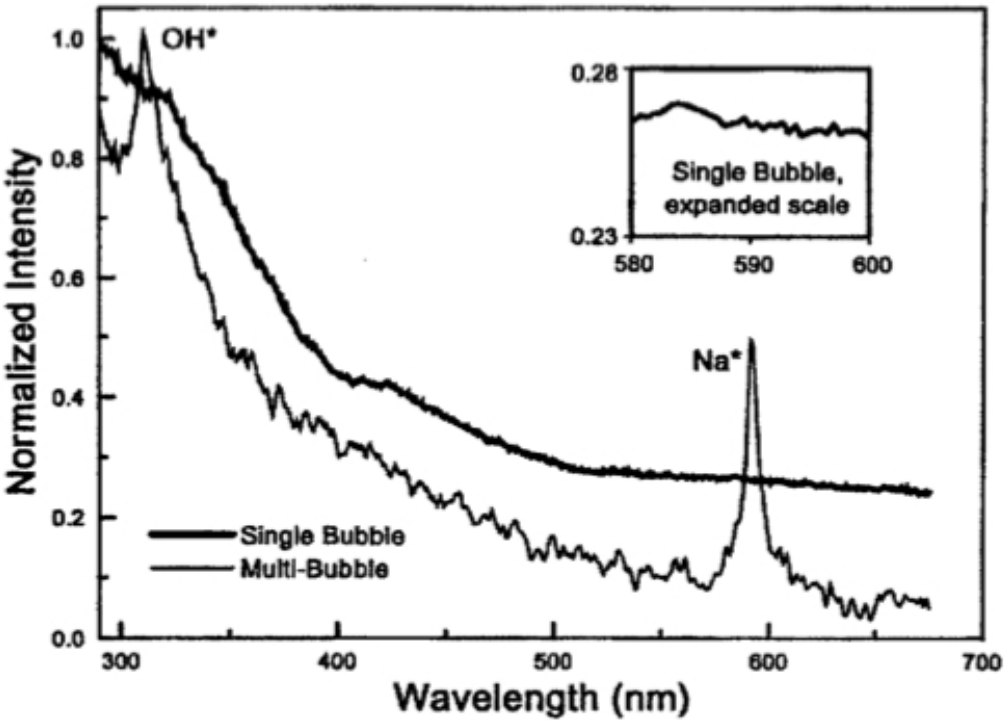

Figure B.12: The spectrum from multi-bubble sonoluminescence (thin line) and singe-bubble sonoluminescence (thick line) spectra in a 0.1M sodium chloride solution are shown. Each spectrum was normalized to its highest intensity. Note the prominence (MBSL) and absence (SBSL, see the inset for an enlargement) of the sodium line near 589 nm. This figure is from Brenner et al. [22].

where the bubble gyrates around the pressure antinode in the sound field. In these cases, the emitted light intensity is low, suggesting that emission lines are generally swamped by the smooth continuous emission.

The exact mechanism for sonoluminescence is currently unknown, but explanations have included a dynamical Casimir force, electrical breakdown, sparks from water jets, asymmetric bubble collapse (fractoluminescence), and thermal processes including molecular recombination, collision-induced emission, molecular emission, excimers, atomic recombination, radiative attachment of ions, and neutral and ion bremsstrahlung radiation. At first, attempts were made to explain the light emission

as a blackbody process. Blackbody emitters predict a pulse width greater than observations with an intensity two orders of magnitude too high. The currently theory of single-bubble sonoluminescence is that the bubble acts as thermal volume emitter. In these models, the bubble is transparent to its own photons. This differs from theories of blackbody radiation, which assume the bubble absorbs all frequencies. The transparent bubble theory is the only theory that explains the frequency independence of the single-bubble sonoluminescence spectrum. The light is created by electron-ion bremsstrahlung, electron-neutral bremsstrahlung, and radioactive recombination, with none of these dominating the emission process. The thermal volume emitter theory also agrees with experiments in the number of photons emitted. It should be noted that the current models are very simple and do not include the effects of water vapor on the bubble temperature, chemical reactions inside the bubble, or possible emission from molecular components.

Sonoluminescence in liquids other than water have different intesntities of light emission due to the different chemical reactions occurring inside the bubble as well as the chemical properties of the liquid. It was discovered shortly after the discovery of single-bubble sonoluminescence that mixing water with freely miscible liquids or dissolving salts in water did not prohibit stable single-bubble sonoluminescence. Weak, unstable single-bubble sonoluminescence has been seen in alcohols such n-dodecane, 1-pentanol, 1-butanol, Si oil, ethanol, 1-propanol, and 2-proponal. Formamide and adiponitrile produced strong light emission and were the first liquids where spectral lines were observed, though their bubbles were shown to be in unstable orbits around the antinode in the standing pressure field. It is unknown which other liquids may

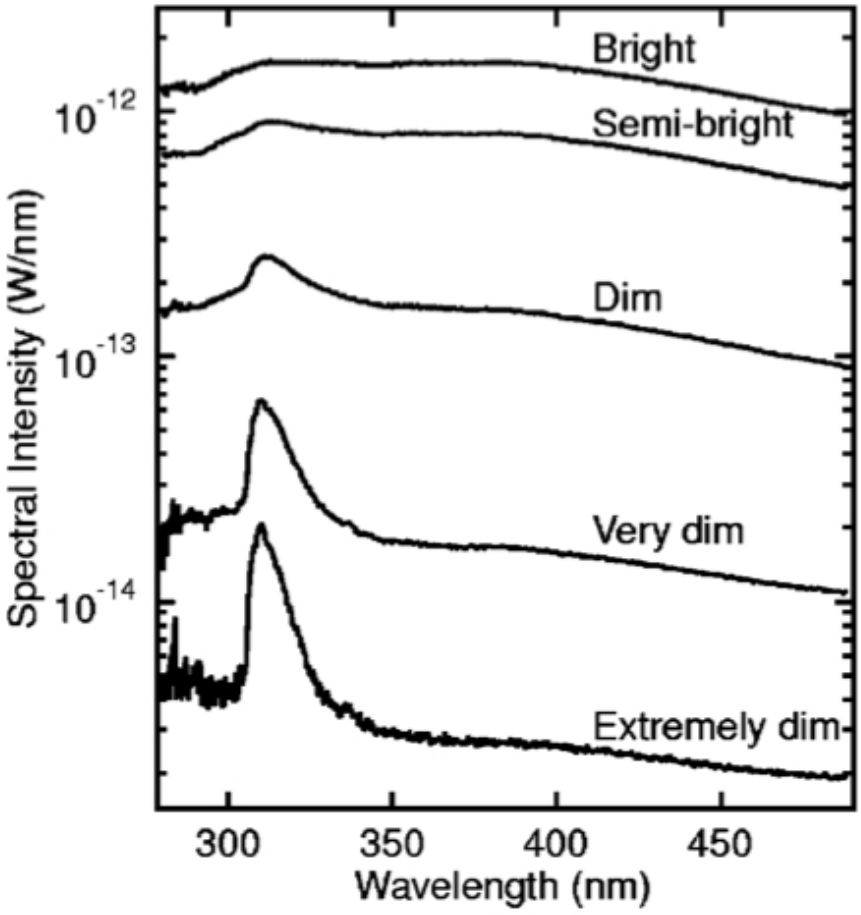

Figure B.13: The dependence of the spectra of argon single-bubble sonoluminescence (for a partial pressure of ∼150 torr at 25 °C) on the forcing pressure is shown. Spectra are shown for five levels of overall brightness. The OH line is vanishing in the thermal bremsstrahlung spectrum with increasing forcing pressure p_a. This figure is from Brenner et al. [22].

exhibit sonoluminescence or under what conditions it may occur.

B.6 Ultrasonic Bubble Chambers as Dark Matter Detectors

In Section B.2 the current generation of bubble chambers was discussed. Heavy refrigerants are used in these bubble chambers because of their high content of nuclei

such as fluorine. It has also been shown by these and other experiments that bubble chambers are threshold detectors meaning that only particles particles greater than a certain energy will cause cavitation in the chamber. This provides a powerful discrimination against many potential backgrounds such as cosmic-ray muons, which must be shielded against in other dark matter experiments. The background then only comes from neutrons and alpha particles from the rock surrounding the underground experiments or from any radioactivity from the components of the apparatus. The main challenge in current dark matter bubble chambers is avoiding spontaneous nucleation caused by impurities in the detector liquid or from surface defects in the vessel. COUPP, which does not use a gel matrix to mitigate these problem, the glass bell jar must be made exceedingly smooth and the liquid must be made free of any impurities in order to achieve the active lifetime needed for dark matter detection. In the superheated droplet detectors, the gel matrix obviates the problems from impurities or surface defects but significantly decreases the active mass of the detectors. Progress in both types of bubble chambers has been extraordinary, but there is still much to be done to stay competitive with the liquid nobel and cryogenic crystal detectors.

The experiments on triggered cavitation in acoustic fields mentioned in Section B.4 and described in West [16] and elsewhere in the literature showed that heavy refrigerants such as Freon-113 ($Cl_2FC\text{-}CClF_2$) [17, 18], Freon-11 (CCl_3F) [19, 20], Freon-114B2 ($C_2Br_2F_4$) [19], Freon-12 (CCl_2F_2) [19], Freon-115 (C_2ClF_5) [19], and C_2Cl_4 [21] are sensitive to recoil energies on the order of those expected from WIMP-like dark matter. These liquids would be ideal candidates for an ultrasonic dark

matter detector since they have already been studied in ultrasonic cavitation experiments and contain chlorine and/or fluorine nuclei. Ultrasonic cavitation in these liquid can be achieved at room temperatures with driving pressures around a few atmospheres.

The parameter space for Freon ultrasonic bubble chamber experiments is similar to the parameter space for single-bubble sonoluminescence in water. West and Howlett [21] reported seeing sonoluminescence flashes from some individual bubbles in C_2Cl_4, and Hahn and Peacock made the same claim about Freon 11 [19]. It is unlikely this was single-bubble sonoluminescence but instead multi-bubble sonoluminescence (a very different and well-understood process) as it would predate the widely reported discovery of single-bubble sonoluminescence in 1989 by more than two decades. In any case, seeing any sonoluminescence from these liquid is promising as it provides an additional means of studying the dark matter.

Ultrasonic bubble chambers trap single bubbles at an antinode in the standing acoustic field in the chamber. There, the bubble oscillates according to Rayleigh-Plesset equation as shown in Section B.5. It is possible to study this oscillating bubble even if it does not undergo sonoluminescence. Processes such as Mie scattering, where a laser is scattered off a spherical bubble, allow the radius of the bubble to be measured a function of time, which allows for the maximum and ambient radii to be determined. From these parameters and the formalism reviewed in section B.4, bounds can be placed on the energy deposited by the incident WIMP. This signal is in addition to the acoustic signals that are generated through the high-frequency oscillations of the bubble and those looked for in current dark matter bubble chambers

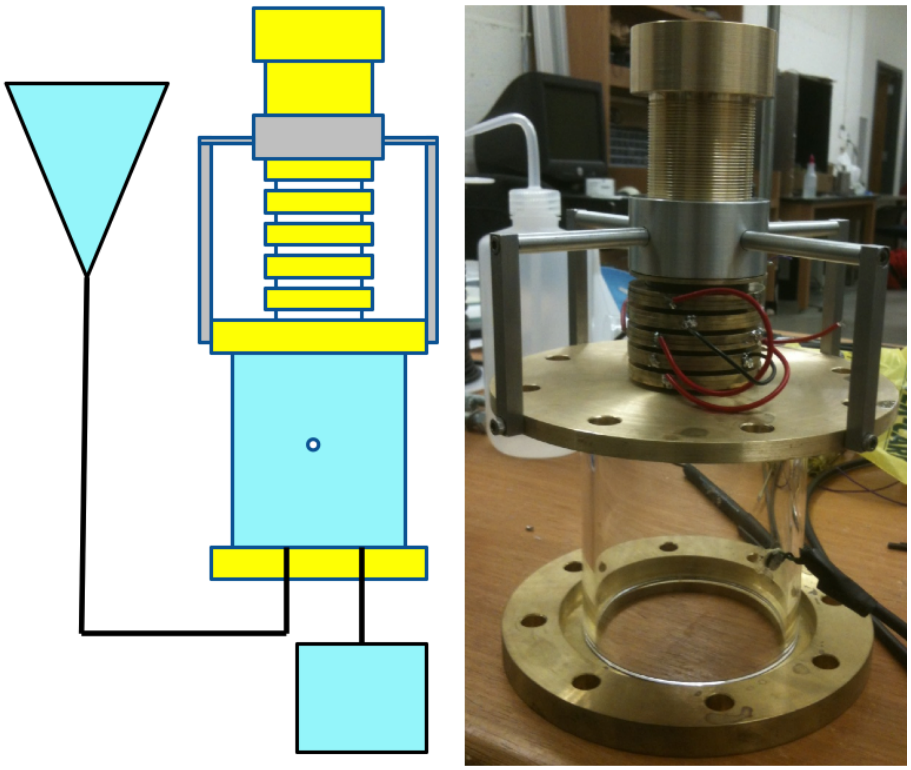

Figure B.14: An ultrasonic bubble chamber prototype.

from the initial deposit of energy by the WIMP. Microphone transducers are needed in the ultrasonic bubble chamber in order to tune the chamber to the appropriate driving frequency and are sensitive to the sound waves produced by the oscillating bubble. In addition, the stereoscopic imaging techniques of COUPP could also be used.

In Fig. B.14, we show a prototype that has been constructed at Washington University of an ultrasonic bubble chamber that has not yet been thoroughly tested. The chamber consists of a pyrex glass cylinder closed off by two brass plates. The current configuration of the chamber has a full brass cap on the bottom without the viewport shown in the picture. The driving pressure in the chamber is controlled by a stack of piezoelectric transducers affixed to the top of the chamber and wired

together in series. A large brass screw is threaded into an aluminum scaffolding in the top of the chamber to match the weight of the transducer stack to the top brass plate to maximize energy transfer to the plate. The top brass plate makes contact with the fluid inside the chamber and its vibration produces the standing wave in the chamber. A smaller transducer is affixed to the side of the chamber to be able to acoustically tune the chamber to its resonance frequency and to listen to the high-frequency vibrations from the oscillations of trapped bubbles.

The electronics on the bubble chamber are simple. The driving frequency of the transducer stack is controlled by a function generator that is fed into an audio amplifier. The small transducer on the side of the chamber can be read out directly by an oscilloscope.

The chamber as described here has been assembled, but much work is needed to improve the filling and draining mechanisms the chamber. After the plumbing of the chamber is improved, the chamber can be filled with degassed water and calibrated by producing single-bubble sonoluminescence from either nucleating a bubble via a boiling element of from high-energy neutrons. The chamber can then be filed with some kind of Freon or C_2Cl_4 and the response of the chamber to neutrons, alpha particles, and other radiation can be investigated. From a theoretical perspective, this method of detecting dark matter shows considerable promise.

References

[1] Archambault, S. et al., 2012, Phys. Lett. B, 711, 153

[2] Behnke, E. et al. 2011, PRL,106, 021303

[3] Felizardo, M. et al. 2012, PRL, 108, 201302

[4] Glaser, D. A., 1952, Phys. Rev. 87, 665

[5] Apfel, R. E. 1979, Nucl. Instr. Meth. 163, 603

[6] Giuliani, F., Morlat, T., & Girard, T. A. 2007, PRD, 75, 063503

[7] Morlat, T, et al. 2007, Nucl. Instr. Meth. Phys. Res. A, 580, 274

[8] Collar, J. et al. 2000, PRL, 85, 3083

[9] Archamault, S. et al. 2011, New J. Phys., 13, 043006

[10] Felizardo, M. et al. 2010, PRL, 105, 211301

[11] Neilson, R. 2012, "Dark Matter Search Results from COUPP 4 kg Bubble Chamber", talk, ICHEP, Melbourne

[12] Seitz, F. 1958, Phys. Fluids, 1, 2

[13] Aleksandrov, Y. A. et al. 1967, *Bubble Chambers*, Indiana University Press: Bloomington

[14] Henderson, C. 1970, *Could and Bubble Chambers*, Methuem and Co. Ltd: London

[15] Lieberman, D, 1959, Phys. Fluids, 2, 466

[16] West, C. D. 1998, ORNL/TM-13683, 263

[17] Hahn, B. 1961, Il Nuovo Cimento, 22, 650

[18] Greenspan, M. & Tschiegg, C. E. 1967, J. Res. Nat. Bur. Stand. C, 71, 299

[19] Hahn, B. & Peacock, N. 1963, Il Nuovo Cimento, 28, 334

[20] Greenspan, M. & Tschiegg, C. E. 1982, J. Acoust. Soc. Am. 72, 1327

[21] West, C. & Howlett, R. 1968, Britt. J. Appl. Phys. (J. Phys. D), 1, 247

[22] Brenner, M. P., Hilgenfeldt, S., & Lohse, D. 2002, Rev. Mod. Phys., 74, 425

[23] Hilgenfeldt, S., Lohse, D., & Brenner, M. P. 1966, Phys Fluids, 8, 2808

[24] Plesset, M. S., 1954, J. App. Phys., 25, 96

Appendix C

The Gravitational Potential of the Galactic Disk

This derivation follows from work by Toomre [1] and by Mo, van den Bosch and White [2] (hereafter MVW).

To derive the gravitational potential from a given density function, specifically that corresponding to a double-exponential disk, we first consider an infinitesimally thin disk of surface density

$$\Sigma(R) = \Sigma_0 e^{-R/R_d} \tag{C.1}$$

and apply those results to a disk of finite thickness.

Toomre states that if an arbitrary surface density $S(R)$ is expressed as a Bessel integral

$$S(R) = \int_0^\infty J_0(kR) k \tilde{S}(k) dk, \tag{C.2}$$

where

$$\tilde{S}(k) = \int_0^\infty J_0(kx) x S(x) dx, \tag{C.3}$$

then by the Fourier-Bessel integral theorem and because

$$d\Phi(R, z) = J_0(kR) e^{-k|z|} dk \tag{C.4}$$

satisfies the Poisson equation

$$\nabla^2 \Phi = -4\pi\rho G, \tag{C.5}$$

the total gravitational potential from the surface can be written as

$$\Phi(R, z) = 2\pi G \int_0^\infty J_1(kR) \tilde{S}(k) e^{-k|z|} dk. \tag{C.6}$$

In MVW, the total gravitational potential is given by

$$\Phi(R, z) = -2\pi G \int_0^\infty J_0(kR) \tilde{S}(k) e^{-k|z|} dk. \tag{C.7}$$

By applying the identity$J_0'(x) = -J_1(x)$, and integrating by parts, it can be shown that eqs. 6 and 7 are equal. Binney and Tremaine [3] give

$$\Phi(R, \phi, z) = -2\pi G \sum_{m=-\infty}^{\infty} \int_0^\infty dk e^{im\phi - k|z|} J_m(kR) \int_0^\infty dR' R' J_m(kR') \Sigma_m(R'), \tag{C.8}$$

agreeing with MVW for the axisymmetric $m = 0$ case.

The gravitational potential for the infinitesimally thin disk can then be calculated

by substituting the Fourier transform of eq. C.1 for $\tilde{S}(k)$ in eq. C.7. Noting the integral

$$\int_0^\infty J_0(kx) x e^{-x/R_d} dx = \frac{R_d^2}{(1+k^2 R_d^2)^{3/2}}, \tag{C.9}$$

we can write

$$\begin{aligned} \Phi(R,z) &= -2\pi G \int_0^\infty J_0(kR)\tilde{\Sigma}(k) e^{-k|z|} dk \\ &= -2\pi G \int_0^\infty J_0(kR) \int_0^\infty \Sigma_0 J_0(kx) x e^{-x/R_d} dx e^{-k|z|} dk \\ &= -2\pi G \Sigma_0 R_d^2 \int_0^\infty \frac{J_0(kR) e^{-k|z|}}{(1+k^2 R_d^2)^{3/2}} dk. \end{aligned} \tag{C.10}$$

This expression agrees with (11.4) in MVW.

Now we want to calculate the potential for a double-exponential disk. Following MVW, consider an infinitesimally thin disk with surface density $S(R,z) = \Sigma(R)\delta(z)$ where $\delta(z)$ is a Dirac delta function with the corresponding potential $\Phi(R,z) = g(R,z)$. $\Sigma(R)$ and $g(R,z)$ are arbitrary functions related by the Poisson equation. The disk can be thickened by replacing the Dirac delta function with a function $h(z)$ that describes the vertical density distribution. For the double-exponential disk, $h(z) = e^{-|z|/z_d}$. The potential of the thick disk is found by adding an infinite number of thin disks weighted by $h(z)$, i.e.

$$\Phi(R,z) = \int_{-\infty}^\infty g(R, z-z') h(z') dz'. \tag{C.11}$$

For an arbitrary density distribution $\rho(R,z)$,

$$\Phi(R,z) = -2\pi G \int_0^\infty dk J_0(kR) \int_{-\infty}^\infty dz' \tilde{\rho}(R,z') e^{-k|z-z'|} \tag{C.12}$$

where $\tilde{\rho}(R,z')$ is the Fourier-Bessel transform (eq. C.3) of $\rho(R,z)$ in the R variable. The double-exponential density distribution used to model the Galactic disk is given by

$$\rho(R,z) = \frac{\Sigma_0}{2z_d} e^{-R/R_d} e^{-|z|/z_d}. \tag{C.13}$$

We can now write down the potential, using eq. C.9 and eq. C.12.

$$\begin{aligned}
\Phi(R,z) &= -2\pi G \int_0^\infty dk J_0(kR) \int_{-\infty}^\infty dz' \tilde{\rho}(R,z') e^{-k|z-z'|} \\
&= -2\pi G \int_0^\infty dk J_0(kR) \int_{-\infty}^\infty dz' \int_0^\infty dx J_0(kx) x \rho(r,z') e^{-k|z-z'|} \\
&= -2\pi G \int_0^\infty dk J_0(kR) \int_{-\infty}^\infty dz' \int_0^\infty dx J_0(kx) x \frac{\Sigma_0}{2z_d} e^{-x/R_d} e^{-|z|/z_d} e^{-k|z-z'|} \\
&= -2\pi G \frac{\Sigma_0}{2z_d} \int_0^\infty dk J_0(kR) \int_{-\infty}^\infty dz' e^{-k|z-z'|} e^{-|z|/z_d} \int_0^\infty dx J_0(kx) x e^{-x/R_d} \\
&= -2\pi G \frac{\Sigma_0}{2z_d} \int_0^\infty dk J_0(kR) \int_{-\infty}^\infty dz' e^{-k|z-z'|} e^{-|z|/z_d} \frac{R_d^2}{(1+k^2R_d^2)^{3/2}} \\
&= -2\pi G \frac{\Sigma_0 R_d^2}{2z_d} \int_0^\infty dk \frac{J_0(kR)}{(1+k^2R_d^2)^{3/2}} \int_{-\infty}^\infty dz' e^{-k|z-z'|} e^{-|z|/z_d} \\
&= -2\pi G \frac{\Sigma_0 R_d^2}{2z_d} \int_0^\infty dk \frac{J_0(kR)}{(1+k^2R_d^2)^{3/2}} \left[\int_{-\infty}^0 dz' e^{-k(z-z')} e^{z/z_d} \right. \\
&\quad \left. + \int_0^z dz' e^{-k(z-z')} e^{-z/z_d} + \int_z^\infty dz' e^{k(z-z')} e^{-z/z_d} \right] \\
&= -2\pi G \frac{\Sigma_0 R_d^2}{2z_d} \int_0^\infty dk \frac{J_0(kR)}{(1+k^2R_d^2)^{3/2}} 2z_d \frac{e^{-k|z|} - (kz_d) e^{-|z|/z_d}}{1-k^2z_d^2} \\
&= -2\pi G \Sigma_0 R_d^2 \int_0^\infty dk \frac{J_0(kR)}{(1+k^2R_d^2)^{3/2}} \frac{e^{-k|z|} - (kz_d) e^{-|z|/z_d}}{1-k^2z_d^2}.
\end{aligned} \tag{C.14}$$

The above expression agrees with the formula given for the potential from a double-exponential disk in MVW (11.8) and the potentials we have used to characterize the thin and thick disk contributions to both the Galactic rotation curve and the local vertical force profile.

References

[1] Toomre, A. 1963, ApJ, 138, 385

[2] Mo, H., van den Bosch, F., and White, S. *Galaxy Formation and Evolution* (Cambridge University Press, Cambridge, 2010) p.496

[3] Binney, J. and Tremaine, S. *Galactic Dynamics* (Pinceton University Press, Princeton, 2008) p.106

Appendix D

Code for Solving Poisson's Equation

```
1         program GalacticDM
2 c This code is used to calculate the dark matter distribution
3 c in the Galaxy given a distribution of visible matter. It
4 c uses some parts of the king_gen program written by Dr.
5 c Pijush Bhattacharjee to solve Poisson's equation and to
6 c derive the dark matter properties.The ability to calculate
7 c the dark matter distribution for an arbitrary set of dark
8 c matter parameters in an interative manner has been added as
9 c well as the calculation of the verical force. The visible
10 c potential has been modified to reflect that developed after
11 c an extensive survey of the visible matter distribution in
12 c the Milky  Way.
```

```
13 c
14 c SOME GENERAL NOTES:
15 c --All integrals are done by a sum over a large number of
16 c grid points by either a trapezoidal method or Simspon's
17 c method
18 c --Any visible matter potential can be used by changing the
19 c appropriate parameters in the vis_matter subroutine
20 c --A lowered isothermal (King) distribution is used for dark
21 c matter phase-space distribution
22 c --Reference to Binney and Tremaine (B&T hereafter) will be
23 c to the 2nd Edition --As written in Dr. Bhattacharjee's code:
24 c "Given the density at all grid points, the poisson eq.
25 c \nabla^2\Phi=4\pi G\rho in 2-dim
26 c (axisymmetric) case is solved by SPHERICAL HARMONICS
27 c expansion method. Actually, it solves the scaled
28 c (dimensionless) Poisson eqn.
29 c \nabla^2\phi=\lambda\rho, where now \phi, and \rho are
30 c dimensionless potentials and density respectively defined as
31 c follows:
32 c \Phi=vstar^2 * \phi, \rho_dimensional=rhostar*\rho, and
33 c \nabla^2_dimensional=lstar^{-2}\nabla^2.
34 c The scale factors are lstar=1 kpc, vstar=100 km.s^{-1},
```

```
c rhostar=1 GeV.cm^{-3}.
c The length coordinate is r_dimensional=lstar*r.
c With these scale factors, lambda=0.142306067. So, the rho,
c phi, r, etc. are dimensionless as in
c C.P. Wilson, Astron.J. 80 (1975) 175."
c ----------------------------------------------------------------
      implicit real*8(a-h,o-z)
      parameter(itmax=50,irmax=1002,ictmax=1001,kmax=16,
     1   nkmax=(kmax+2)/2)
      common r(irmax),ct(ictmax),am(irmax),rking
      common point,sigma
      dimension rhovis(irmax,ictmax),phivis(irmax,ictmax),
     1 amvis(irmax)
      dimension rhodm(irmax,ictmax),phidm(irmax,ictmax),
     1 amdm(irmax)
      dimension psi(irmax,ictmax),phidmp(irmax,ictmax),
     1 v_c(irmax)
      dimension vdisp(irmax,ictmax),v_esc(irmax,ictmax)
      character(80)  :: filename1 = ' ',filename2 = ' ',
     1   filename3 = ' ', filename4 = ' ',filename5 = ' ',
     1   filename6 = ' '
      external func0,func2
```

```
57          iz=350
58  c Here is where the limits on the contral dark matter density
59  c irho, the sigma paramter, jsig, and the factor parameter can
60  c be set for the iterative solution of many dark matter models
61          do 71 irho=500,500,1
62                  arho=500
63          do 72 jsig=145,155,5
64                  asig=jsig/100d0
65          do 73 kfac=17,17,1
66                  afac=kfac*1d0
67  c Open the various data files to be written
68          write(filename1,'(a,i3.3,a,i3.3,a,i3.3,a)')'potential',
69         1 irho,'_',jsig,'_',kfac,'.dat'
70          write(filename2,'(a,i3.3,a,i3.3,a,i3.3,a)')'speeds',
71         1 irho,'_',jsig,'_',kfac,'.dat'
72          write(filename3,'(a,i3.3,a,i3.3,a,i3.3,a)')'densities',
73         1 irho,'_',jsig,'_',kfac,'.dat'
74          write(filename4,'(a,i3.3,a,i3.3,a,i3.3,a)')'masses',
75         1 irho,'_',jsig,'_',kfac,'.dat'
76          write(filename5,'(a,i3.3,a,i3.3,a,i3.3,a)')'slopes',
77         1 irho,'_',jsig,'_',kfac,'.dat'
78          write(filename6,'(a,i3.3,a,i3.3,a,i3.3,a)')'force',
```

```
79        1 irho,'_',jsig,'_',kfac,'.dat'
80          open(7,file=filename1,status='unknown')
81          open(8,file=filename2,status='unknown')
82          open(9,file=filename3,status='unknown')
83          open(10,file=filename4,status='unknown')
84          open(27,file=filename5,status='unknown')
85          open(28,file=filename6,status='unknown')
86  c ---------------------------------------
87            pi=3.141592653589793d0
88  c ---------------------------------------
89  c Unlike Dr. Bhattacharjee's program, this program iterates
90  c over many dark matter models so the user is not prompted
91  c for the dark matter model parameters are before
92          rhodm0=arho
93          sigma=asig
94          factor=afac
95          sigma2=sigma*sigma
96  c psi0 determines the truncation radius of the King distribution.
97          psi0=factor*sigma2
98  c down is the denominator in the expression for rhodm
99  c (B&T 4.111 when reformulated for rho_0 instead of rho_1)
100             down1=dexp(psi0/sigma2)*derf(dsqrt(psi0/sigma2))
```

```
101               down2=dsqrt(4.d0*psi0/(pi*sigma2))*
102      1           (1.d0+(2.d0*psi0)/(3.d0*sigma2))
103               down=down1-down2
104            if(down.le.0.d0)pause 'denominator in rhodm is <= 0'
105  c rking is the King radius (B&T 4.106) defined as
106  c rking=Sqrt[(9 sigma^2)/(4 Pi G rhodm0)]
107             rking=7.952607d0*sigma/dsqrt(rhodm0)
108  c phidm0 is the central boundary condition
109             phidm0=0.d0
110  c The gridpoints are defined here
111            r(1)=0.d0
112            r(2)=0.005d0
113            do 11 ir=3,irmax
114            if(r(ir-1).gt.100.d0)then
115             r(ir)=1.04d0*r(ir-1)
116            else
117             r(ir)=1.04d0*r(ir-1)
118            endif
119   11       continue
120            dct=0.001d0
121            do 12 ict=1,ictmax
122              ct(ict)=(ict-1)*dct
```

```
123 c          print*,'ict=',ict,'ctheta=',ct(ict)
124  12     continue
125 c ----------------
126 c In Dr. Bhattacharjee's code was checked by comparing the
127 c solutions from a Miamoto-Nagai potential to the analytic
128 c solutions. This code was also checked this was, but these
129 c functions have been removed for clarity. Here we call the
130 c subroutine which defines the visible density of the Milky
131 c Way. The visible potential is calculated by the
132 c Poisson solver.
133         call vis_matter(rhovis,phivis)
134 c The visible mass within r(ir) is stored, and the dark
135 c matter potential is initialized here.
136         do 95 ir=1,irmax
137          amvis(ir)=am(ir)
138          do 96 ict=1,ictmax
139           phidm(ir,ict)=0.d0
140  96      continue
141  95      continue
142 c THIS IS THE MAIN LOOP
143         do 81 it=1,itmax
144           do 17 ict=1,ictmax
```

```
145 c The central dark matter density and potential are define
146 c and the previous DM potential is recorded
147             rhodm(1,ict)=rhodm0
148             phidmp(1,ict)=phidm(1,ict)
149             psi(1,ict)=psi0
150             do 18 ir=2,irmax
151 c The scaled potential Phi is calculated here.
152             psi(ir,ict)=psi0-(phidm(ir,ict)+phivis(ir,ict))
153 c            if(psi(ir,ict).le.0.d0)print*,'psi(ir,ict)=',
154 c     1        psi(ir,ict),'ir=',ir
155             if(psi(ir,ict).le.0.d0)psi(ir,ict)=0.d0
156 c Up is the numerator to calculating the dark matter density
157 c (B&T 4.111). Down was defined before the main loop.
158             up1=dexp(psi(ir,ict)/sigma2)*
159      1       derf(dsqrt(psi(ir,ict)/sigma2))
160             up2=dsqrt(4.d0*psi(ir,ict)/(pi*sigma2))*
161      1       (1.d0+(2.d0*psi(ir,ict))/(3.d0*sigma2))
162             up=up1-up2
163 c The dark matter density is calculated and cuts off at
164 c zero density.
165             if(up.le.0.d0)then
166                rhodm(ir,ict)=0.d0
```

```
167              else
168                  rhodm(ir,ict)=rhodm0*up/down
169              endif
170               phidmp(ir,ict)=phidm(ir,ict)
171   18         continue
172   17        continue
173  c The Poisson solver is is called to colve for the dark
174  c matter potential at each point after calculating the
175  c density above.
176           call poisson(rhodm0,phidm0,rhodm,phidm)
177  c Now check convergence
178           if(it.eq.1)go to 81
179           print*,'phidm(4,4)=',phidm(4,4),'
180       1    phidmp(4,4)=',phidmp(4,4)
181           test=(phidm(4,4)-phidmp(4,4))/phidmp(4,4)
182           print*,'it=',it,'  conv test=',test
183           amdm(1)=am(1)
184           do 19 ir=2,irmax
185  c  The dark matter mass within r(ir) is recorded as amdm
186            amdm(ir)=am(ir)
187            do 20 ict=1,ictmax
188           if(dabs((phidm(ir,ict)-phidmp(ir,ict))/phidmp(ir,ict)).
```

```
189       1       le.1.d-4)then
190          iconv=1
191         else
192          iconv=0
193         endif
194         if(iconv.eq.0)go to 81
195   20    continue
196   19    continue
197         go to 101
198   81     continue
199  c The number of iterations is printed
200   101        print*,'it=',it
201         if(iconv.eq.0)print*,'no convergence in itmax=',itmax
202          print*,'it=',it,'  itmax=',itmax
203  c The headers to all the data files are written here
204         write(*,103)sigma,rhodm0,factor,it,itmax
205         write(7,104)sigma,rhodm0,factor,it,rking
206         write(8,103)sigma,rhodm0,factor,it,itmax
207         write(8,*)'%rtilde    r      v_c      v_esc    vdisp'
208         write(9,103)sigma,rhodm0,factor,it,itmax
209
210         write(9,*)'%rtilde    r     rhodm      rhovis   rhotot'
```

```
211           write(10,103)sigma,rhodm0,factor,it,itmax
212           write(10,*)'%rtilde   r    amdm    amvis    amtot'
213           write(27,103)sigma,rhodm0,factor,it,itmax
214           write(27,*)'%rtilde     r    sldm1     slvis1'
215           write(28,103)sigma,rhodm0,factor,it,itmax
216           write(28,*)'r     z     force     psiro'
217    103    format(1x,'%sigma=',d11.4,1x,'rhodm0=',d11.4,1x,
218         1   'factor=',d11.4,1x,'it=',i3,1x,'itmax=',i3)
219    104    format(1x,'%sigma=',d11.4,1x,'rhodm0=',d11.4,1x,
220         1   'factor=',d11.4,1x,'it=',i3,1x,'rking=',d11.4)
221   c Here, the rotational speed, velocity dispersion, escape
222   c velocity, and vertical force are calculated.
223           do 92 ict=1,ictmax
224            vdisp(irmax,ict)=0.d0
225             do 93 ir=1,irmax-1
226             if (ict.eq.1)then
227   c The circular speed is calculate here
228               v_c(ir)=dsqrt(r(ir)*(phivis(ir+1,1)-phivis(ir,1)+
229         1          phidm(ir+1,1)-phidm(ir,1))/(r(ir+1)-r(ir)))
230             endif
231   c The potential for the vertical force is exported here.Given
232   c the grid spacing, it is difficult  to get points are exactl
```

```
233 c R=8.3 kpc so points around there are collected. The final
234 c vertical force is interpolated from these points using
235 c Mathematica.
236           rx=r(ir)*dsqrt(1-ct(ict)*ct(ict))
237           if (rx.ge.8.0.and.rx.le.8.4)then
238           zcoord=r(ir)*ct(ict)
239           phiro=phivis(ir,ict)+phidm(ir,ict)
240           psiro=psi(ir,ict)
241           write(28,128)rx,zcoord,phiro,psiro
242  128      format(d11.4,1x,d11.4,1x,d11.4,1x,d11.4)
243           end if
244           if (ir.eq.1.and.ict.ge.2)then
245             vdisp(1,ict)=vdisp(1,1)
246           else
247            uplim=dsqrt(2.d0*psi(ir,ict))
248 c The escape velocity is calculated here as sqrt[2*Psi(r,z)].
249            v_esc(ir,ict)=uplim
250            point=psi(ir,ict)
251             if(uplim.le.0.d0)then
252 c The velocity dispersion is calcualted as the ratio of the
253 c two integrals Int[v^2 f(v) dv]/Int[v^2 f(v) dv] where the
254 c integrals are calculated by the Simpson's method subroutine.
```

```
255              vdisp(ir,ict)=0.d0
256             else
257              call qsimp(func0,0.d0,uplim,aj0)
258              call qsimp(func2,0.d0,uplim,aj2)
259              vdisp(ir,ict)=dsqrt(aj2/aj0)
260             endif
261           endif
262           if (ict.eq.1)then
263  c The total density, mass, and rtilde are computer here.
264            rhotot=rhodm(ir,1)+rhovis(ir,1)
265            amtot=amdm(ir)+amvis(ir)
266            rtilde=r(ir)/rking
267  c The logarithmic close of the visible and dm densities are
268  c calculated here
269            if(ir.ne.1)then
270            dmln1=dlog(rhodm(ir,1))
271            dmln2=dlog(rhodm(ir+1,1))
272            visln1=dlog(rhovis(ir,1))
273            visln2=dlog(rhovis(ir+1,1))
274              rln1=dlog(r(ir))
275              rln2=dlog(r(ir+1))
276              sldm1=(dmln2-dmln1)/(rln2-rln1)
```

```
277 c sldm1 is the logarithmic slope of rhodm:
278 c sldm1=d(ln(rhodm))/d(ln(r))
279 c          sldm=sldm1*rhodm(ir,1)/r(ir)
280 c sldm is the slope of rhodm: sldm=d(rhodm)/d(r)
281            slvis1=(visln2-visln1)/(rln2-rln1)
282 c slvis1 is the logarithmic slope of rhovis:
283 c slvis1=d(ln(rhovis))/d(ln(r))
284 c          slvis=slvis1*rhovis(ir,1)/r(ir)
285 c slvis is the slope of rhovis: slvis=d(rhovis)/d(r)
286          endif
287          if(ir.ne.1)then
288            print*,'rtilde      r      sldm1      slvis1'
289            write(*,127)rtilde,r(ir),sldm1,slvis1
290            print*,'-----------------------------------------'
291          endif
292          print*,'rtilde    r      v_c      v_esc    vdisp'
293          write(*,102)rtilde,r(ir),v_c(ir),v_esc(ir,1),
294        1   vdisp(ir,1)
295          print*,'-----------------------------------------'
296          print*,'rtilde    r     rhodm      rhovis    rhotot'
297          write(*,102)rtilde,r(ir),rhodm(ir,1),rhovis(ir,1),
298        1   rhotot
```

```
299           print*,'-------------------------------------------------'
300           print*,'rtilde      r      amdm      amvis          amtot'
301           write(*,102)rtilde,r(ir),amdm(ir),amvis(ir),amtot
302           print*,'-------------------------------------------------'
303           write(7,106)r(ir),psi(ir,1)
304           write(8,102)rtilde,r(ir),v_c(ir),v_esc(ir,1),
305          1   vdisp(ir,1)
306           write(9,102)rtilde,r(ir),rhodm(ir,1),rhovis(ir,1),
307          1   rhotot
308           write(10,102)rtilde,r(ir),amdm(ir),amvis(ir),amtot
309           if(ir.ne.1)then
310             write(27,127)rtilde,r(ir),sldm1,slvis1
311             print*,'-----------------------------------------'
312           endif
313   102     format(d11.4,1x,d11.4,1x,d11.4,1x,d11.4,1x,d11.4)
314   106     format(d11.4,1x,d11.4)
315   127     format(d11.4,1x,d11.4,1x,d11.4,1x,d11.4)
316         endif
317   93    continue
318         v_esc(irmax,ict)=dsqrt(2.d0*psi(irmax,ict))
319   92    continue
320          v_c(irmax)=v_c(irmax-1)
```

```
321 c         close(7)
322           close(8)
323           close(9)
324           close(10)
325           close(27)
326           close(28)
327    73     continue
328    72     continue
329    71     continue
330           stop
331           end
332   c END OF THE MAIN PROGRAM
333   c Here the subroutines start.
334   c ---------------------------------------------------------------
335           subroutine vis_matter(rhovis,phivis)
336   c In this subroutine, the density profile for the Milky Way
337   c is given. The potential of the Milky Way is calculated via
338   c the Poisson subroutine
339           implicit double precision(a-h,o-z)
340           parameter(irmax=1002,ictmax=1001)
341           common r(irmax),ct(ictmax),am(irmax),rking
342           dimension rhovis(irmax,ictmax),phivis(irmax,ictmax)
```

```
343 c ------------
344         pi=3.141592653589793d0
345 c Give the parameters of the model:
346         rsun=8.3d0
347 c rsun is the Galactocentric distance of the Sun in kpc
348         disksd1=90.d0
349         disksd2=10.d0
350 c disksd is the disk surface density in units of
351 c M_{sun}.pc^{-2} at the solar radius.
352 c Note, below we make the conversion pc^(-2)=10^6 kpc^(-2).
353         disksh1=0.35d0
354         disksh2=0.9d0
355 c disksh is the disk scale height in units of kpc.
356         disksl1=3.d0
357         disksl2=3.5d0
358 c disksl is the disk scale length in units of kpc.
359         blgm=1.02d10
360 c        blgm=100000.d0
361         blgb=0.25814952431130184d0
362 c        blgb=10.d0
363 c blgm is the bulge mass in M_sol
364 c blgb is the b parameter of the Plummer model in kpc
```

```
365           fact1=3.797861165d03
366           fact2=fact1/1.d11
367   c fact1=[10^{11}M_{sun}/(1 kpc)^3]/rhostar
368           rhov1=fact1*(disksd1*1.d-5/(2.d0*disksh1)
369          1          *dexp(rsun/disksl1))
370           rhov2=fact1*(disksd2*1.d-5/(2.d0*disksh2)
371          1          *dexp(rsun/disksl2))
372           rhoblg0=fact2*3*blgm/(4*pi*blgb*blgb*blgb)
373           rhov0=rhov1+rhov2+rhoblg0
374   c        rhov=rhoblg0
375   c Put the central potential zero as the boundary condition.
376           phiv0=0.d0
377           do 25 ict=1,ictmax
378              rhovis(1,ict)=rhov0
379   c Initialize phivis(1,ict)=0
380            phivis(1,ict)=0.d0
381           do 26 ir=2,irmax
382            z=r(ir)*ct(ict)
383            rcap=r(ir)*dsqrt(1.d0-ct(ict)*ct(ict))
384            rhonum=3.d0*blgm/(4.d0*pi*blgb*blgb*blgb)
385            rhodom=(1.d0+r(ir)*r(ir)/(blgb*blgb))**(-5.d0/2.d0)
386   c rhoblg is the bulge density given by the Plummer Model
```

```
387           rhoblg=fact2*rhonum*rhodom
388  c rhdisk1/2 are the two disk components
389           rhodsk1=fact1*disksd1*1.d-5/(2.d0*disksh1)
390         1   *dexp(-(rcap-rsun)/disksl1)*dexp(-z/disksh1)
391           rhodsk2=fact1*disksd2*1.d-5/(2.d0*disksh2)
392         1   *dexp(-(rcap-rsun)/disksl2)*dexp(-z/disksh2)
393           rhodsk=rhodsk1+rhodsk2
394  c ------------------------------------------------------
395             rhovis(ir,ict)=rhoblg+rhodsk
396             rtilde=r(ir)/rking
397             if(rtilde.ge.25.0d0)rhovis(ir,ict)=0.d0
398  c ------------------------------------------------------
399  c Initialize all the other phivis(ir,ict)=0
400             phivis(ir,ict)=0.d0
401    26       continue
402    25       continue
403           call poisson(rhov0,phiv0,rhovis,phivis)
404  c So now we have all the phivis(ir,ict).
405           return
406           end
407  c ******************************************************
408           subroutine poisson(rho0,phi0,rho,phi)
```

```
c This is the poisson subroutine as written by
c Dr. Bhattacharjee (most of his comments are left unaltered
c in this subroutine) using the methods of Wilson, Pendergast
c and Tomer.
c ***************************************************
      implicit real*8(a-h,o-z)
      parameter(irmax=1002,ictmax=1001,kmax=16,
     1 nkmax=(kmax+2)/2)
      common r(irmax),ct(ictmax),am(irmax),rking
      dimension rho(irmax,ictmax),phi(irmax,ictmax)
      dimension phi_0(irmax),phi_k(nkmax,irmax),
     1 phi1_k(irmax),phi2_k(irmax),g(nkmax,irmax)
      external plgndr
       pi=3.141592653589793d0
c ---------------------------------------------
      alamda=0.142306067d0
c ---------------------------------
c Calculate the g_k(r) at all the grid points and store them.
c Remember our k runs only over even k: 0,2,4,6,....
c We will do this by defining g_k(ir)=g(nk,ir) where k=2*nk-2,
c i.e., nk=(k+2)/2. Thus when nk=1,2,3,4,...., k=0,2,4,6,....
c ---------------------------------
```

```
431           g(1,1)=rho0
432           do 21 nk=1,nkmax
433            k=2*nk-2
434             if(nk.ge.2)g(nk,1)=0.d0
435             do 22 ir=2,irmax
436  c The integration is done by the trapizoidal method. plgndr
437  c are the Legendre polynomials.
438               area=0.d0
439                 do 23 ict=1,(ictmax-1)
440                  area=area+0.5d0*(ct(ict+1)-ct(ict))*(rho(ir,ict)
441         1          *plgndr(k,0,ct(ict))+rho(ir,ict+1)
442         2           *plgndr(k,0,ct(ict+1)))
443   23              continue
444               g(nk,ir)=(2.d0*k+1.d0)*area
445   22          continue
446   21          continue
447  c All g_k(r) have been calculated and stored as g(n,ir)
448  c with k=2n-2
449  c ---------------------------------------------------
450  c Now do the four integrals to get phi_k at every grid points
451  c Again do all integrals by brute force area sum over a
452  c fine grid.
```

```
c ---------------
        phi_0(1)=phi0
c vint1=int_0^r(ir) (t*g_0(t))dt.
c vint2=int_0^r(ir) (t*t*g_0(t))dt
c The integrals are identified by their upper limits.
        vint1=0.d0
        vint2=0.d0
        am(1)=0.d0
c am(ir) is the mass contained within r(ir).
        do 31 ir=2,irmax
          vint1=vint1+0.5d0*(r(ir)-r(ir-1))*(r(ir)*g(1,ir)
     1      +r(ir-1)*g(1,ir-1))
          vint2=vint2+0.5d0*(r(ir)-r(ir-1))*(r(ir)*r(ir)*g(1,ir)
     1      +r(ir-1)*r(ir-1)*g(1,ir-1))
         phi_0(ir)=phi0+alamda*(vint1-vint2/r(ir))
         am(ir)=4.d0*pi*2.6324d07*vint2
c am is in units of M_sun.
c Note that the above way of doing the integrals gives
c phi_0(1)=phi_0(2)=phi0, which is consistent with the
c boundary condition that the radial derivative of phi
c at origin is zero.
 31     continue
```

```
475  c ------------------------
476  c Now do vint3=int_r^infty t^(1-k)g_k(t)dt
477           do 41 nk=2,nkmax
478             k=2*nk-2
479             vint3=0.d0
480             phi1_k(1)=0.d0
481             phi1_k(irmax)=0.d0
482  c ---------------
483  c             iirmax=irmax-1
484             do 42 ir=(irmax-1),2,-1
485  c now the integrals are identified by their LOWER limit
486               vint3=vint3+0.5d0*(r(ir+1)-r(ir))*(r(ir)**(1-k)*
487         1       g(nk,ir)+r(ir+1)**(1-k)*g(nk,(ir+1)))
488               phi1_k(ir)=r(ir)**k*vint3
489    42         continue
490  c ------------------------------------------------------
491  c vint4=int_0^r t^(k+2)g_k(t)dt
492  c The integrals are again identified by their UPPER limits.
493             vint4=0.d0
494             phi2_k(1)=0.d0
495  c ----------------
496               do 43 ir=2,irmax
```

```
497               vint4=vint4+0.5d0*(r(ir)-r(ir-1))*(r(ir)**(k+2)*
498      1          g(nk,ir)+r(ir-1)**(k+2)*g(nk,(ir-1)))
499               phi2_k(ir)=r(ir)**(-k-1)*vint4
500   43        continue
501   c ------------------------------------------------------
502             do 44 ir=2,irmax
503               phi_k(nk,ir)=(-alamda/(2.d0*k+1.d0))*
504      1          (phi1_k(ir)+phi2_k(ir))
505   44        continue
506   c ------------------------------------------------------------
507   c Since in the above nk loop, ir runs from 2, we need to
508   c supply the value for ir=1, i.e., the origin also. So,
509           phi_k(nk,1)=0.d0
510   c Also, in the above, nk loop runs from only 2. So we need
511   c to give the value for nk=1 (i.e., k=0) also, which we
512   c give below in the ir loop.
513   41    continue
514   c ------------------------------------------------------------
515         do 51 ict=1,ictmax
516           phi(1,ict)=phi0
517   51    continue
518   c ---------------------------------------
```

```
519          do 52 ir=1,irmax
520            phi_k(1,ir)=phi_0(ir)
521   52     continue
522   c ------------------------------------
523          do 61 ir=2,irmax
524            do 62 ict=1,ictmax
525              sumphi=0.d0
526              do 63 nk=1,nkmax
527                k=2*nk-2
528                sumphi=sumphi+phi_k(nk,ir)*plgndr(k,0,ct(ict))
529   63           continue
530              phi(ir,ict)=sumphi
531   62         continue
532   61       continue
533   c ------------------------------------------------------
534          return
535          end
536   c *******************************************************
537          double precision FUNCTION PLGNDR(L,M,X)
538   c This subroutine defines the Legendre polynomials needed for
539   c the Poisson Solver. See Numerical Recipes
540          implicit real*8(a-h,o-z)
```

```
      IF (M.LT.0.OR.M.GT.L.OR.ABS(X).GT.1.d0)PAUSE 'bad arguments'
      PMM=1.d0
      IF (M.GT.0) THEN
        SOMX2=DSQRT((1.d0-X)*(1.d0+X))
        FACT=1.d0
        DO 11 I=1,M
          PMM=-PMM*FACT*SOMX2
          FACT=FACT+2.d0
11      CONTINUE
      ENDIF
      IF (L.EQ.M) THEN
        PLGNDR=PMM
      ELSE
        PMMP1=X*(2*M+1)*PMM
        IF (L.EQ.M+1) THEN
          PLGNDR=PMMP1
        ELSE
          DO 12 LL=M+2,L
            PLL=(X*(2*LL-1)*PMMP1-(LL+M-1)*PMM)/(LL-M)
            PMM=PMMP1
            PMMP1=PLL
12        CONTINUE
```

```
563               PLGNDR=PLL
564             ENDIF
565           ENDIF
566           RETURN
567           END
568   c ***********************************************************
569           SUBROUTINE QSIMP(FUNC,A,B,S)
570   c This defines an integration by Simpson's method.
571   c See Numerical Recipes
572            implicit real*8(a-h,o-z)
573           PARAMETER (EPS=1.d-4, JMAX=20)
574           OST=-1.d30
575           OS= -1.d30
576           DO 11 J=1,JMAX
577             CALL TRAPZD(FUNC,A,B,ST,J)
578             S=(4.d0*ST-OST)/3.d0
579             IF (dABS(S-OS).LT.EPS*dABS(OS)) RETURN
580             OS=S
581             OST=ST
582    11      CONTINUE
583           PAUSE 'Too many steps.'
584           END
```

```
585 c ***********************************************************
586       SUBROUTINE TRAPZD(FUNC,A,B,S,N)
587 c This defines an integration by the trapezoidal rule.
588 c See Numerical Recipes
589        implicit real*8(a-h,o-z)
590       IF (N.EQ.1) THEN
591         S=0.5d0*(B-A)*(FUNC(A)+FUNC(B))
592         IT=1
593       ELSE
594         TNM=IT
595         DEL=(B-A)/TNM
596         X=A+0.5d0*DEL
597         SUM=0.d0
598         DO 11 J=1,IT
599           SUM=SUM+FUNC(X)
600           X=X+DEL
601  11       CONTINUE
602         S=0.5d0*(S+(B-A)*SUM/TNM)
603         IT=2*IT
604       ENDIF
605       RETURN
606       END
```

```
607 c ***********************************************
608         double precision function func0(x)
609 c This is the numerator for the velocity
610 c dispersion calculation
611         implicit real*8(a-h,o-z)
612         common point,sigma
613         func0=x*x*(dexp((point-0.5d0*x*x)/
614        1  (sigma*sigma))-1.d0)
615         return
616         end
617 c ***********************************************************
618         double precision function func2(x)
619 c This is the denominator for the velocity
620 c dispersion calculation
621         implicit real*8(a-h,o-z)
622         common point,sigma
623         func2=x*x*x*x*(dexp((point-0.5d0*x*x)/
624        1  (sigma*sigma))-1.d0)
625         return
626         end
627 c ***********************************************************
```